



**ScuDo**  
Scuola di Dottorato ~ Doctoral School  
WHAT YOU ARE, TAKES YOU FAR

Doctoral Dissertation  
Doctoral Program in Mechanical Engineering (29<sup>th</sup> Cycle)

# **Thermomechanical Response of Advanced Materials under Quasi-Instantaneous Heating**

## **PhD Thesis**

By

**Federico Carra**

\*\*\*\*\*

**Supervisor(s):**

Prof. L. Peroni

Alessandro Bertarelli

**Doctoral Examination Committee:**

Prof. M. Avalle, Università degli Studi di Genova

Prof. M. Beghi, Politecnico di Milano

Prof. D. Paolino, Politecnico di Torino

Prof. G. Valentino, University of Malta

Prof. D. Ziemanski, Cracow University of Technology

Politecnico di Torino  
2017



## Declaration

I hereby declare that, the contents and organization of this dissertation constitute my own original work and does not compromise in any way the rights of third parties, including those relating to the security of personal data.

Federico Carra

2017

\* This dissertation is presented in partial fulfillment of the requirements for **Ph.D. degree** in the Graduate School of Politecnico di Torino (ScuDo).



## **Acknowledgment**

I would like to warmly thank my CERN supervisor Alessandro Bertarelli for all the help, support and teachings provided in these years, and Prof. Lorenzo Peroni for the possibility he gave me to pursue this PhD program.

A special thanks goes to all the guys of the engineering unit in the CERN design office, that contributed to this work with discussions and ideas: Linus Mettler, Paolo Gradassi, Antonio Lafuente, Joanna Swieszek, Michele Pasquali, Giorgia Gobbi, Carlotta Accettura, Carlo Zanoni, Claudio Fichera, Marco Garlasché, Nicola Mariani, Guillaume Maitrejean, Norbert Kuder, Jorge Guardia and I'm probably forgetting someone. Also thanks to Alessandro Dallochio and Martina Scapin, who inspired the concepts explored in this PhD thesis and helped me a lot at CERN and at Politecnico di Torino.

Finally, I would like to thank the CERN colleagues from my group, EN-MME, for the constant support, and in particular the people of the Mechanical Measurements Laboratory for the numerous tests done on the materials studied in this project. I also acknowledge the work of several people from the BE-ABP and EN-STI groups, for the particle tracking and energy deposition calculations which constituted the input data for my thermomechanical numerical analyses.

Part of the work described in this thesis was developed in the scope of the EuCARD-2 Project, WP11 "ColMat – HDED", co-funded by the partners and the European Commission under Capacities 7<sup>th</sup> Framework Programme, Grant Agreement n. 312453. The research leading to these results has also received

funding from the European Union's Horizon 2020 Research and Innovation programme under Grant Agreement n. 730871.

## **Abstract**

The study of the thermomechanical response of materials to a time-dependent heat load is of paramount importance in the design of a variety of components widely adopted in the industry and in research laboratories. Three regimes can be identified in the thermomechanical problem, depending on the heating rate: quasi-static, slow-transient and quasi-instantaneous heating. This PhD thesis focuses on the latter scenario, where the heat deposition rate is high enough to lead to the origination of stress waves, propagating from the locally-heated zone to the surrounding of the structure, and superposing with the quasi-static stress field.

In the first part of the thesis, the dynamic response of materials to quasi-instantaneous heating is evaluated as a function of the stress waves generated. At low thermal energies, stress waves remain below the yield stress of the material, in the elastic regime. When the amplitude of the wave surpasses the yield stress of the material, plasticity takes place and the signal is dispersed into an elastic wave travelling at the speed of sound, and plastic waves at lower velocity. Finally, the shock regime can be attained only at critical levels of energy and pressure induced by the fast heating. This scenario features a sharp discontinuity in temperature, pressure and density, requiring the adoption of finite element codes for the solution of the thermomechanical problem. The hydrostatic response of shocked materials depends on the equation of state (EOS), while the deviatoric contribution to the stress tensor is controlled by the strength model. Failure models govern fracture mechanisms due to void coalescence, spallation and micro-spallation. Examples of the main categories of EOS, strength and failure models, are given in this thesis. A

new method to explore unusual regions of the EOS, based on intense isochoric heating driven by particle beams, is also introduced.

In the second part of the thesis, the several phenomena induced by a quasi-instantaneous heating, due to particle beam impact on the matter, are explored in detail. Such phenomena involve changes of phase, cylindrical pressure waves at the elastic, plastic and shock regime, as well as spallation and micro-spallation fracture. To explore each of these mechanisms, numerical studies by means of implicit and explicit finite element codes are presented and combined, when available, with analytical methods and experimental tests performed in particle accelerator facilities.

In the final part of the thesis, the studies performed are applied to the design and engineering of CERN HL-LHC accelerator components known as collimators. These components, closely interacting with the beam particles, are potentially submitted to accidental impacts, whose consequences on the collimator and on the overall machine must be minimized. With this goal, new composites were developed at CERN in recent years to replace the carbon-fibre-reinforced carbon (CFC) currently adopted in the present LHC, combining the good thermal and electrical properties of metals with the high thermal stability of carbon allotropes such as graphite and diamond. The most promising ones are Copper-Diamond (CuCD) and Molybdenum-Graphite (MoGr); these materials were fully characterized in order to derive EOS and constitutive models necessary for the study of their response under intense isochoric heating. To prove the accuracy of such models, and to experimentally verify the collimator resistance under the direct impact of proton beams involving energy densities typical of the HL-LHC design scenarios, a test was devised and performed in 2015 at the CERN HiRadMat facility. Three collimator jaws, in CFC, MoGr and CuCD, were extensively instrumented, and submitted to proton impacts at increasing intensities.

Experimental results of the tests and comparisons with the numerical predictions are presented.

## Publications

Some concepts and figures have appeared previously in the following publications:

F. Carra *et al.* (2017). The “Multimat” experiment at CERN HiRadMat facility: advanced testing of novel materials and instrumentation for HL-LHC collimators. *Journal of Physics: Conference Series*, Vol. 874, Issue 1, 20 July 2017, Article number 012001.

M. Scapin, L. Peroni and F. Carra (2016). Investigation and mechanical modelling of pure molybdenum at high strain-rate and temperature. *Journal of dynamic behaviour of materials*, Vol. 2 n. 4, pp. 460-475. ISSN 2199-7446.

M. Scapin, C. Fichera, F. Carra and L. Peroni (2015). Experimental investigation of the behaviour of tungsten and molybdenum alloys at high strain-rate and temperature. *EPJ Web of Conferences*, Vol. 94, 01021.

A. Bertarelli, F. Carra, N. Mariani and S. Bizzaro (2014). Development and testing of novel advanced materials with very high thermal shock resistance. *Proc. Tungsten, Refractory and Hardmetals Conference*, Orlando, May 2014.

F. Carra *et al.* (2014). Mechanical engineering and design of novel collimators for HL-LHC. *Proceedings of IPAC'14*, Dresden, Germany, 2014.

L. Peroni, M. Scapin, F. Carra and N. Mariani (2013). Investigation of dynamic fracture behavior of graphite. In B. Basu, *Damage assessment of structures X*, Trans Tech Publications Inc, pp. 103-110. ISBN 978-303785796-0.

F. Carra *et al.* (2013). Behaviour of advanced materials impacted by high energy particle beams. *Journal of Physics: Conference Series*, Vol. 451, conference 1.

F. Carra, M. Scapin, A. Bertarelli and L. Peroni (2013). Un set-up sperimentale per lo studio del comportamento di materiali impattati da fasci di particelle ad elevata energia. *Proc. 42° Convegno nazionale AIAS*, AIAS 2013 – 232.

A. Bertarelli *et al.* (2013). An experiment to test advanced materials impacted by intense proton pulses at CERN HiRadMat facility. *Nuclear Instruments and Methods in Physics Research B*, Vol. 308, pp. 88–99.

A. Bertarelli, V. Boccone, F. Carra, F. Cerutti, A. Dallochio, N. Mariani, L. Peroni, M. Scapin (2011). Limits for beam induced damage: reckless or too cautious? *Proc. Chamonix 2011: Workshop on LHC Performance*.

# Contents

1. Introduction.....	1
1.1 Quasi-static heating.....	5
1.2 Slow-transient heating.....	6
1.3 Quasi-instantaneous heating .....	8
1.4 Examples of quasi-instantaneous heating events in particle accelerators.....	14
1.5 Inaccuracy of the heat equation at space and time nanoscales .....	22
1.6 Structure of the thesis .....	24
1.7 Glossary.....	25
References.....	27
2. Dynamic deformation and stress waves .....	31
2.1 Elastic waves.....	32
2.2 Plastic waves.....	39
2.3 Shock waves .....	43
2.3.1 Hydrodynamic material state .....	45
2.3.2 Shock in elastoplastic materials .....	49
2.3.3 Considerations on thermally-induced shock waves .....	53
2.4 Glossary.....	55
References.....	57

3. Description of the dynamic response: equation of state and constitutive models .....	59
3.1 Equation of state .....	60
3.1.1 Linear .....	62
3.1.2 Mie-Grüneisen for crystals, porous materials and compounds ....	63
3.1.3 Tabular .....	67
3.1.4 Conventional experimental methods .....	69
3.1.5 EOS study by isochoric heating test .....	70
3.2 Strength models .....	76
3.2.1 Linear viscoelasticity .....	78
3.2.2 Johnson-Cook viscoplasticity .....	81
3.2.3 Zerilli-Armstrong viscoplasticity .....	84
3.3 Failure models .....	86
3.3.1 Johnson-Cook failure model .....	87
3.3.2 Spallation models .....	89
3.4 Glossary .....	92
References .....	95
4. Modelling of phenomena associated to quasi-instantaneous heating .....	99
4.1 Change of phase .....	105
4.1.1 Melting .....	106
4.1.2 Vaporization .....	107
4.1.3 Plasma phase transition .....	108
4.2 Uniaxial stress waves .....	108
4.2.1 Axial oscillations .....	109
4.2.2 Flexural oscillations .....	119
4.3 Cylindrical stress waves .....	121
4.3.1 Elastic and Plastic waves .....	125
4.3.2 Shock waves .....	132

4.4	Stress wave interface interactions .....	138
4.5	Spallation .....	142
4.6	Hydrodynamic tunneling .....	146
4.7	Glossary .....	147
	References .....	151
5.	Novel materials for particle accelerator components .....	156
5.1	LHC collimation system .....	158
5.2	Collimator jaw materials: requirements and development .....	163
5.3	Collimator jaw materials: microstructure and production methods 165	
5.3.1	Carbon-fibre-reinforced carbon .....	165
5.3.2	Molybdenum-Graphite .....	166
5.3.3	Copper-Diamond .....	168
5.4	Characterization campaign and material modelling .....	169
5.4.1	Thermal properties .....	170
5.4.2	Elastic constants .....	171
5.4.3	Strength and failure behaviour .....	175
5.4.4	Summary of results .....	177
5.5	Glossary .....	178
	References .....	179
6.	Experimental testing of novel materials under quasi-instantaneous heat deposition .....	183
6.1	The HiRadMat facility at CERN .....	183
6.2	Collimator materials under proton impact: the HRMT-23 experiment 185	
6.2.1	Design and experimental set-up .....	185
6.2.2	Instrumentation .....	187
6.2.3	Beam parameters .....	191
6.3	HRMT-23 experimental results .....	193

6.3.1	CFC jaw .....	193
6.3.2	MoGr jaw .....	196
6.3.3	CuCD jaw.....	198
6.4	Glossary.....	203
	References.....	203
7.	Numerical analyses of novel materials under quasi-instantaneous heat deposition.....	205
7.1	Numerical models .....	208
7.1.1	Linear elasticity .....	209
7.1.2	Elastoplasticity .....	209
7.2	Numerical results .....	212
7.2.1	CuCD .....	212
7.2.2	MoGr.....	225
7.2.3	CFC.....	230
7.3	Glossary.....	237
	References.....	239
8.	Conclusions .....	240
	References.....	249



# List of Figures

Figure 1. Microstructure of a solid-oxide fuel cell (a), with details of cathode, in lanthanum strontium cobalt ferrite, (b) and anode, in nickel oxide and yttria-stabilized zirconia (c) [1], [2].....	6
Figure 2. Left: Flexural displacement ( $x$ direction) over the time of a 1 meter collimator jaw, simply supported at the extremities, under the effects of a 30 kW load applied for 10 s. The transient analysis is interrupted after 30 s, and the discontinuity in the curve (right) represents an extrapolation of the structure recovering its undeformed position [5]. .....	8
Figure 3. Temperature evolution over time on the cylindrical bar, at the longitudinal position $L = 0.1$ m, for different materials. The heated extremity is at $L = 0$ . .....	12
Figure 4. Pressure evolution over time on the cylindrical bar, at the longitudinal position $L = 0.1$ m, for different materials. The heated extremity is at $L = 0$ . .....	12
Figure 5. Temperature distribution on the LHC dump [16]. Note the spiral pattern dilution. ....	14
Figure 6. Stored energy in current and future particle accelerators.....	16
Figure 7. Plot of maximum deposited power versus duration of deposition, showing the different dynamic responses that can be induced in matter by interaction with particle beams. Points represent cases of beam impacts. Source: [19]. .....	17
Figure 8. Beryllium rods damaged by an off-axis beam impact at the CERN SPS in the 1970s.....	18
Figure 9. Tevatron collimators impacted by 1.8 MJ proton beam: tungsten (left) and stainless steel (right). ....	18
Figure 10. Stainless steel vacuum chamber damaged at the transfer line between the SPS and the LHC (CERN). Vacuum chamber outside (top); inner wall impacted by the beam (centre); inner wall opposite to the beam impact (bottom). .....	19
Figure 11. Effects of impact tests on LHC tungsten collimator, upstream view. Note the presence of two longitudinal grooves and extensive debris on the bottom of the vacuum chamber.....	20

Figure 12. Effects of a 700 kJ proton beam impacting on three tungsten-alloy specimens, numbered 1 to 3. The beam is coming from the left. The ejecta are made of a combination of molten and vaporized fragments, and solid debris.....	21
Figure 13. Functional elements made of novel composites under development at CERN for future beam intercepting devices. Left: Molybdenum-Graphite (MoGr) features a graphitic matrix reinforced with molybdenum carbide, with the possible addition of dopants and carbon fibres. Right: Copper-Diamond (CuCD), the reinforcement is made of diamond particles dispersed in a copper matrix.....	22
Figure 14. (a) Longitudinal wave generated by the application of a dynamic force on the extremity of a cylindrical rod. The particle motion is in the same direction of the wave propagation. (b) Generation of a shear wave by the application of a dynamic torque, with particle displacement orthogonal to the beam axis, and shock travelling along the longitudinal direction.....	36
Figure 15. Hollomon’s hardening law for three metals: stainless steel (blue), $k_1=1400$ MPa, $n_1=0.43$ ; copper (cyan), $k_2=530$ MPa, $n_2=0.44$ ; aluminium alloy (red) $k_3=780$ MPa, $n_3=0.17$ . Source: [8]. .....	40
Figure 16. Wave front on a 2024 aluminum cylinder at given time instants. Note the constant velocity of propagation of the elastic front up to the yield stress. In the plastic domain, the velocity decreases with the increase of stress.....	42
Figure 17. Plastic wave, strain profile as a function of the longitudinal coordinate $x$ at different time instants. ....	43
Figure 18. Shock front, hydrodynamic treatment.....	45
Figure 19. Characteristic Hugoniot curve and Rayleigh line in the pressure vs. specific volume plane.....	49
Figure 20. $\sigma - \epsilon$ curve for a material in uniaxial strain conditions. The extension of the elastic strain has been exaggerated for the sake of clarity.....	51
Figure 21. Hugoniot curve in stress and strain coordinates for an elastic-perfectly plastic material.....	52
Figure 22. Hugoniot curve and Rayleigh line for three different elastic – perfectly plastic materials. ....	54
Figure 23. Regions of interest in an EOS of a fictitious material.....	61
Figure 24. Calculated EOS for Al 2024 T3 with different compaction ratios. Shock parameters are reported in Table 6. The compaction ratio for a solid without porosities is 100%. ....	66

Figure 25. Example of tabular equation of state. The different phases are highlighted. ....	68
Figure 26. SESAME table 3550, built for tungsten. Left: pressure as a function of density and temperature. Right: Energy as a function of density and temperature. ....	69
Figure 27. Idealized shock profile. ....	70
Figure 28. Comparison between a mechanical shock (0-1-2) and an isochoric heating event (0-1'-2). ....	71
Figure 29. HiRadMat beam impact on specimens of six different materials, courtesy of V. Boccone. Inermet, in black, is a 95% tungsten alloy. The specimens are three per material, 3 cm long each. The peak energy, calculated for a beam of transverse size 0.25 mm, is reported in GeV/cm <sup>3</sup> /proton, and has to be scaled by the number of impacting particles. The maximum number of particles per pulse is 3.7×10 <sup>13</sup> . ....	72
Figure 30. Shock on a tungsten target. In green, the shock is induced by a mechanical impact, in red, by a thermal energy deposition. Continuous lines are referred to the load phase and dashed lines to the release phase. ....	76
Figure 31. Elastoplastic material, shock wave and release. ....	77
Figure 32. Generalized Maxwell solid in one dimension, adopted for the definition of uniaxial viscoelastic models in ANSYS [17]. The spring stiffnesses are $\mu^i$ , the dashpot viscosities are $\eta^i$ , and the relaxation time is defined as the ratio of viscosity to stiffness, $\tau^i = \eta^i / \mu^i$ . ....	79
Figure 33. Left: viscoelastic behaviour of an isostatic graphite sample tested at high strain rate in the Hopkinson bar test bench. Right: specimen after the test [15]. ....	81
Figure 34. Johnson-Cook model for molybdenum produced by Plansee (DE). Left: quasi-static tensile test ( $\epsilon = 10 - 3 s - 1$ ); right: dynamic tensile test ( $\epsilon = 103 s - 1$ ) [20]. ....	84
Figure 35. Zerilli-Armstrong models for two pure molybdenum grades and a tungsten heavy alloy (IT180). Effects of temperature and strain rate on the equivalent stress are highlighted [23]. Static tests: $\epsilon = 10 - 3 s - 1$ ; dynamic tests: $\epsilon = 103 s - 1$ . ....	86
Figure 36. Johnson-Cook failure model, definition of fracture strain at large tensile pressure-stress ratios. ....	88

Figure 37. Energy density generated by a proton beam impact on a graphite target rod,  $L = 1$  m,  $\varnothing = 15$  mm, courtesy of M. I. Frankl. The beam energy is 440 GeV and the  $\sigma$  is 0.25 mm. The specific energy is normalized to one proton. ....100

Figure 38. Energy density generated by a proton beam impact on cylindrical targets made of different materials,  $L = 1$  m,  $\varnothing = 15$  mm, courtesy of M. I. Frankl. The beam energy is 440 GeV and the  $\sigma$  is 0.5 mm. Results are normalized to one proton. Note the position of the energy density peak, which is decreasing in amplitude and increasing in depth with the decrease of the material density and atomic number. Inermet is a 95% tungsten alloy, TZM is a 99% molybdenum alloy, Glidcop is a copper grade reinforced by dispersion of aluminium oxide, and copper-diamond is a new composite material developed at CERN with a copper matrix and diamond reinforcements. ....101

Figure 39. Time history of thermal power and energy deposited by impacting bunches on a target. The bunch width  $t_d$  is exaggerated for a simpler reading of the plot. The bunch population is constant. ....102

Figure 40. Phenomena correlated with particle beam impact. 1) Beam impact close to the active surface of a thick target. 2) Impact on a cylindrical rod. ....103

Figure 41. 3D  $p$ - $v$ - $T$  surface for copper. Source: [9].  $M$ , melting region;  $R$ , evaporating region with the critical point,  $CP$ ; solid, liquid, gas, liquid+gas, and plasma (arrows indicate the decrease in plasma nonideality parameter) physical states;  $H1$  and  $Hp$ , principal and porous Hugoniot;  $S$ , release isentropes of shock-compressed metal;  $IEX$ , isobaric expansion;  $DAC$ , static compression in diamond anvil cells;  $LM$ , density of liquid metal at room pressure; and  $LHC$ , states generated in copper by the LHC beam covering strongly coupled plasma region. ....106

Figure 42. Left: dynamic axial stress scaled to  $\sigma_{ref}$  as a function of time at the centre and one quarter of the rod. Right: dynamic stress at the end of the deposition over the length. Source: [17].....110

Figure 43. Ideal wave profile in uniaxial stress conditions (red) and real profile (black).....111

Figure 44. Left: energy and energy density generated by a proton beam impact on a graphite rod. Courtesy of M. I. Frankl. The beam energy is 440 GeV and the  $\sigma$  is 0.25 mm. Results are normalized to one proton. Right: energy deposition profile in the space and reference system; the rod is shown with a section view along the  $YZ$  plane. ....112

Figure 45. Left: specific heat and density of isostatic graphite as a function of temperature. Right: coefficient of thermal expansion as a function of temperature. ....	113
Figure 46. Numerical model, total axial strain over time at $x,y=0$ at three longitudinal positions. ....	114
Figure 47. Left: thermal energy deposition along the transverse coordinate $y$ ( $y = 0$ is the beam axis, $y = -4$ mm = $-h/2$ is the free surface) in the most loaded longitudinal section. Right: Total axial strain over time in the most loaded longitudinal section ( $z = 75$ mm), for different transversal positions. ....	115
Figure 48. Vertical (red) and axial (blue) particle velocity over time at $x = 0$ , $y = h/2$ , $z = L/2$ . ....	116
Figure 49. Left: total axial strain along the rod at $t = t_d$ and $y = -h/2$ . Right: total axial strain as a function of $y$ at upstream and downstream ends, for $t = t_d$ . ....	117
Figure 50. Propagation of the two planar waves from the ends of the rod. $\epsilon_z$ is measured at $y = -h/2$ . After 90 $\mu$ s, the two waves have almost completed $1/2$ period and are close to the opposite ends. ....	118
Figure 51. Reflection of the two waves and return to the initial configuration, after one full period. ....	118
Figure 52. Left: flexural oscillation. Right: flexural dynamic stress. Source: [15], pp. 7–8. ....	120
Figure 53. Left: numerical model, flexural oscillation for an eccentricity $\eta=0.6R$ . Right: dynamic flexural strain. Note that the slow flexural wave superposes with faster axial waves described in section 4.2.1. ....	121
Figure 54. Left: HRMT-14 sample holder. Right: sample geometry. ....	126
Figure 55. Left: geometry for the analysis. Note the graphite ring spacers which are used to separate adjacent samples on the same longitudinal array. Sample diameter is 40 mm and thickness 30 mm. Right: axial section view of the target ( $y$ here is the radius), temperature at the end of the thermal pulse. Beam is coming from the left. Inermet180 matrix melts at 1616 K. ....	127
Figure 56. Left: equivalent plastic strain at the end of the thermal pulse on the M6.2 Inermet180 sample. Right: equivalent plastic strain at $t=500\mu$ s. Deformations are in real scale. ....	129

Figure 57. Left: pressure during the thermal pulse along the target axis ( $r=0$ ), for elements at different $z$ . Right: pressure on three elements at $z=13.5\text{mm}$ , for three different radial coordinates. ....	130
Figure 58. Left: sound speed calculated on three elements at $r=0$ , with different $z$ . Right: flow stress at the end of the simulation ( $t=594\mu\text{s}$ ) saturated at 1 kPa to show the molten material ( $\sigma_y=0$ ). ....	130
Figure 59. Left: Axial strain measurement with strain gauge at $r=20\text{mm}$ , $L=15\text{mm}$ vs. simulation. Right: Radial velocity measurement with LDV at $r=20\text{mm}$ , $L=15\text{mm}$ vs. simulation. ....	130
Figure 60. Upstream (left) and downstream (right) faces of the Inermet180 <i>M6.2</i> specimen impacted by $2.7 \times 10^{12}$ protons at 440 GeV during the HRMT-14 experiment. The droplets on the upstream face come from the near specimen <i>M6.1</i> , which was NEG-coated. Coating melted and deposited on <i>M6.2</i> . ....	132
Figure 61. Optical microscope observations of the Inermet180 <i>M6.2</i> specimen. Left: upstream face 100x. Right: downstream face 500x, with focus on the hole region. ....	132
Figure 62. Temperature (top left), pressure (top right), sound speed (bottom left) and density (bottom right) on the cylinder at $t=1\text{ns}$ . 2D axisymmetric model. The radial coordinate is magnified for the sake of clarity. ....	134
Figure 63. Pressure wave along the radius at $t=50\text{ns}$ . ....	135
Figure 64. Left: pressure wave along the radius, for $z=220\text{mm}$ , at different time instants. Right: pressure during time on three elements with $z=220\text{mm}$ and different radial coordinate. ....	136
Figure 65. Propagation of the pressure wave inside the cylinder, with reflection to the free surface. 2D axisymmetric model. The radial coordinate is magnified for the sake of clarity. ....	137
Figure 66. Density change induced by the wave propagation. 2D axisymmetric model. The radial coordinate is magnified for the sake of clarity. Note the low density value in correspondence of the beam axis, which triggers the hydrodynamic tunnelling (see section 4.6). ....	137
Figure 67. Longitudinal wave propagating from material <i>A</i> to material <i>B</i> . (1): wave propagation before the interface; (2),(3): at the interface, the wave is partly reflected and partly transmitted, with direction of stress and particle velocity depicted for the case $Z_A > Z_B$ . ....	138

Figure 68. Section view of the tertiary collimator jaw. The beam travels along the direction $z$ , orthogonal to the $XY$ plane shown. ....	141
Figure 69. Left: geometry for the analysis. Diameter is 40 mm, length 30 mm; the samples have a half-moon shape, with the flat face offset by 2 mm with respect to a perfect half-cylinder. Right: $H6.2$ sample at the end of the simulation. The hole created by the impact is elliptical, with vertical axis 8.8mm and horizontal axis 7mm. The plastic deformation on the free surface also creates two “lips” spaced vertically by 10.1mm. ....	144
Figure 70. Comparison between acquired image and simulation of $H6.2$ sample 125 $\mu$ s after the impact. On top of the specimen $H6.2$ , in the camera acquisition also $H6.1$ (first from the left) and $H6.3$ (first from the right) are partially visible.....	144
Figure 71. Views of the $H6.2$ Inermet180 specimen after extraction from the HRMT-14 test bench. The crater created by the impact is elliptical, with vertical axis 9.4mm and horizontal axis 8.7mm. The plastic deformation on the free surface also creates two “lips” spaced vertically by 13.3mm. ....	145
Figure 72. Density history in the case of 1 FCC bunch impacting on a copper target. Simulation parameters reported in section 4.3.2. Three elements along the axis ( $r=0$ ) are shown. ....	146
Figure 73. CERN accelerator complex. ....	157
Figure 74. Scheme of the LHC collimation system, courtesy of E. Quaranta. ....	159
Figure 75. 3D view of the HL-LHC collimator. ....	160
Figure 76. HL-LHC collimator jaw section. ....	161
Figure 77. Left: MoGr plate for prototyping (150 $\times$ 100 $\times$ 25 mm <sup>3</sup> ). Right: CuCD samples for bending tests. ....	165
Figure 78. Left: CFC jaw of an LHC secondary collimator. Right: Microscopy of a pitch-derived carbon fibre. Source: [16]. ....	166
Figure 79. SEM observation of MoGr polished surface. The graphite matrix is dark grey and the carbide particles are light grey. ....	167
Figure 80. Optical observation of copper-diamond surface. ....	169
Figure 81. Left: thermal expansion coefficient and right: specific heat of the collimator materials. The reference system is the same reported in Figure 76. ..	170

Figure 82. Left: thermal conductivity and right: thermal diffusivity of the collimator materials. The reference system is the same reported in Figure 76. ..	171
Figure 83. Left: scheme of the experimental setup for acquisition of the flexural frequencies of material plate-like specimens. Right: numerical modal analysis, first flexural mode. ....	174
Figure 84. Left: scheme of the experimental setup for acquisition of the torsional frequencies of material plate-like specimens. Right: numerical modal analysis, first torsional mode. ....	174
Figure 85. Left: fixture for 4-point bending tests. Right: flexural strength of CuCD [14].....	176
Figure 86. Left: flexural strength of CFC. Right: flexural strength of MoGr [14]. ....	176
Figure 87. HiRadMat facility, experimental area. ....	185
Figure 88. CFC (top), MoGr (bottom left) and CuCD (bottom right) jaws. .	186
Figure 89. Left: three-jaw stack, simply supported at the extremities. Right: tank section view. Note the vacuum windows position and the protection shielding. ....	186
Figure 90. HRMT-23 test bench. The light for visual inspections is provided by a LED system. ....	187
Figure 91. Left: HiRadMat experimental area. Right: bunker for the electronics. ....	187
Figure 92. Left: HL-LHC jaw section, strain gauge and temperature probe configuration. Right: movable mirror for laser-Doppler vibrometer and HD camera acquisition. ....	188
Figure 93. Strain gauges and temperature probes on CFC (left) and CuCD (right) jaws.....	189
Figure 94. Left: water reservoir connections for the two HL-LHC jaws. Right: optical fibres on the CuCD jaw.....	190
Figure 95. Comparison of peak energy depositions on MoGr for HL-LHC and HiRadMat beams. Fluka analysis courtesy of E. Skordis.....	192
Figure 96. Views of the damage on the downstream Glidcop tapering of the CFC jaw. The high temperatures generated by the impact are also highlighted by the oxidation of the Glidcop surface and of the BPM button. ....	193

Figure 97. View of a section (between 80 and 280 mm along $z$ ) of the CFC jaw after extraction from the tank. Top right: zoom of the two scratches at $\eta y = -2.5 \text{ mm}$ and $\eta y = +2.5 \text{ mm}$ . .....	195
Figure 98. View of the downstream MoGr tapering. No sign of damage to the component or to the BPM is evident. ....	197
Figure 99. View of a section (between 130 and 390 mm along $z$ ) of the MoGr jaw after extraction from the tank. Top right: zoom of the scratch at $\eta y = 0$ . ....	197
Figure 100. View of the downstream MoGr tapering of the CuCD jaw. No sign of damage to the component or to the BPM is evidenced. ....	199
Figure 101. Micro-jetting and micro-spallation of the CuCD jaw under the <i>impact #39</i> (48 bunches impacting at a distance of 0.18 mm from the free surface). .....	200
Figure 102. View of the first 37 cm of the CuCD jaw. Note the longitudinal grooves produced by the impacts at medium and high intensity. ....	201
Figure 103. Detailed view of the effect of impacts on the CuCD jaw at different vertical positions. ....	201
Figure 104. <i>Impacts #45</i> and <i>#46</i> . Note the cracks generated on the free surface of the jaw and the damage at the block/block contact. ....	202
Figure 105. Specific heat of copper, Glidcop and CuCD as a function of temperature. The specific heat of CuCD is calculated by rule of mixture above 600 °C, with the diamond properties with temperature referenced in [3]. ....	207
Figure 106. Temperature on the downstream tapering of the CFC jaw after <i>impact #13</i> (left) and <i>impact #7</i> (right). Areas in red are above the melting point of Glidcop. The model is symmetric on the section plane parallel to $XZ$ . The main difference between the two cases is the $\eta_x$ parameter, equal to 3.05 mm in <i>impact #7</i> , and to 5 mm in <i>impact #13</i> . ....	208
Figure 107. Schematic of the 4-point bending test (left) and axial strain and stress distribution through the thickness of the sample (right). ....	210
Figure 108. Left: Applied bending moment as a function of the measured strain at the bottom face of the sample. Right: flexural strength $\sigma f_{emaxtot}$ (blue), the hardening curve $\sigma eq_{\epsilon eq tot}$ (red) and $\sigma eq_{\epsilon eq pl}$ (black) for the CuCD bending test. ....	212

Figure 109. Strain gauge positioning and nomenclature, with the acquired strain direction in each point under parenthesis. <i>T</i> is the top face, <i>B</i> the bottom face, <i>BF</i> the back face, <i>FFT</i> and <i>FFB</i> the front face top and bottom gauges.....	212
Figure 110. Left: energy peak on the CuCD absorber over the <i>z</i> coordinate for impact #32. Right: total energy per longitudinal section. FLUKA maps are courtesy of E. Skordis.....	213
Figure 111. Left: temperature distribution after <i>impact #32</i> on the CuCD jaw. The peak is found on the 3 <sup>rd</sup> CuCD block. The model presents a symmetry along the section plane parallel to <i>XZ</i> . Right: temperature distribution on the 5 <sup>th</sup> CuCD block ( <i>z</i> = 400 ÷ 500 mm).....	213
Figure 112. Left: single CuCD block FE model. Right: model of a jaw section around a single-block. The models are symmetric along a plane parallel to <i>XZ</i> .	215
Figure 113. Left: FE model of three adjacent CuCD absorber blocks including the clamps, housing and cooling pipes. Right: FE mesh of a full collimator jaw. The models are symmetric along a plane parallel to <i>XZ</i> .	215
Figure 114. <i>Impact #32</i> , CuCD: transverse strain on the back face of block 5, single-block model. Comparison between experimental data, elastic model and elasto-plastic model.....	217
Figure 115. <i>Impact #32</i> on CuCD, Fourier transform of measurement and simulation (top left and right). Note that much of the high-frequency content in the measurement signal is attributable to the intrinsic noise of the probes (bottom).	218
Figure 116. <i>Impact #32</i> , CuCD, transverse strain on the back face of block 5: comparison between different FE models. ....	218
Figure 117. <i>Impact #32</i> , CuCD, transverse strain on the back face of block 5: three-block model with varying coefficient of friction (frictional: $c_f = 0.3$ ; frictionless: $c_f = 0$ ).....	219
Figure 118. Homogeneous elastic (top right), homogeneous viscoelastic (bottom left) and mesoscale elastic (bottom right) models of a CuCD rod impacted at the left side with the sine excitation with half-period 2 $\mu$ s shown on the top left. The 2D model assumes plain strain conditions.....	221
Figure 119. Pressure wave along the bar transverse coordinate in the three different models, as a response to the sine excitation with half-period 2 $\mu$ s shown in Figure 118: homogenous elastic (top left), homogeneous viscoelastic (top right) and inhomogeneous mesoscale elastic (bottom).....	222

Figure 120. Pressure wave along the bar transverse coordinate in the three different models, as a response to the sine excitation with half-period  $10 \mu\text{s}$  (bottom right): homogenous elastic (top left), homogeneous viscoelastic (top right) and inhomogeneous mesoscale elastic (bottom). .....223

Figure 121. Qualitative temperature evolution for the beam parameters of the analysed CuCD *impact #32*: 4 batches of 6 bunches each, with 50 ns bunch length and 225 ns spacing between batches (top). The largest amplitudes are below 450 kHz but there is some notable frequency content up to about 2MHz (bottom)...224

Figure 122. Left: energy peak on the MoGr absorber over the  $z$  coordinate for *impact #26*. Right: total energy per longitudinal section. FLUKA maps are courtesy of E. Skordis.....225

Figure 123. Left: temperature distribution after *impact #26* on the MoGr jaw. The peak is found on the 2<sup>nd</sup> MoGr block. The model presents a symmetry along the section plane parallel to XZ. Right: temperature distribution on the 8<sup>th</sup> MoGr block ( $z = 875 \div 1000 \text{ mm}$ ), which is loaded with the highest total energy (Figure 122, right). .....226

Figure 124. *Impact #26*, MoGr: transverse strain on the bottom face of block 8. Time history of 300  $\mu\text{s}$  (left) and 1.5 ms (right). .....227

Figure 125. *Impact #26*, MoGr: transverse strain on the bottom face of block 8. Comparison between experimental and numerical results. ....228

Figure 126. *Impact #26* on MoGr: Fourier transform of measurement and simulation (top left and right). An FFT of the acquired signal before the impact, indicative of the noise, is also shown (bottom).....229

Figure 127. Left: energy peak on the CFC absorber over the  $z$  coordinate for *impact #7*. Right: total energy per longitudinal section. FLUKA maps are courtesy of E. Skordis.....231

Figure 128. Left: temperature distribution after *impact #7* on the CFC absorber. Right: section view of the absorber along a plane parallel to XZ, vertically offset by  $-5 \text{ mm}$ , showing the maximum temperature achieved.....231

Figure 129. *Impact #7*, CFC: experimental transverse and axial strain on the back face of the jaw, at a longitudinal coordinate  $z = 780 \text{ mm}$ . .....233

Figure 130. *Impact #7*, CFC: numerical transverse and axial strain on the back face of the jaw, at a longitudinal coordinate  $z = 780 \text{ mm}$ .....234

Figure 131. <i>Impact #7</i> , CFC: images of the total axial strain at different time instants: 7.85 $\mu\text{s}$ (top left), 25 $\mu\text{s}$ (top right), 50 $\mu\text{s}$ (center left), 75 $\mu\text{s}$ (center right), 100 $\mu\text{s}$ (bottom left) and 150 $\mu\text{s}$ (bottom right).....	235
Figure 132. HRMT-23 post-mortem: dismounting of the MoGr jaw (left) and of the oxidized BPM button of the CFC downstream tapering (right).....	245
Figure 133. HRMT-23 post-mortem: CuCD block 4, upstream (left) and downstream (right). .....	245
Figure 134. M6 specimens in MoGr for experimental characterization with the split-Hopkinson pressure bar. ....	246
Figure 135. Inner view of the Multimat test bench. The aluminum tank is hidden in this view. The beam comes from the right. ....	247
Figure 136. Left: mock-up of the Geneva mechanism. Right: driven wheel parameters as function of the cam angle. ....	248
Figure 137. Left: specimen supporting system. Right: carbon foam rod.....	248
Figure 138. Examples of potential industrial applications for the novel metal-carbon and ceramic-carbon composites under development for particle accelerators, studied in this PhD thesis.....	249

## List of Tables

Table 1: Velocities of elastic waves.....	10
Table 2: Velocities of elastic waves with different boundary conditions. ....	39
Table 3: Coefficients of the Hugoniot equation. Source: [1] p. 108, [9], [10]. .....	48
Table 4: Thermophysical properties. Source: [13] .....	53
Table 5: Critical shock stress and strain for the three materials, compared with the strain level experienced at the onset of melting. ....	55
Table 6: Shock and thermodynamic properties. Source: [3], p. 133. ....	64
Table 7: Johnson-Cook constitutive constants, calculated for $\epsilon_0 = 1 \text{ s}^{-1}$ and $T_r = \text{room temperature}$ . Source: [19]. ....	83

Table 8: Zerilli-Armstrong constants for BCC and FCC materials. Source: [21]. .....	85
Table 9: Johnson-Cook failure model constants. Source: [21],[24]. .....	89
Table 10: Comparison between theoretical spall strength of brittle materials, calculated with the Grady model, and experimental measurements. Source: [26]. .....	91
Table 11: Comparison between theoretical spall strength of ductile materials, calculated with the Grady model, and experimental measurements. Source: [26]. .....	92
Table 12: Isostatic graphite properties and parameters of the impacting proton beam. $E_k$ is the particle energy, $n_{tot}$ the total number of protons and $t_d$ the pulse length. $L$ , $W$ and $H$ are the dimensions along $x$ , $y$ and $z$ . .....	113
Table 13: Properties of Inermet180 adopted in the simulations of HRMT-14 [29]. The fracture energy is used in the failure model to simulate the creation and propagation of a crack. ....	128
Table 14: Beam impact parameters for tests at medium ( <i>type 1</i> specimens) and high intensity ( <i>type 2</i> ). This section focuses on the medium intensity tests.....	128
Table 15: Material models [32],[33] and beam parameters for the impact of an FCC proton bunch on an OFE-Copper target 1 m long and 8 mm in diameter. The Fluka maps were kindly provided by Y. Nie. ....	133
Table 16: Shock impedance for different materials. The sound speed is calculated in uniaxial stress conditions. ....	140
Table 17: LHC and HL-LHC operational parameters. $E_k$ is the particle energy, $\Delta t$ the bunch spacing, $N_b$ the number of bunches, $n_b$ the number of particles per bunch, $E_{tot}$ the total energy stored in the beam, $L$ is the ring circumference, $R$ the bending radius and $f$ the revolution frequency.....	158
Table 18: Summary of thermo-physical properties of the collimator materials; results reported are at room temperature. For temperature-dependent results, see Figure 81 and Figure 82.....	177
Table 19: HiRadMat beam parameters. ....	184
Table 20: HRMT-23 instrumentation summary. ....	188

Table 21: HRMT-23 parameters. $\eta_x$ is the horizontal distance between the impact point and the free surface of the jaw absorber, $N_p$ is the total number of thermal pulses, $E_{tot}$ is the maximum energy stored in a proton pulse.....	191
Table 22: HRMT-23, high-intensity impacts on the CFC jaw. $N_b$ is the number of bunches, $n_{tot}$ the pulse intensity, $E_{tot}$ the stored beam energy, $t_d$ the pulse length, $\eta_x$ and $\eta_y$ are the horizontal and vertical beam impact coordinate with respect to the origin of the coordinate system defined in Figure 92.....	194
Table 23: HRMT-23, high-intensity impacts on the MoGr jaw. ....	196
Table 24: HRMT-23, medium and high intensity impacts on the CuCD jaw. ....	199
Table 25: Summary of the elastic constants for the three jaw materials. The reference system is always as per Figure 75.....	209
Table 26: Characteristics of the case study for CuCD.....	213
Table 27: CuCD homogeneous and inhomogeneous model parameters. ....	221
Table 28: Characteristics of the case study for MoGr. ....	225
Table 29: Characteristics of the case study for CFC.....	231



# Chapter 1

## Introduction

The study of the effects of a temperature change on materials has been of paramount importance in engineering since the beginnings of human history. A change of temperature, positive or negative, in a component, induces deformations, strains and stresses which can potentially lead to the component failure. *Vice versa*, the mechanical energy dissipated, for example, in a braking system, or in an impact between a projectile and a target, is converted in thermal energy provoking a rapid increase of the temperature of the elements. The focus of this PhD thesis is more on thermal energy – driven events; however, the mechanical and the thermal problems are, in most of the cases, strictly coupled. The solution methods involve the use of thermodynamics and classic mechanics equations, and the definition of the material equation of state, which constitutes the bridge between the two problems.

For adiabatic problems, the evolution of temperature  $\Theta^l$  in space and time  $t$  on a body under a volumetric heat source  $S$  is governed by the heat equation:

$$C \frac{\partial \Theta}{\partial t} = \nabla \cdot (k \nabla \Theta) + S \quad (1.1)$$

where  $C$  is the material volumetric heat capacity, calculated as the product of specific heat and density, and  $k$  the thermal conductivity. If the material is

---

<sup>1</sup> We prefer in this chapter the notation  $\Theta$  for the temperature [1], to avoid possible confusion with the wave period  $T$ .

*homogeneous* and *isotropic*, its physical properties do not change from point to point and with material orientation, and Eq. (1.1) becomes:

$$\frac{\partial \theta}{\partial t} = a \nabla^2 \theta + \frac{S}{C} \quad (1.2)$$

This is a second-order parabolic partial differential equation (PDE). The parameter  $a$  is called *thermal diffusivity*, calculated as the ratio between the thermal conductivity and the volumetric heat capacity. The thermal diffusivity defines the heat transfer rate of the material and is therefore a key element in the study of transient problems. This equation is known as the *second Fourier's law*, as it can be derived substituting the *first Fourier's law*:

$$\vec{q} = -k \nabla \theta \quad (1.3)$$

in the first law of thermodynamics ( $\vec{q}$  is the heat flux vector):

$$C \frac{\partial \theta}{\partial t} + \nabla \cdot \vec{q} = 0 \quad (1.4)$$

An unconstrained body submitted to an increase or decrease in temperature will experience a change in volume  $V$  depending on its *volumetric thermal expansion coefficient*  $\beta$ , defined as:

$$\beta = \frac{1}{V} \frac{dV}{d\theta} \quad (1.5)$$

The CTE  $\beta$  is expressed in  $K^{-1}$  and is a function of temperature; however, over limited temperature ranges, it can be averaged to a constant value.

The associated change in length along the body directions, which corresponds to the *thermal strain*  $\varepsilon$ , is related to the *linear thermal expansion coefficient*  $\alpha$ :

$$\alpha_{ij} = \frac{\partial \varepsilon_{ij}}{\partial \theta} \quad (1.6)$$

where the strain  $\varepsilon$  and the linear CTE  $\alpha$  are second-rank symmetric tensors. Over a small temperature range  $\Delta T$ ,  $\varepsilon$  can be assumed directly proportional to  $\alpha$ , and the

general constitutive relationship between stress and strain is given by the *Duhamel-Neumann law*:

$$\sigma_{ij} = C_{ijkl}\varepsilon_{kl} - C_{ijkl}\alpha_{kl}\Delta\theta \quad (1.7)$$

The equation contains the components of the fourth-order stiffness tensor  $C_{ijkl}$ . The stiffness tensor has, in the most general case, 36 independent components, which are reduced to 21 in the linear elastic case. For isotropic materials, the independent components are only 2, and the CTE is identical in every direction. The two independent components typically used to build the stiffness tensor of an isotropic materials are the *Lamé parameters*  $\lambda$  and  $\mu$ , or the *Young's Modulus*  $E$  and the *Poisson's ratio*  $\nu$ . In the latter case, through the Duhamel-Neumann equation, the strains and stresses on the body can be written explicitly as:

$$\varepsilon_{ij} = \frac{1}{E} [(1 + \nu)\sigma_{ij} - \nu\delta_{ij}\sigma_{kk}] + \alpha\delta_{ij}\Delta\theta \quad (1.8)$$

$$\sigma_{ij} = \frac{E}{(1 + \nu)(1 - 2\nu)} [(1 - 2\nu)\varepsilon_{ij} + \nu\delta_{ij}\varepsilon_{kk}] - \delta_{ij} \frac{E\alpha\Delta\theta}{1 - 2\nu} \quad (1.9)$$

In this case, the linear CTE  $\alpha$  can be easily derived from the volumetric thermal expansion coefficient  $\beta$  by the relationship  $\alpha = \beta/3$ . We also note that free thermal expansion, or contraction, of a homogeneous and isotropic body induces only normal strain components. The deformation, therefore, is only volumetric and, if the temperature change is uniform throughout, the shape of the body is maintained.

The case just discussed describes a null stress field and is, in practice, extremely uncommon. Even on linear isotropic materials, thermal stresses are almost always a direct consequence of a temperature change. Under the effects of a thermal load, a temperature gradient, and therefore a stress field, will always develop on a material with a finite thermal conductivity, even when the heating or cooling ramps are negligible, as is evident from Eq. (1.2). A fast thermal load application can then further increase the thermal gradient, as also the first term of Eq. (1.2) appears.

In inhomogeneous bodies, a thermal stress will originate even when the gradient is negligible, which can happen in case of high conductivity and/or small size of the body. For example, in a component made of two welded elements with different CTE, a constant temperature over the volume would still imply a

differential thermal expansion (or contraction, for negative  $\Delta\theta$ ) of the two elements and the generation of stresses due to the constrained interface.

Finally, in the simplest case of a linear isotropic and homogeneous body with constant temperature gradient, thermal stresses can still originate if the free deformation is impeded, which is typically what happens in hyperstatic structures. In this case, Eq. (1.9) is reduced to:

$$\sigma_{ij} = -\delta_{ij} \frac{E\alpha\Delta\theta}{1-2\nu} \quad (1.10)$$

or, for a 1D element:

$$\sigma_{11} = -E\alpha\Delta\theta \quad (1.11)$$

Up to this point, we have not focused much on the nature of the thermal load. The only difference between heating and cooling is the sign of the term  $\Delta\theta$ , which is positive in the case of heating, inducing a thermal expansion, and negative in the case of cooling, inducing a thermal contraction. This work focuses on quasi-instantaneous thermal load applications and, as a matter of fact, from the practical point of view it is much easier and common to rapidly inject energy into a system than to remove it. From now, we will thus concentrate on heating-related thermomechanical problems, keeping in mind that most of the concepts would be valid also for cooling problems.

For the sake of simplicity, we can group the thermomechanical problems into three scenarios, based on the thermal load application rate:

- *Quasi-static heating*: the variation of temperature over time is negligible and the temperature gradient for a given load depends on the material thermal conductivity. The steady-state thermal and structural problems can usually be solved sequentially, with the field of stress, strain and displacement depending on the temperature gradient.
- *Slow-transient heating*: the variation of temperature over time is non-negligible, but the heating rate is low enough to allow dynamic effects due to mass inertia of the structure to be neglected. Typically, this scenario can then still be solved with good approximation disentangling the thermal and the structural problems.

- *Quasi-instantaneous heating*: when the heating occurs in a very short time, the core material expansion is prevented by its mass inertia. The dynamics of the problem can no longer be ignored, as the pressure waves generated by the rapid heating superpose with the quasi-static stresses described, in the linear isotropic and homogeneous case, by Eq. (1.9).

The following sections give some practical examples of the different scenarios, focusing in particular on the quasi-instantaneous heating problems which are the core of this thesis.

## 1.1 Quasi-static heating

In quasi-static scenarios, one assumes that the heating process is so slow that the temperature change over time is negligible. In this condition, Eq. (1.1) is reduced to:

$$S = -k\nabla^2\theta \quad (1.12)$$

The parameter controlling the temperature distribution on a body submitted to a given heat source is therefore the thermal conductivity. Typically, in industrial applications, high-conductivity materials are used in cooling systems to minimize the temperature peaks in working conditions. The standard choice, because of the good thermal properties and the relatively low price, is copper. On the other hand, as discussed, the stresses induced on a component by a temperature increase depend also on the differential CTEs of the constitutive parts. This is a challenge in the manufacturing of electronics, for example on CPUs, where a brittle silicon die ( $\alpha \sim 2.5 \text{ K}^{-1}$ ) is usually bonded with a copper heat spreader ( $\alpha \sim 16.5 \text{ K}^{-1}$ ). Standard solutions involve the addition of an intermediate highly-compliant layer, such as indium, to prevent a fracture of the interface. On the other hand, indium has an even higher CTE ( $\alpha \sim 29 \text{ K}^{-1}$ ), and the amount of heat that can be evacuated is in any case limited. The novel composites in the scope of this work present, on top of high thermal conductivity, a low CTE that nearly matches that of silicon, representing a good choice for this kind of applications.

Slow and long heating and cooling ramps are often a limit of industrial solutions working at a high temperature. Another example is related to ceramic fuel cells, typically made of a mixture of solid oxides (Figure 1). The main characteristic of this family of fuel cells is the high operating temperature, generally between 700

and 1200 °C, which activates electrochemically the materials employed. Such temperatures are achievable only by quasi-static heating and cooling processes. This is one of the main reasons for which these fuel cells, in spite of their very high efficiency, are currently limited to stationary applications, such as micro combined heat and power units ( $\mu$ -CHP).

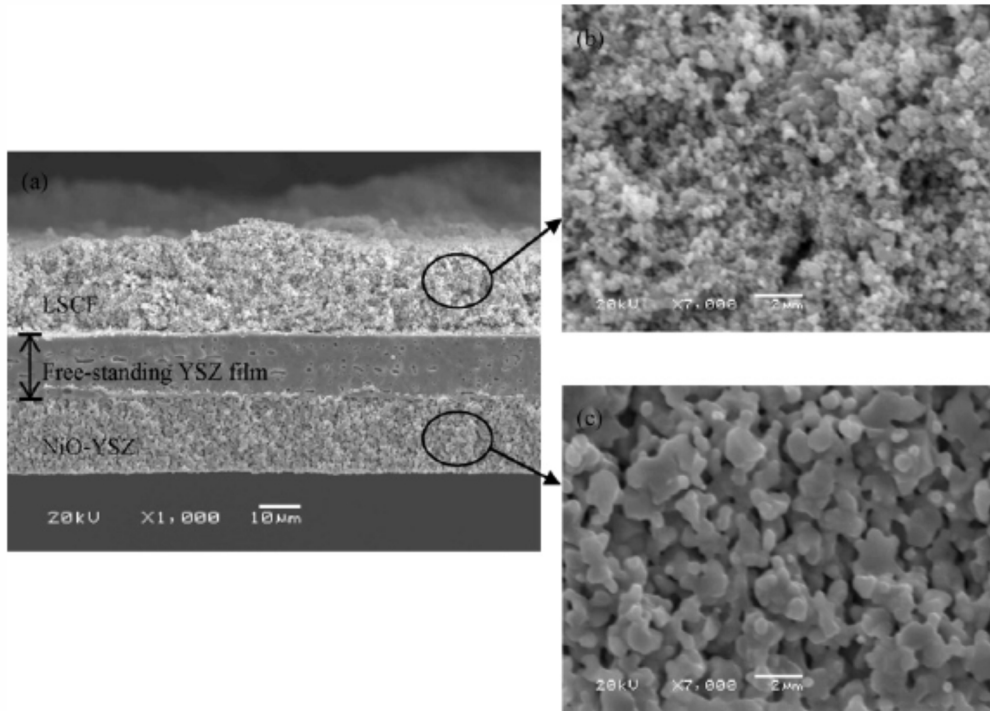


Figure 1. Microstructure of a solid-oxide fuel cell (a), with details of cathode, in lanthanum strontium cobalt ferrite, (b) and anode, in nickel oxide and yttria-stabilized zirconia (c) [1], [2].

## 1.2 Slow-transient heating

We include in this family all the scenarios where the temperature variation over time is non-negligible, so that Eq. (1.2) has to be considered in its entirety, but the load application is slow enough to allow ignoring the dynamics of the structural problem.

Since the thermal diffusivity is a term defining the temperature propagation rate through the material, it is useful to introduce a *characteristic thermal time constant*  $\tau$ , defined as:

$$\tau = \frac{L^2}{a} \quad (1.13)$$

where  $L$  is the typical dimension of the physical system, or *characteristic dimension*;  $\tau$  is the time required for the thermalization of the system. For example, in the case of a spherical particle of radius  $R$  and thermal diffusivity  $a$  submitted to a heat pulse at its surface, the thermalization time is equal to  $R^2/a$ .

The characteristic thermal time constant is an important parameter in the definition of the tools used for the study of thermomechanical transient problems. In general, local rapid heating on a structure, similarly to a mechanical impact, leads to the formation of longitudinal, flexural and transversal stress waves [3]. However, in some conditions, the dynamic response of the structure can be neglected and the structural problem can still be solved, with a good approximation, without dependence on time and sequentially to the thermal problem. One of the first examples in this sense was the extensive study performed in the aerospace engineering field by Boley [4] on flexible spacecraft booms rapidly heated by the solar radiation. Boley approximated these structures to beams and plates, finding that the surface heating produces a time-dependent thermally induced bending, which flexurally deforms the element. Boley defined a parameter, known as *Boley number*, to relate the thermal and structural response of the structure:

$$B = \sqrt{\frac{\tau}{T_{f,1}}} \quad (1.14)$$

with  $T_{f,1}$  corresponding to the period of the first flexural mode, or inverse of the first flexural frequency  $\lambda_{f,1}$ , calculated, for a beam element of length  $l$ , moment of inertia  $I$ , density  $\rho$  and section  $A$ , as:

$$\lambda_{f,1} = \frac{1}{2\pi} \frac{\beta_{f,1}^2}{l^2} \sqrt{\frac{EI}{\rho A}} \quad (1.15)$$

where  $\beta_{f,1}$  is a constant associated to the first flexural frequency and depending on the boundary conditions.

Boley showed that the transverse vibrations of the beam can be neglected when  $B \leq 1$ , thus for highly conductive and/or highly rigid structures.

Dalocchio [5] used this approach to study particle accelerator beam-like components, known as collimators (see section 5.1), submitted to a slow transient

heating, with  $\tau = 13 \text{ s}$  and  $T_{f,1} = 20 \text{ ms}$ , showing numerically that in this case the dynamic response of the structure is not entailed.

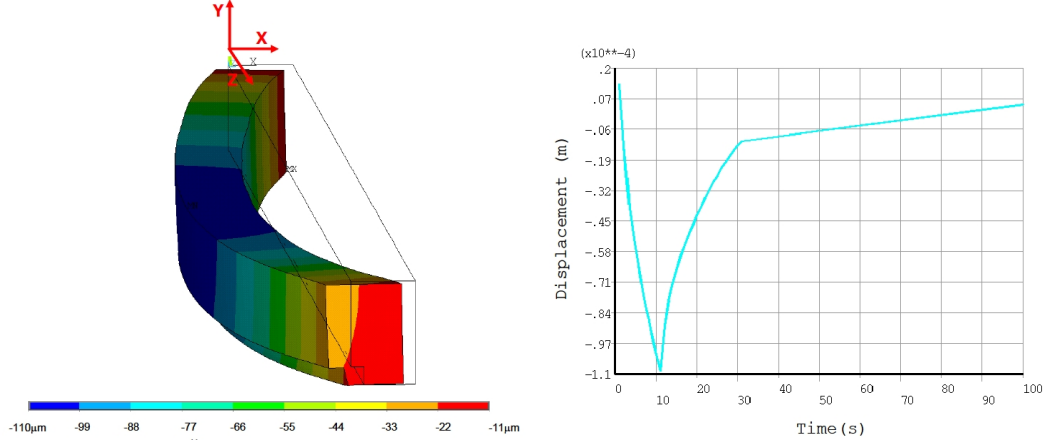


Figure 2. Left: Flexural displacement ( $x$  direction) over the time of a 1 meter collimator jaw, simply supported at the extremities, under the effects of a 30 kW load applied for 10 s. The transient analysis is interrupted after 30 s, and the discontinuity in the curve (right) represents an extrapolation of the structure recovering its undeformed position [5].

### 1.3 Quasi-instantaneous heating

In this scenario, the heat deposition rate is fast enough to lead to the generation of stress waves, propagating through the structure from the locally-heated zone and superposing with the quasi-static stress state. When the thermal energy deposition time  $t_d$  is much smaller than the diffusion time constant  $\tau$ , during the heating the temperature variation in space over the body volume can be neglected, and Eq. (1.1) becomes:

$$S = C \frac{\partial \theta}{\partial t} \quad (1.16)$$

The temperature increase  $\Delta \theta$  on the body can be calculated integrating Eq. (1.16):

$$\int_{\theta_0}^{\theta_0 + \Delta \theta} C d\theta = \int_0^{t_d} S dt \quad (1.17)$$

where  $\theta_0$  is the initial body temperature. For example, in the simplest case, if the heating power  $S$  is constant over the deposition time and density and specific heat are independent of the temperature:

$$\Delta\theta = \frac{S t_d}{C} \quad (1.18)$$

This approximation in general is not accurate, since density and specific heat may exhibit relevant deviations from the initial value, also for very small temperature increase.

The thermal energy deposition on a body induces, on top of a raise in temperature, a pressure increase depending on the equation of state of the material (section 3.1). Pressure waves are therefore generated, similarly to a mechanic impact, and the dynamic stresses associated to the wave propagation can be expressed in indicial notation [6], as:

$$\frac{\partial \sigma_{ij}}{\partial x_j} = \rho \frac{\partial^2 u_i}{\partial t^2} \quad (1.19)$$

where  $u$  is the displacement vector. These equations of motion will hold independently of the stress-strain behaviour of the material. Details on their derivation, and on the wave theory in the elastic, plastic and shock domains, will be given in Chapter 2; however, we introduce here the physical quantity  $c$ , representing the *speed of propagation of an elastic perturbation*:

$$\frac{1}{c^2} \frac{\partial^2 u_i}{\partial t^2} = \nabla^2 u_i \quad (1.20)$$

In the case of a longitudinal acoustic wave,  $c$  is also known as the *speed of sound*. Typical values of the speed of sound for different engineering materials are reported in Table 1 [7]. In the plastic domain, the wave travels at a velocity lower than the speed of sound. At higher intensities, shock waves can originate, inducing in the material a sharp discontinuity in temperature, pressure and density, and propagating faster than the speed of sound.

Table 1: Velocities of elastic waves

<b>Material</b>	<b>Speed of sound (m/s)</b>
Air	340
Aluminum	6 100
Steel	5 800
Lead	2 200
Beryllium alloy	10 000
Glass/window	6 800
Plexiglas	2 600
Polystyrene	2 300
Magnesium	6 400

Source: From [7], p. 23.

The *wave equation* (1.20) is complementary to the *heat equation* (1.2) in the solution of thermomechanical problems with quasi-instantaneous heating. The wave equation is also a second-order partial differential equation, but differently from the heat equation, it is hyperbolic. This difference is relevant at short time and space scales, as it will be explained in section 1.5, because parabolic PDEs do not present a finite signal velocity term, implying an instantaneous signal propagation.

The characteristic time defining the dynamic problem is the wave period  $T$ . In the case of a system with typical dimension  $L$ , the period of a longitudinal elastic wave can be expressed as:

$$T = \frac{2L}{c} \quad (1.21)$$

The wave period  $T$  can be compared with the characteristic thermal diffusion time  $\tau$ , defined in Eq. (1.13), and with the thermal energy deposition time  $t_d$ . For the majority of the materials adopted in engineering components, except on very small time scales, and in case of quasi-instantaneous heating, we have:

$$\tau \gg T, t_d$$

The temperature field generated by the heating can be evaluated with Eq. (1.17). As discussed, the temperature increase gives rise to an increase of pressure which depends on the material and, in particular, on its equation of state. In the case of linear elastic, isotropic and homogeneous materials, the mechanical problem can be solved in its quasi-static terms with Eq. (1.8), (1.9), while dynamic stresses are expressed through Eq. (1.19). In the case of an energy deposition time, or pulse length, even shorter than the typical time constant of the mechanical problem, it is possible to refer to a condition of *isochoric heating*, since the material expansion is prevented by its mass inertia during the time of the heat deposition.

In a more general scenario, and in particular when inelasticity is involved, analytical solutions are extremely complex, and the problem is typically solved numerically, for example by means of finite-element (FE) codes. The stress-strain relationship can then be expressed through strength models which take into account strain and strain-rate hardening and temperature softening effects (section 3.2). Plasticity also involves energy dissipation, namely plastic work, with the generation of additional heat that influences the temperature distribution. The thermomechanical problem has in this case to be solved with a coupled method. It is also interesting to note that, because of the usually negligible magnitude of  $T$  with respect to  $\tau$ , the first numerical codes developed in the 1960s to study highly dynamic events, such as HEMP [8], were typically not considering thermal diffusion at all, and the thermal conductivity was not an input of the analysis.

To quantify what was just stated, a numerical example is proposed in order to compare the thermomechanical response of a simple adiabatic system such as a 1D cylindrical rod, submitted to a rapid temperature increase at one extremity. The rod diameter is 10 mm and the length 1 m, and one of the two extremities is submitted to a temperature increase from 22 to 200 °C in  $10^{-6}$  s. The duration of the pulse is  $10^{-5}$  s, after which the energy of the system remains constant. The behaviour of several materials from Table 1 is examined, under the hypothesis of linear elasticity. The thermal and mechanical phenomena are compared by measuring the temperature and pressure at a distance of 0.1 m from the heated edge. As shown in Figure 3 and Figure 4, the thermal response is in the order of  $10^0 - 10^3$  s, while the pressure wave propagation time is about  $10^{-5} - 10^{-4}$  s. During this very short time, the thermal diffusion does not play a role in the material response. We can also

note, from Figure 4, that the heat deposition time is also much smaller than the mechanical time constant, and we are in a scenario of isochoric heating.

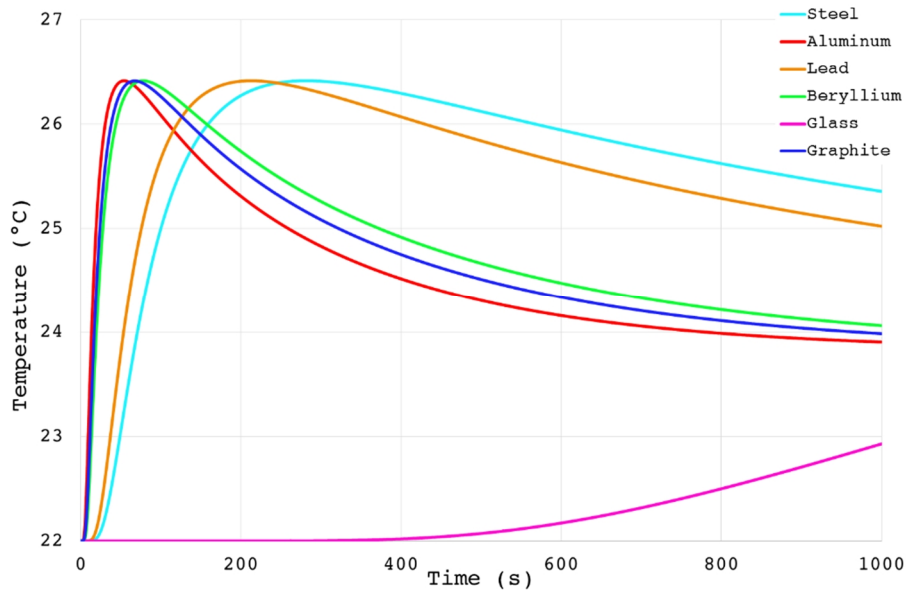


Figure 3. Temperature evolution over time on the cylindrical bar, at the longitudinal position  $L = 0.1$  m, for different materials. The heated extremity is at  $L = 0$ .

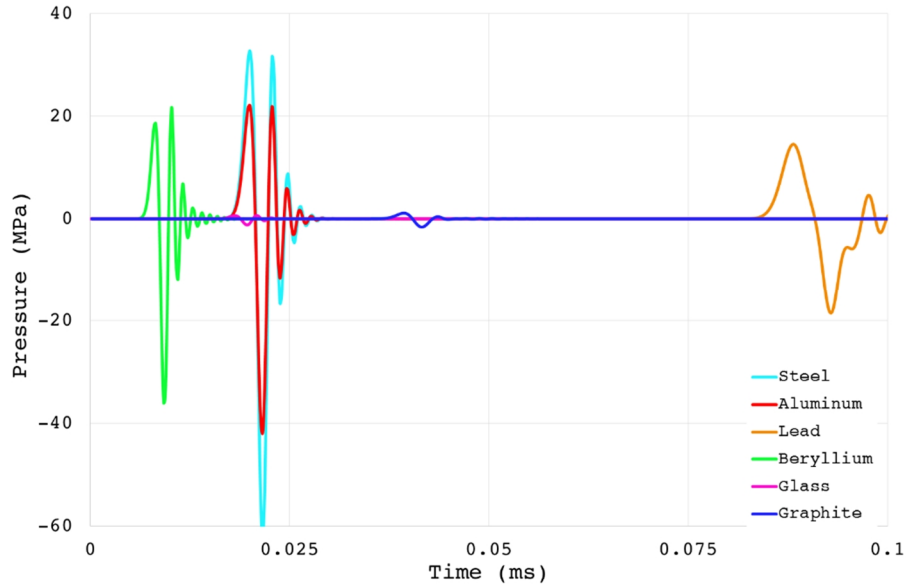


Figure 4. Pressure evolution over time on the cylindrical bar, at the longitudinal position  $L = 0.1$  m, for different materials. The heated extremity is at  $L = 0$ .

Some practical examples involving the generation of thermally induced stress waves include laser applications [9], electrical pulse discharge [10] and particle accelerator components interacting with particle beams [11].

In the case of lasers, the energy deposition time  $t_d$ , or *pulse length*, can be extremely short. In new facilities under construction such as ELI-NP [12] (Magurele, Romania), designed for testing materials in unexplored areas of the equation of state, the pulse length can be reduced down to  $10^{-14}$  s, discharging a power of  $10^{16}$  W on the impacted surface, achieving energy densities in the order of  $10$  MJ/cm<sup>3</sup> on impact spots of  $1$  cm<sup>2</sup>. The tremendous energy density generates plasma on the target surface, and shock waves propagate from the impacted area through the target volume. Similar events can occur, on a smaller scale, also on industrial lasers. For example, in the case of laser machining, in particular at pulse lengths below  $10^{-12}$  s, optical breakdown in air can constitute a severe problem, leading to the discharge of part of the laser energy to functional areas of the machined component, with associated damage.

Electrical pulse discharges are sometimes responsible for similar effects. The breakdown channel of a high-voltage pulse discharge on a fluid, for example, can generate plasma. Yang and co-authors [10] recently studied this phenomenon on water, under pulses generated at a high voltage (15 kV) rapidly releasing an amount of energy high enough to generate shock waves with a pressure up to 50 MPa. In a solid, a similar state is reached at higher energies, when the pressure level is much bigger than the dynamic flow strength of the material. The same concept, with an electric arc discharge in a liquid (typically water), is adopted in the *electrohydraulic forming*, which is used in automotive and other industrial applications to achieve precise tolerances on thin structures of complex shape. A capacitor delivers a high-current pulse across two electrodes, positioned a short distance apart and submerged in the fluid. The electric arc discharge rapidly vaporizes the fluid creating a shock wave. The thin component, which is kept in contact with the fluid, is deformed into an evacuated die. Electrically driven stress waves were also used by Skoro and colleagues [13] to characterize the dynamic response of materials such as tantalum and tungsten under pulsed current, reaching temperature in the order of 2000 K and studying the dynamic response produced.

In terms of energy density induced on the impacted material, proton, ion and electron beams circulating in particle accelerators are similar to the brightest lasers. However, the laser penetration depth depends on the wavelength and on the absorption coefficient of the target, and is typically in the order of  $10^{-9}$  –  $10^{-6}$  m [14]. On the other hand, hadron beams of the modern particle accelerators penetrate much deeper inside the impacted material. The penetration depth is in this case mostly related to the beam transverse section and intensity, to the particle nature and energy, and to the density and atomic number of the target. In the *Large Hadron*

*Collider* (LHC), currently the most energetic particle accelerator in the world, located at CERN (Geneva, Switzerland), the circulating proton beam would penetrate 10 – 15 m in the case of a head-on impact on a carbon structure [15]. At the end of a physics run, the beam is stopped by deviating it against an 8 m – long graphite cylindrical component known as *dump*. Since a head-on impact would involve a penetration deeper than the dump length, on top of structural damage to the dump, the beam is swept along a spiral pattern on the dump upstream face by means of pulsed magnets (Figure 5). In particle accelerators, the pulse length is longer than in the case of lasers, and is typically in the order of  $10^{-9}$  –  $10^{-5}$  s, increasing with the amount of impacting particles.

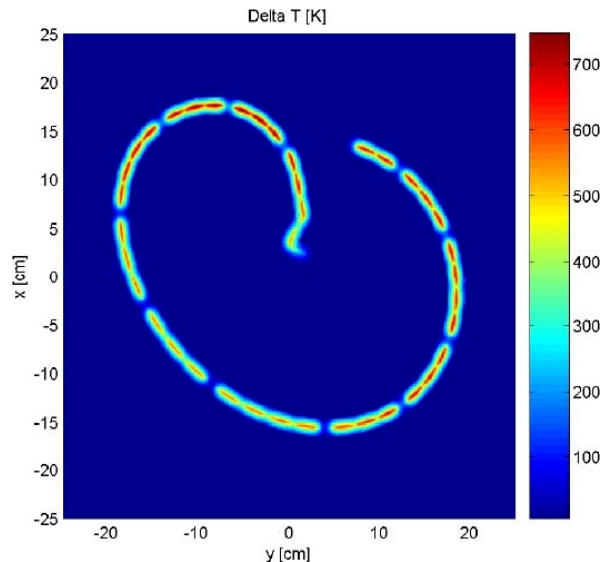


Figure 5. Temperature distribution on the LHC dump [16]. Note the spiral pattern dilution.

It is evident that, while particle and laser beams may in principle produce comparable thermal energy density deposition on a structure, in the case of a particle beam the energy involved is much higher (in the case of the LHC compared to the ELI-NP laser, the energy is higher by orders of magnitude) and, usually, a significant portion of the target length is reached by the impact, with relevant consequences on the component in terms of produced damage. In section 1.4 we give some examples of particle beam – induced effects on the matter, observed in particle accelerators.

#### 1.4 Examples of quasi-instantaneous heating events in particle accelerators

In particle accelerators, a beam constituted of elementary particles such as protons, ions or electrons is accelerated at relativistic speed before colliding against another

beam, travelling in the opposite direction, or a fixed target. This impact generates a multitude of subatomic particles which are analyzed by detectors in advanced experiments, in order to explore the boundaries of existing physics theories composing the *Standard Model*, and solve the countless outstanding mysteries such as, to name only a few, dark matter, matter/antimatter asymmetry and Universe expansion [17]. The higher the energy of the colliding particles and the collision rate (known as *luminosity*), the wider the spectrum of the particles potentially generated. The energy released in particle collisions is such that it recreates extreme conditions, comparable to those existing in the Universe a few moments after the Big Bang. As a quantitative example, particles colliding at an energy of 1 TeV ( $1 \text{ eV} \sim 1.6 \times 10^{-19} \text{ J}$ ) experience a state comparable to that of the Universe about  $10^{-10} \text{ s}$  after the Big Bang [18]. At the moment, the most powerful accelerator is the LHC, at CERN, capable of accelerating protons at an energy of 7 TeV.

When a particle beam impacts on a target, part of its kinetic energy is transferred to the material under the form of heat. Considering the time scales involved, discussed in the previous section, we are in the case of quasi-instantaneous thermal energy deposition. The kinetic energy can be expressed as:

$$E_k = mc^2 - m_0c^2 \quad (1.22)$$

where  $c$  is the speed of light in vacuum,  $m_0$  the mass at rest, e.g. the mass of a particle with zero velocity, and  $m$  is the relativistic mass:

$$m = \frac{m_0}{\sqrt{1 - \frac{v^2}{c^2}}} \quad (1.23)$$

At relativistic speed, the second term of Eq. (1.22), known as *rest energy*, is negligible. A proton, for example, has a rest energy of about 1 GeV, while in modern particle accelerators protons, as explained, reach energies in the order of some TeV. The kinetic energy thus equates the relativistic energy defined by Albert Einstein's famous formula:

$$E_k \approx E = mc^2 \quad (1.24)$$

The particle beam is generally non-continuous, and is divided into *bunches*, each containing an amount of particles typically in the order of  $10^{11}$ . The beam can

be made up of thousands of bunches. It appears evident that, although the energy of a single particle is definitely small, due to the number of constituting particles a beam can store a huge amount of energy in a very limited volume, being potentially destructive for any device that partly or fully intercepts it. The energy stored  $E_s$  in a particle beam can be calculated as:

$$E_s = k_b N_b E \quad (1.25)$$

Where  $k_b$  stands for the number of bunches constituting the beam and  $N_b$  is the number of particles per bunch. Figure 6 summarizes the energy stored in the particle beam of present and future worldwide particle accelerators.

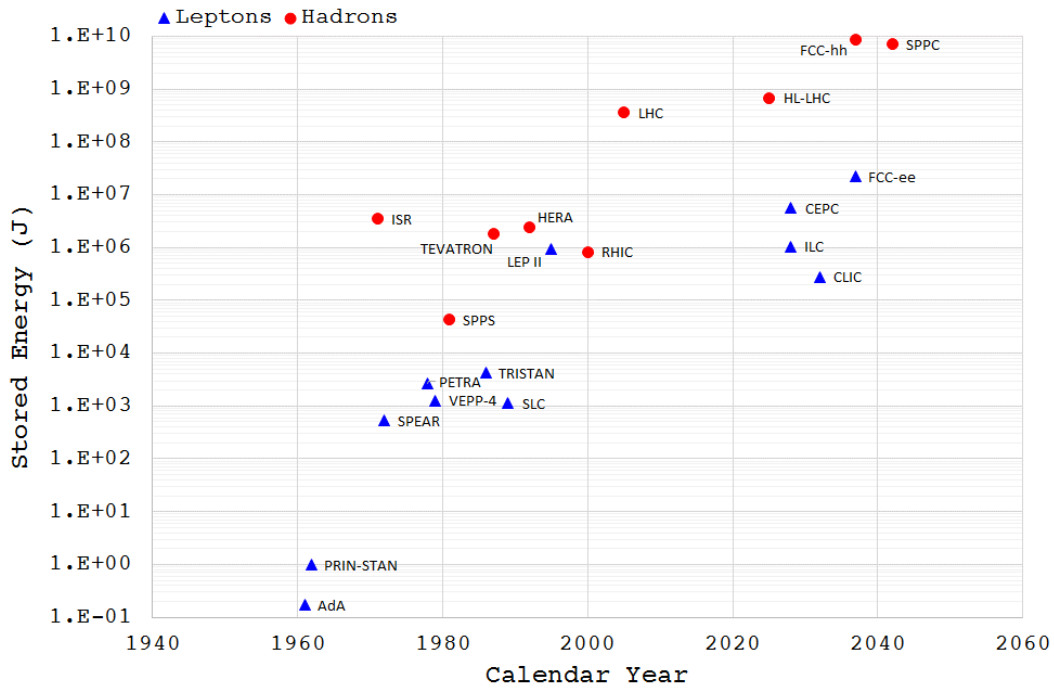


Figure 6. Stored energy in current and future particle accelerators<sup>2</sup>.

<sup>2</sup> The plot refers to hadron and lepton particle accelerators. Hadrons are particles made of quarks held together by the strong force; hadrons typically used in particle accelerators are protons and ions. Leptons are elementary particles not subjected to strong interactions, usually represented in particle accelerators by electrons and antielectrons (or positrons).

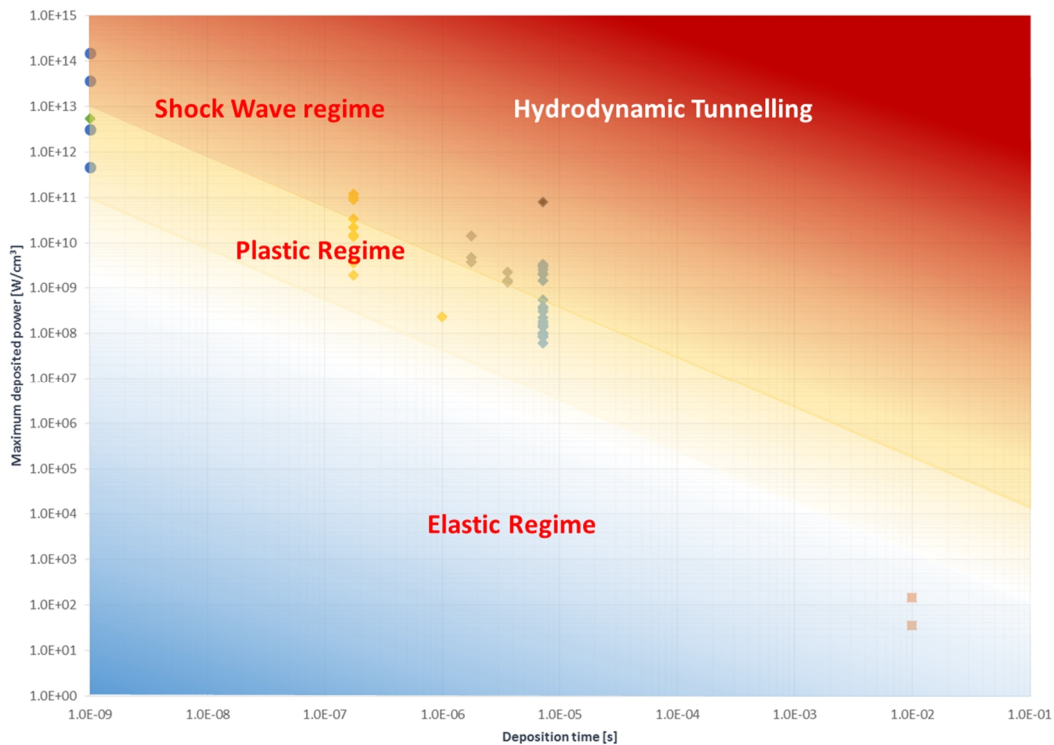


Figure 7. Plot of maximum deposited power versus duration of deposition, showing the different dynamic responses that can be induced in matter by interaction with particle beams. Points represent cases of beam impacts. Source: [19].

The problem of potential damage to particle accelerator structures in case of beam impact dates from the 1970s, with the first accelerators, such as the Intersecting Storage Rings (ISR), at CERN, reaching stored energies in the order of MJ. Different examples of beam impact effects observed in the past decades in international particle accelerators are provided in the next paragraphs [19].

Figure 8 shows the accidental impact of a 500 kW proton beam on beryllium cylindrical rods, 100 mm in length and 3 mm in diameter, in the *Super Proton Synchrotron* (SPS) at CERN in the 1970s [20]. The pulse was 23  $\mu$ s long and occurred with an offset with respect to the rod axis, inducing a flexural response of the components which experienced plasticity and, in the worst case, failure.



Figure 8. Beryllium rods damaged by an off-axis beam impact at the CERN SPS in the 1970s.

In 2003, at the *Tevatron* (FNAL, USA) accelerator, a drift of the 1.8 MJ proton beam was caused by a failure in the superconductive magnets. The beam eventually hit two intercepting devices known as *collimators*, the first one made of tungsten alloy and the second one of stainless steel (Figure 9). Both components were severely damaged, with a 3 mm hole in the tungsten unit and an extended longitudinal indentation in the stainless steel collimator [21].

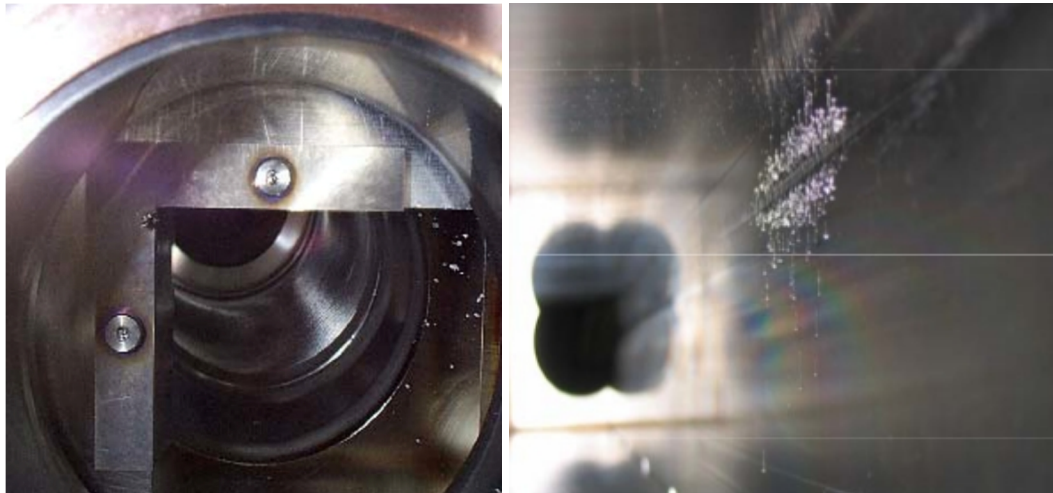


Figure 9. Tevatron collimators impacted by 1.8 MJ proton beam: tungsten (left) and stainless steel (right).

During high-intensity extraction from SPS to the LHC (CERN) in 2004, an incident occurred in which a stainless steel vacuum chamber of a magnet in the transfer line was badly damaged [22]. The proton beam had a stored energy of

2.5 MJ, with a wrong trajectory, which provoked a 110 cm long groove on the side of the impact, with the projection of molten stainless steel droplets on the opposite wall (Figure 10).

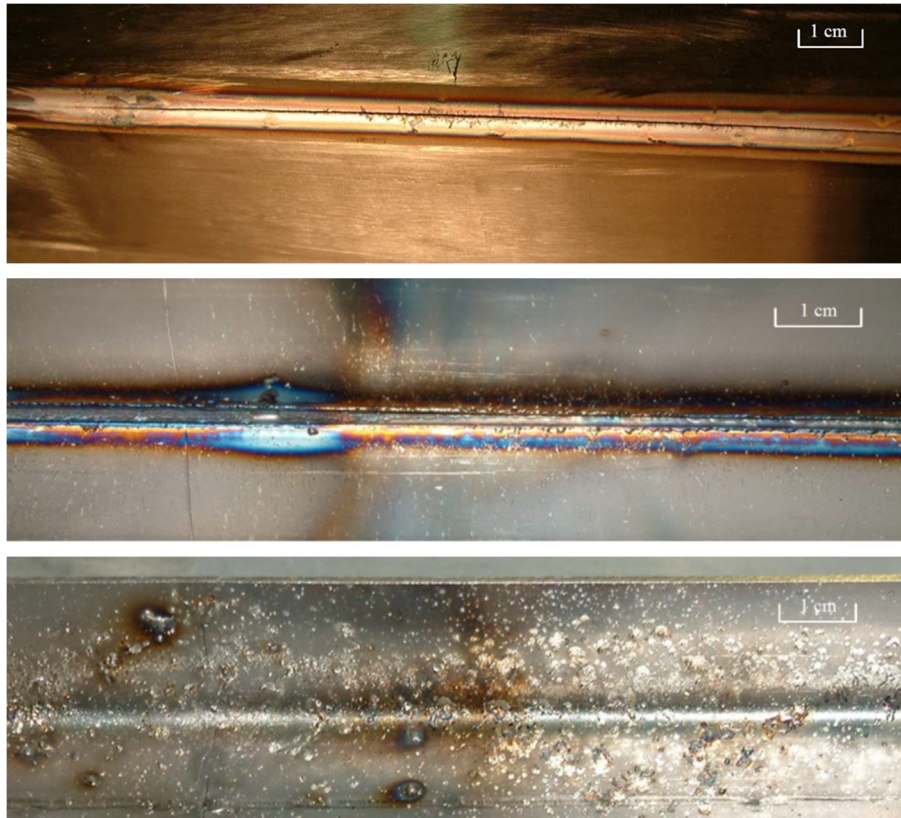


Figure 10. Stainless steel vacuum chamber damaged at the transfer line between the SPS and the LHC (CERN). Vacuum chamber outside (top); inner wall impacted by the beam (centre); inner wall opposite to the beam impact (bottom).

In 2012, we carried out an experiment in the recently commissioned HiRadMat facility at CERN to test the behaviour of an LHC tungsten collimator under the impact of proton beams of different intensity. The beam was extracted from the SPS [23]. The collimator was hit three times, with beam energies from 75 to 670 kJ and pulse length between  $2 \times 10^{-7}$  and  $2 \times 10^{-6}$  s. The damage produced by the two most intense impacts is highlighted in Figure 11, involving material ejection and fragmentation. The 75 kJ impact was, according to simulations, the threshold limit for the generation of plastic strains, and its effect are not visible in the figure.



Figure 11. Effects of impact tests on LHC tungsten collimator, upstream view. Note the presence of two longitudinal grooves and extensive debris on the bottom of the vacuum chamber.

Also in 2012 at the HiRadMat facility, a second test involved the study of the effect of the SPS proton beam on six different materials for present and future use in particle accelerators [24], ranging from metallic alloys mostly made of copper, tungsten and molybdenum, to metal-ceramic composites including diamond or graphite phases [11]. The specimens were either cylindrical, to probe the generated shock waves by means of strain gauges and a laser-Doppler vibrometer under a medium-intensity beam, or half-moons, to induce micro-jetting and micro-spallation on the specimen by high-intensity beams and capture the trajectory of the droplets with a high-speed camera, measuring their velocity. The beam stored energy reached a magnitude of 1.4 MJ and the pulse length was  $3.6 \times 10^{-6}$  s. The high-speed camera allowed to capture for the first time ever the extreme dynamic effects induced on the matter by intense proton beams. The video frames of the impact on three tungsten-alloy targets are shown in Figure 12 [25]. The measured velocity of the ejecta reached 275 m/s and were benchmarked by the author with explicit finite element simulations, which anticipated the result with an accuracy of 85%.

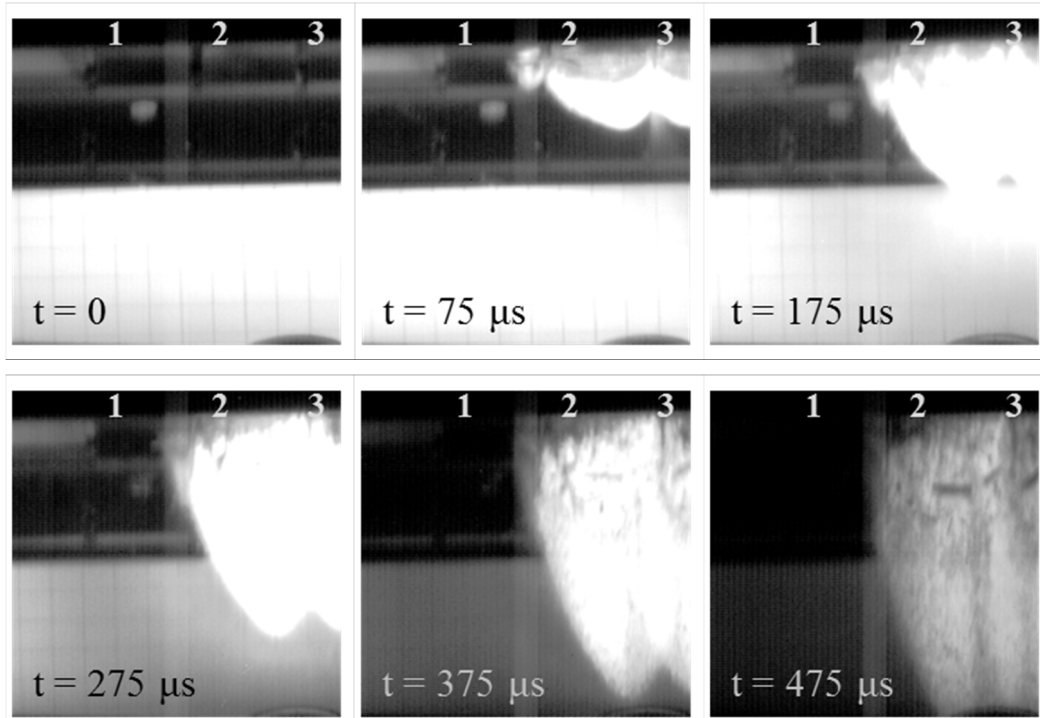


Figure 12. Effects of a 700 kJ proton beam impacting on three tungsten-alloy specimens, numbered 1 to 3. The beam is coming from the left. The ejecta are made of a combination of molten and vaporized fragments, and solid debris.

The effects just reviewed are generated by a combination of phenomena related to rapid local heating. The damage to the structure can locally depend on a *change of phase* due to the high specific energy, with the material state changing from solid to liquid, gas or plasma. At the same time, a *cylindrical pressure wave* will develop from the impact point towards the surroundings of the structure, associated with potential plasticity or fracture. The reflection with a free surface may induce *spallation* phenomena, including *micro-jetting*, with detachment of solid fragments from the surface, and *micro-spallation*, occurring when the rarefaction wave originates on a molten surface, unable to withstand a tensile load. On non-monolithic structures, the shock wave reaches the interfaces, with propagation to the bodies in contact depending on the *shock impedance* of the materials. Finally, at high energies, the beam penetration inside the volume is enhanced by the decrease in density of the impacted material over time. The phenomenon, known as *hydrodynamic tunnelling*, will play an important role in the design of beam intercepting devices for future high-energy particle accelerators, such as the *Future Circular Collider* (FCC) under design at CERN, with beams storing an energy in the order of 10 GJ [26].

With the energy stored in the beams of particle accelerators expected to significantly increase in the coming years (Figure 6), the need of novel materials able to withstand the extreme conditions produced by a beam impact becomes of paramount importance. In fact, no currently available material for use in beam-intercepting devices is expected to survive the design scenarios. For future dumps, possible solutions involve segmented porous graphite [27], liquid metals, fluidised metallic powders [28]. On the other hand, for components which are interacting with the external halo of particles, and require a structural and geometrical stability, the research is orienting towards composites based on metals or ceramics, combined with carbon in its allotropic forms, graphite and diamond (Figure 13). See Chapter 5 for a detailed description of these materials.

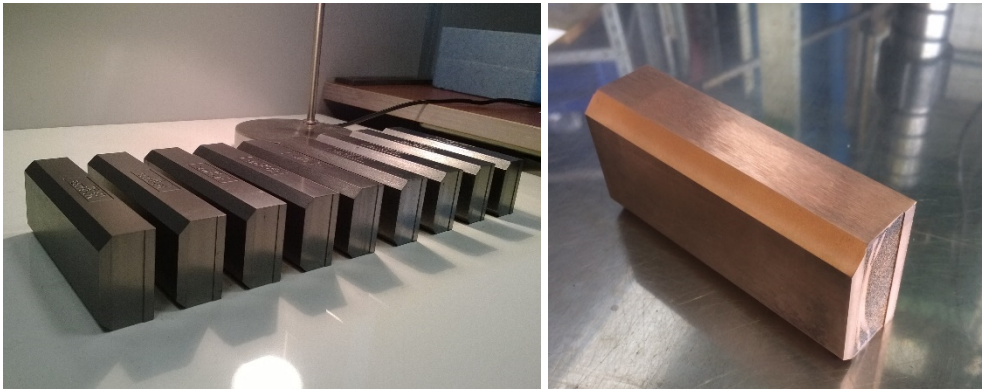


Figure 13. Functional elements made of novel composites under development at CERN for future beam intercepting devices. Left: Molybdenum-Graphite (MoGr) features a graphitic matrix reinforced with molybdenum carbide, with the possible addition of dopants and carbon fibres. Right: Copper-Diamond (CuCD), the reinforcement is made of diamond particles dispersed in a copper matrix.

## 1.5 Inaccuracy of the heat equation at space and time nanoscales

It is important to point out that, due to the small time scales involved in the phenomena discussed in the previous sections, namely in the case of quasi-instantaneous heating of a component, the Fourier laws (1.2), (1.3) may be inaccurate in the prediction of the thermal results. This inconsistency can be illustrated by considering an initial temperature distribution over the volume. After a time  $dt$ , a change in temperature at the boundaries provokes an instantaneous heat flux transmission to every point of the domain towards the colder boundary. This is due to the parabolic nature of the heat equation, which does not present, unlike hyperbolic partial differential equations such as the wave equation (1.20), a finite

signal velocity term (in the wave equation, it is the sound speed). The heat signal propagation speed is infinite, and some authors named this conclusion the *paradox of instantaneous heat propagation* [29]. Of course, this is in contrast with Einstein's special theory of relativity, which states that no signal can travel at a speed higher than the speed of light in vacuum. To correct this inconsistency, Cattaneo [30] and Vernotte [31] proposed a similar model encompassing a *relaxation time*  $\tau_0$ , which is taken to the flux for appearing as an effect of a temperature existing at a time equal to zero (in the case of a generic time  $t$ , the heat flux propagates after a time  $t + \tau_0$ ). The equation now becomes hyperbolic:

$$\nabla^2 \theta - \frac{1}{a} \frac{\partial \theta}{\partial t} - \frac{1}{c^2} \frac{\partial^2 \theta}{\partial t^2} = -\frac{1}{k} \left( S + \tau_0 \frac{\partial S}{\partial t} \right) \quad (1.26)$$

The speed of propagation of the thermal signal now appears, and is called here  $c$ , also known as *speed of second sound*, associated to the phonons:

$$c = \sqrt{\frac{a}{\tau_0}} \quad (1.27)$$

The incongruence of the Fourier's second law at small time scales is now more evident. The characteristic time  $\tau$  calculated with the classical theory, Eq. (1.13), is directly proportional to the characteristic size of the system and inversely proportional to the material diffusivity. At nanoscales, or with hyper-conductive materials,  $\tau$  can ideally become smaller than  $\tau_0$ , which, according to the Cattaneo-Vernotte (CV) model, is in the order of  $10^{-11}$  s. This implies a thermalization of the system faster than the heat flux signal propagation. The system can therefore no more follow the imposed temporal changes and it behaves like a low-pass filter, responding only to the mean value of the heat flux.

It is interesting to note that the modification of a parabolic PDE, describing a dissipative process, with a hyperbolic PDE, which includes a conservative term, can lead to the origination of phenomena such as thermal resonance. However, there are debates over the CV model, with criticisms over the physical approximations introduced. From the practical point of view, the main issues of this approach are the scarcity of analytical solutions of the equation for the majority of physical situations, and the difficulty in defining the relaxation time of real systems. Other approaches have recently been proposed, including for example the relativization of the Fourier's equation through a Lorentz transformation, or models based on the

Boltzmann transport equation [32]; however, they remain of difficult application in physical systems for the same reasons related to the CV model.

According to the CV model, the relaxation time for macroscopic solids is in the order of  $10^{-11}$  s. The phenomena investigated in this thesis involve heat pulse lengths in the order of nanoseconds, or microseconds, and can therefore be thermally solved with the classical Fourier's laws. However, the number of physical problems where the Fourier's laws are less precise is growing, involving for example nanometric systems, hyper-conductive materials such as colloidal suspensions of nanoparticles, laser pulses with a duration of picoseconds or femtoseconds. In these cases, modifications to the classical heat equations are necessary for the solution of the thermal problem.

## 1.6 Structure of the thesis

Chapter 2 focuses on the nature of the dynamic response of materials submitted to quasi-instantaneous heating. The three regimes examined depend on the thermal energy generated on the component, and involve the creation of *elastic*, *plastic* and *shock waves*. Analytical and numerical examples are given, evaluating the response of metallic materials of engineering interest.

Chapter 3 provides the tools for the study of quasi-instantaneous heating. Due to the nonlinearities of the material properties with temperature, strain and strain rate, the analysis of the material response is typically done with finite element codes, both implicit and explicit. The description of a hydrostatic stress state requires the definition of an *equation of state* (EOS) for the material, while the deviatoric component of the stress tensor is associated with the material *constitutive law*, composed by *strength* and *failure models*. The main EOS, strength and failure models are described, together with the methods to derive them. An experimental method to explore unusual regions of the material EOS, involving isochoric heating under high thermal energy, is described and the EOS parameters are analytically calculated in the case of tungsten.

Chapter 4 gives a detailed overview of the main thermal and mechanical phenomena associated with quasi-instantaneous heating of materials, with a focus on the events generated through hadron beam impacts on the matter. Numerical methods developed to study each phenomenon are provided with the use of implicit and explicit FE codes.

Chapter 5 describes an example of application of the methods developed for the case of components submitted to quasi-instantaneous heating due to proton and ion pulse impacts in particle accelerators, such as the LHC at CERN. The design principles and requirements of the components, known as *collimators*, are detailed, and the novel composites devised for use in the future LHC collimation system are introduced. Results of the characterization campaign performed at CERN and Politecnico di Torino on the novel materials are discussed, and models to study their response under quasi-instantaneous thermal irradiation, based on the principles introduced in Chapter 3, are built.

Chapter 6 focuses on an experiment called *HRMT-23*, designed to evaluate the thermomechanical dynamic response of three collimator jaws, embarking current and novel materials, to the impact of intense proton beams at the CERN HiRadMat facility. The experimental configuration, the instrumentation and the beam parameters of HRMT-23 are presented. The experimental outcome of the test on each collimator jaw is then discussed in detail.

Chapter 7 provides a numerical benchmarking of the results of HRMT-23, and analyses the level of maturity of the material models built so far. The simulations are performed with the implicit code ANSYS. The implications of more advanced material models, to be built with additional experimental tests, are analysed, both for homogeneous models and inhomogeneous ones at the mesoscale level.

Chapter 8 summarizes the main results of the thesis, and suggests possible future developments of the work performed.

## 1.7 Glossary

Symbols are listed in chronological order with respect to their appearance in the text.

<b>Symbol</b>	<b>Definition</b>	<b>SI unit</b>
$\theta$	Temperature	K
$C$	Volumetric heat capacity	$\text{J}\cdot\text{m}^{-3}\cdot\text{K}^{-1}$
$t$	Time	s
$S$	Volumetric heat source	$\text{W}\cdot\text{m}^{-3}$

---

$k$	Thermal conductivity	$\text{W}\cdot\text{m}^{-1}\cdot\text{K}^{-1}$
$a$	Thermal diffusivity	$\text{m}^2\cdot\text{s}^{-1}$
$\vec{q}$	Heat flux vector	$\text{W}\cdot\text{m}^{-2}$
$V$	Volume	$\text{m}^3$
$\beta$	Volumetric thermal expansion coefficient	$\text{K}^{-1}$
$\alpha$	Linear thermal expansion coefficient	$\text{K}^{-1}$
$\varepsilon$	Strain	–
$\sigma$	Stress	Pa
$\delta_{ij}$	Kronecker delta	
$C_{ijkl}$	Components of the stiffness tensor	Pa
$\sigma$	Stress	Pa
$\lambda$	Lamé's first parameter	Pa
$\mu, G$	Lamé's second parameter or Shear modulus	Pa
$E$	Young's modulus	Pa
$\nu$	Poisson's ratio	–
$\tau$	Characteristic diffusion time	s
$L$	System characteristic length	m
$R$	Radius of a characteristic spherical system	m
$T_{f,i}$	Period of the $i$ -th flexural mode	s
$B$	Boley number	–
$\lambda_{f,i}$	$i$ -th flexural frequency	Hz
$l$	Length	m
$I$	Moment of inertia	$\text{m}^4$

$A$	Section	$m^2$
$\beta_{f,i}$	Constant of the $i$ -th flexural mode associated to the boundary conditions	–
$x_j$	Coordinates of the position vector	$m$
$u_i$	Components of the displacement vector	$m$
$t_d$	Energy deposition time or thermal pulse length	$s$
$c$	Speed of sound	$m \cdot s^{-1}$
$T$	Wave period	$s$
$m$	Mass	$kg$
$m_0$	Mass at rest	$kg$
$E_k$	Kinetic energy	$J$
$c$	Speed of light in vacuum	$m \cdot s^{-1}$
$v$	Velocity	$m \cdot s^{-1}$
$E$	Energy	$J$
$E_s$	Energy stored in a particle beam	$J$
$k_b$	Number of bunches in a particle beam	–
$N_b$	Number of particles per bunch	–
$\tau_0$	Relaxation time	$s$
$c$	Speed of second sound	$m \cdot s^{-1}$

## References

- [1] P. P. L. Regtien, F. van der Heijden, M. J. Korsten and W. Olthius (2004). Measurement science for engineers. Elsevier, ISBN 9781903996584.

- 
- [2] F. Carra (2009). Analisi termostrutturale agli elementi finiti di una cella a combustibile SOFC. *Tesi di laurea magistrale*, p. 39.
  - [3] M. A. Meyers (1994). Dynamic behaviour of materials. J. Wiley & Sons, ISBN 047158262.
  - [4] B. A. Boley (1972). Approximate analyses of thermally induced vibrations of beams and plates. *Journal of applied mechanics*, Vol. 24, No. 3, pp. 413-416.
  - [5] A. Dallochio (2008). Study of thermomechanical effects induced in solids by high-energy particle beams: analytical and numerical methods. *CERN-THESIS-2008-140*.
  - [6] H. Kolsky (1963). Stress waves in solids. Dover Publications, ISBN 0486610985.
  - [7] J. S. Rinehart (1975). Stress transients in solids. HyperDynamics, ISBN 0913270482.
  - [8] M. Wilkins (1964). Calculation of Elastic-Plastic Flow. *Methods in Computational Physics*, Vol. 3, pp. 211-263.
  - [9] D. Loison (2012). Etude expérimentale et numérique du micro écaillage de cibles métalliques soumises à des chocs laser. *PhD thesis*, ISAE-ENSMA Ecole Nationale Supérieure de Mécanique et d'Aérotechnique.
  - [10] D. Yan, D. Bian, J. Zhao and S. Niu (2016). Study of the electrical characteristics, shock-wave pressure characteristics, and attenuation law based on pulse discharge in water. *Shock and vibration*, Vol. 2016, article ID 6412309.
  - [11] A. Bertarelli *et al.* (2013). An experiment to test advanced materials impacted by intense proton pulses at CERN HiRadMat facility. *Nuclear Instruments and Methods in Physics Research B*, Vol. 308, pp. 88–99.
  - [12] D. L. Balabanski *et al.* (2017). New light in nuclear physics: The extreme light infrastructure. *EPL*, Vol. 117, 28001.
  - [13] G. P. Skoro *et al.* (2010). Tungsten material properties at high temperature and high stress. *Proc. IPAC'10*, Kyoto, Japan.

- 
- [14] M. S. Brown and C. B. Arnold (2010). Fundamentals of laser-material interaction and application to multiscale surface modification. In K. Sugioka *et al.*, *Laser precision microfabrication*, Springer Series in Materials Science 135, ISBN 9783642105227, pp. 91-120.
- [15] R. Schmidt *et al.* (2006). Interaction of the CERN Large Hadron Collider (LHC) beam with carbon collimators and absorbers. *Conf. Proc. C060626*, 1798-1800.
- [16] R. Schmidt *et al.* (2006). Protection of the CERN Large Hadron Collider. *New Journal of Physics*, Vol. 8.
- [17] F. Gianotti (2014). Options and prospects for the future of accelerator based high-energy physics. *Proceedings of IPAC2014*, Dresden, Germany.
- [18] C. Lamberti (2013). Il bosone di Higgs. Aliberti editore, ISBN 8874249934.
- [19] A. Bertarelli (2016). Beam-induced damage mechanisms and their calculation. *CERN Yellow Reports*, v. 2, p. 159, Jan. 2016. ISSN 00078328.
- [20] W. Kalbreier *et al.* (1977). Target stations and beam dumps for the CERN SPS. *CERN-SPS/ABT/77-3*.
- [21] N. V. Mokhov, P. C. Czarapata, A. I. Drozhdin, D. A. Still and R. V. Samulyak (2006). Beam-induced damage to the Tevatron components and what has been done about it. *Proc. 39<sup>th</sup> ICFA, HB2006*, Tsukuba, Japan.
- [22] B. Goddard, V. Kain, V. Mertens, J. Uythoven and J. Wenninger (2005). TT40 damage during 2004 high intensity SPS extraction. *CERN AB-Note-2005-014 BT*.
- [23] M. Cauchi *et al.* (2014). High energy beam impact tests on a LHC tertiary collimator at the CERN high-radiation to materials facility. *Phys. Rev. ST Accel. Beams* 17, 021004.
- [24] F. Carra, M. Scapin, A. Bertarelli and L. Peroni (2013). Un set-up sperimentale per lo studio del comportamento di materiali impattati da

fasci di particelle ad elevata energia. *Proc. 42° Convegno nazionale AIAS*, AIAS 2013 – 232.

- [25] F. Carra *et al.* (2013). Behaviour of advanced materials impacted by high energy particle beams. *Journal of Physics: Conference Series*, Vol. 451, conference 1.
- [26] M. Benedikt and F. Zimmerman (2015). Future circular colliders, *CERN note*, CERN-ACC-2015-164.
- [27] T. Kramer *et al.* (2015). Considerations for the beam dump system of a 100 TeV centre-of-mass FCC-hh collider. *Proc. 6th International Particle Accelerator Conf. (IPAC'15)*.
- [28] O. Caretta *et al.* (2014). Response of a tungsten powder target to an incident high energy proton beam. *Physical Review Special Topics - Accelerators and Beams* 17, 101005.
- [29] E. Marín (2011). Time varying heat conduction in solids. In V. Vikhrenko, *Heat conduction – basic research*, ISBN 9789533074047, pp. 177-202.
- [30] C. Cattaneo (1948). Sulla conduzione del calore. *Atti semin. Mat. Fis. della Università di Modena*, Vol. 3, pp. 83-101.
- [31] P. Vernotte (1958). La véritable équation de la chaleur. *C. R. Acad. Sci.*, Vol. 247, pp. 2013-2015.
- [32] J. Ordonez-Miranda and J. J. Alvarado-Gil (2011). On the stability of the exact solutions of the dual-phase lagging model of heat conduction. *Nanoscale Research Letters*, 6:327.

## Chapter 2

# Dynamic deformation and stress waves

In the previous chapter we have seen that fast heating on a component may induce the generation of waves irradiating from the heated volume towards the boundaries of the structure. The problem is then similar to a generic impact condition, with the difference that in the case of a quasi-instantaneous heating the dynamic response of the structure is originated by the high temperature gradient produced in a short time, while in the case of a mechanical impact, in order to achieve the same temperatures during the release phase, much higher pressures have to be reached during the loading. Quasi-instantaneous heat deposition typically involves an isochoric heating scenario, during which the component deformation is initially prevented by its mass inertia.

The characterization of a material in terms of response to high strain rate phenomena has then, ideally, to be performed combining mechanical impact tests and isochoric heating experiment. Typically, experiments such as shock tubes, detonation, laser and particle beam impacts, generate a state of uniaxial strain and triaxial stress on the material while, for example, in the case of Hopkinson bars, the stress generated is uniaxial and the speed of the elastic wave, as we will see in section 2.1, is different from the former case [1].

When the pulse transmitted to the material has an amplitude higher than the elastic limit, it decomposes into an *elastic* and a *plastic wave*. In this case, the material experiences a hardening, related to the strain and strain rate, and typically, when high temperatures are involved, a temperature-induced softening. It is then important to determine precisely the material response in this domain, with the experimental definition of an adequate *strength model*, which controls the flow stress dependence on strain, strain rate and temperature.

At even higher energies, when the amplitude of the stress waves greatly exceeds the dynamic flow strength of the material, the shear stresses can be neglected and

the stress state is mostly hydrostatic. A *shock wave* develops, characterized by a steep front and discontinuity of pressure, temperature and density. These waves require a state of uniaxial strain, with no lateral material flow, to allow the buildup of the hydrostatic component of the stress to high levels.

This chapter explores the characteristics of the different wave domains. Although several types of waves exist, in this work the focus will mostly be on *longitudinal*, or *dilatational*, waves, where the displacement imposed to the material particles is along the wave direction. Distortional or shear waves and flexural waves will also be treated. In particular, flexural waves are relevant in the study of the isochoric heating of the accelerator components which can be assimilated to beam elements, such as those described in section 5.1.

## 2.1 Elastic waves

Before describing the families of elastic waves, it can be useful to recall the definitions of stress and strain tensors, and the constitutive equations that link the two parameters. In indicial notation:

$$\begin{aligned}\sigma_{ij} &= s_{ij} - p\delta_{ij} \\ \varepsilon_{ij} &= e_{ij} + \frac{1}{3}\Delta\delta_{ij}\end{aligned}\tag{2.1}$$

where  $s$  is the *deviatoric stress tensor* and  $e$  the *deviatoric strain tensor*, while  $p$  is the *pressure* and  $\Delta$  the change in volume of a unit cube, called *dilatation*:

$$\begin{aligned}p &= -\frac{\sigma_{xx} + \sigma_{yy} + \sigma_{zz}}{3} \\ \Delta &= \varepsilon_{xx} + \varepsilon_{yy} + \varepsilon_{zz}\end{aligned}\tag{2.2}$$

Pressure and dilatation define the *hydrostatic* stress and strain tensors. The deviatoric tensor involves shear and distortion, while the hydrostatic component is responsible for a change in volume. In classical mechanics, plasticity is associated only to the deviatoric component of the stress, which is correlated to the deviatoric strain by the constitutive equations [2]. The hydrostatic behavior, which is predominant in the shock wave regime, is on the other hand defined through the equation of state of the material. Actually, assuming that yielding is independent of

the hydrostatic stress is valid only for ideal, defect-less materials. Already in the 1970s, it was proved that the hydrostatic component of stress has an influence on the yielding of materials with artificial or natural defects, such as cracks, notches and porosities [3]. For example, in the case of a material with internal voids, the application of pressure can provoke dislocation movements associated to irreversible strain [4]. Moreover, the presence of a defect will eventually lead to shear stresses, and failure. Finally, from the molecular point of view, the potential energy stored during hydrostatic compression at very high pressure can overcome the binding force of the molecules, and provoke failure during the stress release phase [5].

In index notation, the relation between stress and strain in the elastic domain expressed by Hooke's law is:

$$\begin{aligned}\sigma_i &= C_{ij} \varepsilon_j \\ \varepsilon_i &= S_{ij} \sigma_j\end{aligned}\tag{2.3}$$

$C$  is the *stiffness matrix* and  $S$  the *compliance matrix*. It is more common to write Hooke's law in the second form of Eq. (2.3), because the elastic constants appear explicitly in the compliance matrix. In the case of isotropic materials, the compliance matrix<sup>3</sup> reduces to:

$$[S] = \begin{bmatrix} 1/E & -\nu/E & -\nu/E & 0 & 0 & 0 \\ -\nu/E & 1/E & -\nu/E & 0 & 0 & 0 \\ -\nu/E & -\nu/E & 1/E & 0 & 0 & 0 \\ 0 & 0 & 0 & 1/2G & 0 & 0 \\ 0 & 0 & 0 & 0 & 1/2G & 0 \\ 0 & 0 & 0 & 0 & 0 & 1/2G \end{bmatrix}\tag{2.4}$$

The elastic constants appearing in the matrix are the Young's modulus  $E$ , the shear modulus  $G$  (also called Lamé's second parameter and indicated with  $\mu$ ) and the Poisson's ratio  $\nu$ . The number of independent constants in the case of isotropy

---

<sup>3</sup> In this notation, the tensorial strains associated with shear are  $\varepsilon_{xy}, \varepsilon_{yz}, \varepsilon_{zx}$  and correspond to one half of the engineering shear strains  $\gamma_{xy}, \gamma_{yz}, \gamma_{zx}$ .

is two. For example, assuming  $E$  and  $\nu$  as independent, one can evaluate the other constants:

$$\begin{aligned} G, \mu &= \frac{E}{2(1 + \nu)} \\ K &= \frac{E}{3(1 - 2\nu)} \\ \lambda &= \frac{E\nu}{(1 + \nu)(1 - 2\nu)} \end{aligned} \quad (2.5)$$

where  $K$  is the bulk modulus and  $\lambda$  is Lamé's first parameter. The bulk modulus relates pressure and dilatation:

$$K = -\frac{p}{\Delta} = -\frac{pv_0}{v - v_0} \quad (2.6)$$

where  $v$  is the specific volume, inverse of the density  $\rho$ .

There are several types of elastic waves which can originate and propagate in a material, depending on the motion imposed to the particle<sup>4</sup> with respect to the direction of propagation of the wave. We can in particular identify:

- *Longitudinal waves*, also known as dilatational, irrotational or primary waves. As depicted in Figure 14, these waves involve particle motion in the same direction of the wave propagation, such that  $U_p$ , the particle velocity, is parallel to  $U$ , the wave velocity. In the case of compression waves, the sense of the two vectors is the same, while for rarefaction waves, the sense is the opposite. In the simple example of a striker impacting on a bar, like in a Hopkinson bar experiment, no rotation is involved in the impact, so that only longitudinal waves are generated.
- *Shear waves*, also known as distortional, transverse, equivoluminal or secondary waves. In this case, the particle motion is orthogonal to the direction of the wave propagation (Figure 14). No resulting density change occurs, and the principal strains are all null, such that the deformation is only rotational. As an example, they can occur in rods

---

<sup>4</sup> We define here a particle as a very small portion of the shocked body.

suddenly submitted to torsion, or when the torsional state on a part of the body, given by a torque, is suddenly released, with generation of torsional energy and propagation of a shear wave.

- *Rayleigh waves*: they are generated in presence of a bounding surface, and are similar to gravitational surface waves in liquid. Their amplitude is maximum at the surface and decays exponentially orthogonally to that. They travel at a fraction of the velocity of shear waves, and the particle motion is in the plane perpendicular to the surface, and parallel to the direction of propagation. For sinusoidal Rayleigh waves the trajectory of each particle is an ellipse.
- *Flexural waves*. These waves are particularly relevant in slender elements such as bars, plates, shells [6]. Typically, their period is much longer than that of longitudinal and shear waves, and at these time scales, in the case of quasi-instantaneous heating, heat diffusion may start to be relevant. Flexural waves are not related to longitudinal and shear waves, as the resulting motion equation presents a fourth-order derivative in displacement (2.7). It is therefore a different equation from the hyperbolic Eq. (1.19), and it does not admit the traveling wave solution.

$$EI \frac{\partial^4 w}{\partial x^4} = -\rho A \frac{\partial^2 w}{\partial t^2} \quad (2.7)$$

There are several other types of waves, typically of interest in the fields of seismology, interface studies, science of fluids, such as *Stoneley* and *Love waves*, which are not investigated here because less relevant to the scope of this work.

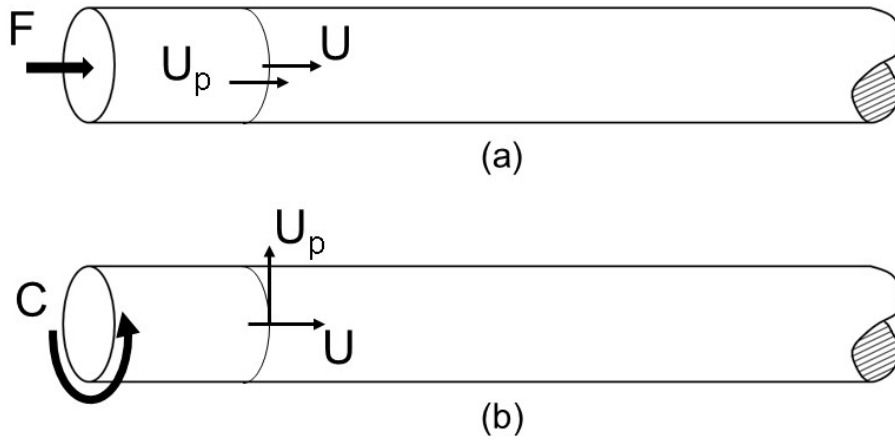


Figure 14. (a) Longitudinal wave generated by the application of a dynamic force on the extremity of a cylindrical rod. The particle motion is in the same direction of the wave propagation. (b) Generation of a shear wave by the application of a dynamic torque, with particle displacement orthogonal to the beam axis, and shock travelling along the longitudinal direction.

The wave equation, already introduced in Chapter 1, will be now examined more in detail, in particular in an unbounded medium where, differently from what takes place in a bar, where planar propagating waves induce a state of uniaxial stress, the general condition is uniaxial strain.

As seen in section 1.3, the wave equation can be derived in the form of Eq. (1.19) independently of the constitutive law of the material or boundary condition [7]. This only requires the application of the conservation of momentum to an infinitesimal volume, assumed as cubic for simplicity in the case of a Cartesian system.

$$\frac{\partial \sigma_{ij}}{\partial x_j} = \rho \frac{\partial^2 u_i}{\partial t^2} \quad (1.19)$$

Moving now to the case of linear elasticity, the constitutive laws (2.3) are applicable, and the wave equation can be expressed in terms of dilatation and Lamé's parameters, recalling the relationships (2.2) and (2.5):

$$\rho \frac{\partial^2 u_i}{\partial t^2} = (\lambda + \mu) \frac{\partial \Delta}{\partial x_i} + \mu \nabla^2 u_i \quad (2.8)$$

The equation of a shear wave is easy to determine, bearing in mind that shear waves do not have a dilatation component. For  $\Delta = 0$ , Eq. (2.8) becomes:

$$\rho \frac{\partial^2 u_i}{\partial t^2} = \mu \nabla^2 u_i \quad (2.9)$$

On the other hand, for longitudinal waves, the displacement vector has no rotational components (*i.e.*, the curl of the displacement is zero), such that:

$$\frac{\partial \Delta}{\partial x_i} = \nabla^2 u_i \quad (2.10)$$

Substituting Eq. (2.10) in Eq. (2.8) it is therefore possible to express the equation of a longitudinal wave:

$$\rho \frac{\partial^2 u_i}{\partial t^2} = (\lambda + 2\mu) \nabla^2 u_i \quad (2.11)$$

Eqs. (2.9), (2.11) are very similar, and the only difference is a constant which determines the velocity of the propagating wave. As already anticipated in Chapter 1, the wave equation can be written as:

$$\frac{1}{c^2} \frac{\partial^2 u_i}{\partial t^2} = \nabla^2 u_i \quad (1.20)$$

where the speed of propagation  $c$  assumes different values depending on the type of wave and of the boundary conditions. It is evident, out of Eqs. (2.9), (2.11), that the velocity of a longitudinal wave in unbounded media is always higher than that of a shear wave. In the case of an elastic wave, the density change in the material is negligible and one can refer to  $\rho_0$  in the expression of  $c$  to underline the elastic nature of the phenomenon. The constant density also implies a constant shape of the wave front during its propagation, as the speed of wave propagation is constant.

It is useful to express the speed of wave propagation in frequently studied scenarios:

$$\begin{aligned}
c &= \sqrt{\frac{M}{\rho}} && \text{Longitudinal wave – uniaxial strain} \\
c &= \sqrt{\frac{E}{\rho}} && \text{Longitudinal wave – uniaxial stress} \\
c &= \sqrt{\frac{K}{\rho}} && \text{Longitudinal wave – hydrostatic stress} \\
c &= \sqrt{\frac{G}{\rho}} && \text{Shear wave}
\end{aligned} \tag{2.12}$$

where  $M$ , also called  $\bar{E}$ , is the modulus of a longitudinal wave in an unbounded medium, related to the other elastic constants:

$$M = \lambda + 2\mu = K + \frac{4}{3}G = \frac{(1 - \nu)E}{(1 + \nu)(1 - 2\nu)} \tag{2.13}$$

Concerning the Lamé's second parameter, the notation  $\mu$  is typically used for a fluid, representing its viscosity, or in any case in combination with the Lamé's first parameter. In general, we will use for the rest of this work the notation  $G$ , representing in elasticity the shear modulus of a material.

The values of elastic wave velocities given in Table 1 were referred to unbounded media. It is possible to calculate the wave velocity for different conditions, through the relationships (2.12). Results are given in Table 2.

Table 2: Velocities of elastic waves with different boundary conditions.

Material	Wave velocity (m/s)			Shear Wave
	Longitudinal wave			
	1-axial stress	1-axial strain	Hydr. stress	
Aluminum	5 100	6 100	5 000	3 100
Steel	5 000	5 800	4 600	3 100
Lead	1 100	1 800	1 600	700
Beryllium	12 800	12 900	8 300	8 600
Glass/window	5 600	6 000	4 300	3 600
Plexiglas	1 600	2 600	800	1 200
Polystyrene	1 700	2 300	1 900	1 000
Magnesium	5 100	6 400	5 100	3 100
Molybdenum	5 700	7 500	6 400	3 400
Tungsten	4 600	5 200	4 000	2 900
Copper	3 800	4 600	3 700	2 300
Diamond	17 300	17 500	11 400	11 500
Graphite	2 500	2 500	1 600	1 700
304SS	5 000	5 600	4 200	3 200

## 2.2 Plastic waves

When the stress amplitude of the wave overcomes the elastic limit of the material, it decomposes into an elastic and a plastic wave. In this case, a material strength model, expressing the relationship between the flow stress and the strain, has to be assessed in order to study the plastic phenomenon (Figure 15).

In the simplest case, useful in the analytical study of plastic problems, the full  $\sigma - \varepsilon$  curve is represented by a *bilinear model*. The first stage, with slope equal to the Young's modulus  $E$ , is elastic, while the second stage, which is plastic, has also

a constant slope, usually called  $E'$ <sup>5</sup>. In numerical codes, more precise results are obtained with the use of a *multilinear model*, where the plastic region of the curve is represented by several linear functions of different slope.

Another common representation of the plasticity law is a power function between the flow stress and the strain (Figure 15). The relationship involves two semi-empirical material parameters to be determined with experimental measures. Several models exist, the most well-known under the names of *Ludwik* and *Hollomon*. In the case of Hollomon's plasticity, the relationship is:

$$\sigma_y = k\varepsilon^n \quad (2.14)$$

Where  $\sigma_y$  is the flow stress,  $n$  is the *strain hardening exponent* and  $k$  is the *strength coefficient*. Hollomon's equation describes a continuous function and, like the bilinear hardening law, is particularly efficient in the analytical modelling of phenomena involving plasticity. With respect to bilinear laws, however, the Hollomon's model in general better approximates the experimental curves, in particular those of metals.

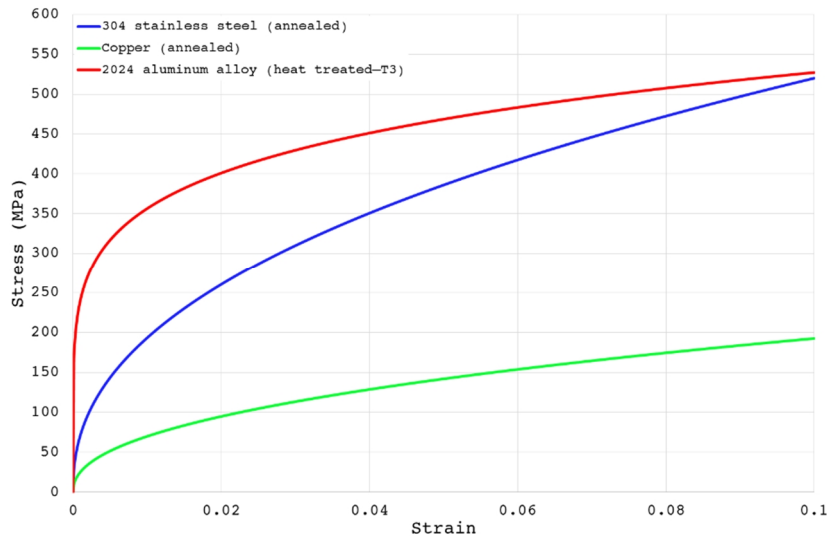


Figure 15. Hollomon's hardening law for three metals: stainless steel (blue),  $k_1=1400$  MPa,  $n_1=0.43$ ; copper (cyan),  $k_2=530$  MPa,  $n_2=0.44$ ; aluminium alloy (red)  $k_3=780$  MPa,  $n_3=0.17$ . Source: [8].

<sup>5</sup> The slope of the plastic line is commonly known as tangent, plastic or hardening modulus. Notations frequently used, on top of  $E'$ , are  $E_t$ ,  $E_p$  and  $T$ .

On top of strain hardening, engineering materials usually show a dependence of the flow stress on strain rate and temperature. Strength models which express this dependence are more complex and require a much higher number of experimental measurements for their full derivation with respect to the examples treated in this chapter, and will be better investigated in section 3.2.

To derive the equation of a longitudinal plastic wave, we can refer to the general equation (1.19), which, as discussed, is valid under any constitutive law. However, now the relationship stress – strain is no longer constant at any point of the curve. In the simple uniaxial stress case:

$$\rho_0 \frac{\partial^2 u}{\partial t^2} = \frac{d\sigma}{d\varepsilon} \frac{\partial \varepsilon}{\partial x} \quad (2.15)$$

Remembering that the strain is the spatial derivative of the displacement, the equation becomes:

$$\frac{\partial^2 u}{\partial t^2} = \frac{d\sigma/d\varepsilon}{\rho_0} \frac{\partial^2 u}{\partial x^2} \quad (2.16)$$

which is again identical to Eq. (1.20) with the velocity  $c$  assuming the more general form:

$$c = \sqrt{\frac{d\sigma/d\varepsilon}{\rho_0}} \quad (2.17)$$

In the elastic domain,  $d\sigma/d\varepsilon = E$  and the velocity of a longitudinal elastic wave in the case of uniaxial stress (2.12) is recalled, and is usually indicated with  $C_0$ . On the other hand, in the plastic domain, in the uniaxial stress state the lateral deformation is allowed and the  $\sigma - \varepsilon$  function is concave. This means that the plastic wave propagates at a speed lower than  $C_0$ , causing a dispersion of the wave front.

The dispersion of the wave front in the case of plasticity can be better shown with a numerical example, considering a cylindrical rod 1 m long, with a diameter of 10 mm, in 2024 aluminum alloy. The material yield stress is 240 MPa, with the hardening law reported in Figure 15 and submitted to a mechanical impact in the

direction parallel to the rod axis, with velocity 60 m/s for 0.1 ms. With reference to Figure 16 and Figure 17, the wave decomposes into an elastic wave, with velocity of 5 000 m/s up to the yield stress, and a plastic wave, with velocity gradually decreasing to 1 000 m/s at the level of maximum stress attained (420 MPa). The velocity of the waves can be easily determined out of Figure 16 and Figure 17 by simply evaluating the change in longitudinal coordinate at every time step, for a given stress or strain.

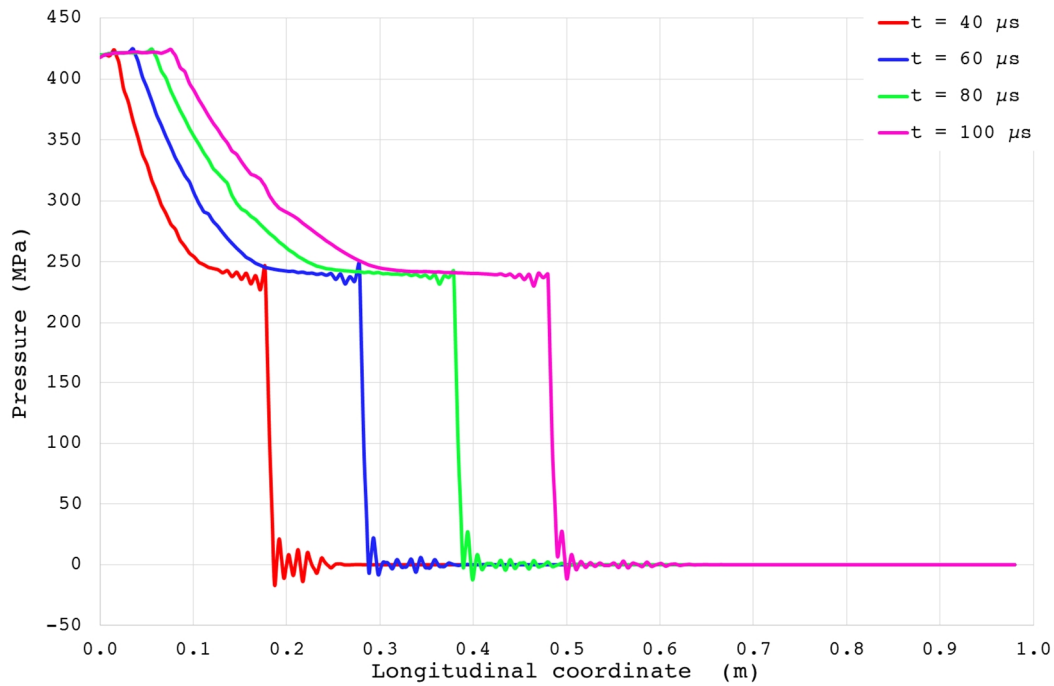


Figure 16. Wave front on a 2024 aluminum cylinder at given time instants. Note the constant velocity of propagation of the elastic front up to the yield stress. In the plastic domain, the velocity decreases with the increase of stress.

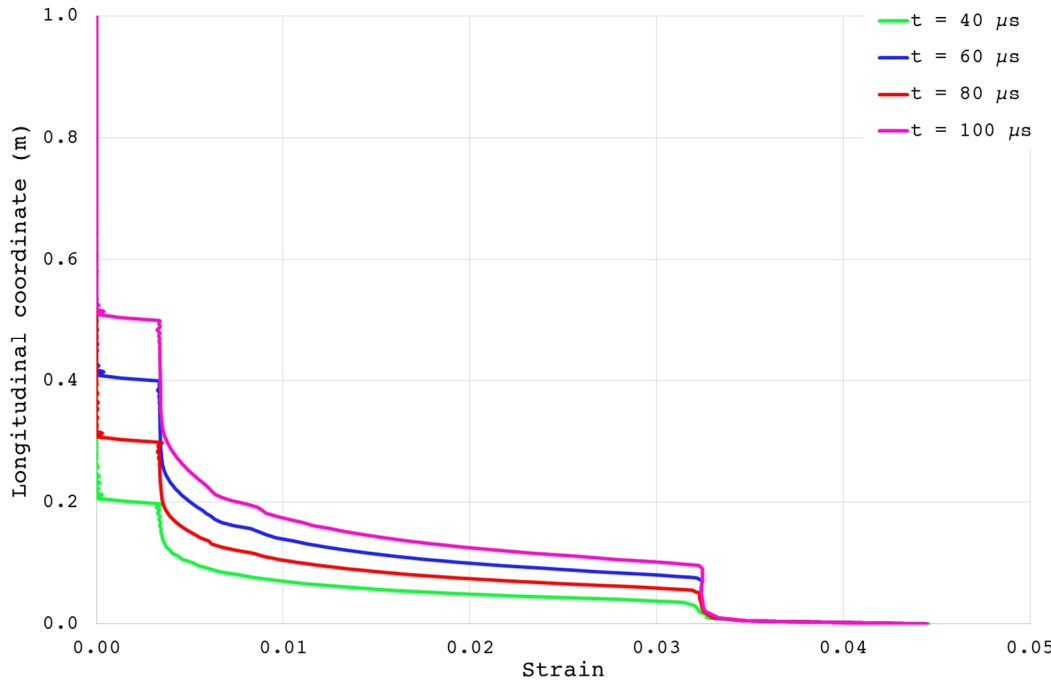


Figure 17. Plastic wave, strain profile as a function of the longitudinal coordinate  $x$  at different time instants.

### 2.3 Shock waves

As seen in the previous section, in uniaxial stress conditions the material constitutive law  $\sigma - \varepsilon$  is a concave function in the plastic domain, and this determines a dispersion of the wave front, with the plastic wave propagating slower than the elastic wave. On the other hand, in uniaxial strain conditions, the function is convex, and its slope  $d\sigma/d\varepsilon$  increases with the plastic strain. Thus, for very high amplitudes of the pressure wave, the plastic front steepens up along its propagation generating a discontinuity in pressure called *shock front*. In this scenario, the wave is called *shock wave* and propagates through the surrounding volume at a speed higher than the initial speed of sound.

The easiest way to study the phenomenon is using an analogy with the pressure variation in an ideal gas [1]. For such a material, the equation of state for an isentropic process is:

$$pV^\gamma = K \quad (2.18)$$

where  $p$  and  $V$  are pressure and volume of the ideal gas,  $K$  is the bulk modulus and  $\gamma$  the *adiabatic index* or *isentropic expansion factor*, defined as the ratio between heat capacity at constant pressure and heat capacity at constant volume:

$$\gamma = \frac{C_p}{C_v} = \frac{c_p}{c_v} \quad (2.19)$$

By differentiating, one finds:

$$\begin{aligned} \gamma p V^{\gamma-1} dV + V^\gamma dp &= 0 \\ \frac{dp}{dV} &= -\gamma \frac{p}{V} \end{aligned} \quad (2.20)$$

Given that the ratio  $p/V$  increases with the pressure, so does  $dp/dV$ . The bulk modulus  $K$  also increases with pressure, and therefore its inverse, the *compressibility*, decreases. Similarly to Eq. (2.17), for an ideal gas the velocity of a disturbance can be written as:

$$c = \sqrt{\frac{dp/dV}{\rho}} \quad (2.21)$$

The wave velocity in an ideal gas therefore increases with the pressure. For a solid material, above the elastic limit there are thus two scenarios:

1. The treatment just seen cannot be extended to the solid, for example in uniaxial stress conditions. In this case, the ratio  $d\sigma/dV$  decreases at increasing stress, implying a dispersion of the wave front, with the plastic wave propagating at a speed lower than the speed of sound (see section 2.2).
2. The solid is in a *hydrostatic condition* and behaves like an ideal gas. Now the ratio  $d\sigma/dV$  increases with the stress, the  $\sigma - \varepsilon$  curve becomes convex, with the plastic wave propagating at a speed higher than the speed of sound. The wave front becomes a discontinuity (*shock front*) and the wave is called *shock wave*.

### 2.3.1 Hydrodynamic material state

The condition needed for the generation of shock waves is therefore the buildup on the component of a hydrostatic stress of magnitude much higher than the material strength. The solid can then be assumed to behave like a fluid, with negligible shear modulus. In the basic treatment of the phenomenon, on top of neglecting shear modulus and hardening, it is assumed that no phase transformations, body forces and heat conduction occur. The heat conduction, as seen in Chapter 1, can be effectively neglected for quasi-instantaneous loads with short pulse length; however, recent numerical codes are able to take into account also the contribution of all these terms, which in reality cannot be fully ignored. In particular, the case of material hardening in the plastic domain will be further investigated in section 2.3.2.

As seen, the fundamental requirement for the generation of a shock wave is that the ratio  $d\sigma/dV$  increases with the stress, leading to pulses with a velocity increasing with the pressure. As discussed in section 2.1, for the derivation of the elastic wave equation, the conservation of momentum is the only equation needed. In the case of shock waves, the conservation of mass, momentum and energy have to be applied for the formulation of the problem. Figure 18 illustrates the material state ahead and behind the shock front.

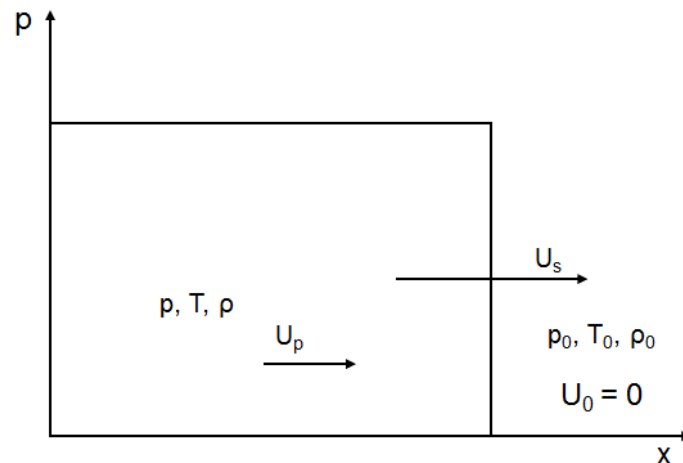


Figure 18. Shock front, hydrodynamic treatment.

The center of the reference system is the shock front and, with this respect, the material ahead is in an unshocked condition of pressure  $p_0$ , temperature  $T_0$  and density  $\rho_0$ , with null velocity  $U_0$ . The shocked material is at  $p$ ,  $T$  and  $\rho$ , and moves

with velocity  $U_p$ . The relative velocity of the front with respect to the unshocked material is  $U_s - U_0 = U_s$ , while the shocked material recedes from the front with a relative velocity  $U_s - U_p$ .

According to the conservation of mass, the mass of material moving towards the front equates the mass receding from the front, therefore:

$$\rho_0 U_s = \rho(U_s - U_p) \quad (2.22)$$

Concerning the conservation of momentum, for which the impulse is equal to the change in momentum, the equation is:

$$p - p_0 = \rho_0 U_s U_p \quad (2.23)$$

where the first term is derived from the impulse and the second depends on the momentum change. The quantity  $\rho_0 U_s$  is very often used in the study of the interaction of the shock waves with an interface, and is called *shock impedance* ( $Z$ ).

Finally, according to the conservation of energy, the work done by the shock wave is equal to the total energy of the shocked material<sup>6</sup>. The same is true also in the unshocked volume, *i.e.* the difference in work is equal to the difference in energy between shocked and unshocked material, and:

$$pU_p = \frac{1}{2}\rho_0 U_s U_p^2 + \rho_0 U_s (E - E_0) \quad (2.24)$$

where  $E$  and  $E_0$  are the internal energies of the shocked and un-shocked material. The three conservation equations are therefore:

$$\begin{cases} \rho_0 U_s = \rho(U_s - U_p) \\ p - p_0 = \rho_0 U_s U_p \\ pU_p = \frac{1}{2}\rho_0 U_s U_p^2 + \rho_0 U_s (E - E_0) \end{cases}$$

---

<sup>6</sup> The total energy is equal to the sum of kinetic and internal energy.

It is convenient to combine the three equations above in a single one, to explicit, for example, the energy generated by the shock as a function of the other quantities:

$$E - E_0 = \frac{1}{2}(p + p_0) \left( \frac{1}{\rho_0} - \frac{1}{\rho} \right) \quad (2.25)$$

This form of the energy conservation is known as *Hugoniot equation*. The unknowns of the equation are  $E$ ,  $p$  and  $\rho$ . The inverse of the density, the specific volume  $v$ , is also often adopted. If we consider the system of three equations (2.22), (2.23) and (2.24), the other two unknowns are  $U_s$  and  $U_p$ . In both cases, an additional equation is needed in order to determine all the parameters as a function of one of them. This fourth equation has different forms, the most common ones relating  $U_s$  and  $U_p$ , or  $E$ ,  $p$  and  $\rho$ , and is defined as the *equation of state (EOS)* of the material:

$$U_s = C_0 + S_1 U_p + S_2 U_p^2 + \dots + S_n U_p^n$$

$$p = f(\rho, E)$$

with  $C_0$  equal to the sound speed of the unstressed material and  $S_1, S_2, \dots, S_n$  parameters of the polynomial expression to be determined by a combination of predictive models and experiments. In general, when phase changes do not occur, a linear equation of state describes sufficiently well the shock response of the material [1]:

$$U_s = C_0 + S_1 U_p \quad (2.26)$$

$$p = K \left( \frac{\rho}{\rho_0} - 1 \right) + \gamma_0 E \quad (2.27)$$

where  $\gamma_0$  is the Grüneisen parameter. More details on this parameter and on EOS in general are given in section 3.1.

Values for  $C_0$  and  $S_l$  can be found in literature for common materials and alloys (Table 3), and can be used for fully determining the shock conditions for values of, for example, pressure reached during the impact. On the other hand, in the case of quasi-static heating, as discussed in Chapter 1, the problem is driven by the temperature sudden increase, but the pressure wave propagating from the impact

point influences all the variables in the body volume reached by the wave. The mechanical and thermal problems are thus coupled, and the characterization of the material response under these conditions is of paramount importance.

Table 3: Coefficients of the Hugoniot equation. Source: [1] p. 108, [9], [10].

Material	$C_0$ (km/s)	$S_1$
Copper	3.958	1.497
2024 aluminum alloy	5.328	1.338
921-T Al	5.041	1.420
304 stainless steel	4.569	1.488
Iron	3.574	1.920
U-Mo alloy	2.565	1.531
Tungsten	4.029	1.242
Nickel	4.581	1.463
Titanium	5.220	0.768
Lead	2.028	1.517

The Hugoniot equation (2.25) is shown graphically in the  $p$ - $v$  diagram of Figure 19. It is defined as the locus of all the shocked states that can be reached in a material during a shock transition. The discontinuity in pressure and density, or *jump condition*, defined by the Hugoniot equation is represented by the line joining the coordinates  $(p_0, v_0)$  and  $(p_1, v_1)$ , which is called *Rayleigh line*. The loading during the shock occurs along the Rayleigh line, which is derived through the equation:

$$\frac{p - p_0}{v - v_0} = -(\rho_0 U_s)^2 \quad (2.28)$$

It is now clear why at higher pressures the velocity of the wave propagation increases: starting from the condition  $(p_0, v_0)$ , the jump to higher pressures on the Hugoniot curve is determined by the slope of the Rayleigh line, which is proportional to the pressure, and therefore to the velocity of the wave, as seen in Eq. (2.21).

While the pressure loading occurs along the Rayleigh line, the unloading follows the isentrope path, which is typically so close to the Hugoniot curve that in engineering problems they can be considered coincident [11]. The area between the Rayleigh line and the Hugoniot curve represents the energy retained in a sample undergoing shock loading, and is responsible for the heating of the sample. The Hugoniot has to be determined by experimental methods, reconstructing it from several points  $(p_i, v_i)$ .

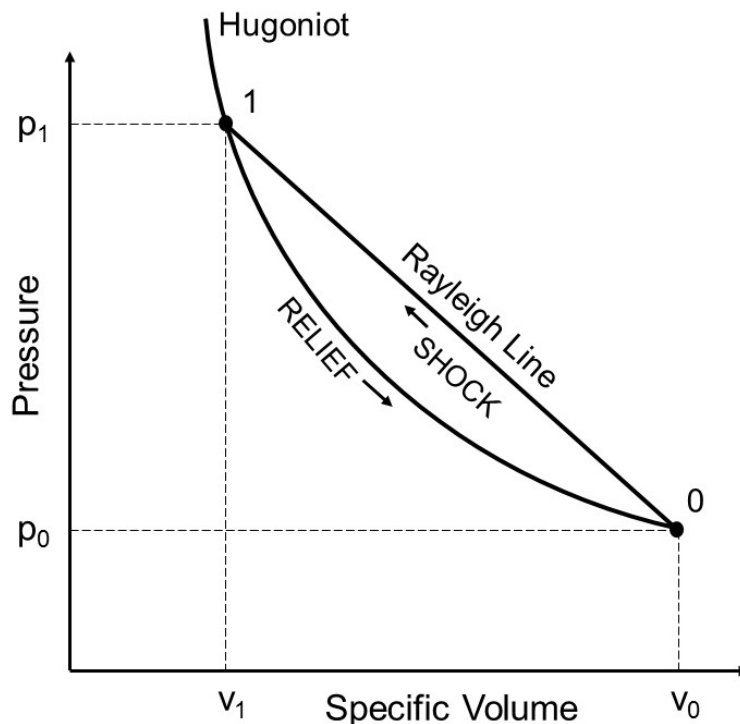


Figure 19. Characteristic Hugoniot curve and Rayleigh line in the pressure vs. specific volume plane.

It is important to point out that, since the applied loading is of finite duration, a rarefaction wave is generated after the load removal. Since any signal travelling in the shocked volume is faster than the compressive wave, the rarefaction wave reaches and attenuate the amplitude of the compression. This phenomenon is very relevant in the cases studied in this work, where the loading is of very short duration, and will recur in the numerical examples showed.

### 2.3.2 Shock in elastoplastic materials

In the previous section the material was assumed to behave like a fluid, with no shear modulus and strength, subjected to pure hydrostatic pressure. This was also

the assumption introduced in the first numerical codes studying the shock phenomenon, and the reason for the term used to define them – *hydrocodes* [11]. In reality, the elastoplastic behavior of the material cannot be neglected, and the Hugoniot curve depicted in Figure 19 must be updated to keep into account the deviatoric component of the stress. In any case, it is evident that the very high stresses needed to trigger the jump condition in a shock cannot be reached in a uniaxial stress scenario, as the amount of hardening experienced by a material before failure is limited under this hypothesis. As discussed at the beginning of section 2.3, the physical scenario under which shock waves can develop is uniaxial strain. In this case, the  $\sigma - \varepsilon$  curve becomes convex (Figure 20), as it can be determined using Eq. (1.8) and imposing:

$$\varepsilon_2 = \varepsilon_3 = 0 \quad (2.29)$$

Defining as  $Y_0$  the equivalent stress according to the Tresca-Guest criterion:

$$\sigma_1 - \sigma_2 = Y_0 \quad (2.30)$$

one can determine the  $\sigma - \varepsilon$  relation in case of uniaxial strain:

$$\sigma_1 = K\varepsilon_1 + \frac{2}{3}Y_0 \quad (2.31)$$

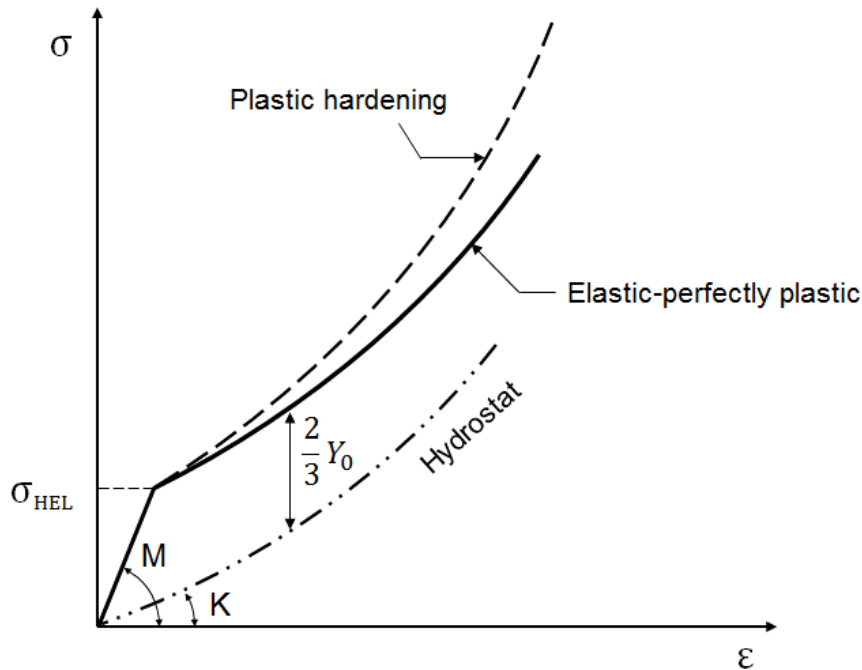


Figure 20.  $\sigma - \varepsilon$  curve for a material in uniaxial strain conditions. The extension of the elastic strain has been exaggerated for the sake of clarity.

The yield stress in uniaxial strain condition is usually indicated with  $\sigma_{HEL}$ , or *Hugoniot elastic limit*. In Figure 20, the initial slope of the hydrostatic curve is the bulk modulus  $K$  and the slope of the elastic line is  $M$ , the modulus of a longitudinal wave in an unbounded medium, defined in Eq. (2.13). We thus find again the relationships showed for the propagation of elastic waves in uniaxial strain and hydrostatic conditions. Again, the material compressibility decreases with the stress, and the bulk modulus increases; on the other hand, in the case of strain or strain rate hardening, the slope of the curve further increases with respect to the elastic-perfectly plastic and the hydrostatic cases.

One can also better understand the jump condition in cases of an elastoplastic material: in uniaxial strain conditions, the velocity of plastic waves is initially lower than that of elastic waves, but it increases with the stress, surpassing at a certain point  $C_0$  and creating the conditions for the generation of a shock front. This concept can easily be explained graphically by drawing the Hugoniot curve, this time in stress and strain coordinates (Figure 21).

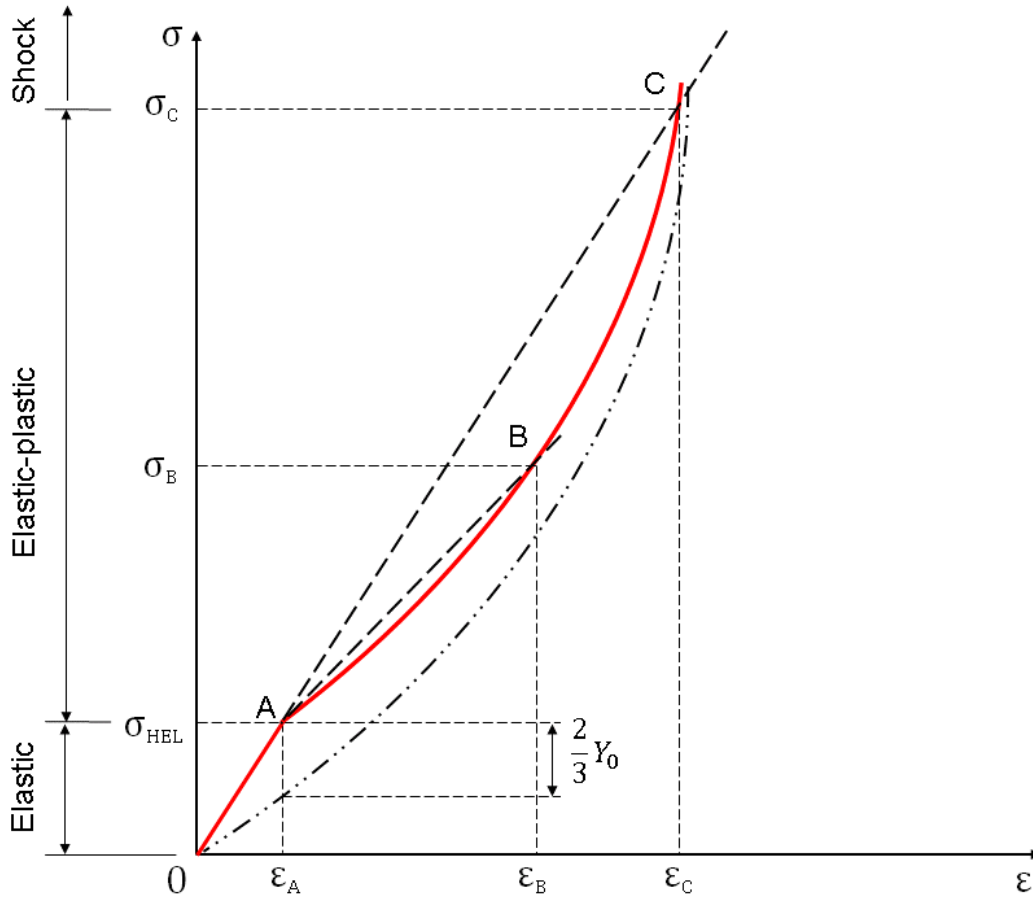


Figure 21. Hugoniot curve in stress and strain coordinates for an elastic-perfectly plastic material.

With reference to Figure 21, a number of considerations can be made:

- The area  $OA$  is characterized by the elastic precursor, with  $\sigma_{HEL}$  onset of plastic wave generation, travelling at a lower speed.
- The elastic precursor propagation speed, for a uniaxial strain condition, is higher than a wave in uniaxial stress.
- $B$  is a generic point in the plastic domain, with waves propagating at a speed depending on the ratio  $dp/d\varepsilon$ . The material deforms plastically without hardening and the curve is parallel to the hydrostat.
- $C$  is the onset of shock wave production. Above  $C$ , the material presents characteristics similar to a fluid.
- Strain and strain rate hardening ease the achievement of the shock condition, as the  $\sigma - \varepsilon$  curve slope is higher and the critical stress  $\sigma_C$  decreases. The entity of the reduction depends on the material, but it is in any case tiny with respect to the magnitude of the critical stress.

### 2.3.3 Considerations on thermally-induced shock waves

The critical stress triggering the generation of shock waves can be reached with mechanical tests (flyer plates, explosives, etc.) or with isochoric heating. In the latter case, due to the high magnitude of the critical stress, one can think to employ a laser or a proton (or ion) beam, to profit from the enormous energy and energy density stored, as seen in Chapter 1. However, there are a number of complications when applying such methods. Let us focus on the most energetic proton beams: the shape of the energy deposition on the matter mostly follows the beam trajectory, with a peak along the beam axis, and typically a Gaussian distribution in the material transversal sections. The waves generated by the impact present a cylindrical pattern and, as it will be discussed in section 4.3, the amplitude of cylindrical waves rapidly decreases during the expansion inside the impacted material. The shock condition is hard to reach even in the most impacted volume [12]. To demonstrate this in a simple way, one can consider three materials already adopted in previous examples of this thesis and reconstruct the Hugoniot curve in uniaxial strain conditions, combining the Hugoniot coefficients reported in Table 3 with the material properties of Table 4.

Table 4: Thermophysical properties. Source: [13]

	<b>Copper annealed</b>	<b>Al 2024 heat treated (T3)</b>	<b>304SS annealed</b>
$E$ (GPa)	110	73	193
$\nu$	0.34	0.36	0.29
$Y_0$ (MPa)	40	310	215
$\rho_0$ (kg/m <sup>3</sup> )	8930	2785	7896
$T_m$ (°C)	1085	660	1400
$\alpha_{0-T_m}$ ( $10^{-6} \times K^{-1}$ )	25.9	37.4	23.3

$T_m$  is the melting temperature of the material and  $\alpha_{0-T_m}$  the secant thermal expansion coefficient between 0 °C and the melting point. To simplify the problem, one can assume elastic – perfectly plastic material to calculate the curve which was seen qualitatively in Figure 21.

Figure 22 reports the calculated Hugoniot curves and Rayleigh lines for copper annealed, stainless steel 304 annealed and aluminum 2024 heat treated, grade T3 [13]. The hydrostat is not reported, as it almost coincides with the elastic-plastic curve. One can also notice the small extension of the elastic domain with respect to the plastic and shock regimes.

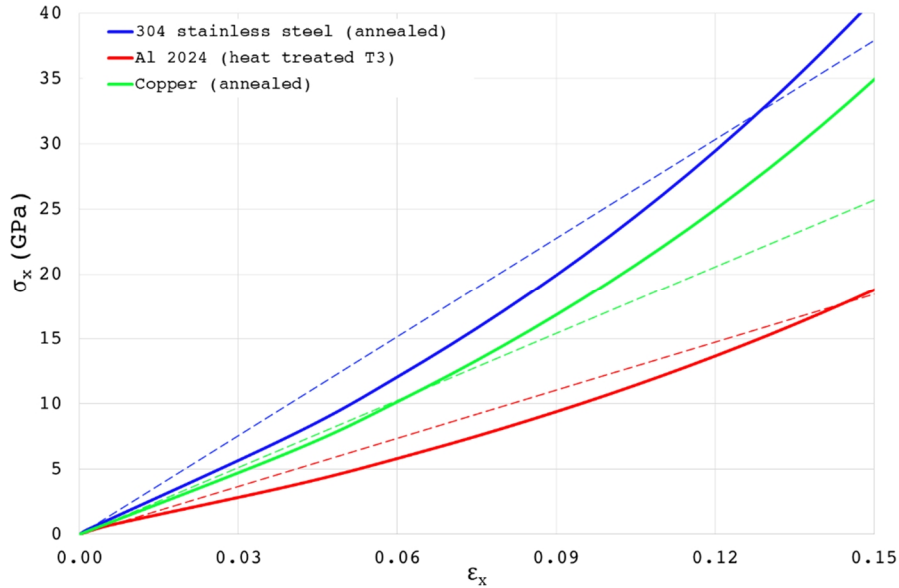


Figure 22. Hugoniot curve and Rayleigh line for three different elastic – perfectly plastic materials.

If the only applied load is thermal, the uniaxial strain experienced by the body can be evaluated through the coefficient of thermal expansion. It is evident that in the examined materials, the strain level induced by the melting is far from the critical conditions (Table 5). This simplified example shows that shock phenomena induced by a rapid heating typically involve a change of phase in the impacted volume. A more elaborated, numerical study of this concept is reported in section 4.3.

Table 5: Critical shock stress and strain for the three materials, compared with the strain level experienced at the onset of melting.

	<b>Copper annealed</b>	<b>Al 2024 heat treated (T3)</b>	<b>304SS annealed</b>
$\sigma_c$ (GPa)	10.7	17.5	32
$\varepsilon_c$ (%)	6.4	14.4	13.1
$\varepsilon_{th,melt}$ (%)	2.8	2.4	3.2

## 2.4 Glossary

Symbols are listed in chronological order with respect to their appearance in the text.

<b>Symbol</b>	<b>Definition</b>	<b>SI unit</b>
$\sigma$	Stress	Pa
$s$	Deviatoric stress	Pa
$p$	Pressure	Pa
$\varepsilon$	Strain	–
$e$	Deviatoric strain	–
$\Delta$	Dilatation	–
$C_{ij}$	Components of the stiffness matrix	Pa
$S_{ij}$	Components of the compliance matrix	Pa
$E$	Young's modulus	Pa
$G, \mu$	Shear modulus or second Lamé's parameter	Pa
$\nu$	Poisson's ratio	–
$K$	Bulk modulus	Pa
$\lambda$	First Lamé's parameter	Pa

$v$	Specific volume	$\text{m}^3 \cdot \text{kg}^{-1}$
$\rho$	Density	$\text{kg} \cdot \text{m}^{-3}$
$U_p$	Particle velocity	$\text{m} \cdot \text{s}^{-1}$
$U$	Wave velocity	$\text{m} \cdot \text{s}^{-1}$
$x$	Position	m
$u$	Displacement	m
$t$	Time	s
$c$	Speed of the wave propagation	$\text{m} \cdot \text{s}^{-1}$
$M$	Modulus of a longitudinal wave in an unbounded medium	Pa
$E'$	Slope of the plastic line in a bilinear plasticity model	Pa
$n$	Hollomon's strain hardening exponent	–
$k$	Hollomon's strength coefficient	Pa
$C_0$	Velocity of the elastic wave <sup>7</sup>	$\text{m} \cdot \text{s}^{-1}$
$V$	Volume	$\text{m}^3$
$\gamma$	Isentropic expansion factor	–
$C_p$	Heat capacity at constant pressure	$\text{J} \cdot \text{K}^{-1}$
$C_v$	Heat capacity at constant volume	$\text{J} \cdot \text{K}^{-1}$
$c_p$	Specific heat capacity at constant pressure	$\text{J} \cdot \text{kg}^{-1} \cdot \text{K}^{-1}$
$c_v$	Specific heat capacity at constant volume	$\text{J} \cdot \text{kg}^{-1} \cdot \text{K}^{-1}$
$p_0$	Pressure of the unshocked material	Pa
$T_0$	Temperature of the unshocked material	K
$\rho_0$	Density of the unshocked material	$\text{kg} \cdot \text{m}^{-3}$

<sup>7</sup> The notation  $C_0$  is often used for a longitudinal elastic wave in uniaxial stress conditions.

$v_0$	Specific volume of the unshocked material	$\text{m}^3 \cdot \text{kg}^{-1}$
$U_0$	Velocity of the wave in the unshocked material	$\text{m} \cdot \text{s}^{-1}$
$U_s$	Velocity of the wave in the shocked material	$\text{m} \cdot \text{s}^{-1}$
$Z$	Shock impedance	$\text{Pa} \cdot \text{s} \cdot \text{m}^{-1}$
$E_0$	Specific energy of the unshocked material	$\text{J} \cdot \text{kg}^{-1}$
$E$	Specific energy of the shocked material	$\text{J} \cdot \text{kg}^{-1}$
$S_1, S_2, \dots, S_n$	Coefficients of the Hugoniot n-grade polynomial in $U_s - U_p$ coordinates	–
$\gamma_0$	Grüneisen parameter	–
$\gamma_0$	Tresca-Guest equivalent stress	Pa
$\sigma_{HEL}$	Hugoniot elastic limit	Pa
$T_m$	Melting temperature	$^{\circ}\text{C}, \text{K}$
$\alpha_{0-T_m}$	Secant coefficient of thermal expansion between $0^{\circ}\text{C}$ and melting temperature	$\text{K}^{-1}$

## References

- [1] M. A. Meyers (1994). Dynamic behaviour of materials. J. Wiley & Sons, ISBN 047158262.
- [2] P. W. Bridgman (1947). The effect of hydrostatic pressure on the fracture of brittle substances. *Journal of Applied Physics*, Vol. 18, p. 246.
- [3] J. R. Rice and D. M. Tracey (1969). On the ductile enlargement of voids in triaxial stress fields. *Journal of the Mechanics and Physics of Solids*, Vol. 17, pp. 201-217.
- [4] V. S. Deshpande and N. A. Fleck (1999). Isotropic constitutive models for metallic foams. *Journal of the Mechanics and Physics of Solids*, Vol. 48, pp. 1253-1283.

- 
- [5] P. A. Allen and C. D. Wilson (2004). Hydrostatic Stress Effect on the Yield Behavior of Inconel 100. *Journal of the Mechanical Behavior of Materials*, Vol. 15, Issue 1-2, pp. 27-48.
  - [6] G. Genta (1992). Principi e metodologie della progettazione meccanica, Vol.2, Levrotto & Bella.
  - [7] H. Kolsky (1963). Stress waves in solids. Dover Publications, ISBN 0486610985.
  - [8] W. D. Callister (2007). Materials science and engineering: an introduction. EdiSES, ISBN 978887959421, p. 152.
  - [9] S. Eliezer, A. Ghatak and H. Hora (1986). Fundamentals of equation of state. World Scientific, ISBN 9810248334, p. 209.
  - [10] R. G. McQueen, S. P. Marsh, J. W. Taylor, J. N. Fritz and W. J. Carter (1970). The equation of state of solids from shock wave studies. In R. Kinslow, *High-velocity impact phenomena*, ISBN 9780323144988, p. 317.
  - [11] J. A. Zukas (2004). Introduction to hydrocodes. *Studies in applied mechanics*, Elsevier, ISBN 0080443486.
  - [12] A. Bertarelli *et al.* (2011). Limits for beam induced damage: reckless or too cautious? *Proc. Chamonix 2011: Workshop on LHC Performance*.
  - [13] J. J. Valencia, P. N. Quested (2008). Thermophysical properties. In *ASM Handbook, Vol. 15: Casting*, ASM International, ISBN 0871700212.

## Chapter 3

# Description of the dynamic response: equation of state and constitutive models

The description of the hypervelocity impact phenomena, and dynamic events in general, requires the development of semi-empirical relationships between the variables controlling the material response, such as pressure or stress, density, energy, temperature and strain. As seen in section 2.3.1, if  $\sigma$  is assumed to depend only on  $\rho$  and  $E$ , the stress tensor reduces to a scalar quantity, and the material response is fully described by the *equilibrium hydrostatic equation of state (EOS)*, which completes a set of equations also including the three laws of conservation of mass (2.22), momentum (2.23) and energy (2.24). However, in dynamic problems, deviations from the hydrostatic condition are relevant, in particular in the case of solid materials. The stress becomes then a function of shear strain, too, and the deviatoric component can no more be ignored. This is even more relevant at stresses below the shock critical condition, with waves propagating at a velocity equal to or lower than the initial speed of sound. The description of the deviatoric behaviour of the material is related to the *constitutive response*, which includes anisotropy, inelastic effects related to strain, strain rate, temperature, internal damping, and fracture. Typically, the tools used to model the  $\sigma - \varepsilon$  relationship are known as *strength models*, while the mechanisms controlling fracture, spallation and fragmentation depend on the *failure models*.

In this chapter, the most relevant equations of state will be introduced, together with the experimental methods adopted to derive them, including a conceptual proposal for the use of isochoric heating methods to explore unusual regions of the EOS. A detailed treatment of the principal strength and failure models will then be given, with examples of models derived in the scope of this thesis.

### 3.1 Equation of state

Equations of state are typically built combining statistical mechanical models and experimental data. In the past, EOS based exclusively on statistical mechanics could be adopted only for highly idealized problems. In recent years, however, more accurate predictive theories have been developed and the role of experiments has changed. The experimental data are no longer inputs for a fitting/optimization process, partly based on theoretical assumptions, but they are now used to benchmark EOS entirely developed with predictive theories, looking for potential weak points or improvements [1]. The higher accuracy of predictive models is beneficial especially in EOS regimes inaccessible to experiments.

As mentioned in section 2.3.1, the typical form of an EOS is a relation between pressure, density and energy, or between the shock velocity and the particle velocity:

$$U_s = C_0 + S_1 U_p + S_2 U_p^2 + \dots + S_n U_p^n$$

$$p = f(\rho, E)$$

However, in principle an EOS can be expressed relating any two independent variables among  $p$ ,  $v$  (or  $\rho$ ),  $E$  (or  $T$ ),  $U_s$ ,  $U_p$ . The knowledge of the heat capacity  $C_v$  and specific heat capacity  $c_v$ , over a wide range of temperatures, is also required to express the temperature as a function of the energy:

$$C_v = \left( \frac{\partial E}{\partial T} \right)_v$$

$$c_v = \left( \frac{\partial C_v}{\partial m} \right)_v$$
(3.1)

where  $m$  is the mass. The most well-known and simplest EOS is the *ideal gas law*, expressing the relation between pressure, volume and temperature for a fluid made of point particles interacting with one another only by elastic collisions. This EOS can be derived either from statistical and kinetic considerations, or empirically, and has the form:

$$p = \rho RT \quad (3.2)$$

where  $R$  is the *specific gas constant*, which can be evaluated as:

$$R = c_p - c_v \quad (3.3)$$

Eq. (3.3) is known as *Mayer's relation*.

In real materials, equations of state are much more complex. In particular, the changes of phase have to be taken into account, and the Hugoniot curve of Figure 19 becomes of the form qualitatively sketched for a fictitious material in the  $T, \rho$  plane of Figure 23.

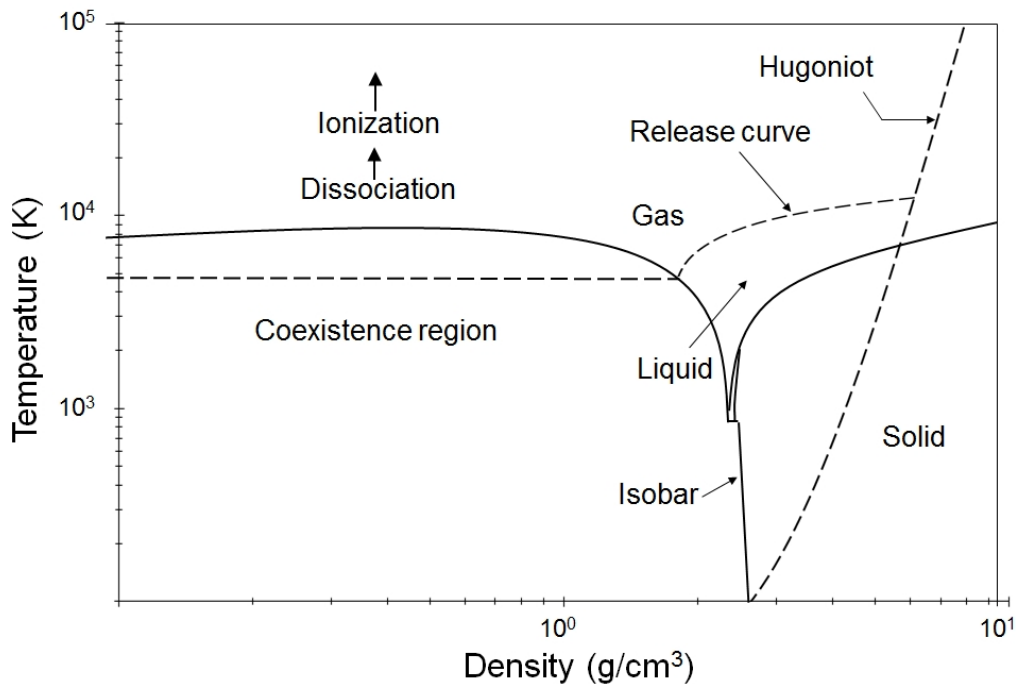


Figure 23. Regions of interest in an EOS of a fictitious material.

With reference to Figure 23, the following regions of interest have to be determined while constructing an equation of state:

- solid phase;
- liquid phase;
- coexistence region liquid/gas;
- gas phase;

- plasma phase;
- transition regions.

In the expression of an EOS, reference to the *cold curve* is often made. The cold curve is defined as the region of the pressure, density, temperature diagram corresponding with the 0 K isotherm. Numerical codes [2] usually express the equation of state as a sum of two components:

$$p = p_c(\rho) + p_T(\rho, E) \quad (3.4)$$

where  $p_c$  represents the cold curve, while the second term  $p_T$  is energy (and therefore temperature) dependent.

Examples of EOS adopted in the scope of this thesis are given below. As explained in sections 2.3.3 and 4.3.1, the material regime that can be reached experimentally by isochoric heating with no change of phase is typically below the shock threshold, and an *EOS linear in density* describes fairly well the material response when no phase transformations are involved [3]. An extension of linear EOS is the *Mie-Grüneisen*, which can be applied to a certain extent also in the liquid phase [4], and is the base for the derivation of EOS for alloys, mixtures and porous materials. When the energies involved in the shock lead to the generation of gas or plasma, or when several solid phases exist in addition to the liquid<sup>8</sup>, separate EOS are built for each phase, locating the phase boundaries by matching free energies. EOS computed in this way are usually expressed in tabular form; an example is the *SESAME* EOS, developed and maintained by the Los Alamos National Laboratory (US) [5].

### 3.1.1 Linear

This simple equation of state expresses the relation between pressure and density with a linear function. With reference to Eq. (3.4), the cold curve has the following form:

$$p_c(\rho) = K \left( \frac{\rho}{\rho_0} - 1 \right) \quad (3.5)$$

---

<sup>8</sup> A common example of material with strongly different solid phases is carbon, which can appear under the form of graphite or diamond.

The proportionality constant is therefore represented by the Bulk modulus. The energy-dependent component of the EOS is:

$$p_T(\rho, E) = \gamma_0 E \quad (3.6)$$

Where  $\gamma_0$  is the *Grüneisen parameter* calculated at  $\rho_0$ :

$$\gamma_0 = \frac{\alpha K}{\rho_0 c_v} \quad (3.7)$$

Combining Eqs. (3.5) and (3.6), one can derive the general expression of the linear EOS:

$$p(\rho, E) = K \left( \frac{\rho}{\rho_0} - 1 \right) + \gamma_0 E \quad (3.8)$$

which, for negligible changes of density, reduces to:

$$p(E) = \frac{\alpha K}{\rho_0 c_v} E \quad (3.9)$$

Eq. (3.9) is simply an expression of Eq. (1.10) for the hydrostatic tensor.

### 3.1.2 Mie-Grüneisen for crystals, porous materials and compounds

The Mie-Grüneisen approximation is a powerful tool for describing an equation of state, because of its simplicity and the fact that it can be directly fit to experimental data without using theoretical models. It is expressed by the relation:

$$p(\rho, E) = p_r(\rho) + \rho\gamma[E - E_r(\rho)] \quad (3.10)$$

where  $p_r$  and  $E_r$  are pressure and energy calculated with respect to a reference curve, which is usually the Hugoniot. The Mie-Grüneisen EOS cannot be used at very high densities and in the regions of expanded liquid and vapor, but its main disadvantage is that it is hard to determine in regions where experimental data are missing. Outside those regions, the product  $\gamma\rho$  can be considered constant [3]:

$$\gamma\rho = \gamma_0\rho_0 \quad (3.11)$$

The shock constants of Table 3 can be integrated with the Grüneisen parameter, for construction of the Mie-Grüneisen EOS (Table 6).

Table 6: Shock and thermodynamic properties. Source: [3], p. 133.

<b>Material</b>	<b><math>C_0</math> (km/s)</b>	<b><math>S_1</math></b>	<b><math>\gamma_0</math></b>
Copper	3.958	1.497	2.0
2024 aluminum alloy	5.328	1.338	2.0
921-T Al	5.041	1.420	2.0
304 stainless steel	4.569	1.488	2.2
Iron	3.574	1.920	1.8
Tungsten	4.029	1.242	1.8
Nickel	4.581	1.463	2.0
Titanium	5.220	0.768	1.2
Lead	2.028	1.517	2.8

The materials investigated in this work are often produced by sintering, or in any case by compaction of a matrix and particle reinforcements. The density of such materials is typically lower than the theoretical one, due to the presence of porosities. The ratio between the two densities is defined as *compaction ratio*, or *relative density*, and can be as low as 0.75 in the case of carbon-fiber reinforced carbon composites [6]. Macroscopic thermo-physical measurements on the material are used to build a linear EOS. It is interesting to formulate the semi-empirical method which can be used to derive an EOS for a material with varying compaction, starting from the constituents (crystals), for which the EOS is known. The Mie-Grüneisen approximation is adopted, calculating  $p_r$  and  $E_r$  with respect to the Hugoniot. In this case, such variables are called  $p_H$  and  $E_H$ . If the reference is the Hugoniot curve, one can adopt Eqs. (2.22), (2.23), (2.24) and (2.26) to describe it for the crystal or for a solid with compaction ratio equal to 1:

$$\rho_0 U_{sH} = \rho(U_{sH} - U_{pH}) \quad (3.12)$$

$$p_H = \rho_0 U_{sH} U_{pH} \quad (3.13)$$

$$E_H = \frac{1}{2} p_H (V_0 - V) \quad (3.14)$$

$$U_{sH} = C_0 + S_1 U_{pH} \quad (3.15)$$

where  $\rho_0$  and  $V_0$  are the initial density and volume of the crystal.

For the porous material, the same laws of mass, momentum and energy conservations are valid:

$$\rho_0^* U_s = \rho(U_s - U_p) \quad (3.16)$$

$$p = \rho_0^* U_s U_p \quad (3.17)$$

$$E = \frac{1}{2} p (V_0^* - V) \quad (3.18)$$

where  $\rho_0^*$  and  $V_0^*$  are the initial density and volume of the porous material, for which the relation between  $U_s$  and  $U_p$  is not known. The computation of the Hugoniot of the porous material can be made starting from the crystal-density Hugoniot, hypothesizing a volumetric dependence for  $\gamma$ . Introducing Eqs. (3.14) and (3.18) in Eq. (3.10):

$$p = p_H \frac{2V - \gamma(V_0 - V)}{2V - \gamma(V_0^* - V)} \quad (3.19)$$

The pressure  $p_H$  can be calculated out of Eq. (3.13), which contains only known (measured) variables. Obviously, for  $V_0 = V_0^*$ , the equation of state is reduced to the EOS of the crystal.

As an example, Figure 24 reports the  $p - V$  curves calculated with Eq. (3.19) and the shock and thermodynamic parameters of Table 6, for Al 2024 T3.

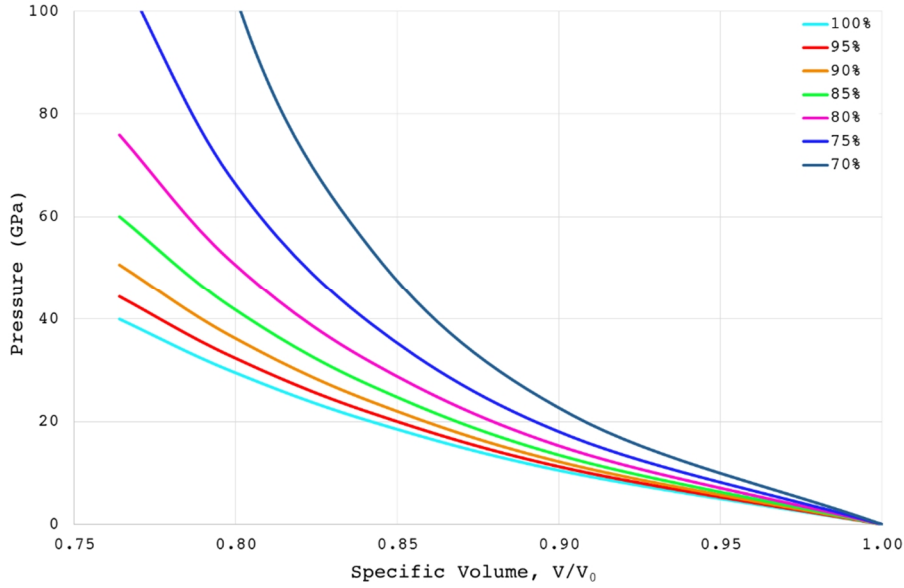


Figure 24. Calculated EOS for Al 2024 T3 with different compaction ratios. Shock parameters are reported in Table 6. The compaction ratio for a solid without porosities is 100%.

A similar process is obtained to build simple EOS for compounds. Apart from widely adopted materials such as stainless steel 304 and aluminum alloys, the EOS of compounds are not available in literature. As a first approximation, the Mie-Grüneisen equation can be used as a reference for EOS based on interpolation methods. For example, for a two-phase mixture, equilibrium takes place between the pressures of the two phases under loading. The Hugoniot pressure responsible for the resulting equilibrium produces different internal energies for the constituents, due to their different EOS. Equation (3.10) for the A and B materials becomes, with reference to the Hugoniot curve:

$$p_{HA} - p = \rho_{0A}\gamma_{0A}[E_{HA} - E_A] \quad (3.20)$$

$$p_{HB} - p = \rho_{0B}\gamma_{0B}[E_{HB} - E_B] \quad (3.21)$$

This means that a difference in temperature exists for the two constituents. A first method to avoid this problem is to calculate the thermal equilibrium condition of the mixture and of the components at 0 K, such that the temperature effects disappears. For each constituent, the cold curve is:

$$p_{0K} - p_H = \rho_0\gamma_0[E_{0K} - E_H] \quad (3.22)$$

One can now combine the 0 K isotherms of the constituents on a mass weighted average basis, assuming a constant specific heat, to obtain the isotherm for the mixture:

$$\begin{aligned}\rho\gamma &= \sum m_{0i}(\rho_0\gamma_0)_i \\ E_k &= \sum m_i E_i\end{aligned}\tag{3.23}$$

The shock Hugoniot of the mixture can now be obtained starting from the mixture cold curve.

Another possibility is to directly apply the mass weighted average to the shock parameters  $C_0$  and  $S_1$ :

$$\begin{aligned}\rho_0 &= \sum m_i \rho_{0i} \\ C_0 &= \sum m_i C_{0i} \\ S_1 &= \sum m_i S_{1i}\end{aligned}\tag{3.24}$$

These methods include significant simplifications. The main issue is that, even in the solid region, they do not consider the difference between a compound and an alloy. A single-phase alloy is structurally different from a composite with the same constituents, as the alloy material is microscopically and macroscopically homogeneous. However, since the calculation of EOS for alloys is a long and complex task, these simplifications are usually adopted when describing an unknown, non-pure material. For a more rigorous treatment of the EOS derivation for mixtures, see [7].

### 3.1.3 Tabular

The most sophisticated form of equation of state is the tabular EOS. A tabular form allows expressing strong nonlinearities and discontinuities, and is typically the best choice when the material is expected to experience important variations in density and energy, as well as changes of phase. A generic tabular equation is shown in Figure 25.

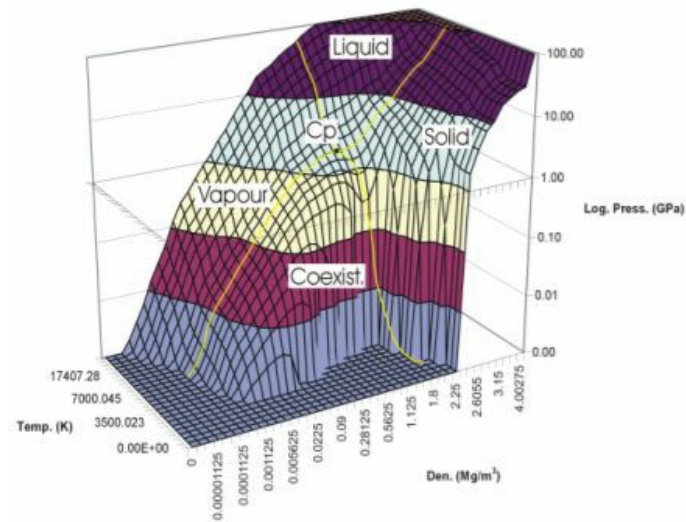


Figure 25. Example of tabular equation of state. The different phases are highlighted.

One of the most renowned tabular EOS is the SESAME, developed and maintained by the Los Alamos Laboratory (US) [5]. The library currently contains data for over 200 materials including metals, minerals, polymers and common mixtures. Most of the tables contain data for very wide ranges of density and energy, and are typically used for applications where such ranges are required, for example when materials undergo phase changes. The global EOS in the SESAME library are formed using various combinations of different thermodynamically consistent theoretical models in different regions, with interpolation between adjacent regions. Theoretical models are combined with empirical ones and with experimental observations and computed by means of the numerical code INFERNO. The range of parameters depends on the material, but typically the density is expressed between  $10^{-3}$  and  $10^7$  kg/m<sup>3</sup> and the temperature between 0 and  $10^9$  K.

The use of the SESAME EOS is particularly advantageous in finite elements codes, and the SESAME library is directly integrated in AUTODYN, which has been adopted together with ANSYS for the simulations of quasi-instantaneous heating discussed in this work. Figure 26 shows an example of SESAME EOS, the table 3550 built for tungsten [8].

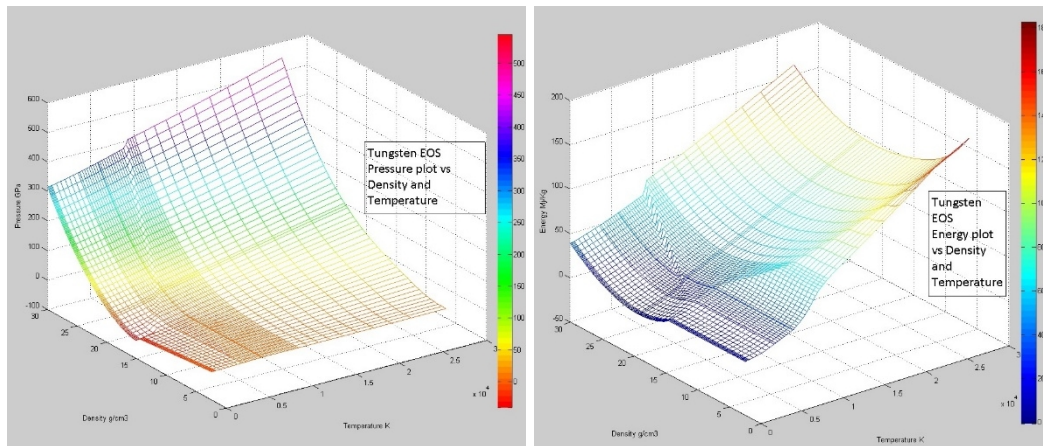


Figure 26. SESAME table 3550, built for tungsten. Left: pressure as a function of density and temperature. Right: Energy as a function of density and temperature.

### 3.1.4 Conventional experimental methods

As explained above, in recent years powerful statistical methods have been developed to build equations of state in regimes inaccessible to experimental techniques. Experimental methods are now mostly used to benchmark the models proposed, revealing possible inconsistencies. Usually, this means exploring with tests the least accessible regions of the EOS, producing shocks entailing high pressure, temperature and density change. Such regimes are reached at high levels of hydrostatic stress (see section 2.3), which can be physically produced only imposing a uniaxial strain condition on the tested specimen. The simplest example is the *flyer-plate technique* [9], where the striker impacts on a target material generating a planar wave, which is measured on the back of the target in terms of induced particle or shock velocity, typically by laser interferometry. The high speed in the striker necessary to reach the shock condition on the target is obtained by using explosives or gas guns. This allows reconstructing the Hugoniot curve up to stresses in the order of 1 TPa [10].

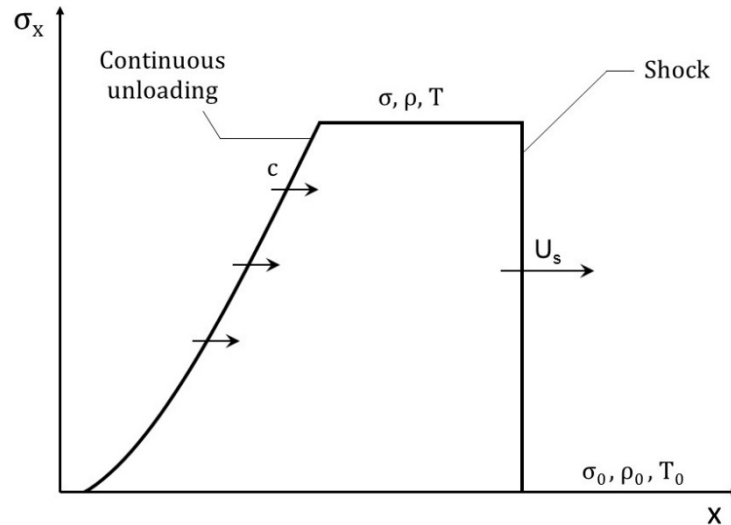


Figure 27. Idealized shock profile.

An important measurement involves the *off-Hugoniot* material response. The decompression curve is very close to isentropic (Figure 19) and its measurement also allows determining a variety of mechanical and physical properties in the shocked state, such as melting, vaporization and polymorphic phase transitions. The main issue is that, while systems such as laser-Doppler vibrometers, interferometers and pressure gauges are fast enough to capture the dynamic response of the shocked material, with acquisition rates easily in the order of some MHz [11], temperature-acquisition systems such as IR cameras are usually limited in this sense to some kHz. Luminescence methods are effective alternatives, but the validity of this technique in the study of opaque materials is limited [1]. Finally, expansion measurements in the vapor region are presently scarce. Most of the literature is constituted of studies, notably on lead, carried out by Fortov and colleagues, where the shock pressures obtained were high enough to allow reaching the liquid-vapor coexistence region during the release [12].

### 3.1.5 EOS study by isochoric heating test

A novel method for the study of the EOS regions which are usually inaccessible to conventional experiments is now proposed, based on a quasi-instantaneous heating of the material produced by the impact of an intense proton beam. In the previous paragraph we have seen that the main limitations of conventional tests are related to the inaccuracy of the study of the material expansion phase, especially for what concerns changes of phase in the vapor and plasma region. This is due to

the fact that, in order to reach such states during the isentropic release phase, in the case of a mechanical test the pressure to be generated at the end of the shock is extremely high. This concept is graphically seen in Figure 28.

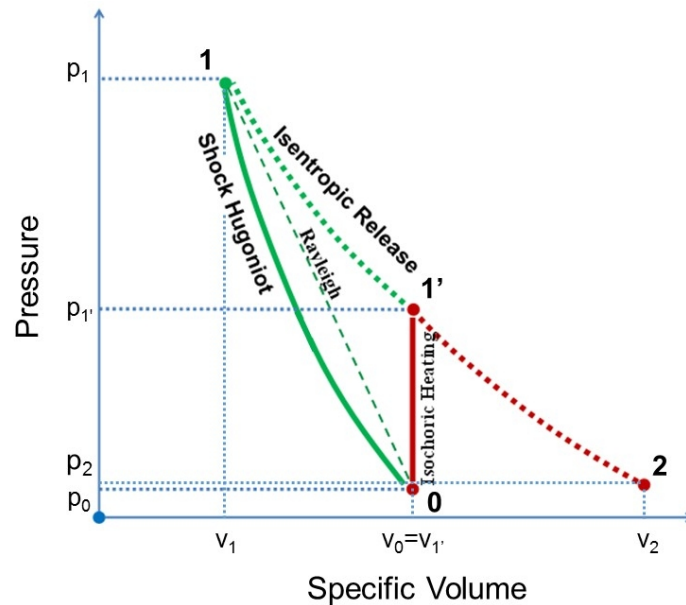


Figure 28. Comparison between a mechanical shock (0-1-2) and an isochoric heating event (0-1'-2).

With reference to Figure 28, in the case of an isochoric heating event, the material is initially at the point 0 of the diagram and is then subjected to a sudden internal energy increase  $\Delta E$ , which corresponds to an increase in temperature and pressure up to the point 1'. Note that, if the heat pulse length is very short (see section 1.3), the material does not experience a change in volume, because this is prevented by its mass inertia, and the density remains constant. In this phase, the material is under compression and may undergo a change of phase, if the thermal energy is high enough. At the end of the pulse, the material relaxation begins; point 2 is a generic position on the release path, where the material pressure is  $p_2$ .

In the case of a mechanical impact, in order to achieve the same conditions 1', the material must first experience a much higher shock pressure and density (position 1). In the release phase, the material expands, crossing the position 1', before reaching the condition 2.

It is therefore much easier to reach conditions of high temperature and internal energy in an isochoric heating test with respect to a conventional mechanical impact experiment. In the isochoric case, a number of unusual phenomena are also observed, such as the change of phase of the material in a compressive state and the

presence of molten material without micro-spallation<sup>9</sup> at a free impacted surface. In principle, this state would allow measuring the sound velocity of the molten material phase, as proved by Hixson and colleagues on liquid lead under a laser impact [13].

From a practical perspective, facilities in which a similar test can be performed should to guarantee a heat pulse energetic enough to reach the shock condition, at least in the impacted volume. An example is the HiRadMat facility at CERN, in which materials and structures can be tested under the impact of a proton beam at the energy of 440 GeV/p, for a total stored energy of about 3 MJ [14]. It is not in the scope of this section to detail how the beam energy is transferred to the impacted body, and how to calculate the pressure, temperature and density generated by the thermal-induced shock. This treatment will be carried out in chapter 4 in a rigorous way. However, as an example for a comparison between an isochoric proton beam impact and a conventional mechanical test, one can consider for HiRadMat an achievable energy density in the order of  $10^7$  J/kg, in the case of impact on tungsten targets (Figure 29).

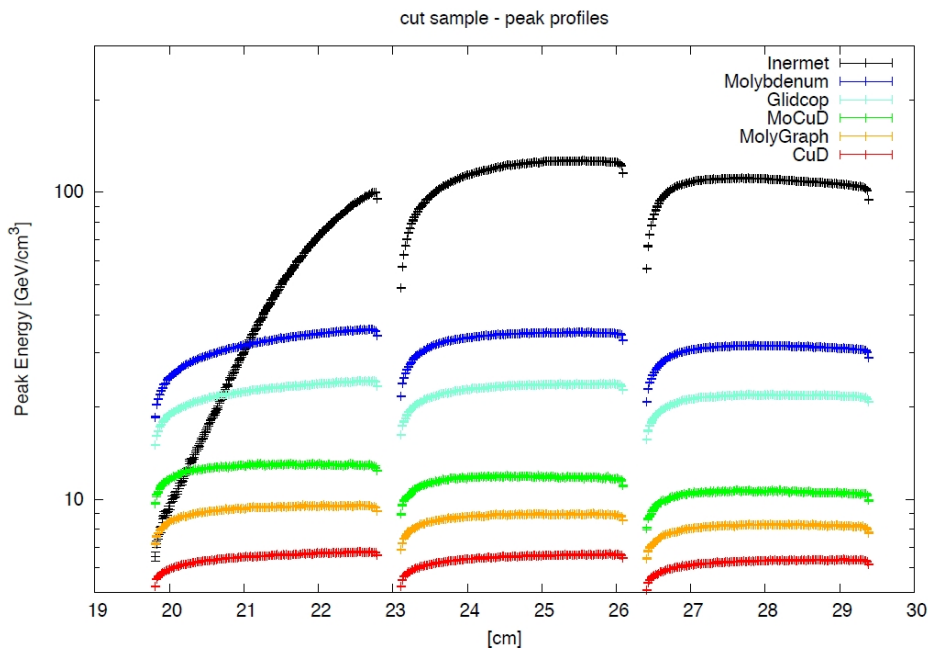


Figure 29. HiRadMat beam impact on specimens of six different materials, courtesy of V. Boccone. Inermet, in black, is a 95% tungsten alloy. The specimens are three per material, 3 cm long each.

<sup>9</sup> As already mentioned, micro-spallation is defined as the ejecta of liquid particles subjected to a tensile state.

The peak energy, calculated for a beam of transverse size 0.25 mm, is reported in GeV/cm<sup>3</sup>/proton, and has to be scaled by the number of impacting particles<sup>10</sup>. The maximum number of particles per pulse is  $3.7 \times 10^{13}$ .

With reference to Figure 28, the material state at each point of the diagram can be calculated with the procedure detailed in the next paragraphs.

### Position 0

This is the unshocked state of the material, which is assumed to be identified.  $v_0$ ,  $\rho_0$ ,  $T_0$ ,  $p_0$  are therefore known parameters:

$$\rho_0 = 19.255 \text{ g/cm}^3$$

$$v_0 = 0.052 \text{ cm}^3/\text{g}$$

$$T_0 = 293 \text{ K}$$

$$p_0 = 0 \text{ Pa}$$

### Position 1'

This is the condition reached by the material at the end of the isochoric heat deposition, or during the release phase after the mechanical shock. Let us calculate this condition for the isochoric heating case.  $E_{1'}$  is the energy deposited by the proton beam and is a known quantity (10 MJ/kg), as well as  $v_{1'}$  and  $\rho_{1'}$  under the isochoric assumption:

$$\rho_{1'} = \rho_0 = 19.255 \text{ g/cm}^3$$

$$v_{1'} = v_0 = 0.052 \text{ cm}^3/\text{g}$$

Referring to the SESAME 3550 equation of state for tungsten, it is possible to calculate the temperature increase as a function of density and energy (Figure 26, right) and subsequently the pressure as a function of temperature and density (Figure 26, left):

---

<sup>10</sup> 1 GeV is about  $1.6 \times 10^{-10}$  J.

$$T_{1'} = 22600 \text{ K}$$

$$p_{1'} = 140 \text{ GPa}$$

### Position 1

In order to achieve, during the release phase which follows the mechanical impact, the same conditions that are generated by an isochoric heating test, the pressure  $p_1$  at the end of the impact has to be much higher than  $p_{1'}$ . The Hugoniot relations reported in section 2.3.1 can be adopted to evaluate the state of the material at the end of the shock, also resorting to the shock parameters of Table 6. The specific volume and the density can be expressed as a function of the pressure:

$$\rho_1 = \frac{1}{v_1} \quad (3.25)$$

$$v_1 = \frac{C_0^2}{2S_1^2 p_1} \left[ \sqrt{1 + \frac{4S_1 v_0}{C_0^2} p_1 + \frac{2S_1(S_1 - 1)v_0}{C_0^2} p_1 - 1} \right] \quad (3.26)$$

Eq. (3.26) directly results from the four equations used to build the Hugoniot (2.22), (2.23), (2.24) and (2.26), while the shock parameters  $C_0$  and  $S_1$  are provided for tungsten in Table 6. On the other hand, the pressure  $p_1$  is at this stage unknown. Two more equations are required to calculate  $p_1$  and  $T_1$ . The first one is a result of the first law of thermodynamics, assuming that the process at the shock front is adiabatic, combined with the Grüneisen equation (3.10), and can be adopted to calculate any point along the Hugoniot:

$$T_1 = T_0 e^{\frac{\gamma_0}{v_0}(v_0 - v_1)} + p_1 \frac{v_0 - v_1}{2c_v} + \frac{1}{2c_v} e^{-\frac{\gamma_0}{v_0}v_1} \int_{v_0}^{v_1} p(v) e^{\frac{\gamma_0}{v_0}v} \left[ 2 - \frac{\gamma_0}{v_0}(v_0 - v) \right] dv \quad (3.27)$$

The Grüneisen parameter  $\gamma_0$  is also reported in Table 6. The argument of the integral is not difficult to calculate, considering that the shock pressure on any point of the Hugoniot is related to the volume by Eq. (3.26), which in terms of generic pressure has the form:

$$p(v) = C_0^2 \frac{v_0 - v}{[v_0 - S_1(v_0 - v)]^2} \quad (3.28)$$

For an exhaustive treatment of the temperature rise associated with a shock wave, and the full derivation of Eq. (3.27), see [3].

At this stage, there are four unknowns,  $p_1$ ,  $T_1$ ,  $v_1$  and  $\rho_1$  and three equations, (3.25), (3.26) and (3.27). The fourth equation required to determine the system is simply the isentropic relation between  $T$  and  $v$ , under the approximation (3.11):

$$T_1 = T_{1'} \cdot e^{-\frac{\gamma_0}{v_0}(v_1 - v_{1'})} \quad (3.29)$$

Since the condition 1', which is reached by the material in the release phase after the mechanical shock, has been identified in the previous paragraph and is known, the system of four equations is fully determined. The results are:

$$\rho_1 = 38.78 \text{ g/cm}^3$$

$$v_1 = 0.026 \text{ cm}^3/\text{g}$$

$$T_1 = 54920 \text{ K}$$

$$p_1 = 990 \text{ GPa}$$

### Position 2

This is a generic position along the isentropic release after 1', and can be determined in a similar way, as a function of the generic  $v_2$ :

$$T_2 = T_{1'} \cdot e^{\frac{\gamma_0}{v_0}(v_{1'} - v_2)} \quad (3.30)$$

$$\rho_2 = \frac{1}{v_2} \quad (3.31)$$

$$p_2 = \frac{\rho_0 T_2}{v_0 c_v} \quad (3.32)$$

All the points of Figure 28 have now been determined. The result is reported in Figure 30.

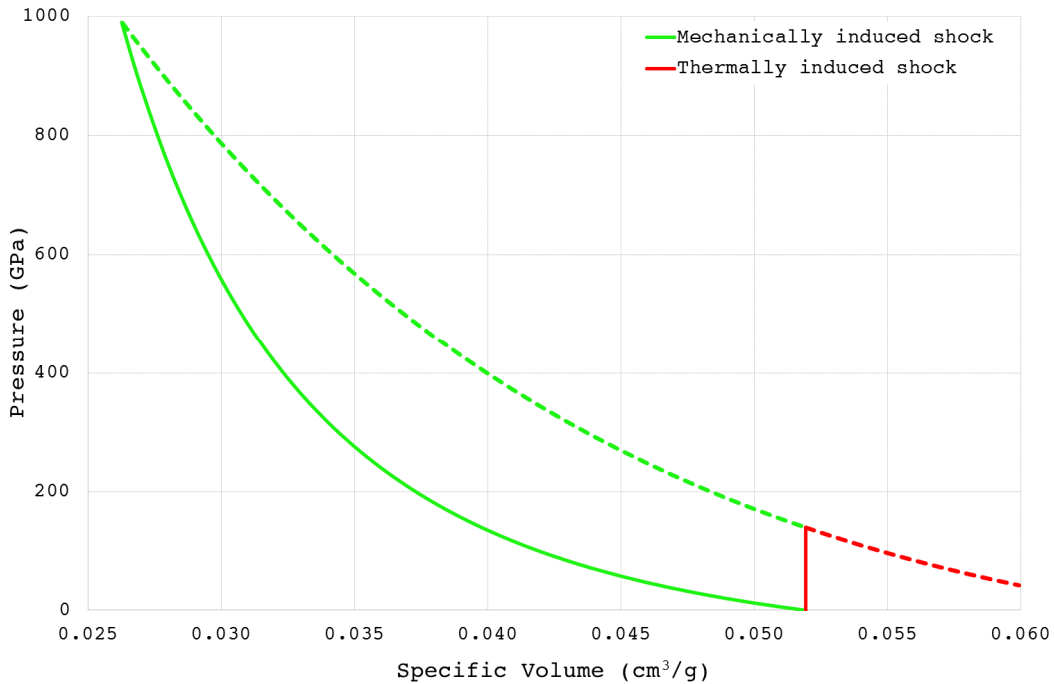


Figure 30. Shock on a tungsten target. In green, the shock is induced by a mechanical impact, in red, by a thermal energy deposition. Continuous lines are referred to the load phase and dashed lines to the release phase.

This example shows how an isochoric heating test can be effective in reaching a temperature region which, in order to be explored by conventional mechanical methods, would require shock pressures in the order of 1 TPa. Pressures of this level, although technically achievable, are quite extraordinary. On top of this, the peculiarities of isochoric heating, such as phase changes occurring in compressive state and the possibility to measure the sound speed of waves in the liquid phase, suggest the use of this method to complement theoretical methods in the construction of detailed equations of state.

### 3.2 Strength models

Equations of state describe the behavior of a purely hydrostatic material. As discussed in section 2.2, since real materials exhibit a shear strength, as well as hardening or softening as functions of strain, strain rate and temperature, the deviatoric component of the stress cannot be ignored. This is of course even more

important in the case of a plastic wave below the critical shock stress, as shown in Figure 16, where the hydrostatic component of the stress becomes of the same order of magnitude of the deviatoric. Extending Figure 16 to the shock domain, the wave in the longitudinal coordinate assumes the shape showed in Figure 31.

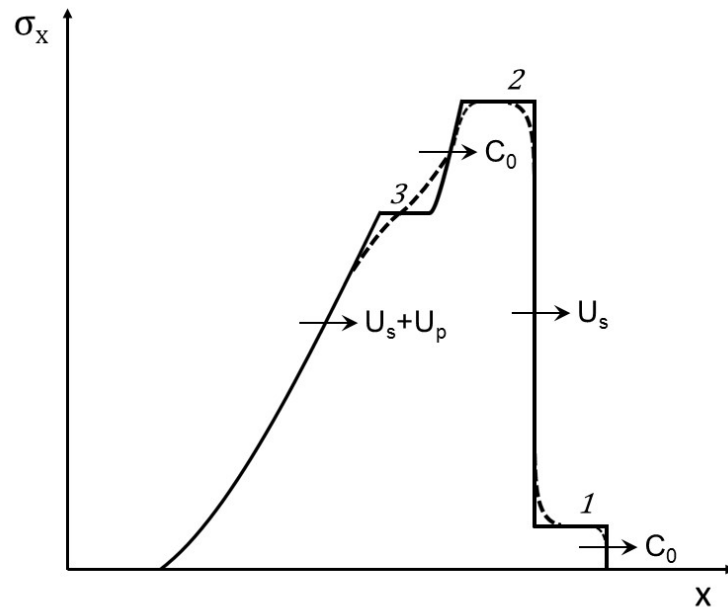


Figure 31. Elastoplastic material, shock wave and release.

In Figure 31, the continuous line represents an elastic – perfectly plastic ideal material behaviour in uniaxial strain condition (Figure 20), while deviations represented with a dashed line come from nonlinearities like viscoelastic or viscoplastic response, strain and strain rate hardening, temperature softening and Bauschinger effects [1].

With reference to Figure 31, in position *1* an elastic precursor is formed at stresses lower than  $\sigma_{HEL}$ . Above  $\sigma_{HEL}$ , a plastic wave generates, until, at sufficiently high stresses, the elastic precursor is overdriven, with a continuous elastoplastic shock front propagating at the speed  $U_s$  (position *2*). At the end of the pulse, the unloading phase (position *3*) presents first an elastic regime, followed then by a continuous elastoplastic rarefaction wave which travels faster than the shock front, and can eventually overtake it reducing its amplitude.

In order to correctly describe these phenomena, a *strength model* must be introduced to complement the equation of state, and account for the fact that an elastic solid retains a memory of its initial configuration. As already introduced in

section 2.2, materials experience a strain-dependent hardening at increasing flow stress. The easiest models represent strain hardening with a *bilinear*, *multilinear* or *power*  $\sigma - \varepsilon$  function. However, the flow stress of a material depends also on other variables, such as strain rate and temperature. In dynamic tests, the material typically experiences a hardening at increasing strain rates, while the temperature has a softening effect. Models which are able to take into account the effects of strain and strain rate on the flow stress are named *viscoplastic*. These models typically separate the strain rate – independent plasticity contribution and the viscous term, and can usually account also for the temperature effects. The onset of plasticity in quasi-static conditions is generally the reference value on which viscoplastic models are built. This point corresponds to  $\sigma_{\text{HEL}}$  in a uniaxial strain regime. On the other hand, deviations from a  $\sigma - \varepsilon$  linearity can occur already in the elastic domain, as highlighted in Figure 31, with the dashed line in the elastic precursor region. This is particularly evident in porous materials [15], but dissipation in the elastic domain can also be related to other effects such as micro-damage, solid-solid transitions for unstable phases, etc. Some authors use the term *internal friction* to refer to the entirety of these phenomena [16]. Internal friction is responsible for the conversion into heat of part of the elastic energy of a vibrating material. The dissipative term is also associated to the damping of the oscillations observed in a specimen subjected to an external alternating force: without internal friction, the amplitude of the vibration should increase indefinitely when driven at the resonant frequency. The models which reproduce damping in the elastic domain are named *viscoelastic*, as they still depend on the strain rate, but in a range below the yield stress. Viscoelastic models are typically described with a relaxation function, and the elastic constants such as Young's and Shear moduli decay with time, resulting in turn in decaying elastic waves with stress relaxation.

Shock wave studies on the elastic precursor can be used to deduce mechanical and physical properties controlling dynamic inelasticity. In the next paragraphs, examples of widely adopted viscoplastic and viscoelastic models are given.

### 3.2.1 Linear viscoelasticity

The time dependent mechanical response of viscoelastic materials is typically more pronounced at high temperatures and stresses. In metals, the phenomenon originates in diffusion processes at the grain boundaries. For polymers, intermolecular interactions and chemical reactions activated by the deformation process are

responsible. *Linear viscoelasticity* is based on the principles of superposition (thus “linear”) and time invariance (thus “elasticity”).

Linearity allows for a superposition of loads similar to linear elasticity: if a given load is doubled, the corresponding strain response will double as well. The time dependence of the shear modulus on time is expressed through a relaxation function which has typically an exponential form:

$$G(t) = G_{\infty} + G_0 e^{-\frac{t}{\tau}} \quad (3.33)$$

where  $G_0$  is known as instantaneous shear modulus,  $\tau$  is a relaxation time constant, characteristic to the material, and  $G_{\infty}$  the long-term shear modulus. The definition is given for a *generalized Maxwell solid*, simplified in one dimension as in Figure 32.

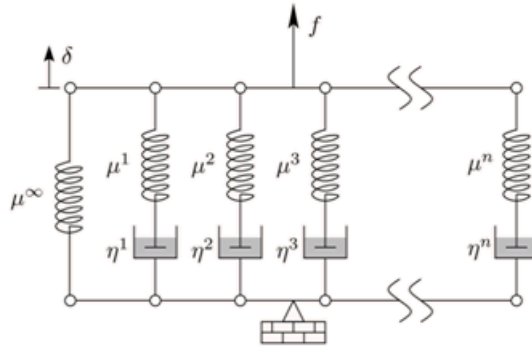


Figure 32. Generalized Maxwell solid in one dimension, adopted for the definition of uniaxial viscoelastic models in ANSYS [17]. The spring stiffnesses are  $\mu^i$ , the dashpot viscosities are  $\eta^i$ , and the relaxation time is defined as the ratio of viscosity to stiffness,  $\tau^i = \eta^i / \mu^i$ .

For a fluid-like material:

$$\lim_{t \rightarrow \infty} G(t) \rightarrow 0 \quad (3.34)$$

while in the case of a viscoelastic solid:

$$\lim_{t \rightarrow \infty} G(t) \rightarrow G_{\infty} \quad (3.35)$$

$G_{\infty}$  is therefore, in the case of a solid, the shear modulus defined in the elastic matrix of Eq. (2.4). The reason for which  $G(t)$  has an exponential form, and is expressed usually with a simple exponential function, is associated with the concept

of *fading memory* of viscoelastic materials [18]. If a first variable, such as the stress acting on the material, has a linear functional time dependence upon the complete past history of another field variable, such as the strain, then the fading memory hypothesis implies that the current value of the stress depends more strongly upon the recent history than upon the distant history of the strain. Mathematically, it can be expressed as:

$$\left| \frac{dG(t)}{dt} \right|_{t=t_1} \leq \left| \frac{dG(t)}{dt} \right|_{t=t_2} \quad \text{for } t_1 > t_2 > 0 \quad (3.36)$$

The validity of this hypothesis is proved by relaxation function experimental measurements available in literature, which so far have produced results in accordance with Eq. (3.36) [18]. The relation between deviatoric stress and strain rate is thus:

$$s(t) = \int_0^t G(t-t') \dot{\epsilon}(t') dt' \quad (3.37)$$

where  $t'$  is the past time. Because of the fading memory hypothesis,  $G(t)$  is a decreasing function, and loading events  $\dot{\epsilon}(t')$  that occurred a long time ago, *i.e.*  $t' \ll t$ , weigh less heavily than recent events,  $t' \approx t$ .

The shear modulus  $G(t)$  can have forms in accordance with the fading memory hypothesis, but different from the simple exponential of Eq. (3.33). In numerical codes such as ANSYS, the shear modulus can be approximated to experimental data through a so-called *Prony series*, which is a linear combination of exponential decay functions with different time relaxation constants  $\tau_i$ ,

$$G(t) = G_\infty + \sum_{i=1}^n G_i e^{-\frac{t}{\tau_i}} \quad (3.38)$$

The time constants  $\tau_i$  are temperature dependent, and typically shorten at higher temperature. In *thermo-rheologically simple* behaviour, all  $\tau_i$  scale with the same factor depending on temperature. This implies that an increase in temperature can be compensated with a decrease in the time scale of the experiment to yield the

same behaviour. A parameter often adopted in viscoelastic models is also the *decay constant*  $\beta$ , defined as the inverse of the relaxation time:

$$\beta = \frac{1}{\tau} \quad (3.39)$$

Porous materials, such as isostatic graphite (Figure 32), can effectively be simplified to generalized Maxwell solids, with the pores representing the dashpots. With reference to Figure 32, graphite relaxation is well reproduced with a decay constant  $\beta = 40 \text{ ms}^{-1}$ . Note that the specimen, tested with a Hopkinson bar, remains in a state of compression even after that the passage of the first pressure wave is completed, which is compatible with the concept of viscoelasticity. Reflecting at the free extremity, the wave becomes then tensile and the specimen breaks once the ultimate strength is reached. For this reason, the successive axial wave periods are shorter.

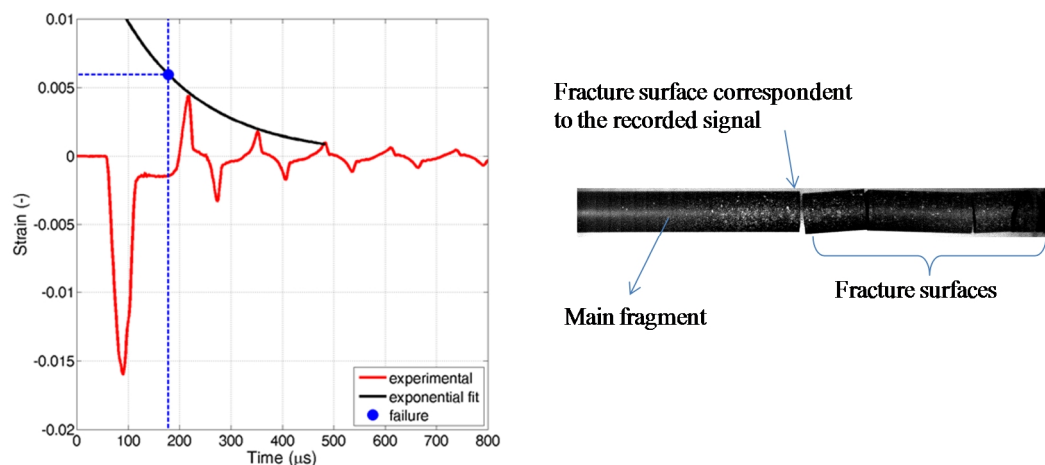


Figure 33. Left: viscoelastic behaviour of an isostatic graphite sample tested at high strain rate in the Hopkinson bar test bench. Right: specimen after the test [15].

### 3.2.2 Johnson-Cook viscoplasticity

While in viscoelastic models the mechanical energy is dissipated even at low stresses, viscoplasticity implies a conservation of the energy as long as the stress remains below the elastic limit. In most viscoplastic models, in the elastic domain a linear relation between stress and strain is assumed, and the material obeys to the Hooke law (section 2.1). Such strength models express then the relation between flow stress and strain, usually taking into account also strain rate and temperature effects. The material is typically assumed to be isotropic, and in numerical codes

such as ANSYS and Autodyn the equivalent stress is calculated with the *Von Mises criterion*. Even when the material yield locus is assumed to be direction-dependent, for example in the *generalized Hill criterion*, common viscoplastic strength models still assume a law of isotropic plasticity.

An example in this sense is the *Johnson-Cook strength model*, which is built empirically, and widely adopted because of its simplicity, which allows disentangling the different contributions to the Von Mises flow stress [19]:

$$\sigma_Y = (A + B\varepsilon_{pl}^n) \left(1 + C \ln \frac{\dot{\varepsilon}_{pl}}{\dot{\varepsilon}_0}\right) \left[1 - \left(\frac{T-T_r}{T_m-T_r}\right)^m\right] \quad (3.40)$$

Where  $\varepsilon_{pl}$  is the plastic strain,  $\dot{\varepsilon}_{pl}/\dot{\varepsilon}_0$  is the dimensionless plastic strain rate,  $T$  is the temperature,  $T_m$  is the melting point,  $T_r$  is the reference temperature at which no softening occurs, and  $A$ ,  $B$ ,  $n$ ,  $C$ ,  $m$  are five constants to be determined experimentally.

The uncoupling of each single phenomenon is evident in Eq. (3.40): for example, when the process is quasi-static and the material is at the reference temperature, only strain hardening occurs, and the strength model becomes a simple power function, of the kind of Hollomon criterion (2.14). With respect to Eq. (2.14), the constant  $A$ , which represents the elastic limit, is added. Such formulation is known as *Ludwik's plasticity*;  $B$  is usually called *strain hardening coefficient* and  $n$  is the *strain hardening exponent*, assuming values between 0, in the case of a perfectly plastic material, and 1, for a piecewise linear model.

The strain rate hardening depends on the constant  $C$ , and the dimensionless strain rate is calculated with respect to a given value of reference strain rate  $\dot{\varepsilon}_0$  at which the model is zeroed. The constants of the Johnson-Cook model are usually given for a value of  $\dot{\varepsilon}_0$  equal to  $1 \text{ s}^{-1}$ .

Finally, the temperature softening effect on the material depends on the thermal exponent  $m$ , as well as on the ratio between the temperature of the material and the melting point. In the case of melting:

$$1 - \left(\frac{T-T_r}{T_m-T_r}\right)^m = 0 \quad \rightarrow \quad \sigma_Y = 0$$

The material behaves then like a fluid. The temperature function convexity depends on the thermal exponent  $m$ : downward if  $m < 1$ , upward if  $m > 1$ .

Table 7: Johnson-Cook constitutive constants, calculated for  $\dot{\epsilon}_0 = 1 \text{ s}^{-1}$  and  $T_r = \text{room temperature}$ . Source: [19].

<b>Material</b>	<b><math>A</math> (MPa)</b>	<b><math>B</math> (MPa)</b>	<b><math>n</math> (-)</b>	<b><math>C</math> (-)</b>	<b><math>m</math> (-)</b>	<b><math>T_m</math> (K)</b>
OFHC copper	90	292	0.31	0.025	1.09	1356
Cartridge brass	112	505	0.42	0.009	1.68	1189
Nickel 200	163	648	0.33	0.006	1.44	1726
ARMCO iron	175	380	0.32	0.015	0.55	1811
2024-T351 aluminum	265	426	0.34	0.010	1.00	775
4340 steel	792	510	0.41	0.014	1.03	877
S-7 tool steel	1539	477	0.18	0.012	1.00	1763
Tungsten alloy	1506	177	0.12	0.016	1.00	1723

The counteracting contributions of strain rate and temperature on the material strength are shown in Figure 34 for pure molybdenum [20]. As a matter of fact, hardening and softening processes have an effect also on the material maximum elongation, which decreases in case of embrittlement and increases in the case of a softer material. However, in numerical codes this effect is not considered within a strength model, which mathematically defines the stress – strain relation over an infinitely wide range. Fracture is in fact simulated by means of a failure model, which complements the strength model in the definition of the material constitutive response.

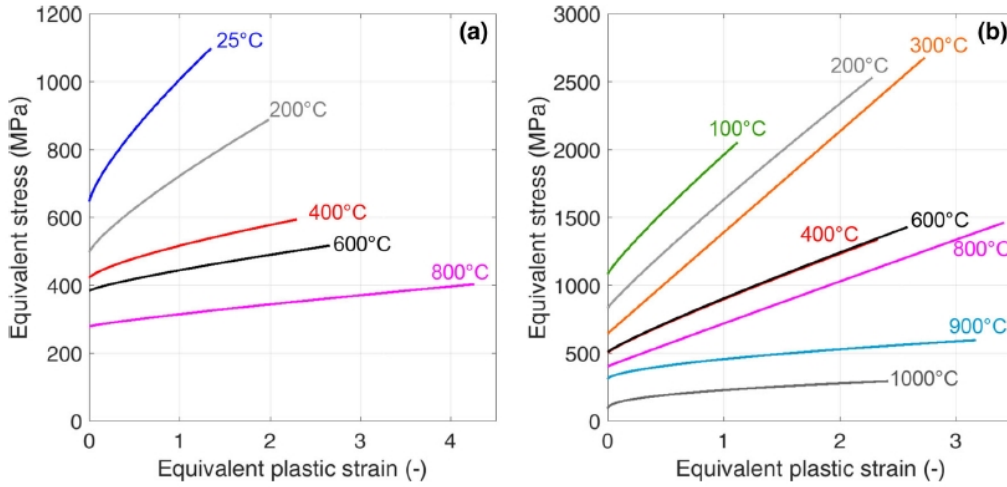


Figure 34. Johnson-Cook model for molybdenum produced by Plansee (DE). Left: quasi-static tensile test ( $\dot{\epsilon} = 10^{-3} \text{ s}^{-1}$ ); right: dynamic tensile test ( $\dot{\epsilon} = 10^3 \text{ s}^{-1}$ ) [20].

A disadvantage of the Johnson-Cook model is that it ignores completely the hydrostatic component of the stress and strain tensors. The hydrostatic stress may be relevant to the yielding of materials with artificial or natural defects, especially at high pressures, as discussed in section 2.1. Also, the asymmetry in the material response to tension and compression is not taken into account.

### 3.2.3 Zerilli-Armstrong viscoplasticity

A typical problem of the Johnson-Cook model is that, because it is built as a simple fit of experimental results, its accuracy strongly decreases outside the limited range of stress data. Zerilli and Armstrong [21] studied an upgrade of the Johnson-Cook model, with the goal of improving the material constitutive relation, by including in the model physical plasticity mechanisms based on simplified dislocation dynamics.

Zerilli and Armstrong separated the flow stress in two components:

$$\sigma = \sigma_{ath}(G) + \sigma_{th}(\dot{\epsilon}, T) \quad (3.41)$$

The *athermal flow stress* component  $\sigma_{ath}$  arises from elastic interactions of the dislocations and depends on temperature only via the weak temperature dependence of the shear modulus. The component  $\sigma_{th}$  is on the other hand required for the dislocations in order to overcome thermally activable short-range obstacles, and

depends therefore explicitly both on temperature and strain rate. It is thus called *thermal flow stress* [22].

A *body-centered cubic* material (BCC), such as iron, presents a strain hardening related to the athermal stress, while the thermal stress is not influenced by the strain amplitude. On the contrary, in copper and other *face-centered cubic* materials (FCC), it is the thermal stress term which increases with the strain, while the athermal stress slope is independent of the strain. The model developed by Zerilli and Armstrong takes into account this difference in the constitutive behaviour of FCC and BCC materials, and proposes two formulations which depend on the material structure:

$$\sigma = \Delta\sigma'_G + \frac{k}{\sqrt{l}} + c_2\sqrt{\varepsilon_{pl}}e^{(-c_3+c_4 \ln \varepsilon_{pl})T} \quad (\text{FCC}) \quad (3.42)$$

$$\sigma = \Delta\sigma'_G + \frac{k}{\sqrt{l}} + c_5e^n + c_1e^{(-c_3+c_4 \ln \varepsilon_{pl})T} \quad (\text{BCC}) \quad (3.43)$$

where  $l$  is the average grain diameter and  $\Delta\sigma'_G$ ,  $c_1$ ,  $c_2$ ,  $c_3$ ,  $c_4$ ,  $c_5$ ,  $n$  and  $k$  are experimental constants related to the dislocation dynamics behaviour of the material.  $\Delta\sigma'_G$  is the contribution due to solutes and initial dislocation density, while  $k$  is the microstructural stress intensity. In the two equations, the last term represents the thermal stress component and the other terms the athermal stress.

Table 8: Zerilli-Armstrong constants for BCC and FCC materials. Source: [21].

Parameter	OFHC copper	Armco iron
$\Delta\sigma'_G$ (MPa)	46.5	0
$c_1$ (MPa)	-	1033
$c_2$ (MPa)	890	-
$c_3$ (K <sup>-1</sup> )	$2.8 \times 10^{-3}$	$7.0 \times 10^{-3}$
$c_4$ (K <sup>-1</sup> )	$1.2 \times 10^{-4}$	$4.2 \times 10^{-4}$
$c_5$ (MPa)	-	266
$n$	-	0.289
$k$ (MPa·mm <sup>1/2</sup> )	5	22

With respect to the purely empirical Johnson-Cook model, Zerilli-Armstrong accounts for the physical mechanisms of plasticity; it is thus semi-empirical and ideally more consistent over a wide range of experimental conditions. Table 8 reports the coefficients of the Zerilli-Armstrong model for an FCC material, oxygen-free copper, and a BCC material, Armco iron.

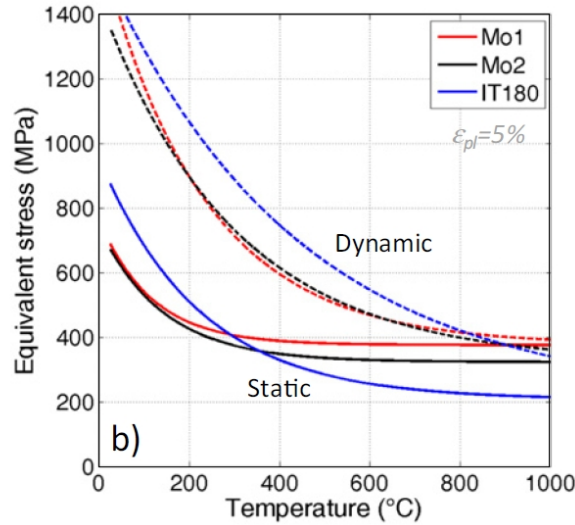


Figure 35. Zerilli-Armstrong models for two pure molybdenum grades and a tungsten heavy alloy (IT180). Effects of temperature and strain rate on the equivalent stress are highlighted [23]. Static tests:  $\dot{\epsilon} = 10^{-3} \text{ s}^{-1}$ ; dynamic tests:  $\dot{\epsilon} = 10^3 \text{ s}^{-1}$ .

### 3.3 Failure models

Describing the strength models, it has been mentioned that they ignore the effects of hardening, softening and hydrostatic stress on the material elongation. In fact, strength models express a function without boundaries, which ideally can model the material up to infinite values of stress and strain. In the material constitutive response, fracture phenomena are evaluated with the definition of an adequate *failure model*. In numerical codes, at every cycle the material strength is updated, until the maximum level of stress or strain, defined by the failure model, is reached. In this case, failure occurs and the flow stress goes to zero, as the material is no longer able to withstand shear loads. This process is similar to what occurs in the case of phase change from solid to liquid or gas. Melting is not considered as failure, and is included in the definition of the strength model: for example, looking at the Johnson-Cook strength model (3.40), when  $T = T_m$  the flow stress becomes null. The difference with fracture, however, is that the process is reversible, as the material will eventually re-solidify during cooldown.

The main categories of failure model adopted in numerical codes are two. In the first one, failure is expressed as a result of *cumulative damage*. The damage function is calculated at every time step, and failure occurs when the damage reaches a threshold, which is conventionally set to 1. A second category of failure models defines the material fracture by *spallation*. As mentioned in section 1.4, spallation is a dynamic phenomenon associated to internal cavitation, occurring when the amplitude of a rarefaction wave exceeds the ultimate strength of the material. With the nucleation and growth of cracks or voids, a region of damage develops, ultimately resulting in complete material separation. Spallation is usually observed at free surfaces, where rarefaction waves are produced by the reflection of the compressive waves generated by the impact. One or more fragments, or *spalls*, are formed, and ejected far from the surface at high speed. However, the phenomenon can occur also at different target positions, as rarefaction waves originate also in axisymmetric configurations, or at the impacted surface at the end of the pulse.

Failure models based on progressive damage usually evaluate the accumulation of plastic strain with respect to the maximum material elongation, and in general better reproduce ductile fracture. On the other hand, spallation models typically verify the maximum principal stress against the material strength to rupture, or the maximum tensile pressure against the hydrodynamic tensile limit, and are better suited for brittle fracture phenomena. However, Grady [26] developed spallation models based on energetic criteria to reproduce also the spalling of ductile materials. Finally, mixed damage/spallation models exist, updating the value of the ultimate strength on the base of the accumulated damage.

### 3.3.1 Johnson-Cook failure model

The Johnson-Cook failure model is based on cumulative damage, defined as:

$$D = \sum \frac{\Delta \varepsilon_{pl}}{\varepsilon_f} \quad (3.44)$$

where  $\Delta \varepsilon_{pl}$  is the increment of plastic strain which occurs during an integration cycle, while  $\varepsilon_f$  is the equivalent strain to fracture, under the current conditions of strain rate, temperature, pressure and equivalent stress [24]. Fracture occurs when  $D = 1$ . Similarly to the Johnson-Cook stress model, this model disentangles the several contributions on the strain to fracture, which is written in the form:

$$\varepsilon_f = \left[ D_1 + D_2 e^{D_3 \frac{\sigma_m}{\bar{\sigma}}} \right] \left[ 1 + D_4 \ln \frac{\dot{\varepsilon}_{pl}}{\dot{\varepsilon}_0} \right] \left[ 1 + D_5 \frac{T - T_r}{T_m - T_r} \right] \quad (3.45)$$

Where  $D_1$ ,  $D_2$ ,  $D_3$ ,  $D_4$  and  $D_5$  are five constants to be determined experimentally; the strain rate and temperature terms are the same appearing in the Johnson-Cook strength model, while here the strain hardening effect also takes into consideration the entity of hydrostatic stress  $\sigma_m$ , with respect to the Von Mises stress  $\bar{\sigma}$ . Notably, the first term follows the form presented by Hancock and Mackenzie [25], considering that the strain to fracture decreases as the hydrostatic stress increases. For this reason, the constant  $D_3$  is always negative. At high levels of hydrostatic stress, above  $\sigma_m/\bar{\sigma} = 1.5$ , the value of the exponential changes, as the failure regime gradually moves from ductile fracture to spallation fracture. The change in the fracture regime is illustrated in Figure 36.

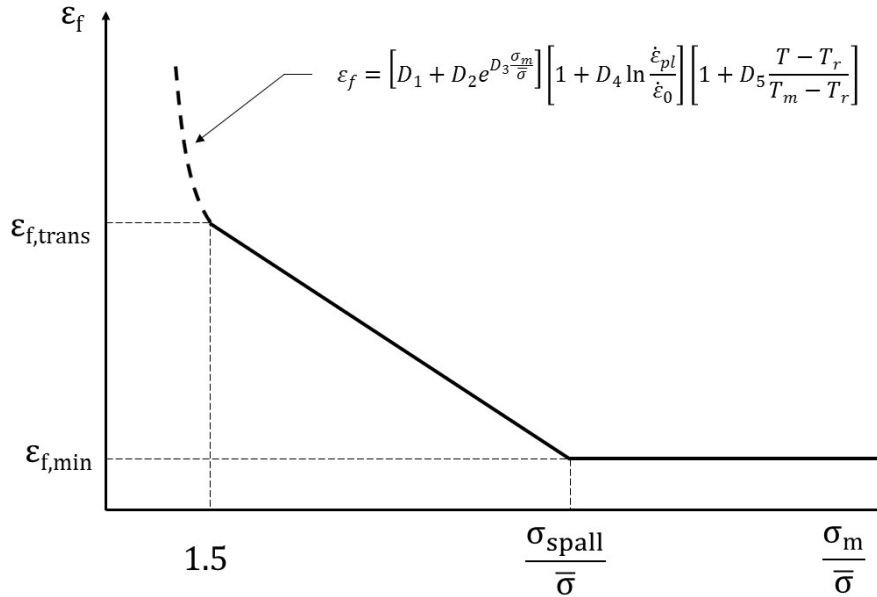


Figure 36. Johnson-Cook failure model, definition of fracture strain at large tensile pressure-stress ratios.

In Figure 36, the dashed line represents the ductile fracture area covered by the Johnson-Cook relation defined in Eq. (3.45). In the transition regime above  $\sigma_m/\bar{\sigma} = 1.5$ , the strain at fracture changes linearly with pressure, as the strain rate and temperature effects appear to be less relevant. Finally, once in the spallation regime, the strain at fracture does not change anymore, as the fracture is totally controlled by the hydrostatic stress. In this regime, the model assumes the simplest possible form of spallation fracture.

Table 9 reports the measured constants of the Johnson-Cook failure model in the ductile failure regime, for different materials.

Table 9: Johnson-Cook failure model constants. Source: [21],[24].

<b>Material</b>	$D_1$	$D_2$	$D_3$	$D_4$	$D_5$
OFHC copper	0.52	4.89	-3.03	0.014	1.12
ARMCO iron	-2.20	5.43	-0.47	0.016	0.63
4340 steel	0.05	3.44	-2.12	0.002	0.61

### 3.3.2 Spallation models

Every spallation model assumes that fragmentation occurs when the tensile pressure, or *tension*, reaches a critical threshold corresponding to the ultimate strength of the material, which is called *spall strength*. The threshold for spallation is therefore:

$$P < P_s \quad (3.46)$$

where  $P$  is the mean tension and  $P_s$  the spall strength. In the simplest spallation models, the spall strength is assumed to be constant, for example in the Johnson-Cook model just described. The value used for  $P_s$  may come from experimental tests; however, the accuracy of the spallation model strongly decreases outside the experimental data range. In addition, a constant spall strength disregards the role of loading prehistory. For this reason, a formulation sometimes adopted combines the spallation model with the cumulative damage theories, imposing a dependence on damage to  $P_s$ :

$$P < P_s(1 - D) \quad (3.47)$$

In this case, the relation is linear and an appropriate damage evolution law must be developed, depending on the nature of the material. Theoretically, it is quite difficult to extend damage theories to the spallation phenomenon, and a model such as that of Eq. (3.47) is typically phenomenological.

Semi-empirical and theoretical models are preferable to evaluate the spall strength of a material. Several studies in this sense were performed by Grady [26], to model the spallation phenomenon for different material classes.

Grady models are developed starting from the relation between the mean tension and the dilatational strain rate  $\dot{\epsilon}$  in a dynamically expanding body:

$$P = \rho c_0^2 \dot{\epsilon} t \quad (3.48)$$

The expression is simply obtained combining Eqs. (2.6) and (2.12), where  $c_0$  is the bulk sound speed, *i. e.* the velocity of propagation of a wave in hydrostatic conditions. Starting from Eq. (3.48), Grady developed models for materials of different nature, based on energetic considerations. The main assumption is that spallation is provoked by an *excess in the kinetic energy* available for fragmentation with respect to the energy dissipated during the fragment formation. This concept was developed for brittle solids, but was successfully extended to ductile solids and to liquids:

- in the case of a brittle solid, the excess kinetic energy is related to the *fracture toughness*  $K_c$  of the material;
- in a ductile material, the excess kinetic energy is related to the *plastic work* performed;
- in a liquid, the excess kinetic energy depends on the surface energy associated with fracture formation. In this case, a spray of droplets is produced, and the phenomenon as already mentioned is called *micro-spallation*.

The spall strength for a brittle solid according to the Grady spall model is:

$$P_s = \sqrt[3]{3\rho c_0 K_c^2 \dot{\epsilon}} \quad (3.49)$$

In some books the Bulk modulus  $K$  appears in the formula, remembering that  $K = \rho c_0^2$ . Table 10 reports theoretical and experimental data on the spall strength of brittle materials.

Table 10: Comparison between theoretical spall strength of brittle materials, calculated with the Grady model, and experimental measurements. Source: [26].

<b>Material</b>	$\rho$ ( $\text{kg}\cdot\text{m}^{-3}$ )	$K$ (GPa)	$K_c$ ( $\text{MN}\cdot\text{m}^{-3/2}$ )	$P_s$ (exp) (GPa)	$P_s$ (thy) (GPa)
Aluminum 6061-T6	2710	72.2	25–30	0.8–1.5	0.86–1.9
Uranium	19050	98.7	60	2.4–3.4	2.1–4.5
Beryllium	1820	100	10–12	0.4–1.3	0.45–1.0
Titanium	4510	105	40–70	2.1–3.9	1.6–3.4
Steel 4340	7870	168	40–80	2.5–5.4	2.0–4.3

In the case of a ductile solid, the fracture energy is no longer related to  $K_c$ , but to a stable void growth up to a critical void volume fraction  $\varepsilon_c$ , after which voids coalesce and a rapid loss of tensile load-carrying capability ensues. According to Grady theory, an appropriate value of  $\varepsilon_c$  for most ductile materials is 0.15. The spall strength of a ductile material is thus:

$$P_s = \sqrt{2\rho c_0^2 Y \varepsilon_c} \quad (3.50)$$

where  $Y$  is the flow stress in simple tension, which in a numerical code is updated at every time step through the strength model. A comparison between experimental and theoretical data, at constant values of  $Y$ , is reported in Table 11.

Table 11: Comparison between theoretical spall strength of ductile materials, calculated with the Grady model, and experimental measurements. Source: [26].

<b>Material</b>	<b><math>K</math> (GPa)</b>	<b><math>Y</math> (GPa)</b>	<b><math>P_s</math> (exp) (GPa)</b>	<b><math>P_s</math> (thy) (GPa)</b>
Aluminum (soft)	72.2	0.015–0.03	0.5–1.1	0.57–0.81
Copper	137	0.025	1.0–2.5	1.0
Tantalum	200	0.7	4.4–6.8	6.5
Tin	111	0.05–0.12	0.6–0.8	1.3–2.0
Titanium Ti-6Al-4V	105	0.8–0.9	4.1–5.0	5.0–5.3

### 3.4 Glossary

Symbols are listed in chronological order with respect to their appearance in the text.

<b>Symbol</b>	<b>Definition</b>	<b>SI unit</b>
$U_s$	Shock velocity	$\text{m}\cdot\text{s}^{-1}$
$C_0$	Velocity of the elastic wave	$\text{m}\cdot\text{s}^{-1}$
$U_p$	Particle velocity	$\text{m}\cdot\text{s}^{-1}$
$S_1, S_2, \dots, S_n$	Coefficients of the Hugoniot n-grade polynomial in $U_s - U_p$ coordinates	–
$p$	Pressure	Pa
$E$	Energy density	$\text{J}\cdot\text{m}^{-3}$
$\rho$	Density	$\text{kg}\cdot\text{m}^{-3}$
$C_v$	Heat capacity at constant volume	$\text{J}\cdot\text{K}^{-1}$

$c_v$	Specific heat capacity at constant volume	$\text{J}\cdot\text{kg}^{-1}\cdot\text{K}^{-1}$
$c_p$	Specific heat capacity at constant pressure	$\text{J}\cdot\text{kg}^{-1}\cdot\text{K}^{-1}$
$m$	Mass	kg
$R$	Specific gas constant	$\text{J}\cdot\text{kg}^{-1}\cdot\text{K}^{-1}$
$p_c$	Pressure of the 0 K isothermal	Pa
$p_T$	Temperature and energy dependent pressure	Pa
$K$	Bulk modulus	Pa
$\rho_0$	Density of the unshocked material	$\text{kg}\cdot\text{m}^{-3}$
$\gamma_0$	Grüneisen parameter of the unshocked material	–
$\alpha$	Thermal expansion coefficient	$\text{K}^{-1}$
$\gamma$	Grüneisen parameter	–
$p_H$	Pressure calculated with respect to the Hugoniot	Pa
$E_H$	Specific energy calculated with respect to the Hugoniot	$\text{J}\cdot\text{kg}^{-1}$
$V_0$	Volume of the unshocked material	$\text{m}^3$
$V$	Volume	$\text{m}^3$
$V_0^*$	Initial volume of the porous material	$\text{m}^3$
$\rho_0^*$	Initial density of the porous material	$\text{kg}\cdot\text{m}^{-3}$
$v_0$	Specific volume of the unshocked material	$\text{m}^3\cdot\text{kg}^{-1}$
$v$	Specific volume	$\text{m}^3\cdot\text{kg}^{-1}$
$T$	Temperature	K
$T_0$	Temperature of the unshocked material	K
$\sigma_{HEL}$	Hugoniot elastic limit	Pa
$\sigma$	Stress	Pa

---

$\varepsilon$	Strain	–
$G$	Shear modulus	Pa
$G_\infty$	Instantaneous modulus	Pa
$G_0$	Long-term shear modulus	Pa
$t$	Time	s
$\tau$	Relaxation time constant	s
$s$	Deviatoric stress	Pa
$e$	Deviatoric strain	–
$\dot{e}$	Deviatoric strain rate	s <sup>-1</sup>
$t'$	Past time	s
$\beta$	Relaxation decay constant	s <sup>-1</sup>
$\sigma_Y$	Flow stress	Pa
$A$	Static elastic limit	Pa
$B$	Strain hardening constant	Pa
$n$	Hardening exponent	–
$\varepsilon_{pl}$	Plastic strain	–
$\dot{\varepsilon}_0$	Reference strain rate	s <sup>-1</sup>
$C$	Strain rate hardening constant	–
$m$	Thermal exponent	–
$T_r$	Reference temperature	K
$T_m$	Melting temperature	K
$\dot{\varepsilon}_{pl}$	Plastic strain rate	s <sup>-1</sup>
$\sigma_{ath}$	Athermal flow stress	Pa

$\sigma_{th}$	Athermal stress	Pa
$l$	Average grain diameter	m
$\Delta\sigma'_G$	Stress due to solutes and initial dislocation density	Pa
$k$	Microstructural stress intensity	Pa·m <sup>1/2</sup>
$n$	Zerilli-Armstrong exponent	–
$c_1, c_2, \dots, c_5$	Constants of the Zerilli-Armstrong strength model	–, Pa
$D$	Damage	–
$\Delta\varepsilon_{pl}$	Plastic strain increment	–
$\varepsilon_f$	Strain at fracture	–
$D_1, D_2, \dots, D_5$	Constants of the Johnson-Cook failure model	–, Pa
$\sigma_m$	Hydrostatic stress	Pa
$\bar{\sigma}$	Von Mises stress	Pa
$P$	Mean tension	Pa
$P_s$	Spall strength	Pa
$K_c$	Fracture toughness	Pa·m <sup>1/2</sup>
$\varepsilon_c$	Critical void volume fracture	–
$Y$	Tensile flow stress	Pa

## References

- [1] J. R. Asai and G. I. Kerley (1987). The response of materials to dynamic loading. *Int. J. Impact Engng.*, Vol. 5, pp. 69 – 99.
- [2] “Ansys AUTODYN User’s Manual – Release 15.0”, ANSYS, Inc. (2013).

- [3] M. A. Meyers (1994). *Dynamic behaviour of materials*. J. Wiley & Sons, ISBN 047158262.
- [4] R. Menikoff (2016). *Complete Mie-Grüneisen Equation of State*. *Los Alamos National Laboratories*, Tech. Report LA-UR-16-21706.
- [5] S. P. Lyon and J. D. Johnson (1992). *SESAME: The Los Alamos National Laboratory Equation of State Database*. *Los Alamos National Laboratories*, Tech. Report LA-UR-92-3407.
- [6] N. Mariani (2014). *Development of Novel, Advanced Molybdenum-based Composites for High Energy Physics Applications*, CERN-THESIS-2014-363.
- [7] R. G. McQueen, S. P. Marsh, J. W. Taylor, J. N. Fritz and W. J. Carter (1970). The equation of state of solids from shock wave studies. In R. Kinslow, *High-velocity impact phenomena*, pp. 348–353, ISBN 9780323144988.
- [8] G. I. Kerley (2003). *Equations of state for Be, Ni, W, and Au*. *SANDIA report*, SAND 2003-3784.
- [9] L. M. Barker and R. E. Hollenbach (1970). Shock-wave studies of PMMA, fused silica and sapphire. *J. Appl. Phys.* 41, pp. 4208–4226.
- [10] M. D. Knudson, R. W. Lemke and C. Deeney (2005). Equation of State Measurements at Ultra-High Pressures on the Sandia Accelerator. *Plasma Science*, 2005. ICOPS '05. IEEE Conference Record – Abstracts.
- [11] A. Bertarelli *et al.* (2013). An experiment to test advanced materials impacted by intense proton pulses at CERN HiRadMat facility. *Nuclear Instruments and Methods in Physics Research B*, Vol. 308, pp. 88–99.
- [12] L. V. Al'tshuler, A. V. Bushman, M. V. Zhernokletov, V. N. Zubarev, A. A. Leont'ev, and V. E. Fortov (1980). Unloading isentropes and the equation of state of metals at high energy densities. *Zh. Eksp. Teor. Fiz.*, Vol. 78, pp. 741–760.

- 
- [13] R. S. Hixson, M. A. Winkler and J. W. Shaner (1986). Sound speed in liquid lead at high temperatures. *International Journal of Thermophysics*, Vol. 7, Issue 1, pp. 161–165.
- [14] I. Efthymiopoulos *et al.* (2011). HiRadMat: a New Irradiation Facility for Material Testing at CERN. *Proc. IPAC'11*, San Sebastián, Spain.
- [15] L. Peroni, M. Scapin, F. Carra and N. Mariani (2013). Investigation of dynamic fracture behavior of graphite. In B. Basu, *Damage assessment of structures X*, Trans Tech Publications Inc, pp. 103-110. ISBN 978-303785796-0.
- [16] H. Kolsky (1963). *Stress waves in solids*. Dover Publications, ISBN 0486610985.
- [17] “Ansys Mechanical User’s Guide – Release 15.0”, ANSYS, Inc. (2013).
- [18] R. M. Christensen (1982). *Theory of viscoelasticity, an introduction*. Academic Press. ISBN 0-12-174252-0.
- [19] G. R. Johnson and W. A. Cook (1983). A constitutive model and data for metals subjected to large strains, high strain rates and high temperatures. *Proceeding of 7<sup>th</sup> International Symposium on Ballistics*, pp. 541–547.
- [20] M. Scapin, L. Peroni and F. Carra (2016). Investigation and mechanical modelling of pure molybdenum at high strain-rate and temperature. *Journal of dynamic behaviour of materials*, Vol. 2 n. 4, pp. 460-475. ISSN 2199-7446.
- [21] F. J. Zerilli and R. W. Armstrong (1987). Dislocation-mechanics-based constitutive relations for material dynamics calculations. *Journal of Applied Physics*, 61 (5): 1816.
- [22] H. Mughrabi and T. Ungár (2002). Long-Range internal stresses in deformed single-phase materials: The composite model and its consequences. In F. R. Nabarro and M. S. Duesbery, *Dislocations in solids*, pp. 343 – 411, ISBN 9780080530451.

- [23] M. Scapin, C. Fichera, F. Carra and L. Peroni (2015). Experimental investigation of the behaviour of tungsten and molybdenum alloys at high strain-rate and temperature. *EPJ Web of Conferences*, Vol. 94, 01021.
- [24] G. R. Johnson and W. A. Cook (1985). Fracture characteristic of three metals subjected to various strains, strain rates, temperature and pressure. *Eng. Fract. Mech.*, Vol. 2 (1), pp. 31 – 48.
- [25] J. W. Hancock and A. C. Mackenzie (1976). On the mechanism of ductile failure in high-strength steels subjected to multi-axial stress states. *J. Mech. Phys. Sol.*, pp. 147 – 175.
- [26] D. E. Grady (1987). The spall strength of condensed matter. *J. Mech. Phys. Solids*, Vol. 36, No. 3, pp. 353 – 284.

## Chapter 4

# Modelling of phenomena associated to quasi-instantaneous heating

In the previous chapter we have seen that, in order to correctly model the response of materials dynamically excited by mechanical or thermal means, it is necessary to determine the equation of state and the constitutive laws, which include strength and failure models. The equation of state determines the material behaviour in hydrostatic stress conditions, such as those reached in the shock regime. However, in practical problems, even in the shock regime the deviatoric component of the stress cannot be neglected, and a strength model must be introduced, typically taking into account the dependence of the flow stress on strain, strain rate and temperature.

In this chapter, a detailed analysis of the different phenomena associated to a quasi-instantaneous heat deposition will be given, with proposed methods for their study and numerical examples. The driving mechanism of the quasi-instantaneous heating case studies is the impact of an intense proton or ion beams. However, the methods proposed are valid also under different scenarios, described in section 1.3, such as laser pulses and electrical breakdown.

In the case of a particle beam impact on a target, the kinetic energy of the beam, which travels at relativistic speed, is partially or totally transferred to the target material under the form of heat. The problem reduces to the study of a body subjected to a significantly non-uniform heat generation rate, which lasts the time of the beam passage. In the section orthogonal to the beam direction, the energy and temperature gradients are very high (Figure 37), since the beam has a transverse size in the order of tenths of mm and deposits energy densities which can reach  $10^5 \text{ J/cm}^3$  in experimental facilities like HiRadMat (see section 3.1.5). The density of beam particles  $n_p$  in the transverse plane, which is the plane orthogonal to the direction of propagation, follows the Gaussian probability density function reported in Eq. (4.1).

$$n_p = n_{max} e^{-\frac{r^2}{2\sigma^2}} \quad (4.1)$$

where  $n_{max}$  is the maximum particle density in the section,  $r$  is the radial coordinate in a cylindrical reference system, and  $\sigma$  is the standard deviation.  $\sigma$  physically expresses the deviation of particles from the ideal trajectory, which is the beam axis, and is therefore a parameter often used to define the beam transverse size.

The thermal energy deposited on the target can be calculated with interaction and transport codes, such as FLUKA [1], [2], MARS [3] and GEANT4 [4]. In the scope of this thesis, energy deposition results calculated with FLUKA<sup>11</sup> were adopted as inputs for the thermo-structural analyses performed.

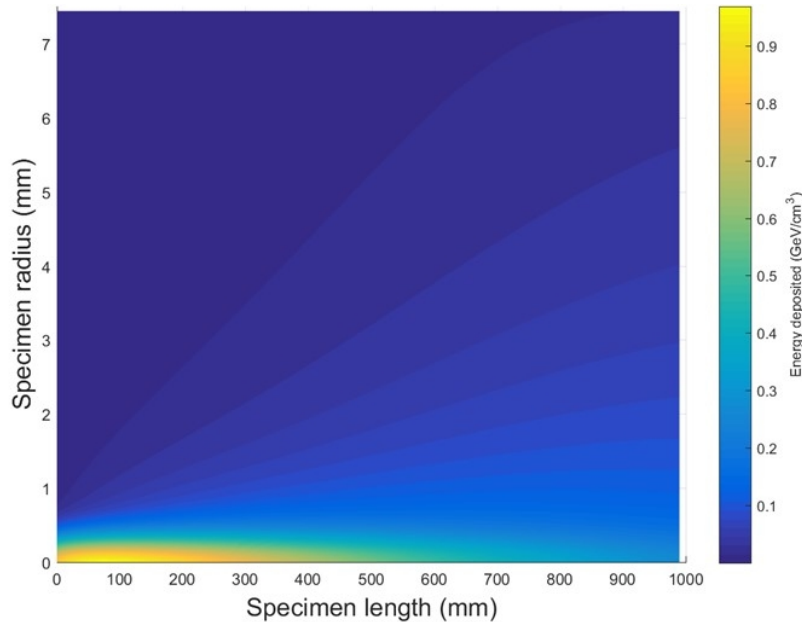


Figure 37. Energy density generated by a proton beam impact on a graphite target rod,  $L = 1$  m,  $\varnothing = 15$  mm, courtesy of M. I. Frankl. The beam energy is 440 GeV and the  $\sigma$  is 0.25 mm. The specific energy is normalized to one proton.

The energy deposition depends on the beam particles interacting first with the electrons of the target material lattice, and successively with the nuclei, producing a cascade of secondary particles in the process, called *particle shower*. High density and atomic number materials are more effective in absorbing the beam particles and

<sup>11</sup> The FLUKA energy density maps adopted for this work were kindly provided by CERN colleagues of the EN-STI-FDA section, who are in charge of the FLUKA code development at CERN.

the shower subsequently generated, and the interaction with the beam induces higher energy densities on the body (Figure 38). The FLUKA maps include specific energies, reported in  $\text{GeV}/\text{cm}^3$ , calculated at each element, or *bin*, of the mesh. The calculation is run with a Monte Carlo method; the energy results are normalized to one proton, and must then be scaled up to the total particle intensity of the beam.

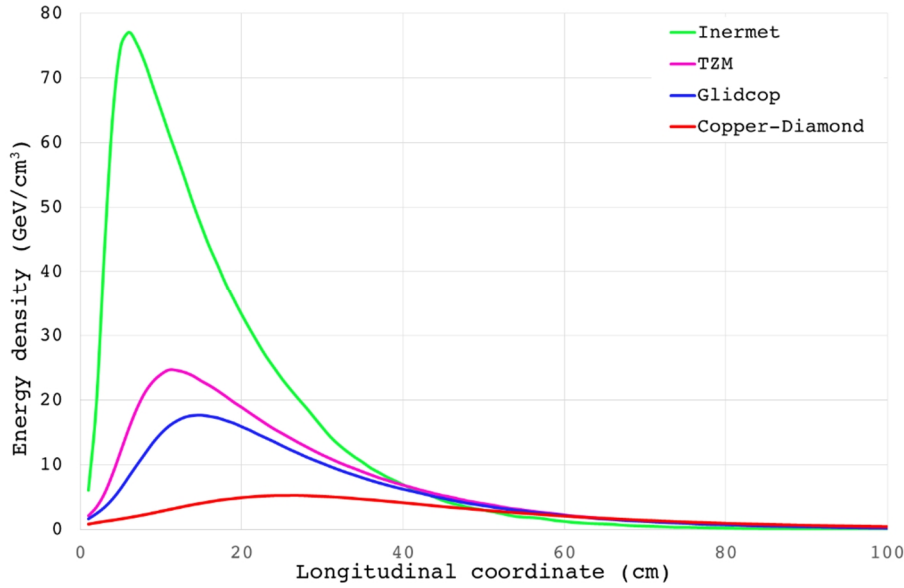


Figure 38. Energy density generated by a proton beam impact on cylindrical targets made of different materials,  $L = 1$  m,  $\varnothing = 15$  mm, courtesy of M. I. Frankl. The beam energy is 440 GeV and the  $\sigma$  is 0.5 mm. Results are normalized to one proton. Note the position of the energy density peak, which is decreasing in amplitude and increasing in depth with the decrease of the material density and atomic number. Inermet is a 95% tungsten alloy, TZM is a 99% molybdenum alloy, Glidcop is a copper grade reinforced by dispersion of aluminium oxide, and copper-diamond is a new composite material developed at CERN with a copper matrix and diamond reinforcements.

The energy calculated with FLUKA is time independent, as the code assumes that the energy is deposited instantaneously on the impacted material. However, in the scope of a thermomechanical analysis, the real duration of the thermal pulse is relevant, and can be calculated as:

$$t_d = \frac{L_b}{v} \approx \frac{L_b}{c} \quad (4.2)$$

where  $t_d$  is the energy deposition time length,  $L_b$  is the axial distance between the first and the last particle of the impacting beam, and  $v$  is the particle velocity, which for relativistic beams is very close to the speed of light in vacuum,  $c$ . Indeed, as discussed in section 1.4, in most accelerators the beam is not continuous, but is made of a series of particle bunches, each spaced by a time interval. The beam

structure at CERN features bunches roughly 30 cm long; this means that the time length of each bunch  $t_{d,i}$ , or *bunch width*, is:

$$t_{d,i} = \frac{3 \times 10^{-1} \text{ m}}{3 \times 10^8 \text{ m/s}} = 1 \text{ ns}$$

In the standard machine configuration, the distance between the head of a bunch and the head of the successive one is 7.5 m. The time distance head-to-head is defined bunch spacing  $\Delta t$ :

$$\Delta t = \frac{7.5 \text{ m}}{3 \times 10^8 \text{ m/s}} = 25 \text{ ns}$$

The bunch spacing thus includes 1 ns of bunch width, plus a time interval without particles of 24 ns. The total length of the pulse is thus:

$$t_d = N_b \Delta t$$

where  $N_b$  is the number of bunches, which for the most energetic accelerators at CERN, the SPS and the LHC, varies between 288 and 2808. The total length of the pulse is therefore comprised between 7.2 and 70.2  $\mu\text{s}$ . In the case of impact on a target, the evolution of energy and power to the target obviously follows the beam structure described above, and is schematized in Figure 39.

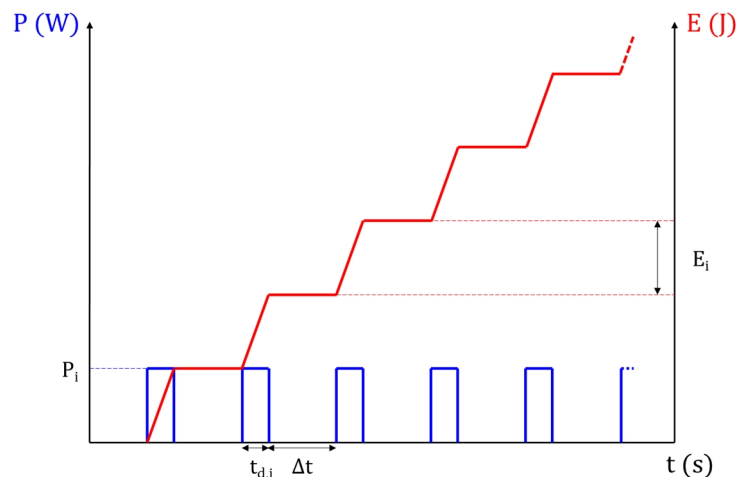


Figure 39. Time history of thermal power and energy deposited by impacting bunches on a target. The bunch width  $t_d$  is exaggerated for a simpler reading of the plot. The bunch population is constant.

The analyses of the material response under beam impact were performed with Finite Element codes, such as ANSYS and Autodyn. The input for the analysis is the FLUKA energy density map, and the thermal load is applied as a heat generation rate according to the time scale showed in Figure 39. In the case of scenarios involving strong nonlinearities, change of phase, as well as short-duration phenomena such as dilatational wave propagation, spallation and fragmentation, the explicit code Autodyn [5] was preferred for the calculation. The methods adopted were typically Lagrangian or smoothed-particle hydrodynamics. Autodyn is particularly suited for the exploration of extreme regimes of the matter, as it allows the direct use of the SESAME tabular equations of state, which encompass a wide range of temperature, pressure and density data, calculated combining theoretical and experimental methods (see section 3.1.3). Additionally, the SPH method present in Autodyn well adapts to the simulation of spallation and micro-spallation phenomena. ANSYS [6] is an implicit code which was adopted for simpler scenarios, including longer simulations targeting at slower beam-impact effects on the matter, such as temperature gradient evolution, flexural oscillations, and permanent modifications to the target shape due to plasticity. ANSYS was adopted also for those problems involving a negligible density change, which can be quite well treated with a linear equation of state, by reason of the faster solution time and unconditional stability.

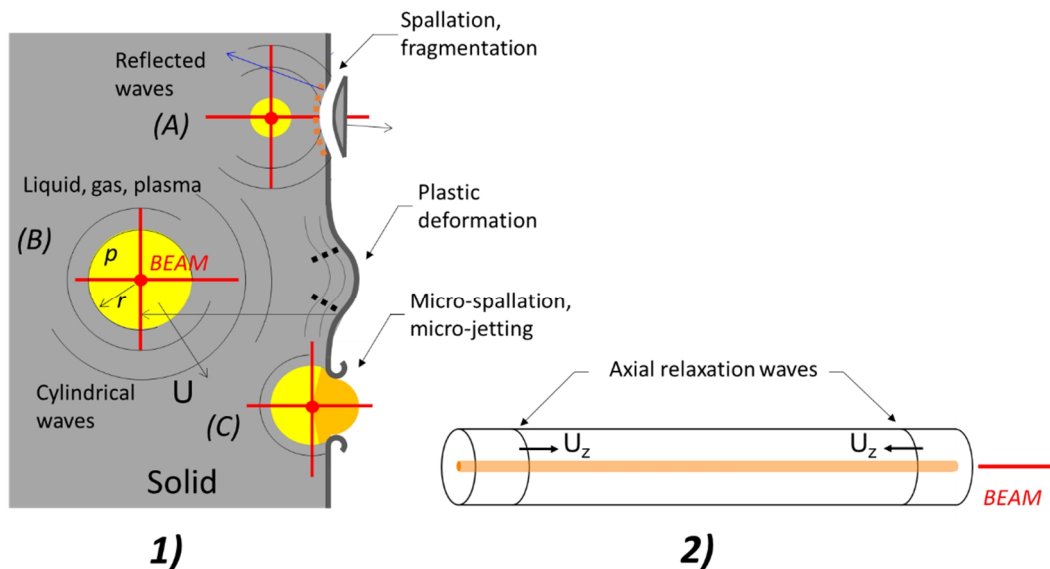


Figure 40. Phenomena correlated with particle beam impact. 1) Beam impact close to the active surface of a thick target. 2) Impact on a cylindrical rod.

Figure 40 summarizes some of the main phenomena which can take place as a consequence of a particle beam impact on targets of different geometry. In modern particle accelerators, the beam energy is high enough to induce a local phase change in the most thermal-loaded region. In the case of an impact close to the surface of a thick target (*I*), a cylindrical wave will develop, propagating radially towards the surroundings at a velocity  $U$ . The wave decays in amplitude during its travel for geometric reasons, as the energy is spread over an increasing volume, and can further be reduced by dissipative effects such as viscoelasticity, viscoplasticity, crack initiation and propagation. It is theoretically possible to achieve a shock condition in this scenario; however, it will be seen later that in current experimental facilities this event is extremely rare. The free surface may initially remain in a solid state, before thermal diffusion, which has a time constants much higher than the dilatational wave period (see section 1.3). However, the compressive wave turns into a tensile one after reflection at the boundary and may provoke spallation fracture if the spall strength of the material is surpassed (*condition A*). In case the impact point is far enough from the free surface, or the spall strength of the material is high enough, spallation does not occur, although a permanent deformation arises for stresses above yield (*condition B*). Moreover, in the case of a grazing impact (*condition C*), a phase change of the free surface material may be induced during the energy deposition. When the liquid surface reflects the pressure wave, the tensile stresses arising cannot be sustained by the material, which is pulverized into minuscule droplets (*micro-spalls*) flying away from the target with a positive divergence. The interesting thing here is that the phase change occurs in a compressed state, while in mechanical tests it is usually produced during the isentropic release, in a tensile condition. Finally, if the surface remains solid, but the pressure of the liquid or gas volume is high enough to provoke its fracture, a spray of liquid, gas and solid particles will be ejected from the surface. This phenomenon is called *micro-jetting* [7].

If the particle beam impacts on a thin rod, the problem is ideally one-dimensional (2). The specimen is in a compressive state due to the sudden temperature increase and the material inertia initially prevents any deformation. Two relaxation planar waves are produced at the free extremities, propagating in opposite directions at the velocity  $U_z$ . The boundary conditions are similar to those of a Hopkinson bar test, and the stress state is ideally uniaxial, while the strain is triaxial. The velocity  $U_z$  in the case of elastic wave can then be calculated with the second equation of the system (2.12) if the amplitude is below the elastic limit, and is lower than the velocity of a wave in an unbounded medium. In the case of an

off-centered impact, the energy distribution is transversally unbalanced, and a thermal moment originates, generating flexural oscillations on the specimens which are usually of relevant amplitude. It will be seen that this problem, although conceptually simple, is complicated in its analytical study by dispersive effects, variable energy density distribution over the sample length, and material nonlinearities.

The two above-mentioned cases involve homogeneous targets. In the case of multi-material components, it is important to determine the mechanisms of wave transmission and reflection between the materials in contact. The next sections will explore the phenomena described, showing practical examples of numerical calculation methods.

## 4.1 Change of phase

The modelling of the change of phase is related to the EOS of the material. This is usually complemented by the strength model, which also contains an information on the solid-liquid transition, as the loss of material strength is accounted for in models such as Johnson-Cook.

If a substance can exist in more than one phase, the stable phase at a given pressure and temperature is the one with the lowest Gibbs free energy [8]. The inclusion of phase transitions in an equilibrium EOS requires only the application of thermodynamics principles. In the case of vaporization, a single EOS describes both the vapor and the condensed phase. To describe melting and solid-solid phase transitions, separate equations of state including the free energy must be generated for each phase.

In the case of nonequilibrium phase transitions, a rate equation must be formulated to describe the time evolution of the composition of the system. Given that each phase has different dynamical properties, this equation is coupled to the hydrodynamic flow equations and must be solved simultaneously.

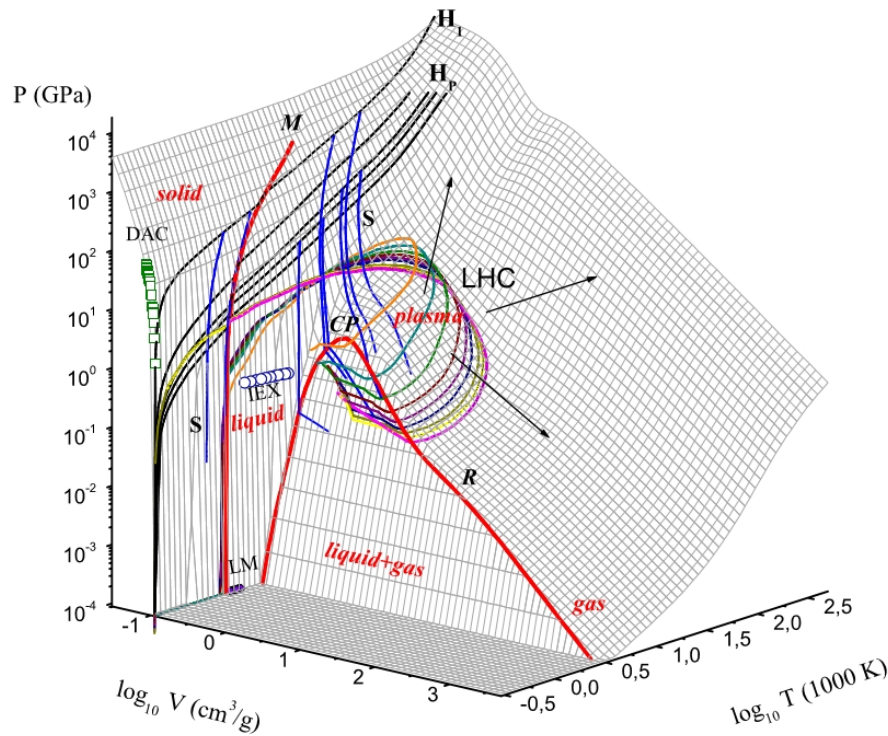


Figure 41. 3D  $p$ - $v$ - $T$  surface for copper. Source: [9].  $M$ , melting region;  $R$ , evaporating region with the critical point,  $CP$ ; solid, liquid, gas, liquid+gas, and plasma (arrows indicate the decrease in plasma nonideality parameter) physical states;  $H_I$  and  $H_p$ , principal and porous Hugoniot;  $S$ , release isentropes of shock-compressed metal;  $IEX$ , isobaric expansion;  $DAC$ , static compression in diamond anvil cells;  $LM$ , density of liquid metal at room pressure; and  $LHC$ , states generated in copper by the LHC beam covering strongly coupled plasma region.

### 4.1.1 Melting

An accurate description of melting is needed not only for describing the EOS, but also to model the loss of material strength and shear modulus above the melting temperature. Static measurements on melting are typically limited to pressure in the order of 10 GPa [10]. Melting is difficult to observe in standard Hugoniot experiments; as discussed in section 3.1.5, quasi-instantaneous heating can be adopted for the description of melting and vaporization. More in general, successful techniques in this sense are those measuring the release wave velocity in a shocked state [11]. Upon melting, there is a rapid drop in velocity from the longitudinal to the bulk value, as the material is no more subjected to deviatoric stress. Most of the existing data confirms that shock-induced melting is a very rapid process, and its general structure can be described with an equilibrium EOS.

Several semi-empirical expressions have been derived to express the pressure dependence of the melting temperature without explicitly treating the liquid phase,

for example expressing the melting curve in terms of the Debye temperature for the solid [12]. Another possibility is to build the melting law by scaling the solid properties, as discussed, and using the free energy to determine the phase boundary. According to several authors [8], this approach gives reasonable results for many materials, and equations of state constructed for practical applications rarely go beyond this level of sophistication. However, for many materials the melting curve is more complex, due to transitions in the solid phases and to changes in the electronic structure not perfectly described by the simplified models. In these cases, a more accurate treatment requires the application of the free energy method, using constructed EOS for both the solid and liquid phases. An example in this sense is the SESAME tabular EOS already described, which combines in a single table numerous equations of state for the different phases.

#### 4.1.2 Vaporization

The treatment of vapor-liquid coexistence region and of expanded fluid states is necessary in the study of the release behaviour following shock loading in several hypervelocity impact problems. In the gas-like regime at low densities, the pressure is determined by the thermal motion of the atoms; in the liquid regime at high densities, it is determined by the intermolecular forces. Equations of state trying to describe both regimes with the existing transition predict an unstable region with  $(\partial p / \partial \rho)_T < 0$  at temperatures below the critical temperature  $T_c$ . This construction does not reproduce the equilibrium behaviour, since the real system can lower its free energy by separating into coexisting liquid and gas phases. The properties of the two phases can be determined by matching pressures and free energies, with a result of coexistence region where the composition of the vapor-liquid mixture varies at a constant pressure.

Even the simplest fluid models are often giving only a rough description of vaporization, but quantitative results can be obtained by fitting of the models with experimental data, which are still at the moment very scarce. In hypervelocity phenomena, the details of the vaporization region are in general important when the temperature on release is above the boiling point, such that substantial momentum and energy are imparted to the vapor cloud. In quasi-instantaneous heating phenomena, as already mentioned, vaporization may occur also during the compressive phase, and the description of the phenomenon is even more relevant. Information on this region of the EOS are particularly valuable and could be one of the most relevant outcomes of an isochoric test run in a particle beam facility.

### 4.1.3 Plasma phase transition

Experimental data and theoretical considerations suggest that vaporization and the properties of fluid in the expansion phase are further complicated by thermal electronic excitation. Most of the measurements in this sense have been performed on mercury, because of its low critical temperature. Results [13] show the existence of a metal-insulator transition and other less known effects of changes in the electronic structure. Kerley [14] performed studies on the metal-nonmetal transition in aluminium using ionization equilibrium theory and numerical codes to compute the thermal electronic contributions. His model predicts the existence of two liquid phases at temperatures in the range 4000–7000 K, a phenomenon not observed in simple fluids.

For this material regime, experimental data are even scarcer, and all the models rely on the combination between theoretical and numerical techniques. Once again, the thermal energy involved in the particle beam of modern accelerator testing facilities may be an important asset in the study of this phenomenon. As an example, see section 4.3 for the simulation and experimental testing of structures reaching temperatures in the order of 50 000 K.

## 4.2 Uniaxial stress waves

In the case of a one-dimensional target, like a rod (Figure 40 – 2), the impact of a proton beam induces a sudden compressive state on the body. Two relaxation waves originate at the free extremities of the rod and propagate towards the center at a velocity equal to, in the elastic regime:

$$c = \sqrt{\frac{E}{\rho}} \quad (4.3)$$

which is the second equation of the system (2.12), as the body is in uniaxial stress conditions. The relaxation waves induce a dynamic tensile stress on the target, superposing with the static stress and relaxing the body compression. As explained in chapter 2, in this condition, similarly to a Hopkinson bar test, it is impossible to build up the pressure necessary to reach the shock jump; however, plasticity could be induced, and in that case the wave velocity would have the more general form:

$$c = \sqrt{\frac{d\sigma/d\varepsilon}{\rho_0}} \quad (4.4)$$

In case the beam impacts with a certain offset with respect to the rod neutral axis, a thermally-induced bending moment is generated in addition to the axial solicitation, and a flexural vibration also takes place.

### 4.2.1 Axial oscillations

Bertarelli and colleagues [15] developed an analytical method to study the problem, and successfully applied it to verify, in the linear elastic assumption, the behaviour of isostatic graphite targets under intense beam impact at the *Neutrinos to Gran Sasso* (CNGS) project carried out in a collaboration between CERN and INFN [16]. The method involves the calculation of the temperature field for a given energy distribution, assumed constant over the rod length, by means of the Fourier's equation which, if the pulse length  $t_d$  is much smaller than the diffusion time constant  $\tau$ , is simplified to (1.16). The material properties are considered constant with temperature. The quasi-static stresses, strains and displacements induced by the temperature increase are then calculated with the Duhamel–Neumann equations (1.8), (1.9) combined with the general kinematic equations relating strains and displacements. In the linear elastic hypothesis, the quasi-static stresses, strains and displacements can then be superposed with the dynamic ones, to define the material response at every time instant.

We focus on the dynamic phenomenon, which was studied by evaluating the axial response of the body under a sudden thermal stress  $\sigma_{ref}$  building up during the deposition and reaching its maximum at  $t_d$ :

$$\sigma_{ref} = E\alpha\Delta T_F \quad (4.5)$$

where  $E$  is the Young's modulus,  $\alpha$  the thermal expansion coefficient and  $\Delta T_F$  is the difference between the temperature on the body at steady-state, under adiabatic hypothesis, and the initial temperature.

Figure 42 shows the evolution of the dynamic axial stress over time and axial coordinate. The analytical model excludes radial inertia contributions.

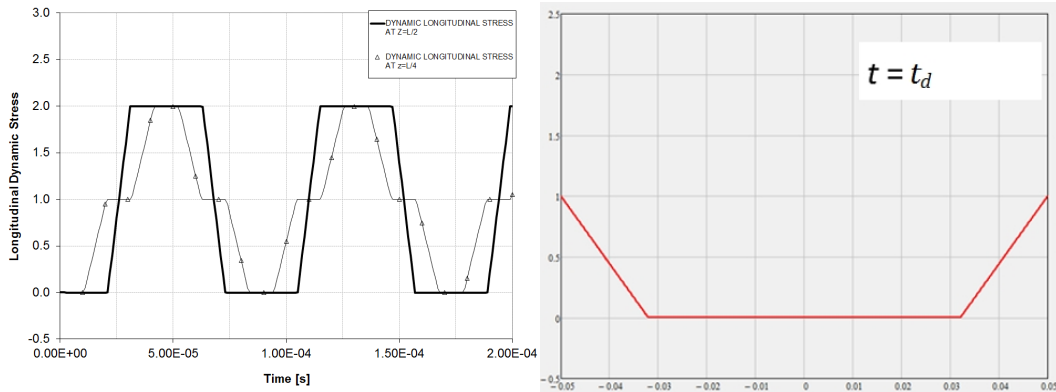


Figure 42. Left: dynamic axial stress scaled to  $\sigma_{ref}$  as a function of time at the centre and one quarter of the rod. Right: dynamic stress at the end of the deposition over the length. Source: [17].

A numerical model was built in the scope of this thesis, with ANSYS, to explore the relevance of the following aspects with respect to the analytical method just described:

- Thermal energy gradient along the rod axis;
- Material nonlinearities with temperature;
- Radial inertia effects (dispersion, radial wave propagation);
- Influence of the boundary conditions and of the plane strain state assumed.

In particular, the assumption of neglecting the radial effects in the problem is strongly dependent on the geometry studied. The analytical method was originally adopted to evaluate the dynamic response of isostatic graphite cylindrical rods with length 100 mm and a diameter 10 mm. As a matter of fact, tests performed by Skalac [18] in the 1950s, based on the studies on cylindrical bars made almost one century before by Pochhammer [19], highlighted a dependence of the material response on the impacted geometry, and a deviation of the wave profile from the ideal shape, with fluctuations along the bar (Figure 43). Such fluctuations, which are known as *dispersion effects* [20], are associated with a decrease of the longitudinal wave propagation velocity, with respect to the ideal value calculated with Eq. (4.3).

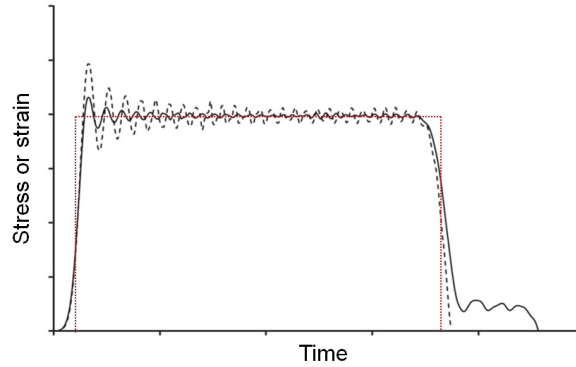


Figure 43. Ideal wave profile in uniaxial stress conditions (red) and real profile (black).

Dispersion is due to radial inertia, caused by the kinetic energy of the material flowing radially outward as the bar is compressed, and wave interaction with the external surfaces of the cylinder [21]. According to Pochhammer, the group velocity  $c_g$  and wave velocity (or phase velocity)  $c_p$  in the case of a longitudinal bar can be calculated as:

$$\frac{c_p}{c_0} = 1 - \nu^2 \pi^2 \left(\frac{r}{\lambda}\right)^2 \quad (4.6)$$

$$\frac{c_g}{c_0} = 1 - 3\nu^2 \pi^2 \left(\frac{r}{\lambda}\right)^2 \quad (4.7)$$

where  $c_0$  is the ideal velocity calculated with Eq. (4.3),  $\nu$  is the Poisson's ratio,  $r$  is the bar radius and  $\lambda$  is the length of the wave. It is evident that the dispersive effects contribute to a decrease of the wave velocity, as the second term of Eqs. (4.6),(4.7) is positive. For a given wavelength, the velocity decreases proportionally with the radius and with the Poisson's ratio, as for high values of  $\nu$  transversal deformations are more relevant.

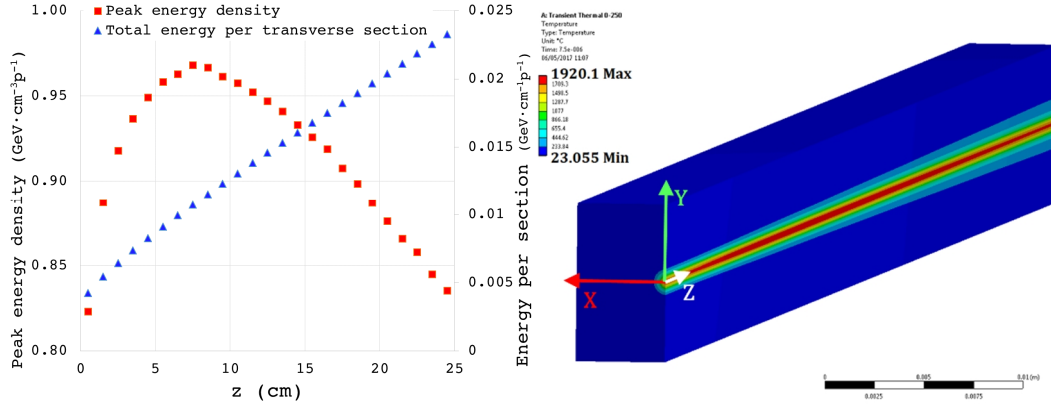


Figure 44. Left: energy and energy density generated by a proton beam impact on a graphite rod. Courtesy of M. I. Frankl. The beam energy is 440 GeV and the  $\sigma$  is 0.25 mm. Results are normalized to one proton. Right: energy deposition profile in the space and reference system; the rod is shown with a section view along the YZ plane.

As to the real thermal load distribution, the energy peak and the energy integral along  $z$  are shown in Figure 44. Notably, in the case under study, the total energy per unit length increases with  $z$  over the full length of the component, as more and more primary and secondary beam/matter interactions take place.

Given that no phase transformations are expected<sup>12</sup> for the energy profile shown in Figure 44, a linear equation of state (3.8) is adopted. All the material properties required for the EOS construction are reported in Table 12 and Figure 45, as well as the geometry and the particle beam data. The material is considered linear elastic; no strength and failure models are applied. The rod is simply supported at both ends. The coordinate system is shown in Figure 44. Note that Figure 45 reports the specific heat at constant pressure, while the EOS adopts the specific heat at constant volume. The two quantities are very close only at low temperature, and are related by the equation:

$$c_p - c_v = \frac{9\alpha^2 v T}{K} \quad (4.8)$$

where  $c_p$  and  $c_v$  are the specific heat capacities at constant pressure and volume respectively,  $\alpha$  is the coefficient of thermal expansion,  $T$  is the temperature in kelvin and  $K$  the bulk modulus.

<sup>12</sup> This can be quickly estimated with Eq. (1.16),(1.18).

Table 12: Isostatic graphite properties and parameters of the impacting proton beam.  $E_k$  is the particle energy,  $n_{tot}$  the total number of protons and  $t_d$  the pulse length.  $L$ ,  $W$  and  $H$  are the dimensions along  $x$ ,  $y$  and  $z$ .

Rod geometry		Material properties		Beam parameters	
$L$ (mm)	250	$E$ (GPa)	11.5	$E_k$ (GeV)	440
$w$ (mm)	9	$K$ (GPa)	4.8	$n_{tot}$	$3.74 \times 10^{13}$
$h$ (mm)	8	$G$ (GPa)	5.2	$t_d$ ( $\mu$ s)	7.5
		$\nu$	0.1	$\sigma$ (mm)	0.25

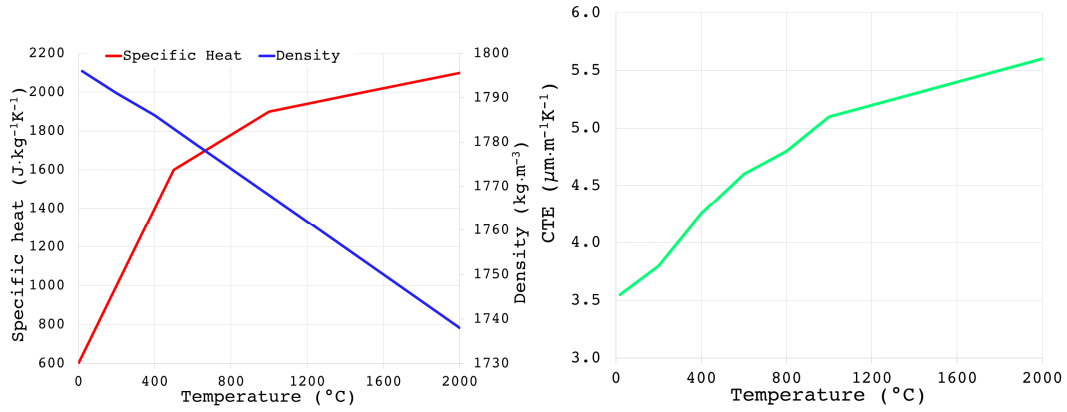


Figure 45. Left: specific heat and density of isostatic graphite as a function of temperature. Right: coefficient of thermal expansion as a function of temperature.

The total strain in  $z$  direction over time is shown in Figure 46, at different longitudinal positions, to compare with Figure 42. With respect to the analytical model, the following considerations can be made:

- The axial phenomenon is overall quite well replicated, with trapezoidal waves with loading/unloading ramps dependent on the finite pulse length;
- It is interesting to note the different amplitude of the two unloading waves, due to the variable thermal energy distribution over  $z$ . The wave coming from the impacted face has smaller amplitude, as the total energy on the first half of the bar is smaller (see Figure 44);
- Dispersive effects are clearly observed.

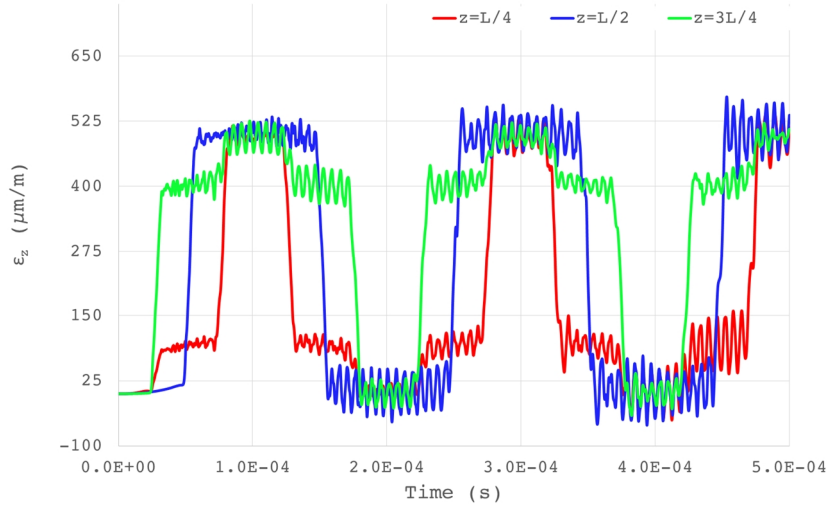


Figure 46. Numerical model, total axial strain over time at  $x,y=0$  at three longitudinal positions.

The last point is worth a more detailed analysis. As seen in Eq. (4.6), the wave velocity can be calculated in an analytical way, and then compared with the numerical results. The length of the wave is equal to  $2L$ , as it is evident from Figure 46 and Figure 50, since the relaxation wave propagates all along the bar, before reflecting and becoming compressive until reaching back the initial free surface. Solving Eqs. (4.6),(4.7) for the parameters reported in Table 12, and calculating the initial sound speed  $c_0$  in pure uniaxial stress conditions with Eq. (4.3), results in:

$$\frac{c_g}{c_0} = 99.998\% \approx 1$$

$$\frac{c_p}{c_0} = 99.999\% \approx 1$$

$$c_p \approx c_g \approx c_0 = 2530 \text{ m/s}$$

The velocity of the two planar waves generated by the impact in this case is therefore very close to the initial sound speed of the material. In this sense, the low value of the Poisson's ratio of graphite is beneficial, as it minimizes the contribution of radial waves to the axial displacement. Dispersive effects, although observable, are not contributing to a sensible diminution of the principal axial wave velocity. To confirm this, it is easy to evaluate the numerically predicted velocity of the wave: the period  $T_z$  can be extracted out of the data shown in Figure 46, and the space is twice the length of the bar.

$$T_z = 0.1974 \text{ ms} ; L = 250 \text{ mm}$$

$$U_z = \frac{2L}{T_z} = 2532 \text{ m/s}$$

where  $U_z$  is the simulated wave velocity in the axial direction, which is basically identical to the expected value of  $c_p = 2530 \text{ m/s}$ . Of course, physically  $U_z$  cannot be higher than  $c_p$ , and this apparent inconsistency is simply due to a small uncertainty in the calculation of the wave period within the simulated data, since the results are saved every  $2 \times 10^{-7} \text{ s}$  and the error in the velocity calculation is  $\pm 3 \text{ m/s}$ .

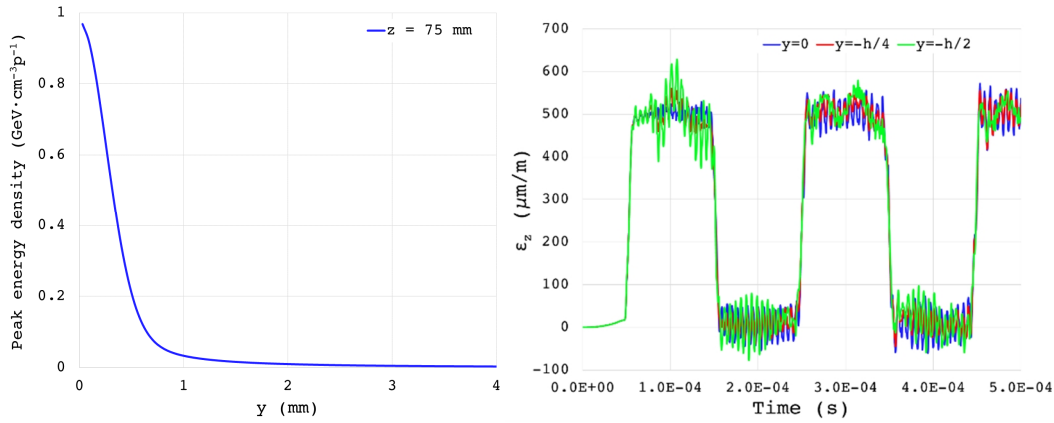


Figure 47. Left: thermal energy deposition along the transverse coordinate  $y$  ( $y = 0$  is the beam axis,  $y = -4 \text{ mm} = -h/2$  is the free surface) in the most loaded longitudinal section. Right: Total axial strain over time in the most loaded longitudinal section ( $z = 75 \text{ mm}$ ), for different transversal positions.

In the classical Pochhammer theory, dispersion is related to the reflection of the axial wave at the lateral surfaces of the bar, which are stress-free. This phenomenon takes place even in the case of a null force gradient along the bar radius or transverse coordinate ( $x, y$ ). In the case under study, however, a strong thermal energy gradient exists along the transversal coordinate of the rod, Figure 47. With reference to the linear equation of state adopted (3.8), this leads to a correspondent pressure increase in the material core:

$$p(\rho, E) = K \left( \frac{\rho}{\rho_0} - 1 \right) + \gamma_0 E ; \gamma_0 = \frac{\alpha K}{\rho_0 c_v} \quad (3.8)$$

In fact, the first term is almost negligible (Figure 45), and pressure and thermal energy are linearly dependent. An irrotational, compressive pressure wave will propagate radially from the material core to the lateral surfaces of the rod, also

contributing to the axial strain because of the non-null Poisson's ratio. On the other hand, this contribution is, in the case study, of small entity and not observable in terms of strain. In fact, referring to Figure 47 (right), and in particular at the time interval  $0 - 5 \times 10^{-5}$  s, one can note the absence of oscillations, even if the radial wave has already reflected several times at the free surface. Looking for example at the  $y$  direction, the period and frequency of the radial wave are indeed:

$$T_y = \frac{2h}{c_0} = 6.3 \mu\text{s}; \lambda_y = 158 \text{ kHz}$$

which is confirmed by the numerical results in Figure 48. The figure also shows that radial waves are reaching the free surface even before the end of the thermal pulse, but the transverse oscillation has negligible contribution<sup>13</sup> to the axial phenomenon. The high-frequency oscillations observed also in Figure 46 and Figure 47 after the arrival of the axial wave ( $5 \times 10^{-5}$  s) are thus mostly due to dispersion.

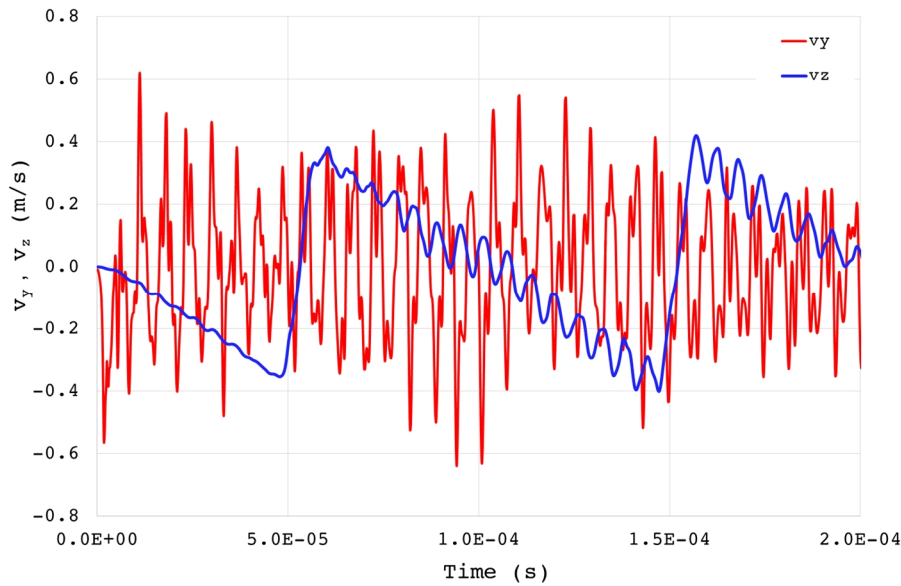


Figure 48. Vertical (red) and axial (blue) particle velocity over time at  $x = 0$ ,  $y = h/2$ ,  $z = L/2$ .

The assumption of constant energy distribution along the rod axis overlooks the asymmetry of the two waves generated at both ends and shown in Figure 46. This

<sup>13</sup> Plotting the particle velocity instead of the strain, the contribution of radial waves to the axial phenomenon is at least now visible.

asymmetry is evident also in Figure 49, which depicts the two axial waves travelling towards the centre of the rod, and compares with Figure 42 (right).

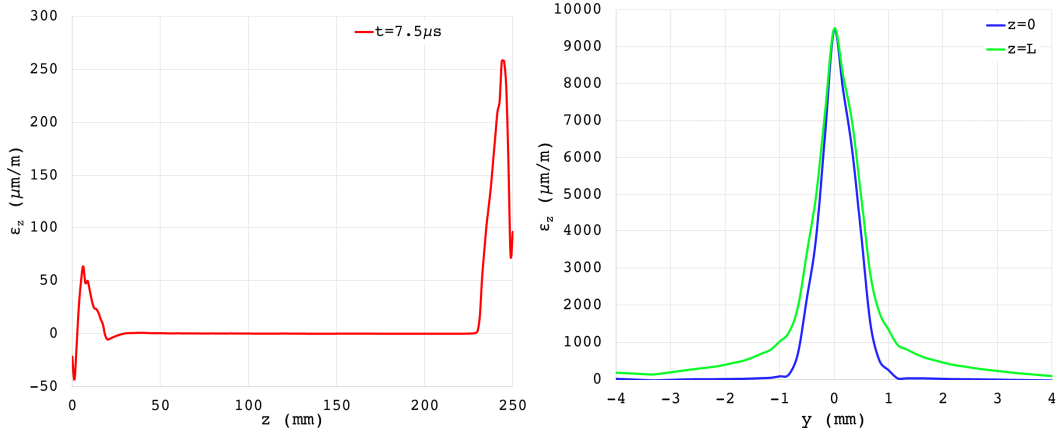


Figure 49. Left: total axial strain along the rod at  $t = t_d$  and  $y = -h/2$ . Right: total axial strain as a function of  $y$  at upstream and downstream ends, for  $t = t_d$ .

Figure 49, left, confirms that a plain strain assumption would fail at describing the material behaviour close to the boundaries. In fact, the strain assumes non-zero values at the free ends. Also, thanks to the three-dimensional model, a bulge of the material free surfaces, due to the non-uniform temperature radial distribution, is highlighted. Boundary effects are traditionally difficult to model analytically, and even the classical Euler-Bernoulli beam theory is valid only at a certain distance from the boundaries. In one-dimensional analytical solutions, strains and stresses are constant on the cross-section. Analytically, the strain assumes a value which is the average along  $y$  and  $x$  of the strain shown in Figure 49, right (Eq. 4.9).

$$\varepsilon_{z=0,L} = \alpha \Delta T_F(z = 0, L) \quad (4.9)$$

Figure 50 and Figure 51 show the propagation of the planar waves from the two free ends, with reflection at the opposite extremity and return to the initial configuration after one full period. Note again that the material which is not reached yet by the planar waves is apparently at rest, see for example the curve  $t = 10 \mu\text{s}$ , for  $z$  comprised between 50 and 200 mm. The contribution of radial waves to the axial oscillation is, in fact, so small that it is not visible in Figure 50. On the other hand, after the passage of the main planar wave, the material vibrates under the effect of dispersive waves with higher frequency and smaller amplitude.

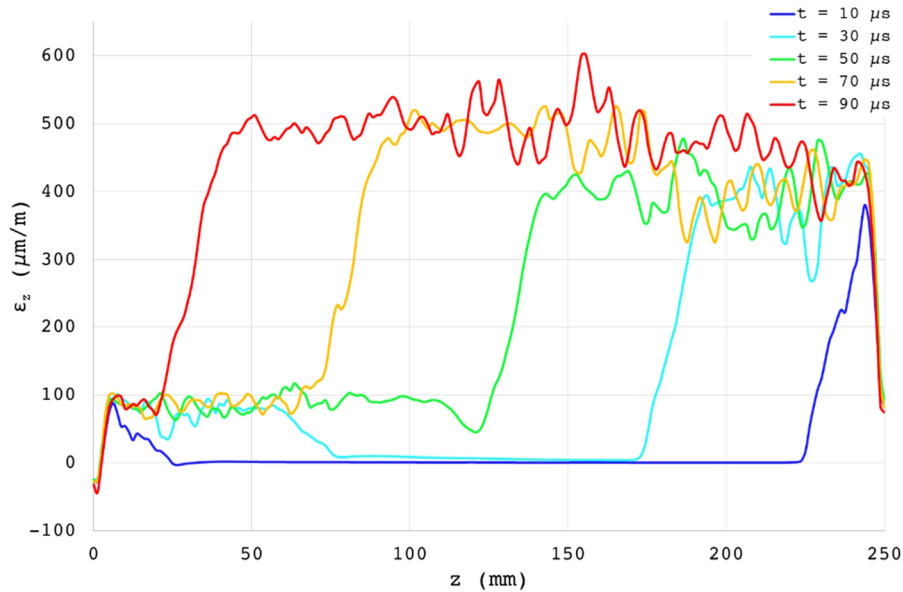


Figure 50. Propagation of the two planar waves from the ends of the rod.  $\varepsilon_z$  is measured at  $y = -h/2$ . After  $90 \mu\text{s}$ , the two waves have almost completed  $\frac{1}{2}$  period and are close to the opposite ends.

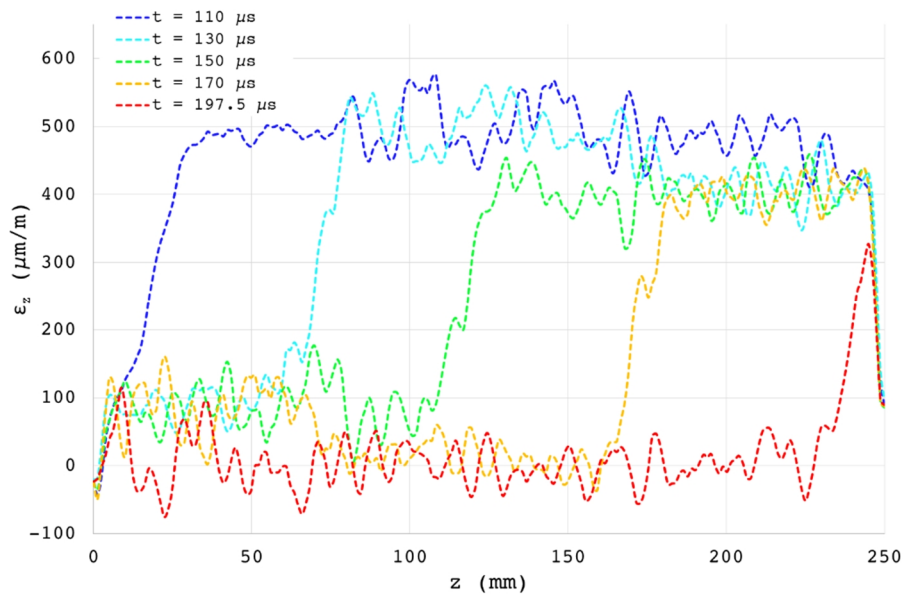


Figure 51. Reflection of the two waves and return to the initial configuration, after one full period.

The main conclusions of the numerical study performed are:

- The positive temperature gradient in  $z$  generated during the energy deposition leads to the formation of two asymmetric planar waves, with amplitude proportional to the average temperature increase at each end. The dynamic response during the wave propagation is then similar to what observed with an analytical model; on the other hand, the wave

asymmetry provokes a rigid motion of the rod along its axis after each period. If no dissipation is involved and no external forces are applied on the rod, the motion will continue for an infinite time.

- The material nonlinearities with temperature have a quantitative, but not qualitative effect on the results.
- The numerical 3D model highlights the consequences of neglecting the radial inertia of the rod. In particular, pure dilatational waves propagating radially from the hot core of the material are observable, but they weakly influence the axial dynamic response. On the other hand, dispersive effects on the planar wave, related to the presence of free lateral surfaces orthogonal to the direction of propagation, are evident. The amplitude of the dispersive oscillations is about 20% of the total dynamic stress and strain. However, these phenomena essentially do not affect the velocity of propagation of the main axial waves.
- The material response in correspondence with the boundaries was successfully simulated. The strain and stress values were also calculated along the transverse coordinate at each free end, and the average values were proved to be identical to those calculated analytically, for a one-dimensional model.

#### 4.2.2 Flexural oscillations

In the analytical model, bending vibrations induced by an off-center beam impact were calculated as a result of the sudden application of an equivalent thermal bending moment. The mode shapes and natural frequencies can be calculated with Eq. (2.7). The amplitude of the moment, and therefore of the induced oscillation, is proportional to the eccentricity  $\eta$ ; results in the original paper [15] are shown for  $\eta = 0.6R$ . For a comparative study, this value was also adopted in the numerical model already presented in the previous section, with the impact occurring at  $0.3h$  and flexural vibrations taking place with displacement  $w$  in the  $y$  direction (Table 12). The flexural displacements and stresses with the analytical method developed by Bertarelli are shown in Figure 52.

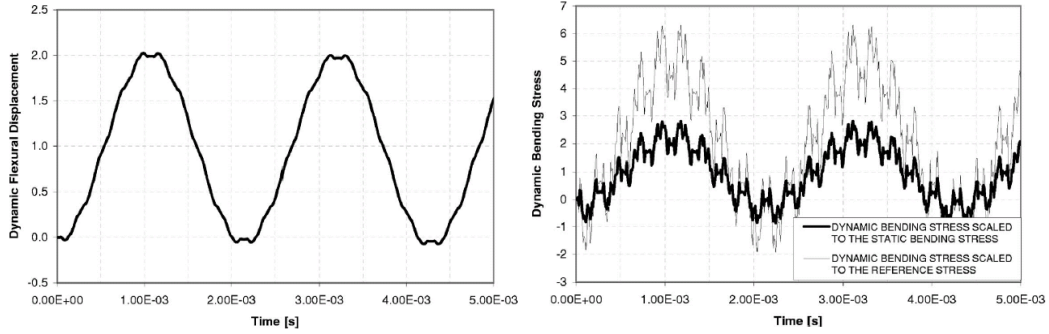


Figure 52. Left: flexural oscillation. Right: flexural dynamic stress. Source: [15], pp. 7–8.

The elementary solution of Eq. (2.7) gives, in terms of frequency:

$$\lambda_{f,i} = \frac{1}{2\pi} \frac{\beta_{f,i}^2}{L^2} \sqrt{\frac{EI_x}{\rho A}} \quad (1.15)$$

In the case of simply supported ends, for the first mode  $\beta_{f,1} = \pi$ . The first flexural frequency and period are thus:

$$\lambda_{f,1} = 146.9 \text{ Hz}; T_{f,1} = 6.8 \text{ ms}$$

The solution can be expressed also in terms of wave velocity  $c'$  [20]:

$$c' = \frac{2\pi c_0}{\Lambda} \sqrt{\frac{I_x}{A}} = \frac{2L}{T_{f,1}} = 73.4 \text{ m/s} \quad (4.10)$$

In the case of a pulse composed of infinitely short waves, the velocity of the flexural wave would tend to infinity, which is unphysical. In fact, Eq. (4.10) is accurate only for wavelengths ten times higher than the half-thickness of the bar [20]. In the case under examination, this geometry assumption is respected. More in general, Rayleigh's correction [22] to Eq. (4.10) can be applied to take into account rotary motion for short wavelengths, while Timoshenko [23] introduced a correction to consider the change in the shape of longitudinal sections with the motion. Applying Rayleigh's method:

$$c' = c_0 \frac{1}{\sqrt{1 + \frac{\Lambda^2 A}{4\pi^2 I_x}}} \quad (4.11)$$

which gives the same results as Eq. (4.10). Applying the correction introduced by Rayleigh, the wave velocity reaches asymptotically the speed of sound for infinitesimal wavelengths. A more precise estimation of the wave velocity comes from Hudson [24], who derived it from the elastic equations, providing the results in tabular form and obtaining good agreement with Timoshenko. Hudson and Timoshenko showed that accounting for the change of section shape results in an even lower wave velocity at high frequency, close to  $0.6c_0$  for Poisson's ratios in the order of 0.3. In the problem under examination, as mentioned, all the approaches lead to the same result, which is confirmed by the identification of the 6.8 ms period of the flexural wave in the numerical model, see Figure 53.

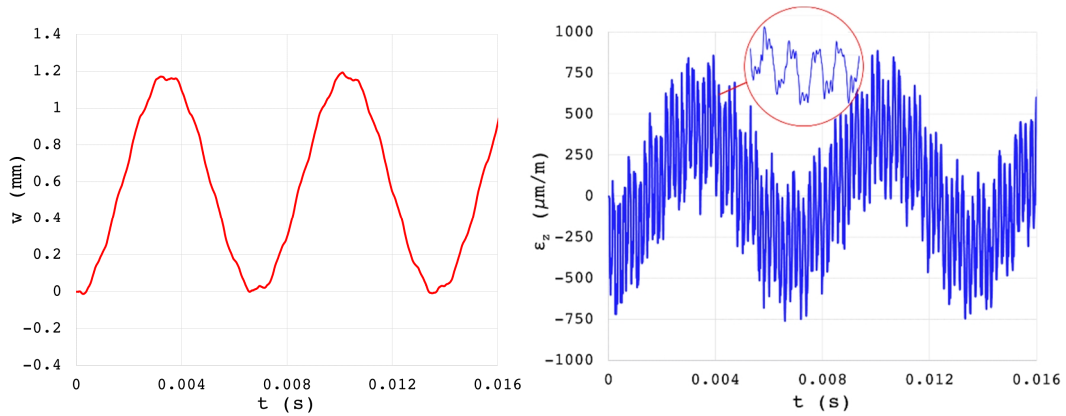


Figure 53. Left: numerical model, flexural oscillation for an eccentricity  $\eta=0.6R$ . Right: dynamic flexural strain. Note that the slow flexural wave superposes with faster axial waves described in section 4.2.1.

### 4.3 Cylindrical stress waves

In the previous paragraph we have seen that even in long and thin bars, a focused particle beam generates waves propagating radially from the material core towards the outer surfaces. While on slender targets this phenomenon is less relevant and intense with respect to the planar waves propagating along the longitudinal axis, in 3D elements the material response at the lateral surface is mostly due to the radial oscillation. Given the shape of the energy distribution, it is easier to study the

material response in cylindrical coordinates. The equation for a dilatational wave (1.20) can be rewritten as:

$$\frac{1}{c^2} \frac{\partial^2 u}{\partial t^2} = \frac{\partial^2 u}{\partial r^2} + \frac{\partial}{\partial r} \left( \frac{u}{r} \right) \quad (4.12)$$

where  $r$  is the radial coordinate. The value of  $c$  depends on the boundary conditions: as shown in section 2.1, in the case of a cylinder constrained radially and longitudinally, or in the case of big radius and length, the wave propagation is like in unbounded media, and the velocity  $c$  is:

$$c_c = \sqrt{\frac{M}{\rho}} = \sqrt{\frac{(1-\nu)E}{(1+\nu)(1-2\nu)\rho}} \quad (4.13)$$

In the case of a disk, the treatment is similar, but a plane stress assumption must be adopted. The axial stress is null and starting from the conservation of momentum on a body particle, as it was done in section 2.1, and applying the kinematic and constitutive equations, it is easy to find that the problem is still solved with Eq. (4.12). However, in this case  $c$  has the expression:

$$c_D = \sqrt{\frac{E}{(1-\nu^2)\rho}} \quad (4.14)$$

In the case of a disk, the wave velocity is therefore often very close to  $c_0$ , as for many materials the value of  $\nu^2$  is negligible. As mentioned, the derivation of the wave equation in cylindrical coordinates is identical to the Cartesian formulation shown in section 2.1 and the mathematics is not reported here for the sake of brevity; however, the interested reader can refer to Sievers [25] for the detailed steps of the derivation.

An important property of radial waves is that their amplitude decreases at increasing radial distance from the axis. This is intuitive, as the same energy amount is spread over an increasing volume. The wave decay can be estimated by solving Eq. (4.12) in radius and time; the solution is given by a Hankel function of the first kind of order zero [26]. The function has a logarithmic singularity for  $r \rightarrow 0$ , such that in the neighbourhood of the source, for an outgoing wave one can express the velocity potential as:

$$\Phi(r, t) \sim \left(\frac{2iA}{\pi}\right) \log(kr) e^{-i\omega t} \quad (4.15)$$

where  $A$  is the amplitude,  $\omega$  is the angular frequency and  $k$  is the wavenumber  $\omega/c$ . It is worth recalling the expression of the velocity potential:

$$\dot{u} = \nabla\Phi \quad (4.16)$$

On the other hand, for  $r \rightarrow \infty$ , thus at large distance from the axis, the velocity potential is given by the asymptotic expansion:

$$\Phi(r, t) \sim A \sqrt{\frac{2}{\pi kr}} e^{i(kr - \omega t - \frac{\pi}{4})} \quad (4.17)$$

This is an important result, as it shows that the velocity potential decays in amplitude proportionally to  $r^{-1/2}$ . The phenomenon is called *cylindrical spreading loss*; similarly, it can be shown that in a spherical system, where the wave source is a point, the *spherical spreading loss* is proportional to  $r^{-1}$ .

Focusing on the cylindrical system, the pressure and velocity decay for an irrotational wave at large radii is also proportional to  $r^{-1/2}$ , as it can be expressed, starting from Eq. (1.19), with the same Hankel functions. As a consequence, the power density of the elastic wave, or *sound intensity*  $I$ , decreases in a cylindrical system proportionally with  $r^{-1}$ :

$$I = p\dot{u} \quad (4.18)$$

The conclusion is also evident when considering that the same total energy is distributed over a cylindrical surface whose area increases linearly with  $r$  as the wave is propagated. For spherical systems, the sound intensity decreases proportionally to  $r^{-2}$ .

Another important property common to both spherical and cylindrical waves concerns the succession of compression and rarefaction waves induced by the

system. Before the outgoing wave reaches a field point<sup>14</sup>, the velocity potential must be identical to zero; because of the nature of the outgoing waves, the potential must return to zero after the passage at the field point. The potential thus vanishes before and after the wave passage at any point in space. Looking at the pressure variation in space  $p'$ , from Eq. (1.19) it can be written as a function of the velocity potential:

$$p' = -\rho \frac{\partial \Phi}{\partial t} \quad (4.19)$$

Integrating  $p'$  over the time for a given radius must give zero as result:

$$\int_{-\infty}^{\infty} p' dt = 0 \quad (4.20)$$

The consequence is that as the cylindrical (or spherical) wave passes a given field point, both compressions ( $p' > 0$ ) and rarefactions ( $p' < 0$ ) will be observed at the field point. This is a sensible difference with respect to planar waves, which ideally, in infinite targets, may consist of compressions or rarefactions only, and is of particular interest in the study of the response to a particle beam impact. As mentioned, in fact, the thermal pulse length  $t_d$ , although extremely short, is not null. This means that, since during the thermal energy deposition the radial wave propagation is relevant, energy will typically be deposited on the material when it is already in a tensile state induced by the first generated rarefaction wave. In the elastic domain, this phenomenon does not add particular complexity to the study of the problem; on the other hand, at higher energies, the reduction in density induced by the rarefaction wave on the material, in addition to possible phase changes, results in a higher penetration of the particle beam inside the target. This phenomenon is known as *hydrodynamic tunneling* [27], and requires a coupling between the particle transport code (such as FLUKA) and the finite-element code (for example Autodyn) to simulate the material response in these conditions.

As already introduced in section 2.3.3, even in modern, highly energetic particle accelerators, the nature of the cylindrical waves generated by particle beam

---

<sup>14</sup> Defined as a point in which the fields (pressure, intensity, velocity, potential, *etc.*) are evaluated.

impacts is typically elastic or elastic-plastic. The shock condition is difficult to reach by reason of the abovementioned considerations. In summary:

- 1) the pressure peak decays rapidly in space and time for a given energy;
- 2) in the first instants during the thermal energy deposition, the energy injected into the system will translate into a pressure increase stronger than the decay induced by the cylindrical problem;
- 3) as soon as the pressure wave propagates far enough from the beam axis, the slope of the pressure rise in time during deposition flattens, and eventually the pressure peak starts decreasing.

The only way to reach the shock regime for an observable time is thus to build up energy by increasing power instead of time. In the next two sections, examples of elastic-plastic and shock waves, generated in existing beam-impact test facilities and future accelerators, will be shown.

#### 4.3.1 Elastic and Plastic waves

The study of cylindrical elastic and plastic wave origination and propagation, as a consequence of a proton beam impact, was behind the *HRMT-14* test conceived in the HiRadMat facility on several materials adopted or under development for beam-intercepting devices [28].

The performed tests entailed the controlled impact of intense proton pulses on specimens made of six different materials. Inermet180 (tungsten heavy alloy with copper and nickel matrix), Glidcop AL-15 (dispersion-oxide-strengthened copper), pure molybdenum and three novel composites, namely Molybdenum-Copper-Diamond, Copper-Diamond and Molybdenum-Graphite. For a comprehensive characterization, experimental data were acquired relying on extensive embedded instrumentation (strain gauges, temperature and vacuum sensors) and on remote-acquisition devices (laser-Doppler vibrometer and high-speed camera).

Two different specimen shapes were chosen for each material (Figure 54): cylindrical disks (*type 1*) for medium intensity tests, to measure radially and axially propagating stress waves; cylinders with a half-moon cross section (*type 2*) for high intensity grazing impacts, allowing melting and spallation phenomena at the flat surface to be visualized and optically acquired. Specimens were arranged in two rows of six into a sample holder maintained under vacuum, to avoid sample oxidation and contamination to the external environment; each row contained up to 10 specimens. The proton beam is extracted from the SPS ring to the HiRadMat

facility, and the proton kinetic energy is equal to 440 GeV. The variable intensity on the two specimen shapes was achieved by acting on the number of proton bunches within the pulse structure (see Figure 39).

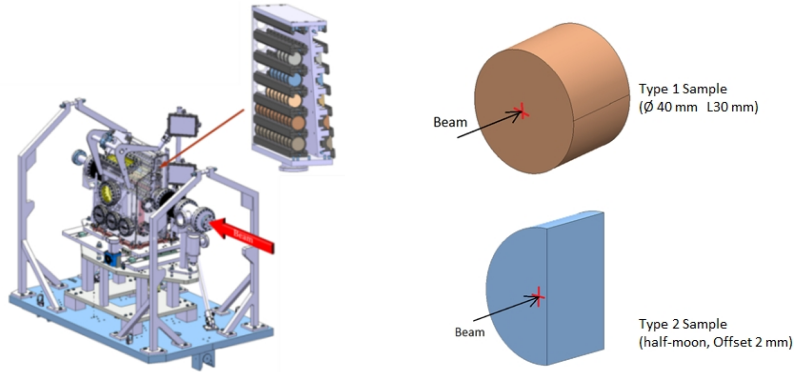


Figure 54. Left: HRMT-14 sample holder. Right: sample geometry.

We focus in this section on the medium intensity tests (*type 1* specimens). The instrumentation was extensively dedicated to the study of the cylindrical problem; the strain gauges were placed on the lateral surface to acquire hoop and axial strains, while the laser-Doppler vibrometer (LDV) measured the radial velocity profile. The use of the vibrometer added redundancy to the measurement, as the radial displacement  $u_r$ , which can be derived integrating the velocity profile, is also directly related to the hoop strain in, an axisymmetric problem, through the expression:

$$\varepsilon_c = \frac{u_r}{r} \quad (4.21)$$

This was of paramount importance, as the strain gauges suffered an electro-magnetic coupling with the beam particles, resulting in a high disturbance of the signal during the first microseconds after the beam impact. The vibrometer, on the other hand, was unaffected by this phenomenon, as it was placed in a shielded bunker, and allowed covering also that time window.

The numerical simulations performed for comparison with the acquired signal and optimization of the material models were done with Autodyn. While for medium intensity shots, described in this section, ANSYS would also have been appropriate, it would have not been suited to the description of the material response in the high intensity tests, where melting and spallation were expected. The same approach was therefore adopted for both scenarios. Good results in the

numerical/experimental benchmarking were obtained in particular for the high-density materials such as Inermet180, Glidcop AL-15 and molybdenum. In low-density composites, the intensity of the acquired signal was low and heavily disturbed by noise. This section focuses on the study of Inermet180, as an example of the dynamic response of a short cylinder under a quasi-instantaneous thermal pulse involving elastic and plastic wave generation.

In principle, the simulation can be done in two dimensions, under the axisymmetric hypothesis, as the Inermet180 target is a cylinder 30 mm long and 40 mm in diameter; however, the specimen supporting system consisted in graphite elements constraining the cylinder in four points (see Figure 55). Furthermore, some of the beam impacts were performed off-axis. The problem was therefore studied with a 3D model.

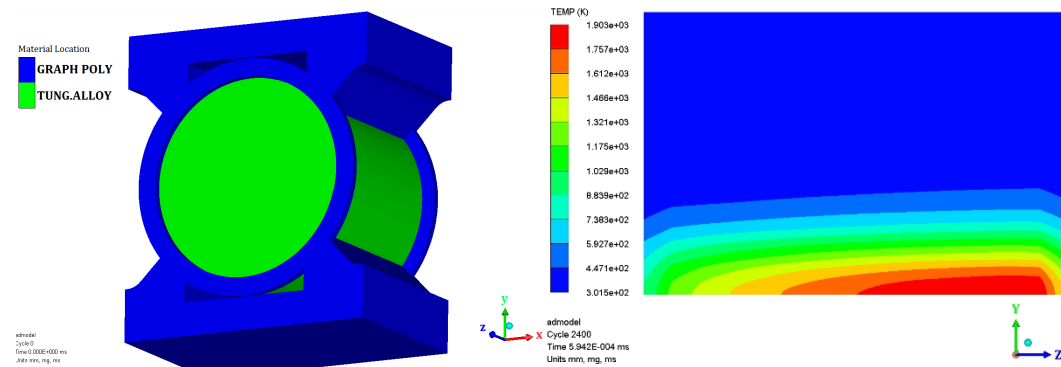


Figure 55. Left: geometry for the analysis. Note the graphite ring spacers which are used to separate adjacent samples on the same longitudinal array. Sample diameter is 40 mm and thickness 30 mm. Right: axial section view of the target ( $y$  here is the radius), temperature at the end of the thermal pulse. Beam is coming from the left. Inermet180 matrix melts at 1616 K.

Inermet180 is a heavy alloy produced by Plansee (DE), with volumetric composition W 95%, Ni 3.5%, Cu 1.5%. It is industrially preferred to pure tungsten for its high machinability; however, the presence of the low-melting matrix is an issue in terms of robustness to beam impact. Isostatic graphite was selected for the supports and spacers for its low shock impedance, which minimizes the wave transmission from the specimens to the structure (see section 4.4). The material models adopted in the simulations are reported for Inermet180 in Table 12, Table 13 and Figure 45, while details on the beam impact are given in Table 14. The EOS of pure tungsten was adapted to that of Inermet180 with the method reported in section 3.1.2, and the melting temperature imposed was that of the Cu-Ni matrix, above which the material loses its shear strength under tension.

Table 13: Properties of Inermet180 adopted in the simulations of HRMT-14 [29]. The fracture energy is used in the failure model to simulate the creation and propagation of a crack.

Equation of State	Strength model		Failure Model	
	Johnson-Cook		Hydrostatic Min. Pressure	
SESAME	$G$	140 GPa	$P_{min}$	-2.7 GPa
	$A$	715 MPa	Fracture Energy	515 J/m <sup>2</sup>
	$B$	177 MPa		
	$n$	0.12		
	$C$	0.016		
	$T_m$	1616 K		
	$\dot{\epsilon}_0$	1 s <sup>-1</sup>		

Table 14: Beam impact parameters for tests at medium (*type 1* specimens) and high intensity (*type 2*). This section focuses on the medium intensity tests.

	Medium intensity test	High intensity test
$E_k$ (GeV)	440	440
$t_d$ ( $\mu$ s)	0.6	1.8
$n_{tot}$ (protons)	$2.7 \times 10^{12}$	$9.5 \times 10^{12}$
$E_{tot}$ (kJ)	8.35	25.1
$E_{max}$ (kJ/cm <sup>3</sup> )	4.8	20.7
$\sigma_x, \sigma_y$ (mm)	1.4 $\times$ 2	1.9 $\times$ 1.9

The simulated specimen is the second Inermet180 in an array of three (*M6.2*), as it is the most loaded. It is interesting to analyse the material state at the end of the deposition. As shown in Figure 55 (right), a significant internal portion of the matrix is molten, but the solid surroundings contain the core expansion and deform plastically (Figure 56). Eventually, a bulge is formed on the external surface.

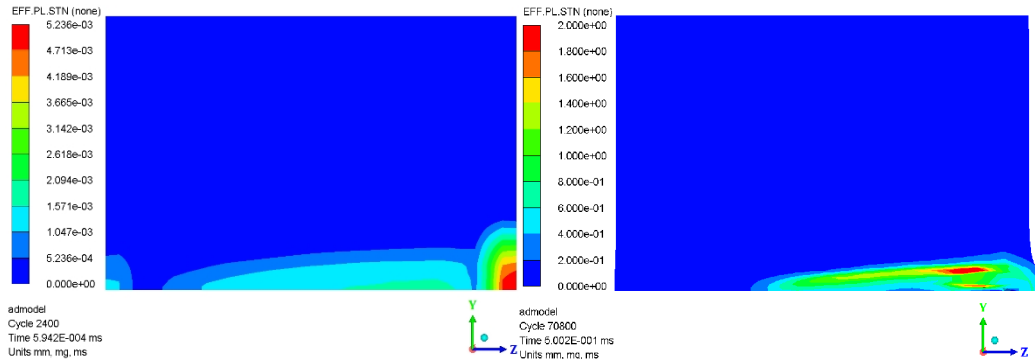


Figure 56. Left: equivalent plastic strain at the end of the thermal pulse on the *M6.2* Inermet180 sample. Right: equivalent plastic strain at  $t=500\mu\text{s}$ . Deformations are in real scale.

While the energy involved in the impact is significant, the pressure wave originated around the beam axis does not have an amplitude sufficient for the material to reach the shock regime. As discussed earlier in this section, this is due to the fact that the distance already travelled by the wave during the deposition is relevant, and the contribution in terms of pressure of successive impacting bunches is not linear but flattens with time (Figure 57), before eventually decreasing as the wave reduces in amplitude with the square root of the radial propagation. In Figure 57, left, it is interesting to note that, while the two elements at the longitudinal coordinate  $z = 22.5$  mm (*red*) and 28.5 mm (*blue*) receive the same energy amount per bunch, their pressure per bunch is close to constant only for one third of the energy deposition time. The blue element, closer to the flat surface, experiences a decrease of the pressure ramp due, on top of the radial decay, to the rarefaction wave that originates at the flat face. The blue element at the end of the deposition shows a pressure even lower than the green one, which is much upstream and receives 20% less in energy per bunch.

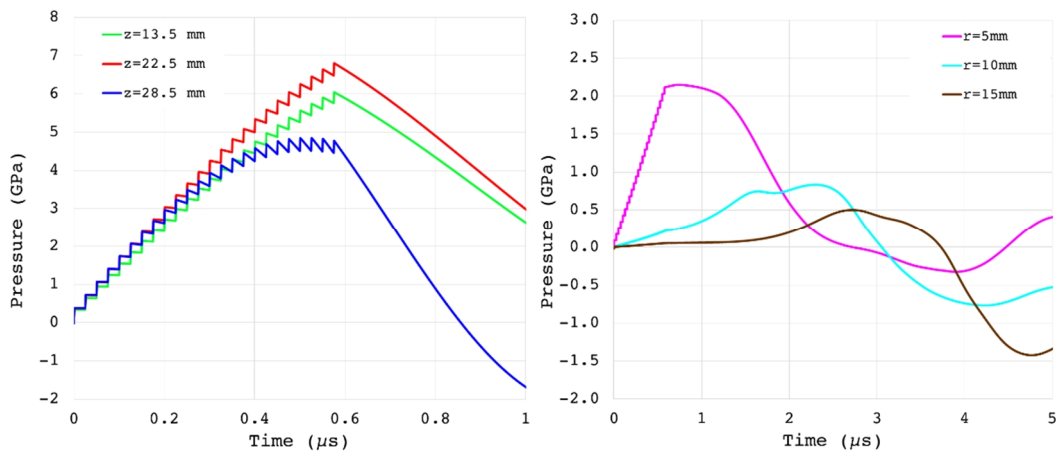


Figure 57. Left: pressure during the thermal pulse along the target axis ( $r=0$ ), for elements at different  $z$ . Right: pressure on three elements at  $z=13.5\text{mm}$ , for three different radial coordinates.

The fact that the material is just in a plastic domain rather than in a shock regime is highlighted in Figure 57, right. During the wave propagation, there is no compaction of the front with formation of a steep pressure discontinuity. The wave, on the other hand, smoothly spreads over the volume, with a dispersion mechanism similar to that shown in space in Figure 16. Another characteristic of the shock phenomenon is that it requires the origination of a supersonic wave which catches the plastic waves ahead and compacts the front. This condition is necessary but not sufficient, as the wave velocity can be higher than the initial speed of sound without reaching the shock critical level (see Figure 21). However, in the problem under examination, the velocity of the wave remains close to  $c_0$ , which is 5063 m/s for Inermet180, and is slightly lower than that for elements plastically deformed, where the ratio  $dp/d\varepsilon$  is lower than the P-wave modulus  $M$  (Figure 58).

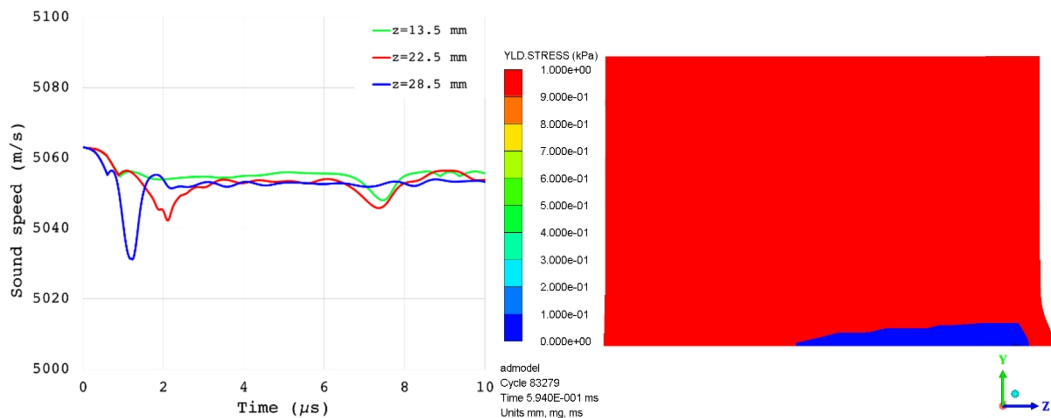


Figure 58. Left: sound speed calculated on three elements at  $r=0$ , with different  $z$ . Right: flow stress at the end of the simulation ( $t=594\mu\text{s}$ ) saturated at 1 kPa to show the molten material ( $\sigma_y=0$ ).

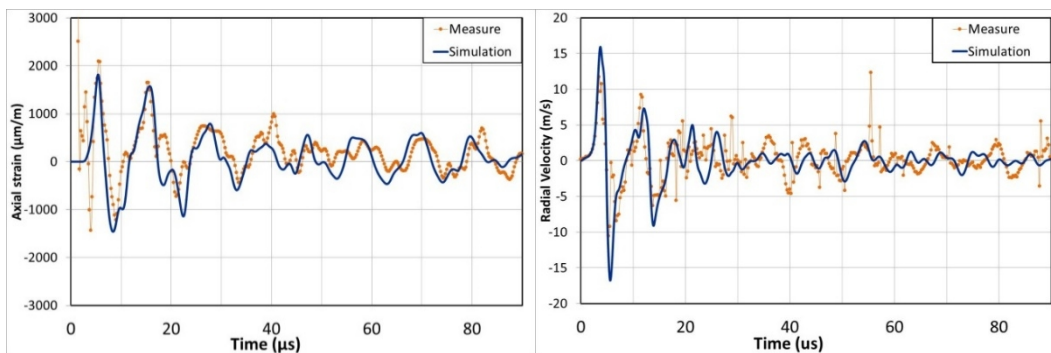


Figure 59. Left: Axial strain measurement with strain gauge at  $r=20\text{mm}$ ,  $L=15\text{mm}$  vs. simulation. Right: Radial velocity measurement with LDV at  $r=20\text{mm}$ ,  $L=15\text{mm}$  vs. simulation.

Figure 59 shows the benchmarking between the experimental acquisition, with strain gauges and LDV, and the numerical analysis. Results are in good accordance, proving that the EOS and strength model adopted for the material are appropriate to reproduce this quasi-instantaneous heating scenario.

As a general consideration on the experienced state reached on the material, it can be observed that even though no shock waves are involved, the temperatures and pressures achieved are quite relevant. However, the rather simple failure model does not predict for this scenario a material failure, as the only elements with flow stress equal to zero at the end of the simulation are those in a molten state (Figure 58, right), which would eventually re-solidify after sample cooling. In 2015, the activation of the sample holder reached levels low enough to allow dismounting of the test bench and extraction of the specimens for examinations. Figure 60 shows views of the simulated *M6.2* Inermet180 specimen, which indeed presents a local failure at the downstream face, were the solicitation was maximum (Figure 56). The damage is not extensive, but it demonstrates nevertheless that the simple hydrodynamic pressure failure model is not sufficient to predict with high precision the material failure behaviour. The spall strength in the model is in fact constant, while according to models such as Grady's (see section 3.3.2) it is also related to density and flow stress, which are updated at every step during the simulation by EOS and strength model. On top of that, according to Grady, spallation depends on the type of failure, which is associated to the material ductility and thus temperature. The author of this thesis considers Grady spall model as a good candidate for reproducing the fracture behaviour of Inermet180 under particle beam impact.



Figure 60. Upstream (left) and downstream (right) faces of the Inermet180 *M6.2* specimen impacted by  $2.7 \times 10^{12}$  protons at 440 GeV during the HRMT-14 experiment. The droplets on the upstream face come from the near specimen *M6.1*, which was NEG-coated. Coating melted and deposited on *M6.2*.

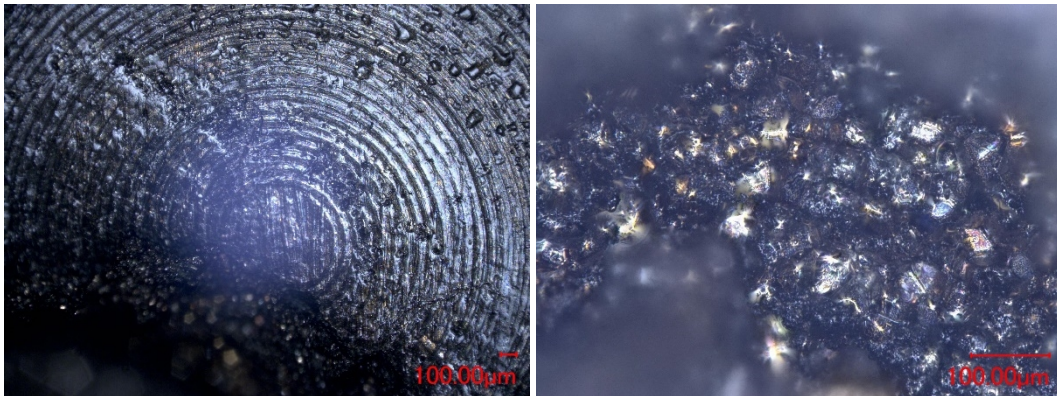


Figure 61. Optical microscope observations of the Inermet180 *M6.2* specimen. Left: upstream face 100x. Right: downstream face 500x, with focus on the hole region.

Further considerations on the failure of materials by spallation under localized quasi-static heating are given in section 4.4, where a dedicated SPH method is adopted for the simulation of this phenomenon.

### 4.3.2 Shock waves

In spite of the nature of loads, geometry and boundary conditions, which naturally tend to disperse the wave profile, a shock regime under particle beam impact can theoretically be achieved, provided that the energy and energy density induced by the beam are sufficiently high. The shock critical threshold is hard to achieve in

current experimental facilities. Even in HiRadMat, which provides the most energetic experimental beam (440 GeV), the pressure wave always disperses during its propagation, as it decays with the radius and, generating plasticity, the sound speed decreases below  $c_0$ . On the other hand, in new accelerators under construction, such the HL-LHC [30] and the FCC [31], the pressure reached on the material during a beam impact may be high enough to trigger a shock wave.

Let us take, for example, the case of the FCC, which in its hadron configuration will accelerate particles up to a kinetic energy of 50 TeV. A simulation was run with Autodyn with a 2D model to observe the material response in case of a single FCC proton bunch on an OFE-copper slender cylinder, with length 1 m and diameter 8 mm. The beam parameters and material models are reported in Table 15. One can notice that the energy and energy density on the target are one order of magnitude higher than the case treated in section 4.3.1, and all the load is deposited in a time which is three orders of magnitude shorter.

Table 15: Material models [32],[33] and beam parameters for the impact of an FCC proton bunch on an OFE-Copper target 1 m long and 8 mm in diameter. The Fluka maps were kindly provided by Y. Nie.

EOS	Strength Model		Failure Model		Beam Parameters	
<i>SESAME 3320</i>	<i>Johnson-Cook</i>		<i>Johnson-Cook</i>		$E_k$	50 TeV
	$G$	46 GPa	$D_1$	0.54	$t_d$	0.5 ns
	$A$	90 MPa	$D_2$	4.89	$n_{tot}$	$2.7 \times 10^{12}$ p
	$B$	292 MPa	$D_3$	-3.03	$E_{tot}$	230 kJ
	$n$	0.31	$D_4$	0.014	$E_{max}$	310 kJ/cm <sup>3</sup>
	$C$	0.025	$D_5$	1.12	$\sigma_x, \sigma_y$	0.1×0.1 mm <sup>2</sup>
	$T_m$	1356 K	$T_m$	1356 K		
	$\dot{\epsilon}_0$	1 s <sup>-1</sup>	$\dot{\epsilon}_0$	1 s <sup>-1</sup>		

The intense energy deposited induces extreme conditions of pressure and energy on the target, with extensive generation of plasma (Figure 62).

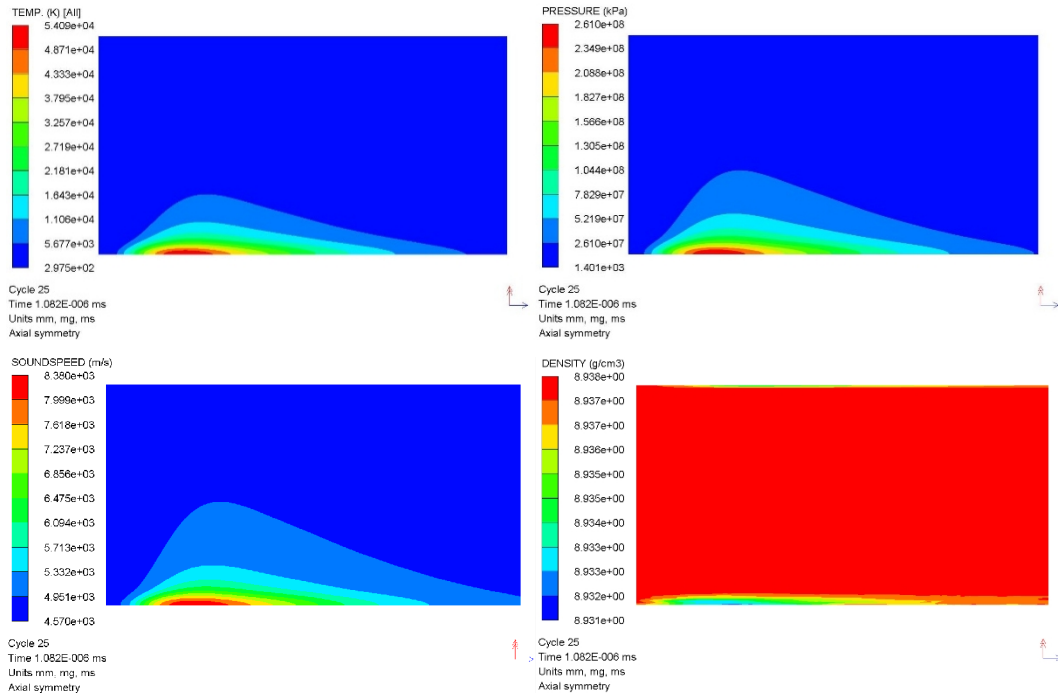


Figure 62. Temperature (top left), pressure (top right), sound speed (bottom left) and density (bottom right) on the cylinder at  $t=1\text{ns}$ . 2D axisymmetric model. The radial coordinate is magnified for the sake of clarity.

The material response is shown in Figure 63. Because of the energy deposition entailing a sudden temperature increase over almost the entire material volume, differently from a mechanical shock there is not a single irrotational wave propagating from the impacted point, but a package of waves propagating at different speed from all the points of the structure towards the external surface. In the region (A), the material is in the elastic domain, and the wave propagates at the speed of sound  $c_0$ , which is 4688 m/s for OFE-copper in the uniaxial strain state. This wave is analogous to the elastic precursor in a mechanical shock. Above  $\sigma_{HEL}$ , the material plasticizes and the wave travels slower than the initial speed of sound, until the region (B) where the wave is supersonic, reaching a peak velocity of propagation of 8380 m/s (Figure 62). In the region (C), the material is in the isentropic release phase behind the shock front; at sufficiently high times, in theory a rarefaction wave would follow the compressive one, but in this scenario the material core is at the plasma state, and cannot sustain any tensile loads, with micro-spallation (and thus failure) occurring. In the region which experienced a change of phase, the hydrodynamic formulation of the shock scenario is perfectly suitable to the description of the problem, as the deviatoric component of the stress is null and the material behaves like a fluid. The velocity of the wave here assumes

a direct dependence on the bulk modulus, according to the third equation of the system (2.12).

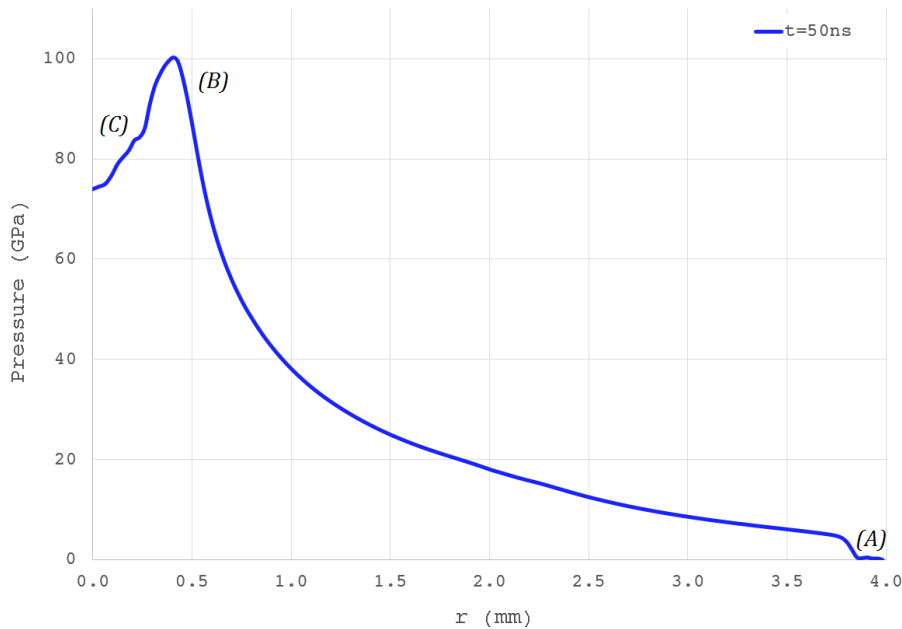


Figure 63. Pressure wave along the radius at  $t=50\text{ns}$ .

The wave at the impact position, which is faster of the plastic waves ahead, catches them up, compacting the front. The material steepens up, reaching the shock condition. Of course, as the wave is cylindrical, there is at the same time a decrease of the wave amplitude, which is mostly due to the radial decay, on top of dispersive and dissipative mechanisms. The front compaction at increasing times can be seen in space in Figure 64, left. Note the discontinuity visible even in spite of the magnified radial coordinate, with the pressure changing abruptly by tens of GPa in  $0.1\text{--}0.2\text{ mm}^{15}$ . Also, it is interesting to observe the change in slope in the material area close to the external surface, after having been reached by plastic waves preceding the shock front. With the arrival of the shock front, the slope of such plastic waves increases, reaching and then surpassing the initial sound speed.

<sup>15</sup> In an ideal world, the discontinuity would be represented by a line orthogonal to the direction of propagation in the pressure/coordinate diagram.

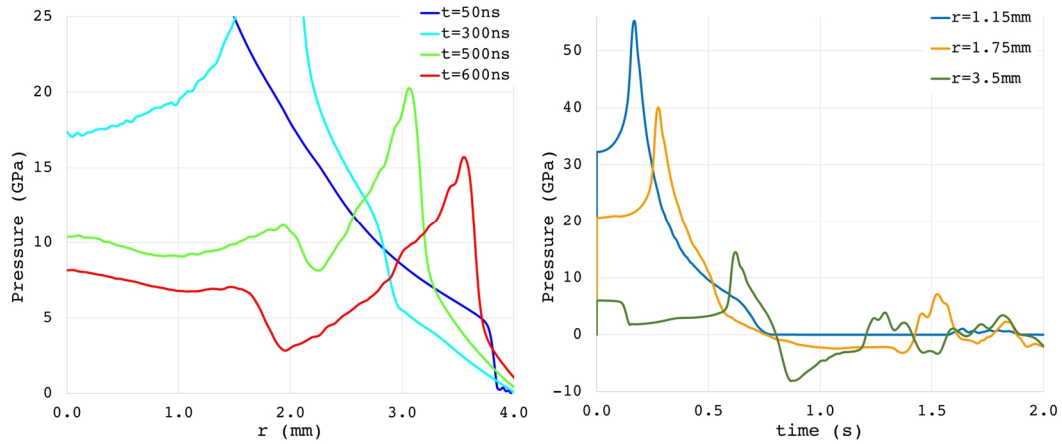


Figure 64. Left: pressure wave along the radius, for  $z=220\text{mm}$ , at different time instants. Right: pressure during time on three elements with  $z=220\text{mm}$  and different radial coordinate.

The same phenomenon of front compaction can be visualized also in the time coordinate in Figure 64, right. In this case, one should look at the rise time, comparing it for example to the scenario of elastic-plastic waves shown in Figure 57 to evaluate the different material response. Concerning Figure 64, right, it is worth pointing out that the element at  $r = 3.5\text{mm}$  experiences, after the thermal pulse, a first pressure decrease after about 200 ns, given by the relaxation wave originated at the free surface; this effect is counteracted by the stronger and stronger plastic waves coming from the material hot core, until the arrival of the shock front.

The propagation of the pressure wave and the changes in pressure induced by the beam impact are shown in Figure 65 and Figure 66.

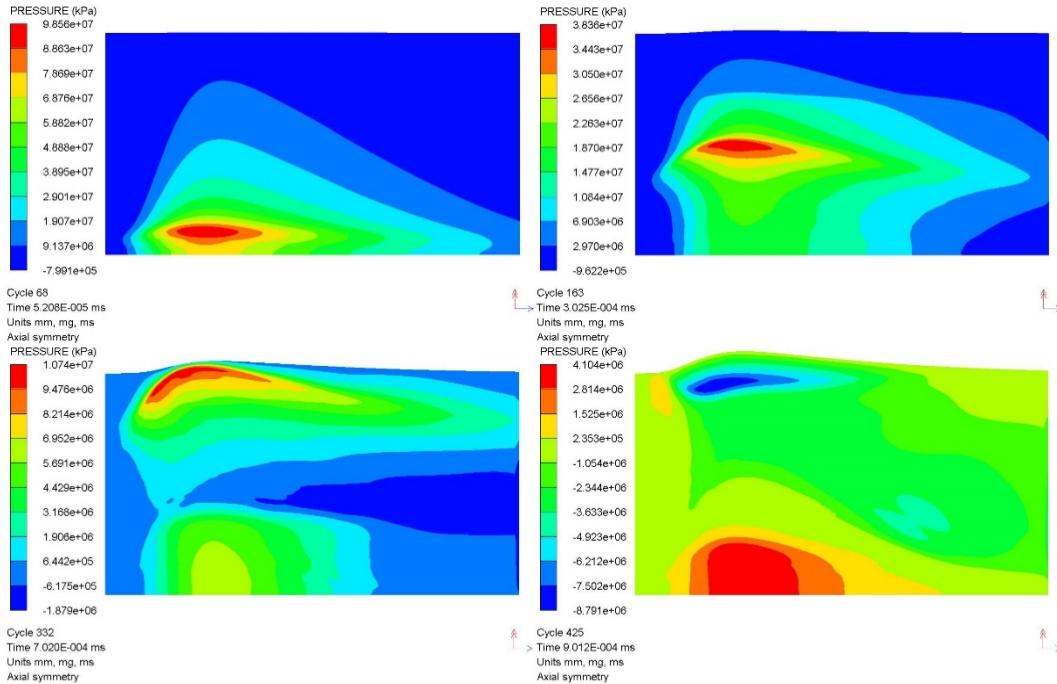


Figure 65. Propagation of the pressure wave inside the cylinder, with reflection to the free surface. 2D axysymmetric model. The radial coordinate is magnified for the sake of clarity.

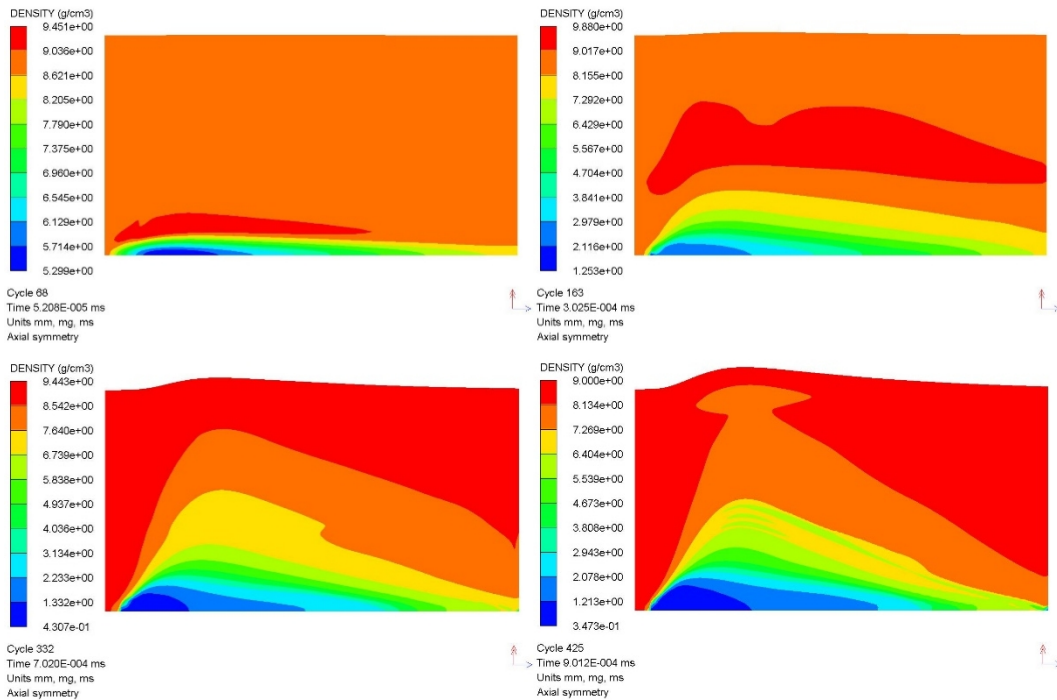


Figure 66. Density change induced by the wave propagation. 2D axysymmetric model. The radial coordinate is magnified for the sake of clarity. Note the low density value in correspondence of the beam axis, which triggers the hydrodynamic tunnelling (see section 4.6).

#### 4.4 Stress wave interface interactions

The transmission and reflection of stress waves through interfaces is very important in the study of the possible consequences of a quasi-instantaneous localized heating. Spallation at the free surface, for example, is directly related to the behaviour of the wave at the interface between the impacted material and vacuum or air. Moreover, engineering components are rarely monolithic: in the case of inhomogeneous, multi-material structures, the wave will transmit from the impacted material to the surrounding elements, inducing dynamic stresses on them.

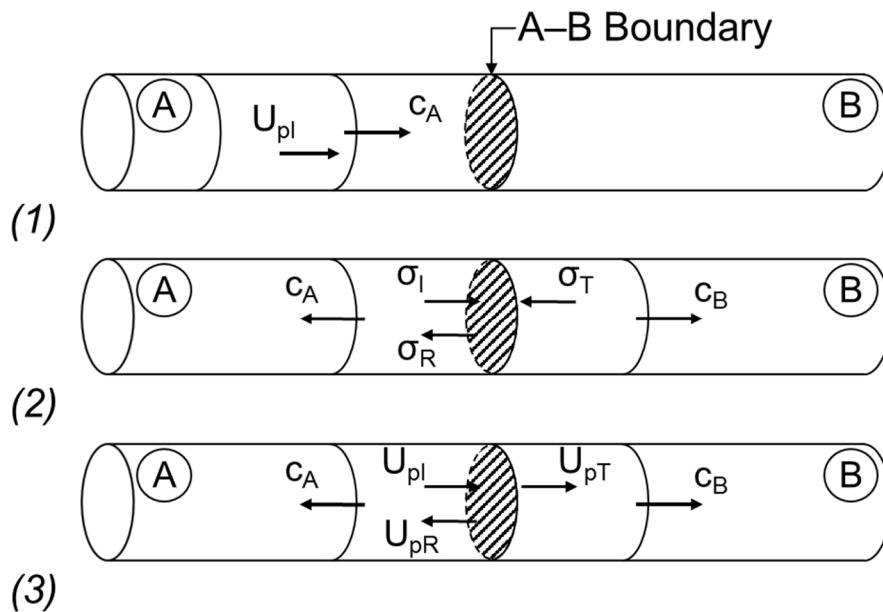


Figure 67. Longitudinal wave propagating from material *A* to material *B*. (1): wave propagation before the interface; (2),(3): at the interface, the wave is partly reflected and partly transmitted, with direction of stress and particle velocity depicted for the case  $Z_A > Z_B$ .

In the linear elastic hypothesis, the amplitude and sign of the incident, transmitted and reflected waves at an interface can be easily calculated. In the case of a 1D problem (Figure 67), the conservation of momentum (2.23) can be written as:

$$\sigma = \rho c U_p \quad (4.22)$$

When the wave travelling through the material *A* encounters an interface with a material *B*, the incident wave will decompose into a reflected and a transmitted component, and for equilibrium:

$$\sigma_I + \sigma_R = \sigma_T \quad (4.23)$$

where  $\sigma_I$ ,  $\sigma_R$  and  $\sigma_T$  are the stresses at the interface associated with the incident, reflected and transmitted waves. Also, for the continuity at the interface, no gaps can be created and matter cannot superimpose itself, and:

$$U_{pI} + U_{pR} = U_{pT} \quad (4.24)$$

where  $U_{pI}$ ,  $U_{pR}$  and  $U_{pT}$  are the particle velocities induced by the incident, reflected and transmitted waves. The particle velocity, according to Eq. (4.22), can be expressed as:

$$\begin{aligned} U_{pI} &= \frac{\sigma_I}{\rho_A c_A} \\ U_{pT} &= \frac{\sigma_T}{\rho_B c_B} \\ U_{pR} &= -\frac{\sigma_R}{\rho_A c_A} \end{aligned} \quad (4.25)$$

where  $c_A$  and  $c_B$  are the wave velocities in the two materials. The reflected particle velocity has a negative sign because a positive stress, when the impedance of material A is higher than that of material B (more on this later), causes a negative particle velocity upon reflection. Combining Eqs. (4.25) and (4.24), one can express the relation in terms of stress:

$$\frac{\sigma_I}{\rho_A c_A} - \frac{\sigma_R}{\rho_A c_A} = \frac{\sigma_T}{\rho_B c_B} \quad (4.26)$$

which, combined with Eq. (4.23), gives as results:

$$\begin{aligned} \frac{\sigma_T}{\sigma_I} &= \frac{2\rho_B c_B}{\rho_B c_B + \rho_A c_A} = \frac{2Z_B}{Z_B + Z_A} \\ \frac{\sigma_R}{\sigma_I} &= \frac{\rho_B c_B - \rho_A c_A}{\rho_B c_B + \rho_A c_A} = \frac{Z_B - Z_A}{Z_B + Z_A} \end{aligned} \quad (4.27)$$

The quantity  $Z$  has already been introduced in section 2.3.1 and is known as *shock impedance*. It is clear that  $Z$  is the key parameter in the determination of the amplitude of transmitted and reflected pulses. When  $Z_B > Z_A$ , the sign of incident and reflected pulse is the same, while if  $Z_B < Z_A$  the reflected pulse is of an opposite sign of the incident pulse. In the two limit conditions of incident wave on a free surface ( $E, c = 0$ ) and on a rigid boundary ( $E, c = \infty$ ), the results are:

$$\begin{aligned} \text{Free surface: } \frac{\sigma_T}{\sigma_I} &= 0; \frac{\sigma_R}{\sigma_I} = -1 \\ \text{Rigid boundary: } \frac{\sigma_T}{\sigma_I} &= 2; \frac{\sigma_R}{\sigma_I} = 1 \end{aligned} \tag{4.28}$$

For this reason, a compressive wave reaching a free surface will turn into a rarefaction wave, potentially generating spallation in the component. Shock impedance values for materials often adopted in particle accelerators are given in Table 16.

Table 16: Shock impedance for different materials. The sound speed is calculated in uniaxial stress conditions.

<b>Material</b>	<b>Shock Impedance (MPa·s/m)</b>
OFE copper	32.3
CuNi 90-10	35.3
Isostatic graphite	4.5
304 stainless steel	39.3
Molybdenum	58.1
Al 6082-T4	13.7
W alloy Inermet180	80.5
Titanium	22.8
Copper-Diamond	29.1
Molybdenum-Graphite	4.2

It now appears evident why isostatic graphite was adopted for the supports of the HRMT-14 specimens described in section 4.3.1. The shock impedance of this material is so low that it allowed studying the specimens in almost free conditions,

as the wave generated by the beam impact is mostly reflected in the material under test. Moreover, thanks to the low shock impedance, the amplitude of the wave transmitted into graphite is very small, minimizing the risk of support failure.

An interesting example of advantageous use of low shock impedance materials at CERN LHC is the configuration adopted in tertiary collimators [34]. These structures, which are described in detail in Chapter 5, are required to be very dense, as they are used as particle absorbers, in order to protect delicate structures such as the superconductive magnets. The active elements are two movable girders, known as *jaws*, which approach the beam axis intercepting the out-of-trajectory particles (see Figure 68).

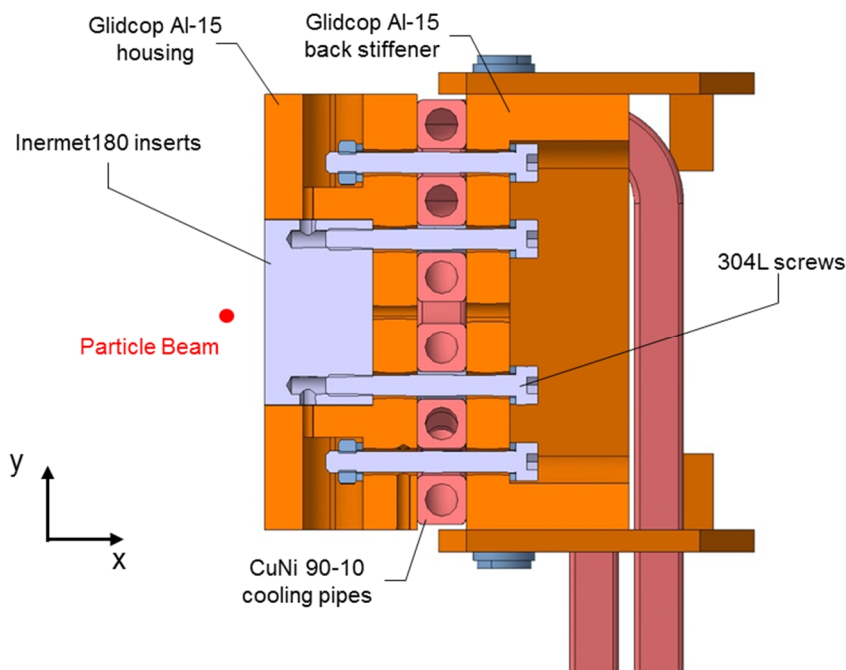


Figure 68. Section view of the tertiary collimator jaw. The beam travels along the direction  $z$ , orthogonal to the  $XY$  plane shown.

The high density requirement is fulfilled by the use of Inermet180 inserts, encapsulated into a housing in Glidcop Al-15, an alloy with 99.7% Cu and 0.3%  $\text{Al}_2\text{O}_3$ , with the same thermophysical properties of copper at room temperature. The housing is brazed to a cooling circuit with copper-nickel pipes, and a Glidcop Al-15 back stiffener enhances the moment of inertia of the structure. The collimator is installed in a vacuum tank, with circular flanges to connect it to the beam pipe. Ultra-high vacuum is in fact required in particle accelerators, to avoid collisions between the beam and air molecules.

In an accidental case, the particle beam could potentially impact the Inermet180 inserts, with possible failure of the component [35]. Replacing a collimator, although not trivial, is not an operation with major impact on the LHC operation; however, a fracture of the cooling pipes, with water flood into the whole vacuum sector, is an accident which would imply a long stop of the accelerator. In this sense, the jaw configuration is beneficial: the wave produced on Inermet180 by the impact would first decay in amplitude along its radial propagation, and would then only partially transmit to the copper alloy housing due to the high Inermet180/Glidcop impedance mismatch, with less risks to the cooling pipes.

## 4.5 Spallation

As already discussed in the previous chapters, spallation takes place when a compressive wave generated during a dynamic event turns into a tensile wave with amplitude higher than the spall strength of the material. In the case of a cylindrical problem such as that induced by a particle beam impact, spallation can be expected at two locations:

- at the material core, where the first compressive wave is followed, at the end of the thermal pulse, by a rarefaction wave;
- at the interface between the impacted material and a material with a lower shock impedance, with the compressive wave reflected and turning into tensile wave; the case of the compressive wave reaching a free surface is included in this scenario.

If the spalling material is still in a solid state, it will produce one or more *spalls*, ejected out of the free surface to the surroundings. This scenario is called by some authors *micro-jetting* [7]. If the material is in a liquid phase, it will not be able to sustain any tensile load, and the tensile wave will produce a spray of microscopic particles, in a process similar to cavitation which is known as *micro-spallation*. Under beam impact, this phenomenon usually takes place at the beam axis, as the energy density in modern accelerators is often high enough to locally melt the material.

The study of material spallation involves the simulation and measurement of the debris cascade. Typical data of interest are the spall velocity, divergence and size. It is evident that a numerical study of these parameters is not possible with a classical Lagrangian mesh. This method in fact can be used only to evaluate the state of the main impacted body, complementing the failure criterion with an

erosion model aiming at the reproduction of the fracture surface. With erosion, however, an element undergoing failure is eliminated from the analysis, and not computed anymore. The simulation of particle detachment, and the monitoring of the ejected particle, can be performed in Autodyn with a *Smoothed-Particle Hydrodynamics* technique (SPH). In this computational method, the material is modelled by discrete elements (particles) with a spatial distance of interaction, known as *smoothing length*, over which their properties are weighted by a kernel function. For example, the material density in a given position  $x$  is:

$$\rho(x) = \sum_{j=1}^n m_j W(|x - x_j|, h) \quad (4.29)$$

where  $m_j$  is the mass of the  $j$ -th particle,  $W$  is the kernel function and  $h$  is the smoothing length. The method typically requires models with an elevate number of elements; a common practice is therefore to model with SPH elements only the volume potentially affected by spallation, whereas the surrounding bodies can be modelled with Lagrangian elements. The two different meshes can then be linked through constraint equations at the interface, imposing material continuity, equilibrium and momentum conservation, to reproduce reflection and transmission of the waves.

The combined SPH/Lagrangian method was implemented in Autodyn for the simulation of high energy beam impacts on HRMT-14 *type 2* samples (see section 4.3.1). We provide here results for the *H6.2* sample, which is the second in an array of three Inermet180 specimens; the material constitutive models and beam parameters are reported in Table 13 and Table 14, while the numerical model is shown in Figure 69.

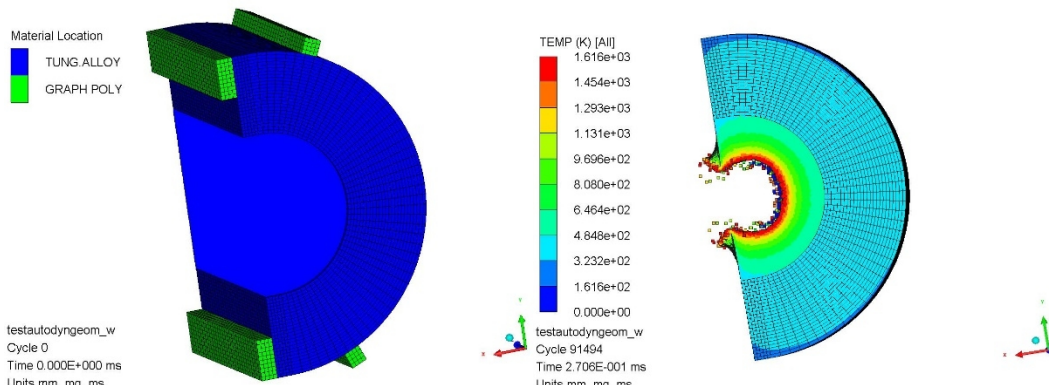


Figure 69. Left: geometry for the analysis. Diameter is 40 mm, length 30 mm; the samples have a half-moon shape, with the flat face offset by 2 mm with respect to a perfect half-cylinder. Right: *H6.2* sample at the end of the simulation. The hole created by the impact is elliptical, with vertical axis 8.8mm and horizontal axis 7mm. The plastic deformation on the free surface also creates two “lips” spaced vertically by 10.1mm.

The beam impact against the Inermet180 target was registered with a high-speed camera; the camera acquisition frames are shown in Figure 12. It can be observed that the debris cascade is mostly made of molten particles emitting a relevant lighting power, with bigger (and darker) solid spalls ejected together with the molten material. The velocity of the cascade front was measured evaluating the position at each frame, by means of a graduated background. As shown in Figure 70, the ejected material front shape and velocity are both consistent with the high-speed camera measurements. The acquired velocity of the fragment front has been estimated in about 275 m/s, well matching the simulated velocity of 316 m/s (difference is about 15%).

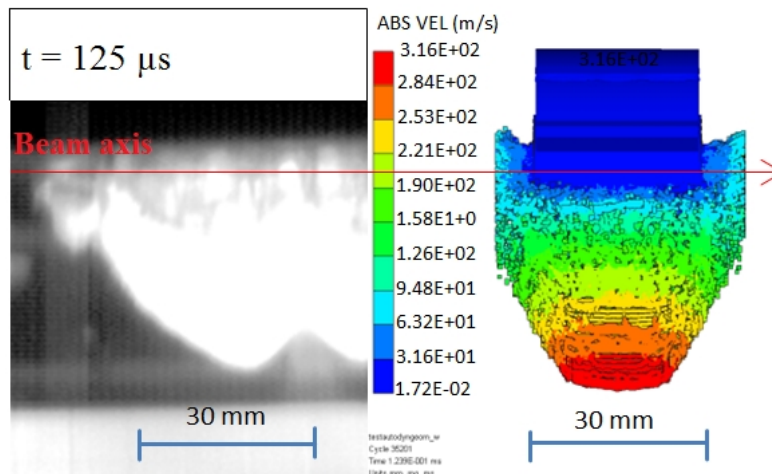


Figure 70. Comparison between acquired image and simulation of *H6.2* sample 125µs after the impact. On top of the specimen *H6.2*, in the camera acquisition also *H6.1* (first from the left) and *H6.3* (first from the right) are partially visible.

In 2015, during the post-mortem analyses, observations were done also on the *H6.2* specimen to compare it with the simulation results. The simulation of the sample post-impact is shown in Figure 69 and can be benchmarked against the visual inspection depicted in Figure 71. As already seen for the same model in section 4.3.1, the simulation slightly underestimates the extent of damage produced on the specimen. On top of the considerations on the failure model already made in section 4.3.1, it is worth adding that the shape of the crater borders in the simulation implies higher plasticity than what observed experimentally. The experimental fracture surface seems more related to a brittle failure; this mechanism was observed on Inermet180 in recent works [36],[37], with the material remaining relatively brittle under dynamic loading at temperatures above the brittle-to-ductile transition temperature of tungsten. For comparison, above 400 °C, the ultimate strain of Inermet180 tested at a strain rate of  $10^3 \text{ s}^{-1}$  is 15%, compared with pure tungsten, which fails at strains above 60% in the same conditions.

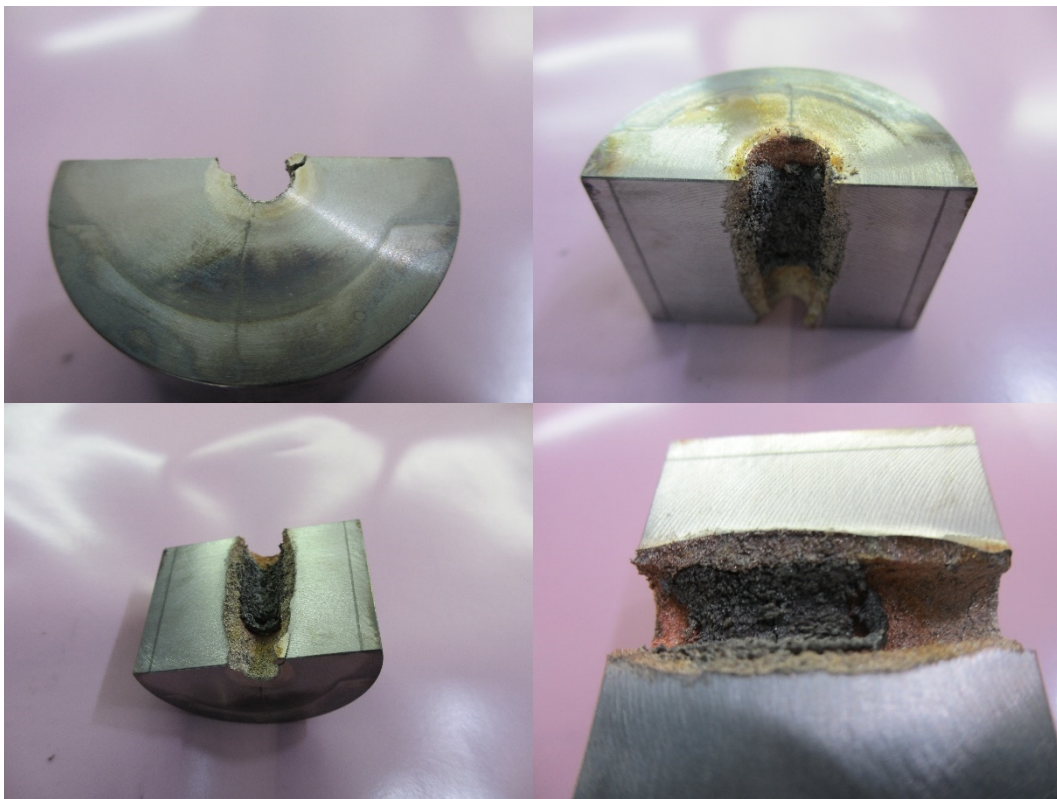


Figure 71. Views of the *H6.2* Inermet180 specimen after extraction from the HRMT-14 test bench. The crater created by the impact is elliptical, with vertical axis 9.4mm and horizontal axis 8.7mm. The plastic deformation on the free surface also creates two “lips” spaced vertically by 13.3mm.

## 4.6 Hydrodynamic tunneling

Earlier in this chapter, we have seen that the simulation of a particle beam impact requires two steps of analysis: in the first one, the deposited energy on the body is evaluated by means of a particle transport code such as FLUKA, while in the second part, the 3D map of internal heat generation is loaded as input for the thermomechanical FE analysis. The analysis performed with FLUKA is normalized to one proton and must then be scaled by the pulse intensity. In case more proton bunches are impacting on the target, the FLUKA map is typically not updated at every impact, as the material at short time scales is supposed to remain close to the initial conditions of density and radiation length.

This hypothesis may fail at higher time scales and energy densities. What happens in this case is that, during the deposition, the change of density produced by compressive and rarefaction waves propagating from the impacted volume becomes relevant, and the energy deposited by subsequent bunches starts to be inaccurate. In the examples shown in this chapter, the density change is mostly irrelevant in all cases but the FCC beam impact on copper (section 4.3.2). The density profile at different instants is shown in Figure 66, while Figure 72 depicts the density history during the analysis for three elements on the beam axis.

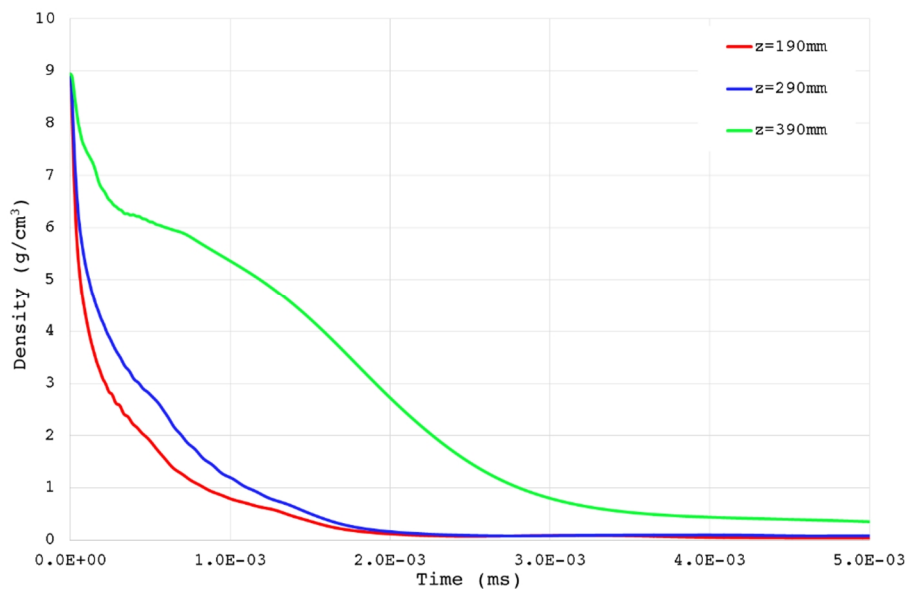


Figure 72. Density history in the case of 1 FCC bunch impacting on a copper target. Simulation parameters reported in section 4.3.2. Three elements along the axis ( $r=0$ ) are shown.

In the case under examination, the pulse is made of one bunch only, but after 50 ns the density change is already 40%. This means that in the FCC scenario, a

new FLUKA map would be required after one bunch, and the energy deposition should be recomputed, to be used as an input for the second bunch in the FEA. A coupling FLUKA/FEA is in this case necessary. Scapin and colleagues performed a soft coupling [38] between FLUKA and LS-Dyna [39], showing that in the case of LHC beam at 7 TeV impacting on tungsten, the difference with respect to the uncoupled analysis is relevant after the first 10 impacting bunches.

With respect to Figure 66 and Figure 72, it is important to remark that the density reduction is related to the change of phase of the material; however, even in the solid state, a rarefaction wave grows at the impacted volume and follows the compressive wave. In any case, the result is a decrease in density, such that subsequent bunches impact on a less dense material, penetrating more and more longitudinally in the matter. For this reason, the phenomenon was called by Tahir and colleagues *hydrodynamic tunneling* [27]. Hydrodynamic tunneling will have to be taken in consideration during the design of high-energy future accelerator beam intercepting devices, and in particular dumps, as neglecting this behaviour would lead to an underestimation of the length necessary to fully absorb the particle beam.

## 4.7 Glossary

Symbols are listed in chronological order with respect to their appearance in the text.

Symbol	Definition	SI unit
$n_p$	Beam particle density	$\text{m}^{-3}$
$n_{max}$	Maximum beam particle density	$\text{m}^{-3}$
$r$	Radial coordinate	m
$\sigma$	Variance of the Gaussian distribution	m
$t_d$	Energy deposition time	s
$L_b$	Beam length	m
$v$	Beam velocity	$\text{m}\cdot\text{s}^{-1}$
$c$	Speed of light in vacuum	$\text{m}\cdot\text{s}^{-1}$
$t_{d,i}$	Time of deposition of i-th bunch	s

$\Delta t$	Bunch spacing	s
$N_b$	Number of bunches	–
$U$	Radial velocity of the wave	m·s <sup>-1</sup>
$U_z$	Axial velocity of the wave	m·s <sup>-1</sup>
$p$	Pressure	Pa
$\rho$	Density	kg·m <sup>-3</sup>
$T_c$	Liquid/gas critical temperature	K
$c$	Speed of sound	m·s <sup>-1</sup>
$E$	Young's modulus	Pa
$\sigma$	Stress	Pa
$\varepsilon$	Strain	–
$c$	Initial sound speed	m·s <sup>-1</sup>
$\sigma_{ref}$	Average axial stress of a rod impacted by a particle beam	Pa
$\Delta T_F$	Temperature increase at steady-state	K
$c_g$	Group velocity	m·s <sup>-1</sup>
$c_p$	Phase velocity	m·s <sup>-1</sup>
$\nu$	Poisson's ratio	–
$\Lambda$	Wave length	m
$x$	Horizontal coordinate	m
$y$	Vertical coordinate	m
$z$	Longitudinal coordinate	m
$L$	Length of the bar	m
$h$	Height of the bar	m

---

$w$	Width of the bar	m
$K$	Bulk modulus	Pa
$G$	Shear modulus	Pa
$E_k$	Kinetic energy	J
$N_{tot}$	Beam intensity	–
$T_z$	Axial wave period	s
$E$	Energy density	J·m <sup>-3</sup>
$\rho_0$	Initial density	kg·m <sup>-3</sup>
$\gamma_0$	Initial Grüneisen coefficient	–
$\alpha$	Coefficient of thermal expansion	K <sup>-1</sup>
$c_v$	Specific heat capacity at constant volume	J·kg <sup>-1</sup> ·K <sup>-1</sup>
$T_y$	Period of the transversal wave	s
$\lambda_y$	Frequency of the transversal wave	Hz
$v_y$	Particle velocity in y direction	m·s <sup>-1</sup>
$v_z$	Particle velocity in z direction	m·s <sup>-1</sup>
$\eta$	Eccentricity	m
$R$	Radius	m
$\lambda_f$	Frequency of the flexural wave	Hz
$\beta_f$	Boundary coefficient	–
$I_x$	Moment of inertia around the $x$ axis	m <sup>4</sup>
$A$	Bar section	m <sup>2</sup>
$L$	Bar length	m
$T_f$	Period of the flexural wave	s

---

$c'$	Velocity of the flexural wave	$\text{m}\cdot\text{s}^{-1}$
$u$	Displacement in $x$ direction	$\text{m}$
$c_C$	Speed of sound in a cylinder	$\text{m}\cdot\text{s}^{-1}$
$M$	Modulus of a longitudinal wave in an unbounded medium	$\text{Pa}$
$c_D$	Speed of sound in a disk	$\text{m}\cdot\text{s}^{-1}$
$M$	Equivalent	$\text{m}^4$
$\Phi$	Velocity potential	$\text{m}^2\cdot\text{s}^{-1}$
$A$	Amplitude of the velocity potential	$\text{m}^2\cdot\text{s}^{-1}$
$\omega$	Angular frequency	$\text{rad}\cdot\text{s}^{-1}$
$k$	Wavenumber	$\text{m}^{-1}$
$\dot{u}$	Velocity in $x$ direction	$\text{m}\cdot\text{s}^{-1}$
$I$	Sound intensity	$\text{W}\cdot\text{m}^{-2}$
$p'$	Pressure variation in space	$\text{Pa}$
$\varepsilon_c$	Hoop strain	–
$u_r$	Radial displacement	$\text{m}$
$A$	Static elastic limit	$\text{Pa}$
$B$	Strain hardening constant	$\text{Pa}$
$n$	Hardening exponent	–
$\dot{\varepsilon}_0$	Reference strain rate	$\text{s}^{-1}$
$C$	Strain rate hardening constant	–
$m$	Thermal exponent	–
$T_m$	Melting temperature	$\text{K}$
$P_{min}$	Hydrostatic tensile stress	$\text{Pa}$

$E_{tot}$	Energy stored in the particle beam	J
$E_{max}$	Energy density peak on the material	J·m <sup>-3</sup>
$\sigma_x$	Variance of the Gaussian distribution along the $x$ coordinate	m
$\sigma_y$	Variance of the Gaussian distribution along the $y$ coordinate	m
$D_1, D_2, \dots, D_5$	Constants of the Johnson-Cook failure model	–, Pa
$U_p$	Particle velocity	m·s <sup>-1</sup>
$Z$	Shock impedance	Pa·s·m <sup>-1</sup>
$m$	Mass	kg
$W$	Kernel function	–
$h$	Smoothing length	m

## References

- [1] G. Battistoni *et al.* (2007). The FLUKA code: Description and Benchmarking. *Proc. of the Hadronic Shower Simulation Workshop 2006*, Fermilab, AIP Conference Proceeding.
- [2] A. Fassò, A. Ferrari, J. Ranft and P. R. Sala (2005). FLUKA: a Multi-particle Transport Code. CERN-2005-10 (2005), INFN/TC\_05/11, SLAC-R-773.
- [3] O. E. Krivosheev and N. V. Mokhov (1997). A New MARS and its Applications, [Fermilab-Conf-98/043](#), 1998 and SARE3 KEK Proceedings 97-5.
- [4] S. Agostinelli *et al.* (2003). GEANT4 – a simulation toolkit. *Nucl. Instrum. Methods Phys. Res. Sect. A*, 2003;506(3):250–303.
- [5] “Ansys AUTODYN User’s Manual – Release 15.0”, ANSYS, Inc. (2013).

- [6] “Ansys Mechanical User’s Guide – Release 15.0”, ANSYS, Inc. (2013).
- [7] D. Loison (2012). Etude expérimentale et numérique du micro écaillage de cibles métalliques soumises à des chocs laser. *PhD thesis*, ISAE-ENSMA Ecole Nationale Supérieure de Mécanique et d'Aérotechnique.
- [8] J. R. Asai and G. I. Kerley (1987). The response of materials to dynamic loading. *Int. J. Impact Engng.*, Vol. 5, pp. 69 – 99.
- [9] N. A. Tahir, *et al.* (2009). Large Hadron Collider at CERN: Beams generating highenergy-density matter. *Physical Review E*, 79.
- [10] J. F. Cannon (1974). Behavior of the Elements at High Pressures, *Journal of Physical and Chemical Reference Data*, Vol. 3, Issue 3.
- [11] R. G. McQueen, J. N. Fritz and C. E. Morris (1984). The velocity of sound behind strong shock waves in 2024 Al. In J. R. Asay, R. A. Graham and G. K. Straub, *Shock waves in condensed matter–1983*, Elsevier Scienc publ., ISBN 9780444869043.
- [12] P. A. Urtiew and R. Grover (1977). The melting temperature of magnesium under shock loading. *Journal of Applied Physics*, Vol. 48, 1122.
- [13] F. Hensel (1981). Thermophysical properties of metallic fluids in the sub- and supercritical region. In J. V. Sengers, *Proceedings of the eighth symposium on thermophysical properties*, National bureau of Standard, Gaithersburg AD, pp. 151–158.
- [14] G. Kerley (1986). Theoretical equation of state for aluminum. *International Journal of Impact Engineering*, Vol. 5.
- [15] A. Bertarelli, A. Dallochio and T. Kurtyka (2008). Dynamic Response of Rapidly Heated Cylindrical Rods: Longitudinal and Flexural Behavior, *J. Appl. Mech.*, Vol. 75, issue 3, 031010.
- [16] R. Acquafredda *et al.* (2006). First events from the CNGS neutrino beam detected in the OPERA experiment. *New Journal of Physics*, Vol. 8, 303.

- 
- [17] A. Bertarelli (2016). Beam-induced damage mechanisms and their calculation. *CERN Yellow Reports*, v. 2, p. 159, Jan. 2016. ISSN 00078328.
- [18] R. Skalak (1957). Longitudinal impact of semi-infinite circular elastic bar. *J. Appl. Mech. Trans. ASME*, Vol. 24 pp. 59–64.
- [19] L. Pochhammer (1876). On the propagation velocities of small oscillations in an unlimited isotropic circular cylinder, *J. Reine Angew. Math.*, 81, 324.
- [20] H. Kolsky (1963). *Stress waves in solids*. Dover Publications, ISBN 0486610985.
- [21] M. A. Meyers (1994). *Dynamic behaviour of materials*. J. Wiley & Sons, ISBN 047158262.
- [22] J. W. Strutt, B. Rayleigh (1894). *The theory of sound*, Vol. 1.
- [23] S.P. Timoshenko (1921). On the correction for shear of the differential equation for transverse vibrations of prismatic bars. *Philosophical magazine*, Series 6, 43, pp. 744–746.
- [24] G. E. Hudson (1943). Dispersion of Elastic Waves in Solid Circular Cylinders. *Phys. Rev.* 63, pp. 46–51.
- [25] P. Sievers (1974). Elastic waves in matter due to rapid heating by an intense high-energy particle beam. CERN-LabII-BT-74-2.
- [26] J. L. Davis (1988). *Wave propagation in solids and fluids*. Springer-Verlag, ISBN 9781461283904.
- [27] N. Tahir *et al.* (2016). Beam induced hydrodynamic tunneling in the future circular collider components. *Phys. Rev. Accel. Beams*, Vol. 19, 081002.
- [28] A. Bertarelli *et al.* (2013). An experiment to test advanced materials impacted by intense proton pulses at CERN HiRadMat facility. *Nuclear Instruments and Methods in Physics Research B*, Vol. 308, pp. 88–99.

- [29] F. Carra *et al.* (2013). Behaviour of advanced materials impacted by high energy particle beams. *Journal of Physics: Conference Series*, Vol. 451, conference 1.
- [30] G. Apollinari, I. Béjar Alonso, O. Brüning, M. Lamont, L. Rossi (2014). High-Luminosity Large Hadron Collider (HL-LHC): preliminary design report. CERN, Geneva, Switzerland, *Rep. CERN*, CERN-2015-005, 2015.
- [31] M. Benedikt and F. Zimmerman (2015). Future circular colliders, *CERN note*, CERN-ACC-2015-164.
- [32] G. R. Johnson and W. A. Cook (1983). A constitutive model and data for metals subjected to large strains, high strain rates and high temperatures. *Proceeding of 7<sup>th</sup> International Symposium on Ballistics*, pp. 541–547.
- [33] G. R. Johnson and W. A. Cook (1985). Fracture characteristic of three metals subjected to various strains, strain rates, temperature and pressure. *Eng. Fract. Mech.*, Vol. 2 (1), pp. 31–48.
- [34] F. Carra *et al.* (2014). Mechanical engineering and design of novel collimators for HL-LHC. *Proceedings of IPAC'14*, Dresden, Germany, 2014.
- [35] A. Bertarelli *et al.* (2011). Limits for beam-induced damage: reckless or too cautious? *Proceedings of Chamonix 2011 workshop on LHC performance*, Chamonix (F), 24–28 January 2011.
- [36] M. Scapin (2015). Mechanical characterization and modeling of the heavy tungsten alloy IT180, *International journal of refractory metals and hard materials*, vol. 50, pp. 258–268.
- [37] L. Peroni, M. Scapin and A. Tridello (2016). Analysis of the dynamic behaviour of tungsten in post-necking regime. *1<sup>st</sup> International Conference on Impact Loading of Structures and Materials*, Torino (Italia), 22–26 May 2016.

- 
- [38] M. Scapin, L. Peroni, V. Boccone and F. Cerutti (2014). Effects of High-Energy Intense Multi-Bunches Proton Beam on Materials. *Computers & structures*, vol. 141, pp. 74–83.
- [39] B. Gladman *et al.* (2007). LS-DYNA® Keyword User’s Manual – Volume I – Version 971, LSTC.

## Chapter 5

# Novel materials for particle accelerator components

In the previous chapters we have seen that the most critical scenarios involving quasi-instantaneous heating of components under a thermal load take place under the effect of a hadron beam impact. Currently, the particle accelerator with the highest energy stored in the circulating beams is the *Large Hadron Collider* (LHC) at CERN, the *European Organization for Nuclear Research*. CERN is an intergovernmental organization with more than 20 Member States<sup>16</sup>. Its seat is in Geneva but its premises are located on both sides of the French-Swiss border. CERN's mission is to enable international collaboration in the field of high-energy particle physics research and to this end it designs, builds and operates particle accelerators and the associated experimental areas. At present more than 11 000 scientific users from research institutes all over the world are using CERN's installations for their experiments.

The LHC is only the last machine in a complex made of a chain of accelerators with increasingly higher energies (Figure 73). Each machine injects the beam into the next one, which takes over to bring the beam to an even higher energy, and so on. The complex allows studies in the field of particle physics, which recently led to the discovery of the theorized Higgs Boson at CERN in 2012 [1], but also in biological, chemical, material science, as well as the new hadron therapies for medical purposes. The construction and commissioning of the LHC spanned almost 15 years and involving scientists and engineers from all over the world. It consists of two rings installed in a 27 km long circular tunnel at a depth ranging from 50 to 175 m underground, between France and Switzerland. It is a synchrotron, where two counter rotating hadron beams are guided around their circular orbit by powerful superconducting magnets (8.3 T) cooled in a bath of superfluid helium

---

<sup>16</sup> [www.cern.ch](http://www.cern.ch)

(up to 1.9 K). Particles are accelerated and brought into collision in four large detectors.

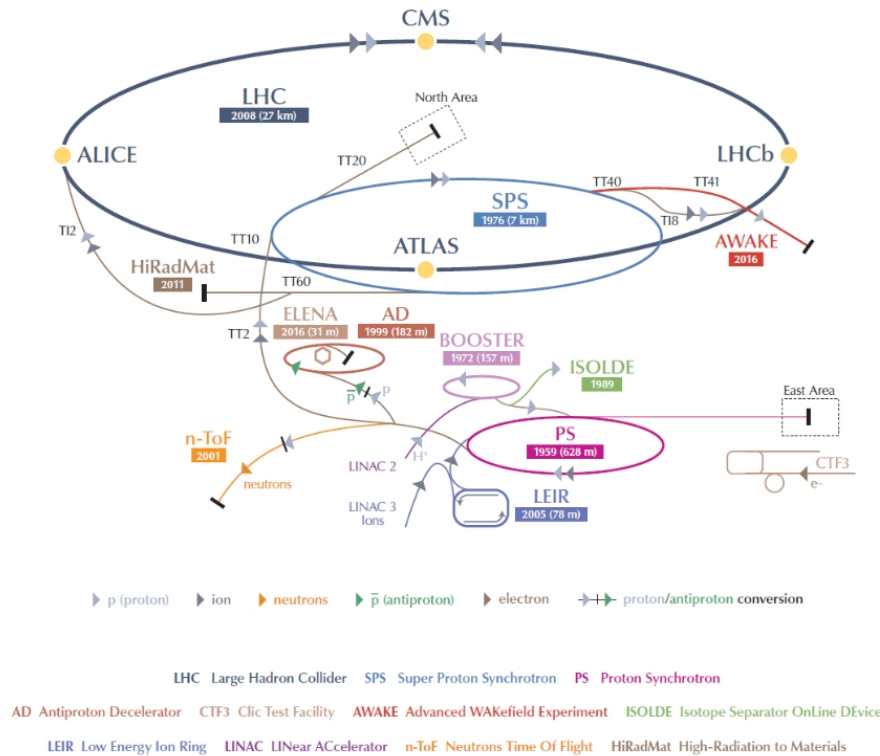


Figure 73. CERN accelerator complex.

In the next years, an upgrade of the LHC is planned with the goal of increasing the *luminosity* of the accelerator [2]. The luminosity is a parameter related to the number of collisions which can be produced and analyzed in the detectors, and depends on parameters such as beam intensity, energy, transverse size, as well as the crossing angle of impact between the two particle beams. The operational parameters of LHC and its upgrade, named HL-LHC, are reported in Table 17.

Table 17: LHC and HL-LHC operational parameters.  $E_k$  is the particle energy,  $\Delta t$  the bunch spacing,  $N_b$  the number of bunches,  $n_b$  the number of particles per bunch,  $E_{tot}$  the total energy stored in the beam,  $L$  is the ring circumference,  $R$  the bending radius and  $f$  the revolution frequency.

	<b>Nominal LHC</b>	<b>HL-LHC</b>
$E_k$ (TeV)	7	7
$\Delta t$ (ns)	25	25
$N_b$	2808	2748
$n_b$	$1.15 \times 10^{11}$	$2.2 \times 10^{11}$
$E_{tot}$ (MJ)	362	678
$L$ (m)	26 658	26 658
$R$ (m)	2 804	2 804
$f$ (kHz)	11.25	11.25

As highlighted in Table 17, the amount of energy stored in the circulating beams of the LHC and HL-LHC is enormous<sup>17</sup>, and it can be discharged in few  $\mu$ s on surrounding structures known as *beam intercepting devices* (BID). Examples of BID, already anticipated in Chapter 1, are targets, dumps and collimators. In this PhD thesis we mostly focus on collimators; however, the studies and considerations made can indeed be extended to the other categories of BID, and more in general to any component which is subjected to a sudden and fast increase of temperature.

## 5.1 LHC collimation system

Currently, there are about 110 collimators in the LHC, with two main functions: *beam cleaning* and *machine protection* [3]. Beam cleaning consists of the interception of the particles deviating from the ideal trajectory and constituting the *beam halo*, limiting the thermal losses to the superconductive magnets and detectors. In nominal operation, collimators intercept only a small fraction of the beam particles, and the thermal load is in the case of nominal LHC equal to 4.5 kW on the most loaded collimator in steady-state conditions [4]. On the other hand, in case of accidental orbit errors, the collimators provide machine protection,

<sup>17</sup> In terms of equivalent kinetic energy, the HL-LHC beam has the same energy of an object of 460 tons, such as a *Zefiro 300* high-speed train, traveling at a speed of 200 km/h.

shielding other delicate accelerator components from a potential beam impact. In this situation, the collimator could be directly hit by one or more proton bunches, and must withstand a significant energy density deposited in few microseconds.

The collimation optimal performance is ensured by a multi-stage system with three main collimator families, depending on the transverse distance from the particle beam, or aperture. The three families are named primary, secondary and tertiary collimators (Figure 74). Differences exist between the three collimator families, mostly in terms of adopted materials; however, the general design guidelines are the same. Moreover, in view of HL-LHC, the design concepts have been even more standardized, such that the future collimators will share almost the totality of the components with the exception of the active jaw material [6]. A 3D cutaway of the HL-LHC collimator, with identification of the main element, is shown in Figure 75.

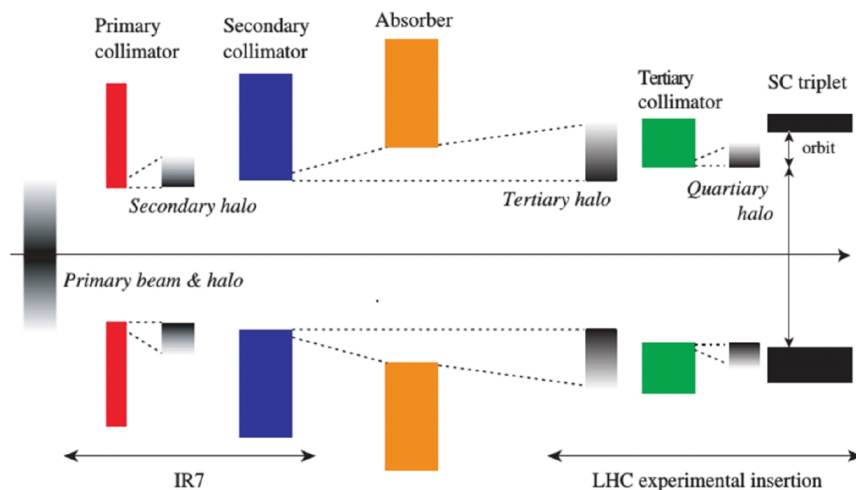


Figure 74. Scheme of the LHC collimation system, courtesy of E. Quaranta.

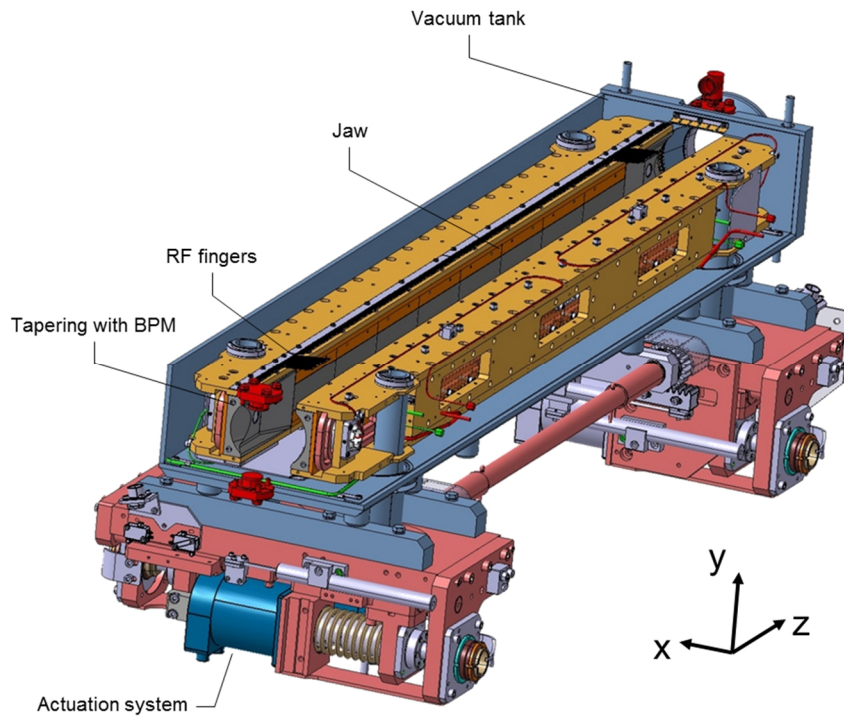


Figure 75. 3D view of the HL-LHC collimator.

With reference to Figure 75, it is possible to identify the following main elements common to all collimators:

- *Vacuum tank*: it is made of austenitic stainless steel plates, electron-beam welded, and connected to the beam line by means of a collar and flange at each extremity. The required vacuum pressure depends on the position in the accelerator: the lowest pressure is required at the experimental areas ( $10^{-10}$  mbar) [2]. The tank is placed on a supporting system with different orientations, depending on the scope of the specific collimator. The orientation can be horizontal, vertical or skew. The beam cleaning plane changes accordingly.
- *Jaws*: they are two movable girders constituting the core element of the collimator, providing the halo cleaning function by approaching the beam through a dedicated actuation system. The jaws are in Glidcop Al-15 and sustained by one shaft at each extremity, with a hinge/simple support configuration which guarantees the jaw expansion under the thermal load.
- *Actuation system*: the jaws are actuated by means of stepper motors, whose rotation is translated into a linear movement in  $x$  direction by

means of leadscrews. The maximum stroke per jaw is 35 mm. A 5<sup>th</sup> axis is also available, for displacement in the  $y$  direction.

- *RF fingers*: they are made of a copper-beryllium alloy and are used for avoiding abrupt changes in the volume surrounding the beam axis, minimizing the RF impedance.
- *Tapering*: this conical element has a function similar to the RF fingers, and is used to provide a smooth transition between the beam line geometry and the jaw narrow aperture. It also hosts the Beam Position Monitor (BPM) [5], a device adopted to measure the beam position with respect to the collimator jaws, facilitating the jaw alignment.

The tank is mounted on a support giving different orientations to the system (horizontal, vertical and skew), to collimate the beam at different phase spaces. It is worth analyzing the jaws more in detail, as they are the functional elements responsible for beam cleaning and machine protection. The HL-LHC jaw design (Figure 76) is an evolution of the jaws of collimators currently installed in the LHC, such as the tertiary shown in Figure 68. The HL-LHC design can now host both brittle and ductile absorber materials, and is thus compatible with all the collimator families [6].

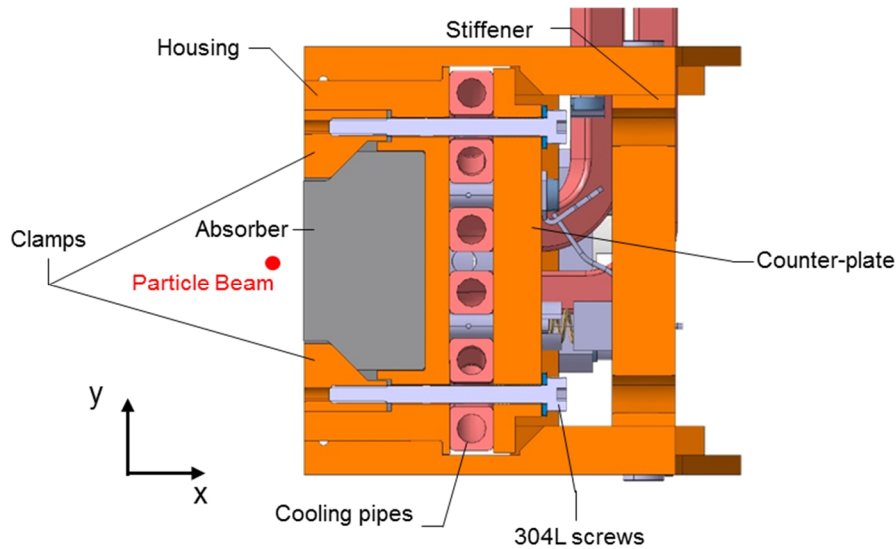


Figure 76. HL-LHC collimator jaw section.

- *Absorber*: it is the element actively intercepting the beam particles, and absorbing most of the thermal load in nominal and accidental conditions. The absorber material must have a low density in the case of primary and secondary collimator jaws, which have a distance from

the beam axis in the order of 1 mm [7], to decrease the beam-induced energy density. In the case of tertiary collimator jaws, which are more opened, the material is denser. In currently installed collimators, carbon-fibre-reinforced carbon (CFC) is adopted for primaries and secondaries, and the tungsten heavy alloy Inermet180 for the tertiaries. The total active length of the absorber is 1 m, which can be achieved through the use of several adjacent blocks, typically 125 mm long (or more)<sup>18</sup>.

- *Clamping system*: it provides a pressure between the absorber and the housing, to minimize the thermal resistance at contact. Clamps are made of Glidcop Al-15 elements fastened to the counter-plate by means of stainless steel M4 screws. Glidcop, as already mentioned in the previous chapters, is an oxide dispersion-strengthened copper alloy with very high resistance to creep and stress relaxation, high annealing temperature, and overall better properties at elevated temperature than other copper alloys.
- *Housing*: it hosts the absorber inserts and is brazed to the cooling pipes. It must possess good thermal properties, as it is on the thermal path between the high thermally loaded absorber and the heat sink, represented by the cooling pipes. It is also made of Glidcop Al-15.
- *Cooling circuit*: it is constituted of two pipes per jaw, brazed to the housing and to the counter-plate with a silver-based alloy. The coolant is water at room temperature; a copper-nickel alloy (CuNi 90-10) is adopted for the pipes because of the good properties in terms of resistance to corrosion and oxidation under high water flows.
- *Counter-plate*: it allows the fastening of the clamping system and is brazed to the cooling pipes to center the position of the neutral axis of the brazed assembly, minimizing the residual bending deformation after brazing. It is made of Glidcop Al-15 to ease the brazing process.
- *Stiffener*: it is made of three plates creating a “C” shape and its main role is to increase the moment of inertia of the structure, decreasing the bending deformation in operation. Since in nominal operation it is subjected to a non-negligible thermal load, a good conductor is required, and the material is again Glidcop Al-15.

---

<sup>18</sup> The block length depends on the material adopted and on the production technique.

## 5.2 Collimator jaw materials: requirements and development

As explained in the previous section, the most delicate component of the collimator is the absorber, as it is in direct contact with the beam halo and, in case of accident, it can even be directly impacted by the particle beam. The design cases for collimators are based on the LHC design figures [8],[9], and the thermal loads have been recalculated for HL-LHC collimators:

- A. *1 hour beam life time*: this is the nominal design case for collimators in steady-state operation. The thermal load is calculated considering the depletion of the full beam on the collimation system in one hour, which translates into 20.7 kW on the most loaded HL-LHC collimator.
- B. *0.2 hours beam life time*: the collimator in nominal condition (*case A*) is rapidly submitted to a five times higher thermal load for a duration of 10 s, corresponding to 103.5 kW on the most loaded HL-LHC collimator. The heating ramp lasts 10 ms, which is slow enough to prevent the rise of dynamic stresses in the component, as discussed in section 1.3.
- C. *Beam injection error*: the full SPS beam, made of 288 bunches at 450 GeV, is discharged after injection on the collimator jaw in a time of 7.2  $\mu$ s. This scenario can take place only on primary and secondary collimators, and is, among the four, the one entailing the highest energy density on the impacted component. This accident is triggered during the injection of the beam from the LHC, because of errors in the kicker magnets which deflect the beam vertically. In this case, the incoming beam is not injected correctly in the ring but starts to oscillate around the reference orbit, with the risk to hit the downstream aperture and eventually the collimators.
- D. *Asynchronous beam dump*: it involves a direct impact of a number of LHC bunches on the collimator jaw. In the case of primary and secondary collimators, the number of impacting bunches is eight, while for tertiary collimators, it is one. Physically, this accident is triggered by an abnormal firing<sup>19</sup> of the 15 magnet kicker modules which are used to extract the beam from the LHC and direct it towards the dump.

---

<sup>19</sup> Abnormal means either too anticipated, or too delayed with respect to the required time window.

Abnormal dumps have only effects on horizontal collimators and to a lesser extent on skew collimators, as the dump kick acts on the horizontal plane.

In the scope of this PhD thesis, the cases of interest are *C* and *D*, as they involve a dynamic response of the impacted structure to the quasi-instantaneous thermal load. These cases are extremely unlikely, as the behaviour of the beams in the SPS and LHC is constantly monitored with instruments such as BLMs (Beam Loss Monitors) and BPMs, and an interlock system based on the instrumentation reading is in place, such that the beam is dumped before reaching the accidental conditions. Nevertheless, the possibility of such accidents is not zero, and the design of collimators must consider this eventuality.

The properties of collimator materials shall satisfy the requirements implied by all the aforementioned design scenarios, including the quasi-static and slow-transient ones. In particular, on the basis of the considerations made in Chapter 1, from the thermomechanical point of view the material should possess high thermal conductivity, specific heat, melting temperature and ductility; at the same time, coefficient of thermal expansion and density should be minimized. Additional requirements include high electrical conductivity, machinability, radiation hardness, low magnetic susceptibility.

No existing material meets all the aforementioned requirements. The CFC adopted in currently installed primary and secondary collimators is robust to the particle beam impacts, but its poor electrical conductivity penalizes it in terms of RF impedance. An R&D program has been therefore launched at CERN in recent years [7] to explore and develop a number of novel materials for HL-LHC collimators aiming to combine the excellent properties of graphite or diamond, specifically the low density, high thermal conductivity and low thermal expansion, with those of metals or transition-metal-based ceramics, which possess high mechanical strength and good electrical conductivity. The study was performed in collaboration with international partners, also in the scope of European Projects such as EuCARD [10], EuCARD-2<sup>20</sup> and ARIES<sup>21</sup>. The best materials developed are *molybdenum-graphite* (MoGr) and *copper-diamond* (CuCD) (Figure 77). The study of the response of MoGr and CuCD under quasi-instantaneous heating

---

<sup>20</sup> <http://eucard2.web.cern.ch/>

<sup>21</sup> <http://aries.web.cern.ch/>

requires the derivation of material models similar to those described in Chapters 2-3, and the implementation of numerical calculation methods based on the examples reported in Chapter 4. The characterization of the properties required to build the material models for the novel materials is summarized in section 5.4 and the properties are compared to those of CFC.



Figure 77. Left: MoGr plate for prototyping ( $150 \times 100 \times 25 \text{ mm}^3$ ). Right: CuCD samples for bending tests.

### 5.3 Collimator jaw materials: microstructure and production methods

In the previous chapters, the material response to a quasi-instantaneous heating has been analyzed. The problem can be studied numerically and, in some cases and under certain simplifications, analytically. The precision of the results strongly depends on the accuracy of the equation of state and constitutive law of the material. However, collimator materials are either non-conventional composites (CFC, CuCD) or even totally new materials developed at CERN with the collaboration of international partners (MoGr). As external data sources are scarce or non-existing, in recent years studies have been performed within the CERN R&D program to evaluate the thermo-physical collimator material properties, and results were published under the form of journal articles [11],[12], master theses [13],[14],[15] and PhD theses [4],[16],[17]. In this section and in section 5.4, the existing literature on material observations and production method is examined, together with the results of conventional thermo-physical tests and new methods of material testing conceived in the scope of this thesis. Material models based on the existing experimental data are then proposed, for use in numerical codes.

#### 5.3.1 Carbon-fibre-reinforced carbon

CFC is the material currently adopted in primary and secondary collimators. The specific grade, called AC-150k and produced by the Japanese company *Tatsuno*<sup>22</sup> under the form of plates, is a 2D composite with 40% carbon fibres randomly

---

<sup>22</sup> <http://www.tatsunojapan.com>.

oriented in a graphite matrix to create several layers parallel to the  $YZ$  plane (Figure 78). The contribution of fibres enhances the mechanical properties in the  $YZ$  plane, while in the  $x$  direction the properties are lower, as they depend on the inter-planar bonding only. Moreover, the plates are hot-rolled in the  $z$  direction, which is slightly preferential with respect to  $y$ , such that the resulting material is orthotropic. The achievable sizes are in the order of  $25 \times 100 \times 150 \text{ cm}^3$ ; this implies that a monolithic jaw absorber can be obtained, differently from MoGr and CuCD, which at the moment are limited to functional lengths of 125 mm and require multi-block polyolithic absorbers (Figure 75).

Thanks to the material low thermal expansion coefficient and density, as well as the high melting point<sup>23</sup> and internal friction, CFC shows high robustness to particle beam impact, and for this reason was chosen as the jaw absorber for LHC primary and secondary collimators<sup>24</sup>. However, the low electrical conductivity discourages the use of this material for HL-LHC collimators, due to its high contribution to the RF impedance of the machine.

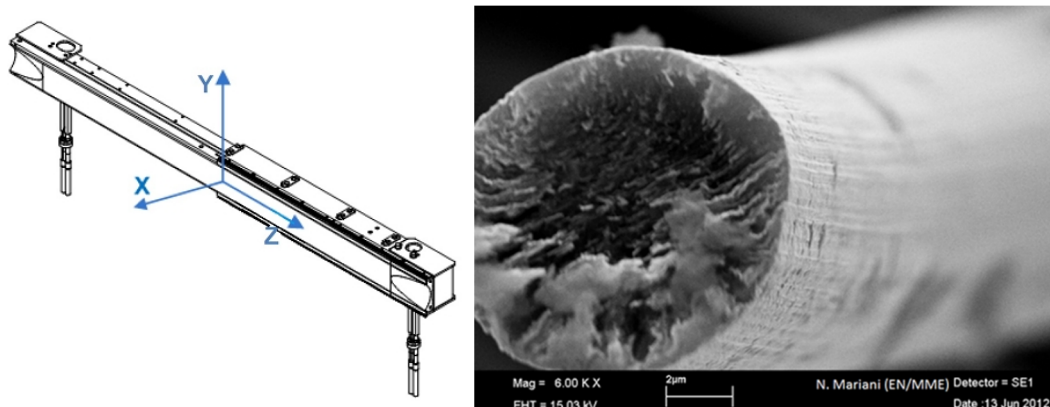


Figure 78. Left: CFC jaw of an LHC secondary collimator. Right: Microscopy of a pitch-derived carbon fibre. Source: [16].

### 5.3.2 Molybdenum-Graphite

MoGr was co-developed by CERN and the Italian SME *BrevettiBizz*<sup>25</sup> with the goal of increasing the electrical conductivity of secondary collimators while maintaining or improving the beam impact robustness of currently adopted CFC jaws.

<sup>23</sup> Note that graphite does not melt at room pressure, as it sublimates at about 4000 K. In the equation of state, the melting phase is present at temperatures above 4300 K for pressures higher than 10 MPa, which are easily reached in the case of beam impact.

<sup>24</sup> In the case of tertiary collimators, the density of CFC is not high enough to fulfil the beam cleaning function. Inermet 180 is instead adopted for its high particle absorption properties.

<sup>25</sup> [www.brevetibizz.com](http://www.brevetibizz.com).

MoGR is sintered starting from powders of graphite and molybdenum, with the possible addition of other constituents like carbon fibres and metal dopants, depending on the composite grade and desired thermo-physical properties. Natural graphite powder is used in the form of flakes, with a maximum diameter of about 45  $\mu\text{m}$ . Molybdenum powder has 5  $\mu\text{m}$  particle size. Carbon fibres are in the range of 250  $\mu\text{m}$  to 3 mm in length, with diameter of about 10  $\mu\text{m}$ . After mixing, powders are compacted at room temperature in a green body, which then undergoes the sintering process, with a technique known as *Spark Plasma Sintering* (SPS). The use of this method implies a heat generation in the sintered material and mould by the passage of an electric current, which induces resistive losses. SPS allows reaching high heating rates and pressure, facilitating shorter sintering times at very high temperatures. The sintering temperature exceeds 2600  $^{\circ}\text{C}$ , slightly above the melting point of the molybdenum carbide produced in the process. The liquid phase, constituted by molten molybdenum carbide, is believed to largely catalyze graphitization; carbon atoms, having greatly increased mobility inside the molten carbide, can more easily reconstruct and bond the graphitic structures. After sintering, a pressure-less thermal treatment is performed on composite at temperatures exceeding 2000  $^{\circ}\text{C}$ , in order to relax the internal stresses induced by the hot-pressing and allow material outgassing.

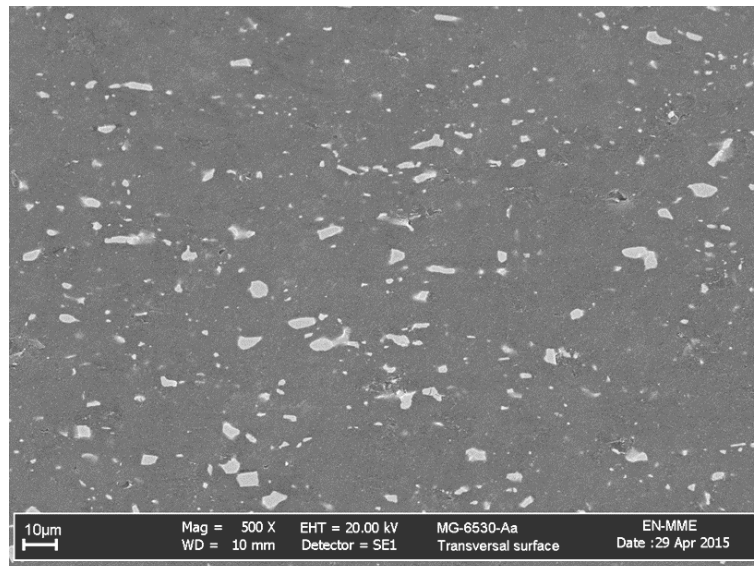


Figure 79. SEM observation of MoGr polished surface. The graphite matrix is dark grey and the carbide particles are light grey.

As a result, the final material is made of a well-oriented graphitic matrix (>95% vol.), strengthened with small molybdenum carbide particles of size around 5  $\mu\text{m}$  (Figure 79). With respect to CFC, the molybdenum carbides improve the

bonding between the basal planes, increasing the degree of isotropy of the material. Still, the two preferential directions are on the sintering plane, where the material reaches thermomechanical properties typical of a highly graphitized matrix, namely very high thermal and electrical conductivities, low thermal expansion coefficient, good mechanical strength.

Several different grades of MoGr were developed in the past years at CERN, modifying parameters such as initial powder composition, presence of dopants, presence of carbon fibres, sintering cycle and post-sintering thermal treatment. In the scope of this work, we will focus on the so-called grade MG-6530Aa, which was also tested in the HiRadMat facility in 2015. This grade has an initial composition of 90.5%<sub>vol</sub> carbon powders, 4.5%<sub>vol</sub> Mo and 5%<sub>vol</sub> carbon fibres, without additional doping metals.

As it will be shown in section 5.4, the properties along the two directions defining the sintering plane are identical, and higher than the third direction, parallel to the sintering pressing vector. The material is thus transversely isotropic.

### **5.3.3 Copper-Diamond**

CuCD is a composite material produced with the SPS technique, by hot pressing a mixture of copper and diamond powders at a temperature slightly lower than copper melting [18]. The grade of interest for collimators is produced by the Austrian company *RHP Technology*<sup>26</sup>. As copper and diamond are not chemically affine, a proper interface between the two constituents is assured by the addition of a small quantity of binders such as boron, zirconium, molybdenum, chromium, etc. During the sintering, these elements form carbides which provide a reliable bond between diamond and copper.

---

<sup>26</sup> <http://www.rhp-technology.com>.

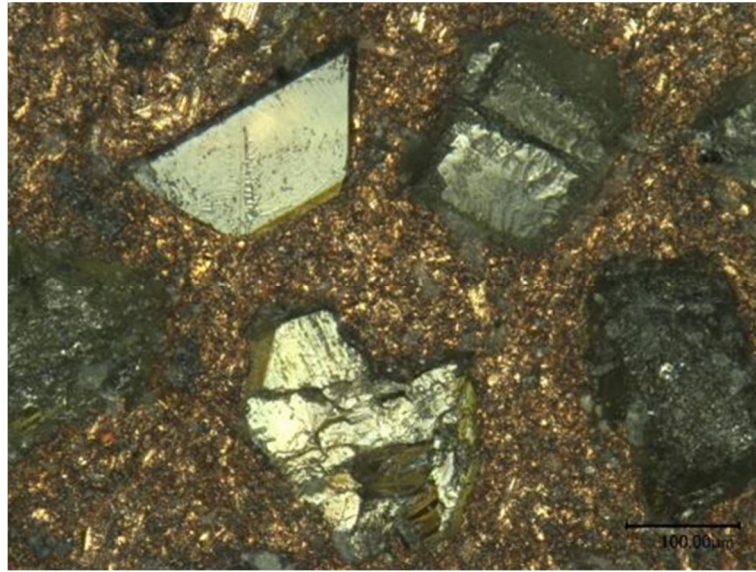


Figure 80. Optical observation of copper-diamond surface.

The final result is a copper matrix with embedded diamonds (Figure 80). Copper provides the mechanical resilience and the electrical conductivity, and contributes to the thermal conductivity of the composite. Diamonds are about 100  $\mu\text{m}$  in size, and they enhance even further the thermal conductivity of the composite, reducing its density and thermal expansion coefficient. The material is isotropic. The grade typically adopted in collimators contains 66%<sub>vol</sub> of diamonds, 33%<sub>vol</sub> of copper and roughly 1%<sub>vol</sub> of binders (chromium or boron).

## 5.4 Characterization campaign and material modelling

When dealing with novel materials, for which literature studies do not exist yet, it is convenient to start with simplified material models, which can be derived through dedicated laboratory tests, and to increase the complexity of the model as soon as more advanced testing methods are developed. The models, although simplified, should allow predicting the results in the case of beam impact with a good degree of approximation, and the simplifications must be justified from a physical point of view.

For most of the design cases, collimator materials do not experience melting, and the entity of the waves produced does not surpass the critical shock threshold, mostly because of the considerations made in Chapters 3 and 4 on the nature of cylindrical waves. In terms of equation of state, it is then reasonable to adopt a linear equation of state of the type of Eq. (3.8):

$$p(\rho, E) = K \left( \frac{\rho}{\rho_0} - 1 \right) + \gamma_0 E ; \gamma_0 = \frac{\alpha K}{\rho_0 c_v} \quad (3.8)$$

At the impacted volume, the material is subjected to a strong hydrostatic state, and its response depends mostly on the EOS. It is then important to precisely measure the properties involved in its construction.

#### 5.4.1 Thermal properties

Specific heat at constant pressure and coefficient of thermal expansion were measured at CERN over a wide range of temperatures, by means of a *differential scanning calorimeter* [19] and a *dilatometer* [20] (Figure 81). The density was measured with a *hydrostatic scale* (Table 18). The different temperature range of the measurement reflects the range of application for the materials. Note that the specific heat at constant volume can be calculated with Eq. (4.8).

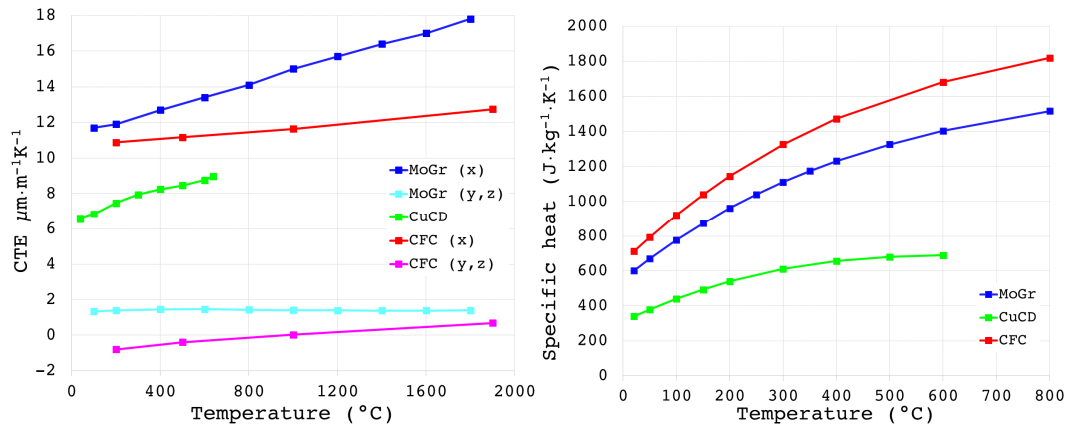


Figure 81. Left: thermal expansion coefficient and right: specific heat of the collimator materials. The reference system is the same reported in Figure 76.

As seen in Chapter 1, when studying longitudinal stress waves induced by isochoric heating, thermal diffusion can usually be ignored, as the characteristic diffusion time  $\tau$  is typically much larger than the period of the dynamic response. However, in the scope of this work also longer-time phenomena are analyzed, such as flexural vibrations and residual deformations resulting on the structure when the vibration evanishes. The thermal problem is therefore also solved in time, and the derivation of thermal diffusivity and thermal conductivity is required. These properties were measured with a *laser-flash* technique [21] and results are reported in Figure 82.

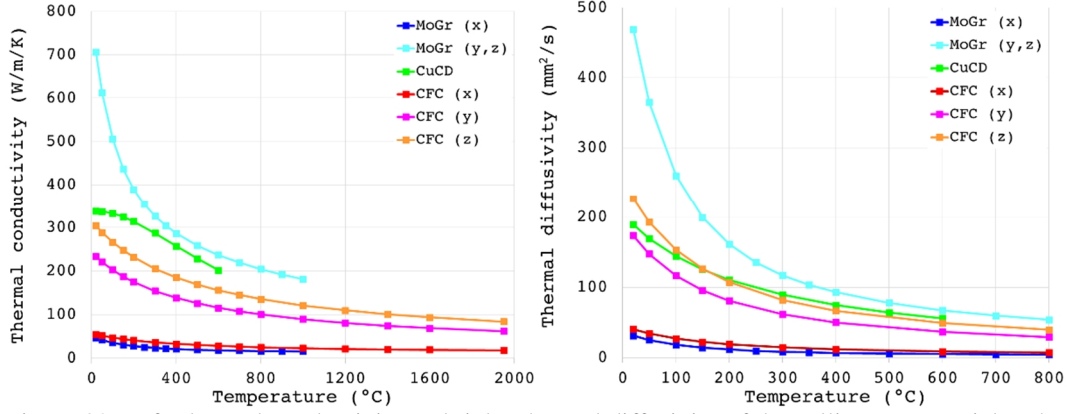


Figure 82. Left: thermal conductivity and right: thermal diffusivity of the collimator materials. The reference system is the same reported in Figure 76.

### 5.4.2 Elastic constants

The three materials have different structures and this has an influence on the elastic equations and on the calculation of the bulk modulus. Indeed, CFC is orthotropic, while MoGr is transversely isotropic and CuCD is isotropic. Recalling Eq. (2.3):

$$\varepsilon_i = S_{ij} \sigma_j, \quad (2.32)$$

it is now preferable to write the compliance matrix  $[S]$  in its general form for orthotropic materials:

$$[S] = \begin{bmatrix} 1/E_x & -\nu_{yx}/E_y & -\nu_{zx}/E_z & 0 & 0 & 0 \\ -\nu_{xy}/E_x & 1/E_y & -\nu_{zy}/E_z & 0 & 0 & 0 \\ -\nu_{xz}/E_x & -\nu_{yz}/E_y & 1/E_z & 0 & 0 & 0 \\ 0 & 0 & 0 & 1/2G_{yz} & 0 & 0 \\ 0 & 0 & 0 & 0 & 1/2G_{zx} & 0 \\ 0 & 0 & 0 & 0 & 0 & 1/2G_{xy} \end{bmatrix} \quad (5.1)$$

As the matrix is symmetric, the following relations stand:

$$\begin{aligned}
-\frac{\nu_{yx}}{E_y} &= -\frac{\nu_{xy}}{E_x} \\
-\frac{\nu_{zx}}{E_z} &= -\frac{\nu_{xz}}{E_x} \\
-\frac{\nu_{zy}}{E_z} &= -\frac{\nu_{yz}}{E_y}
\end{aligned} \tag{5.2}$$

In the case of an orthotropic material like CFC, the number of independent constants of the compliance matrix is thus nine. If the material exhibits identical properties in one plane and different properties in the direction normal to this plane, such as in the case of MoGr, it is called transversely isotropic. Transverse isotropy is a special case of orthotropy, but the independent constants of the compliance matrix are now only five. Let us consider, in fact, the plane of isotropy  $YZ$  (Figure 76), as in the case of MoGr. The relations (5.2) are of course still valid, and in addition:

$$\begin{aligned}
E_y &= E_z \\
G_{xy} &= G_{zx} \\
\nu_{xy} &= \nu_{xz} \\
G_{yz} &= \frac{E_z}{2(1 + \nu_{yz})}
\end{aligned} \tag{5.3}$$

Finally, in the simplest case of an isotropic material such as CuCD, the properties are the same in all directions and the number of independent elastic constants is further reduced to two, as shown in Eq. (2.4).

Independently of the material structure, the bulk modulus can still be calculated with Eq. (2.6), as it is defined as the ratio between pressure and compression (or negative dilatation). For an orthotropic material, the parameter is usually called *effective bulk modulus* [22], and it can be derived from the terms of the compliance matrix:

$$K = \left( \sum_{i,j=1}^3 S_{ij} \right)^{-1} \quad (5.4)$$

The elastic constants were measured at CERN with the *impulse excitation technique* (IET). With this method, the fundamental frequencies of material specimens are excited with a smaller hammer and acquired by means of a transducer. Typically, the flexural and torsional frequencies are acquired, as they are directly related to the Young's and shear moduli. As seen, in the case of flexural vibrations of a 1D element of length  $L$ , section  $A$ , density  $\rho$  and moment of inertia  $I$ , for an isotropic material:

$$\lambda_{f,i} = \frac{1}{2\pi} \frac{\beta_{f,i}^2}{L^2} \sqrt{\frac{EI_x}{\rho A}} \quad (1.15)$$

while the expression for the torsional frequencies, derived from the study of shear waves treated in section 2.1 is:

$$\lambda_{t,i} = \frac{\beta_{t,i}}{L} \sqrt{\frac{G}{\rho}} \quad (5.5)$$

Because of limitations due to the production process of the collimator materials, it is difficult to achieve slender specimens. International Standards dealing with the IET [23],[24] suggest corrections to take into account the deviations of the specimen from the 1D hypothesis, such that the evaluation of the elastic constants for an isotropic material can be performed directly after the acquisition of the flexural and torsional frequencies. On the other hand, in the case of orthotropic materials, it is not possible to derive relations similar to (1.15) and (5.5) due to the coupling between the independent elastic constants, which are now nine, and the triaxiality given by the specimen shape.

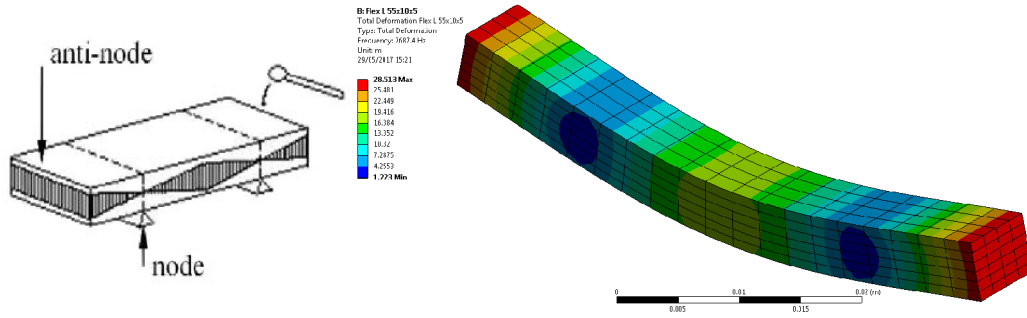


Figure 83. Left: scheme of the experimental setup for acquisition of the flexural frequencies of material plate-like specimens. Right: numerical modal analysis, first flexural mode.

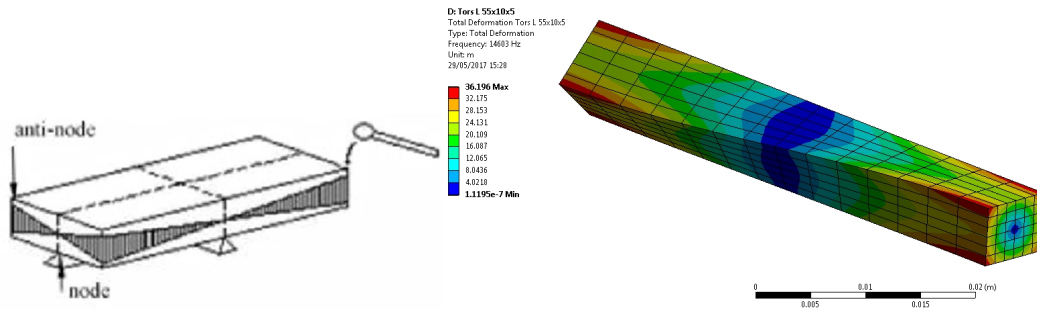


Figure 84. Left: scheme of the experimental setup for acquisition of the torsional frequencies of material plate-like specimens. Right: numerical modal analysis, first torsional mode.

The problem was therefore solved numerically with ANSYS, through a modal analysis of the specimens. The natural frequencies are found from the generalized equation of motion, solving the eigenvalue problem of the associated homogeneous ODE. Modal shapes are the eigenvectors of the system. When damping is ignored, the homogeneous ODE has the form:

$$[M]\{\ddot{U}\} + [K]\{U\} = 0 \quad (5.6)$$

Where  $[M]$  is the mass matrix,  $\{\ddot{U}\}$  is the acceleration vector,  $[K]$  is the stiffness matrix and  $\{U\}$  is the displacement vector. The solution of Eq. (5.6) can be written under the form:

$$([K] - \lambda[M])\{\Phi\} = 0 \quad (5.7)$$

$$(\lambda = \omega^2)$$

where  $\lambda$  is the eigenvalue,  $\{\Phi\}$  is the eigenvector and  $\omega$  the circular natural frequencies. Eigenvalues are calculated from the equation:

$$\det([K] - \lambda[M]) = 0 \quad (5.8)$$

The determinant is null only at a set of discrete eigenvalues  $\lambda_i$  or  $\omega_i^2$ , and there is an eigenvector  $\{\Phi_i\}$  satisfying Eq. (5.7) and corresponding to each eigenvalue. The natural frequencies  $f_i$  are simply:

$$f_i = \frac{\omega_i}{2\pi} \quad (5.9)$$

Note that the frequencies of the collimator material specimens are known, as they result from the IET measurements. In this case, the unknown of Eq. (5.8) are the terms of the stiffness matrix, which depend on the elastic constants. The calculation was performed with the optimization module within ANSYS, starting at the first cycle by imposing, for each material under analysis, the initial constants of Eq. (5.1) by educated guess. The initial guess is based on the analysis of the initial  $\sigma - \varepsilon$  slope of bending tests (section 5.4.3), on comparisons with similar existing materials, as well as, in the case of multi-material composites such as CuCD, on the rule of mixture. The targets of the analyses are the first and second flexural frequencies, as well as the first and second torsional frequencies, measured with the IET. The optimization module runs iterative analyses adjusting the values of the elastic constants until reaching a convergence of the frequencies within the specified tolerance. The optimization technique adopted was the Multi-Objective Genetic Algorithm (MOGA) [25]. The computational time of the problem can be reduced by imposing boundaries for each elastic constants; for example, the Poisson's ratios were specified in the range between 0 and 0.5.

The results of the experimental/numerical estimation of the elastic constants are reported in Table 18.

### 5.4.3 Strength and failure behaviour

The three materials are brittle, and they show scarce hardening at room temperature and under quasi-static testing. A spallation model seems adequate to describe the failure of the materials. Currently, the only tests performed to define the material resistance and strength under tensile load are four-point bending tests [26] at room temperature. A bending test on brittle materials usually overestimates the ultimate strength with respect to a tensile test, as the specimen is subjected to the maximum stress only at the points with the maximum distance with respect to

the neutral axis, *i.e.* at the external surface. For this reason, moreover, the results of bending tests have typically a dependence on the surface state. However, traction tests on brittle materials are complex and sometimes unreliable, since the sample often breaks in proximity of the grips. Future tests to derive the material behaviour under pure tension, possibly including strain rate and temperature hardening and softening, are being studied; for example, MoGr can be machined under the form of specimens for Split-Hopkinson pressure bar tests at Politecnico di Torino.

The results of bending tests on collimator materials are reported in Figure 85 and Figure 86.

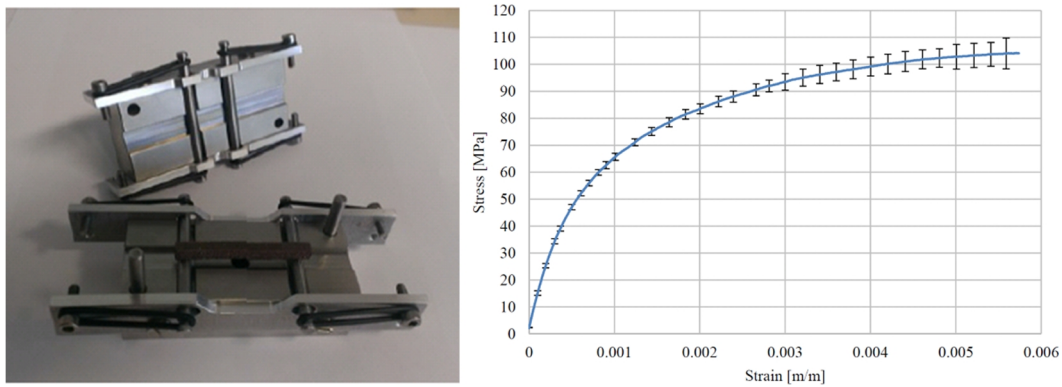


Figure 85. Left: fixture for 4-point bending tests. Right: flexural strength of CuCD [14].

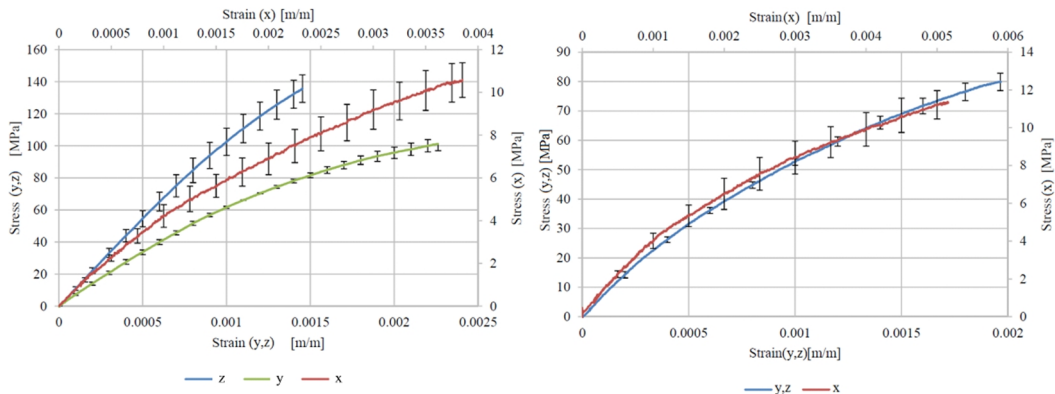


Figure 86. Left: flexural strength of CFC. Right: flexural strength of MoGr [14].

Due to the low strain hardening, MoGr and CFC are initially modelled as elastic orthotropic materials. Nonlinearities related to plasticization of the copper matrix are on the other hand observed in CuCD, for which a power hardening law based on Hollomon's plasticity (2.14) is included in the material model.

### 5.4.4 Summary of results

A summary of the thermo-physical results obtained on CFC, MoGr and CuCD, and showed in the previous section, is given in Table 18.

Table 18: Summary of thermo-physical properties of the collimator materials; results reported are at room temperature. For temperature-dependent results, see Figure 81 and Figure 82.

Property	Direction	CFC	MoGr	CuCD
Density (kg m <sup>-3</sup> )	–	1.89	2.50	5.25
Thermal diffusivity (mm <sup>2</sup> s <sup>-1</sup> )	<i>x</i>	40.4	31.4	189.2
	<i>y</i>	173.6	468.9	189.2
	<i>z</i>	226.7	468.9	189.2
Specific heat (J kg <sup>-1</sup> K <sup>-1</sup> )	–	712	601	340
Thermal conductivity (W m <sup>-1</sup> K <sup>-1</sup> )	<i>x</i>	54.2	47.2	337.9
	<i>y</i>	233.1	706.2	337.9
	<i>z</i>	304.4	706.2	337.9
Thermal expansion coefficient (μm m <sup>-1</sup> K <sup>-1</sup> )	<i>x</i>	10.89	11.70	6.56
	<i>y</i>	–0.80	1.33	6.56
	<i>z</i>	–0.80	1.33	6.56
Young's modulus (GPa)	<i>x</i>	2.8	4.7	160.0
	<i>y</i>	57.5	76.7	160.0
	<i>z</i>	93.0	76.7	160.0
Shear's modulus (GPa)	<i>xy</i>	3.5	3.8	75
	<i>yz</i>	10.6	33.0	75
	<i>zx</i>	6.5	3.8	75
Poisson's ratio (–)	<i>xy</i>	0.11	0.10	0.07
	<i>yz</i>	0.10	0.16	0.07
	<i>zx</i>	0.10	0.10	0.07
Flexural strength (MPa)	<i>x</i>	10.7	11.5	104
	<i>y</i>	102	80	104
	<i>z</i>	133	80	104
Flexural strain to failure (μm m <sup>-1</sup> )	<i>x</i>	3820	5140	5750
	<i>y</i>	2260	1960	5750
	<i>z</i>	1470	1960	5750

## 5.5 Glossary

Symbols are listed in chronological order with respect to their appearance in the text.

<b>Symbol</b>	<b>Definition</b>	<b>SI unit</b>
$E_k$	Kinetic energy	J
$\Delta t$	Bunch spacing	s
$N_b$	Number of bunches	–
$n_b$	Number of particles per bunch	–
$E_{tot}$	Beam stored energy	J
$L_{ring}$	LHC circumference	m
$R_{ring}$	LHC bending radius	m
$f_{ring}$	LHC revolution frequency	Hz
$x$	Transversal coordinate in the collimator reference system	m
$y$	Vertical coordinate in the collimator reference system	m
$z$	Longitudinal coordinate in the collimator reference system	m
$p$	Pressure	Pa
$\rho$	Density	kg·m <sup>-3</sup>
$K$	Bulk modulus	Pa
$E$	Energy density	J·m <sup>-3</sup>
$\gamma_0$	Grüneisen parameter	–
$\alpha$	Thermal expansion coefficient	K <sup>-1</sup>
$\rho_0$	Initial density	kg·m <sup>-3</sup>
$c_v$	Specific heat capacity at constant volume	J·kg <sup>-1</sup> ·K <sup>-1</sup>

$\varepsilon$	Strain	–
$S_{ij}$	Components of the compliance matrix	Pa
$\sigma$	Stress	Pa
$E$	Young's modulus	Pa
$G$	Shear modulus	Pa
$\nu$	Poisson's ratio	–
$\lambda_{f,i}$	i-th flexural frequency	Hz
$L$	Length of the rod	m
$I$	Moment of inertia of the rod	m <sup>4</sup>
$A$	Section of the rod	m <sup>2</sup>
$\beta_{f,i}$	Constant of the i-th flexural mode associated to the boundary conditions	–
$\lambda_{t,i}$	i-th torsional frequency	Hz
$\beta_{t,i}$	Constant of the i-th torsional mode associated to the boundary conditions	–
$[M]$	Mass matrix	kg
$[K]$	Stiffness matrix	N·m <sup>-1</sup>
$\{\ddot{u}\}$	Acceleration vector	m·s <sup>-2</sup>
$\{u\}$	Displacement vector	m
$\lambda_i$	i-th eigenvalue	s <sup>-2</sup>
$\{\Phi_i\}$	i-th eigenvector	m
$\omega_i$	Circular natural frequency	rad·s <sup>-1</sup>

## References

- [1] G. Aad *et al.* (2012). Observation of a new particle in the search for the Standard Model Higgs boson with the ATLAS detector at the LHC. *Physics Letters B*, Vol. 716 1, pp. 1–29.

- 
- [2] G. Apollinari, I. Béjar Alonso, O. Brüning, M. Lamont and L. Rossi (2015). High-Luminosity Large Hadron Collider (HL-LHC): Preliminary Design Report (CERN). *Rep. CERN*, CERN-2015-005.
  - [3] R. Assmann *et al.* (2002). Requirements for the LHC Collimation System. *Proc. EPAC 2002*, Paris, France.
  - [4] A. Dallocchio (2008). Study of thermomechanical effects induced in solids by high-energy particle beams: analytical and numerical methods. *CERN-THESIS-2008-140*.
  - [5] A. Dallocchio *et al.* (2011). LHC collimators with embedded beam position monitors: a new advanced mechanical design. *Proc. IPAC'11*, San Sebastián, Spain.
  - [6] F. Carra *et al.* (2014). Mechanical engineering and design of novel collimators for HL-LHC. *Proc. IPAC'14*, Dresden, Germany.
  - [7] E. Quaranta *et al.* (2016). Towards optimum material choices for HL-LHC collimator upgrade. *Proc. IPAC'16*, Busan, Korea.
  - [8] O. Brüning *et al.* (2004). LHC Design report. *Rep. CERN*, CERN-2004-003-V-1, ISSN 0007-8328.
  - [9] A. Bertarelli *et al.*, (2013). Updated robustness limits for collimator materials. *Proceedings of the 2013 MPP Workshop*, CERN-ACC-2014-0041, Annecy, France.
  - [10] J. P. Koutchouk and A. Szeberenyi (2014). EuCARD: final project report. *Rep. CERN*, EuCARD-BOO-2014-006.
  - [11] A. Bertarelli, F. Carra, N. Mariani and S. Bizzaro (2014). Development and testing of novel advanced materials with very high thermal shock resistance. *Proc. Tungsten, Refractory and Hardmetals Conference*, Orlando, May 2014.
  - [12] A. Bertarelli *et al.* (2015). Innovative MoC – graphite composite for thermal management and thermal shock applications. *31<sup>st</sup> Thermal Measurement, Modeling & Management Symposium (SEMI-THERM)*, pp. 56–59, ISSN 1065-2221.

- 
- [13] J. Guardia (2015). Development and characterization of a novel graphite-matrix composite material for thermal management applications. Master thesis, Universidad de Zaragoza, CERN-THESIS-2015-360.
- [14] M. Borg (2016). Numerical modelling and experimental testing of novel materials for LHC collimators. *Master thesis*, University of Malta.
- [15] L. Bianchi (2017). Thermophysical and mechanical characterization of advanced materials for the LHC collimation system. Master thesis, Università di Pisa, CERN-THESIS-2017-043.
- [16] N. Mariani (2014). Development of Novel, Advanced Molybdenum-based Composites for High Energy Physics Applications, CERN-THESIS-2014-363.
- [17] E. Quaranta (2017). Investigation of collimator materials for the High-Luminosity Large Hadron Collider. *PhD thesis*, Politecnico di Milano.
- [18] M. Kitzmantel (2015). Developments and Novelties in Thermal Management by RHP-Technology. *EuCARD-2 Workshop on Applications of Thermal Management Materials*, 6 November 2015, CERN.
- [19] ASTM E1269-11 (2011). Standard Test Method for Determining Specific Heat Capacity by Differential Scanning Calorimetry. *American Society for Testing and Materials International*.
- [20] ASTM E228-11 (2011). Standard Test Method for Linear Thermal Expansion of Solid Materials With a Push-Rod Dilatometer. *American Society for Testing and Materials International*.
- [21] ASTM E1461-13 (2013). Standard Test Method for Thermal Diffusivity by the Flash Method. *American Society for Testing and Materials International*.
- [22] J. J. Buck, D. L. McDowell and M. Zhou (2013). Microstructure-performance relations of ultra-high-performance concrete accounting

for effect of alpha-quartz-to-coesite silica phase transformation. *International Journal of Solids and Structures*, Vol. 50 pp. 1879–1896.

- [23] ASTM C1259-01 (2001). Standard Test Method for Dynamic Young's Modulus, Shear Modulus, and Poisson's Ratio for Advanced Ceramics by Impulse Excitation of Vibration. *American Society for Testing and Materials International*.
- [24] ASTM C747-93 Standard Test Method for Moduli of Elasticity and Fundamental Frequencies of Carbon and Graphite Materials by Sonic Resonance. *American Society for Testing and Materials International*.
- [25] “Ansys Mechanical User’s Guide – Release 15.0”, ANSYS, Inc. (2013).
- [26] ASTM C1161-02c (2002). Standard Test Method for Flexural Strength of Advanced Ceramics at Ambient Temperature. *American Society for Testing and Materials International*.

## Chapter 6

# Experimental testing of novel materials under quasi-instantaneous heat deposition

In order to evaluate the response of materials to quasi-instantaneous heating, constitutive models are built on the basis of laboratory measurements, such as those described in section 5.4. The verification of material models must be performed through experimental tests where the thermal load is applied with an isochoric process: as seen in Chapter 1, this is possible by means of lasers, electrical pulse and proton or ion beams. However, the energy deposited by a laser has a penetration depth of few microns; in tests under electric pulsed current, on the other hand, the geometry is limited to thin wires, which can be typically machined out of metals only. For tests with proton or ion beams, the highest thermal energies can be reached experimentally in facilities connected to high-energy particle accelerators. Currently, the most energetic beam for material testing under proton and ion impact is provided at the HiRadMat facility [1], at CERN. A test in HiRadMat, named *HRMT-23*, was performed in 2015 [2] to verify the response of LHC and HL-LHC collimator jaws made of CFC, CuCD and MoGr, comparing the experimental results with the numerical simulations to verify the validity of the models developed. The jaws were also tested under loads equivalent to the accidental scenarios reported in section 5.2, to validate the experimental choices for HL-LHC collimators. This chapter focuses on the experimental details of *HRMT-14*, including the design and preparation, instrumentation and post-mortem observations and measurements.

### 6.1 The HiRadMat facility at CERN

HiRadMat (*High irRadiation to Materials*) is a facility dedicated to material testing under high-intensity pulsed particle beams, built at CERN in 2011 [1]. Previous

tests of robustness and damage effects on BIDs and material specimens were performed in ad-hoc installations in the SPS TT40 transfer beam line to LHC and CNGS in 2004 and 2006 (section 1.4). The difficulty in performing such important tests on temporary installations and the potential impact on operating transfer lines were the main motivations for building HiRadMat, which was purposely designed to study beam shock impacts on materials and accelerator components.

HiRadMat uses an extracted primary proton or ion beam from the SPS (Figure 73). The main beam parameters are listed in Table 19. The beam spot size at the focal point of the experiment can be varied from 0.05 to 5 mm<sup>2</sup>, which, together with the variable beam intensity, offers sufficient flexibility to test materials at different deposited energy densities (Figure 87).

Table 19: HiRadMat beam parameters.

	<b>Protons</b>	<b>Ions (Pb<sup>82+</sup>)</b>
$E_k$ (GeV)	440	173.5
$N_{b,max}$	288	52
$n_{b,max}$	$1.7 \times 10^{11}$	$7 \times 10^9$
$n_{tot,max}$	$4.9 \times 10^{13}$	$3.6 \times 10^{11}$
$E_{tot,max}$ (kJ)	31 400	21
$\Delta t_{min}$ (ns)	25	100
$t_d$ ( $\mu$ s)	7.2	5.2

Beyond the needs of CERN, HiRadMat is open to other users and is also included in the ARIES HORIZON2020 European Project<sup>27</sup> in the transnational access program, to facilitate its use by international teams. HiRadMat is not an irradiation facility, where large doses on equipment can be accumulated. It is rather a test area, designed to perform single experiments to evaluate the effect of high-intensity pulsed beams on materials or accelerator component assemblies in a controlled environment. The facility is designed for a maximum of  $10^{16}$  protons per year, distributed among 10 experiments, each having a total of  $10^{15}$  protons or about 100 high-intensity pulses. This limit allows reasonable cool-down times for the

<sup>27</sup> <http://aries.web.cern.ch/>

irradiated objects (from a few months to a year) before they can be analysed in specialized facilities.

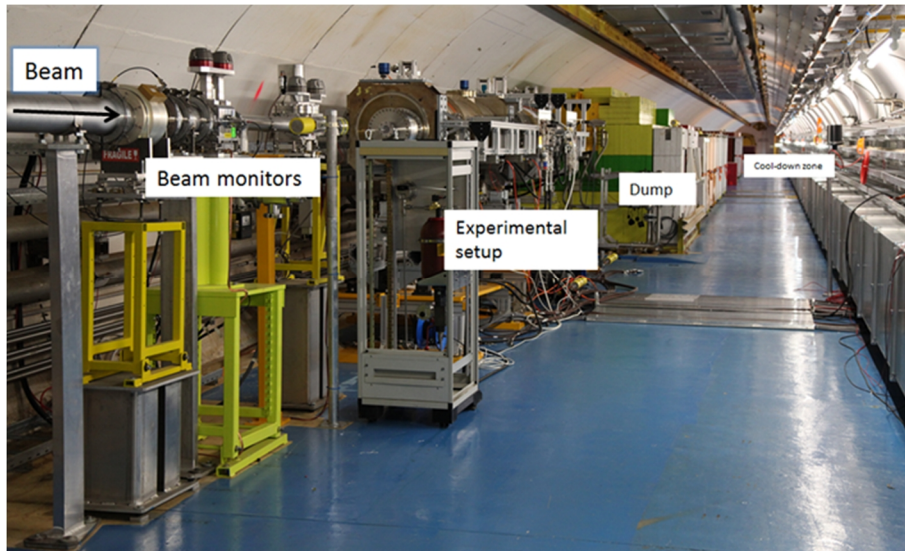


Figure 87. HiRadMat facility, experimental area.

## 6.2 Collimator materials under proton impact: the HRMT-23 experiment

In order to qualify the new collimator design (Figure 75) and the advanced materials against the nominal and accidental scenarios defined for HL-LHC, as well as to benchmark the models derived from experimental test in laboratory and used in numerical models, an experiment, named *HRMT-23*, was performed at the CERN HiRadMat facility in July 2015.

### 6.2.1 Design and experimental set-up

HRMT-23 involved the testing under direct SPS beam impact of three collimator jaws (Figure 88):

- LHC secondary collimator jaw in CFC
- HL-LHC jaw in MoGr
- HL-LHC jaw in CuCD

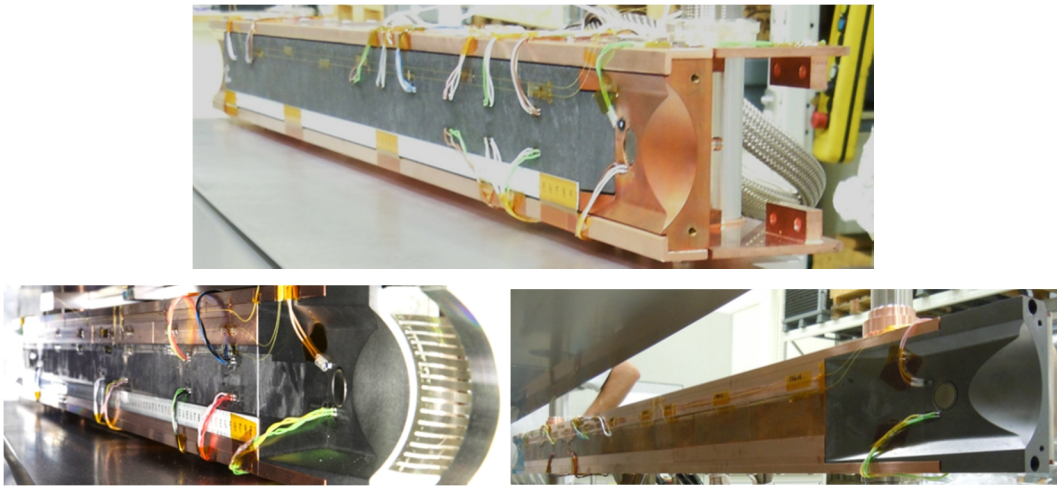


Figure 88. CFC (top), MoGr (bottom left) and CuCD (bottom right) jaws.

The three jaws were positioned inside a stainless steel tank, maintained under vacuum to avoid possible contamination to the external ambient in case debris were generated by the intense beam impacts. The tank was equipped with radiation-hard optical windows, to allow the visual inspection of the jaws during and after the experiment; after past experiences of HiRadMat tests such as HRMT-14 [3], a movable protection system was studied to shield the optical windows against impact-generated debris, which would have impeded the visual access to the jaws (Figure 89).

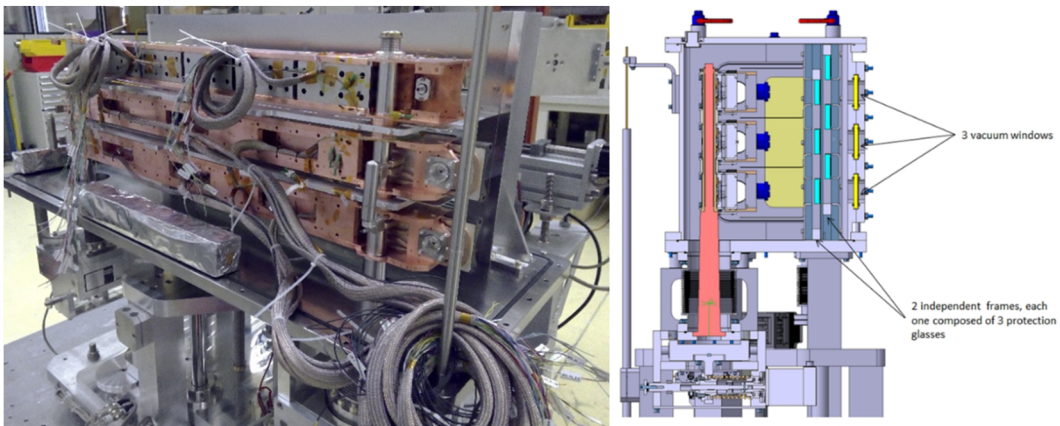


Figure 89. Left: three-jaw stack, simply supported at the extremities. Right: tank section view. Note the vacuum windows position and the protection shielding.

The beamline vacuum windows were made of CFC-reinforced beryllium, designed to withstand the maximum intensity of the SPS beam. The horizontal actuation system was inspired by collimator movable tables, with a total stroke of 35 mm in order to allow impacting each jaw at several depths; vertically, the

actuation involved the movement of the whole tank, with a stroke of  $\pm 140$  mm to completely cover the three-jaw stack. The test bench (Figure 90) was assembled and instrumented in a building on the surface, placed on an aluminium table, and then transported in the HiRadMat tunnel. The total mass of the test bench with the jaws was roughly 1600 kg.



Figure 90. HRMT-23 test bench. The light for visual inspections is provided by a LED system.

## 6.2.2 Instrumentation

In order to gather as much as possible information on the jaw response to the proton beam impacts, an extensive instrumentation system was developed. Radiation-hard measurement devices were embarked in the test bench or in direct proximity, while the most delicate instruments were located inside a protected bunker, in the tunnel parallel to the target area (Figure 91), and the optical path to the target area was provided by mirrors.

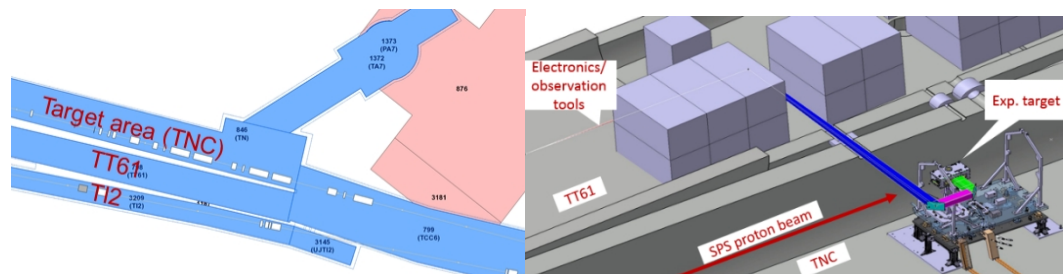


Figure 91. Left: HiRadMat experimental area. Right: bunker for the electronics.

Table 20: HRMT-23 instrumentation summary.

HRMT-23 instrumentation	Sampling frequency
Electrical strain gauges	4 MHz
Temperature probes	200 Hz
Optical microphones	50 kHz
Water pressure sensor	100 kHz
Fiber Bragg grating	500 Hz
US probes (Omniscan)	–
Inspection HD Camera (4K)	–
High-Speed Camera	20 kfps
Laser-Doppler Vibrometer	4 MHz

*Strain gauges.* A total of 126 strain gauges were installed on the three jaws to monitor the propagation of the stress wave provoked by the particle beam impact in the absorber and housing. With reference to Figure 92, each measurement point featured two strain gauges, oriented at  $0^\circ/90^\circ$  with respect to the beam axis to measure strains along  $z$  and  $x/y$ . A special high-temperature glue was used to fix the strain gauges to the jaw material.

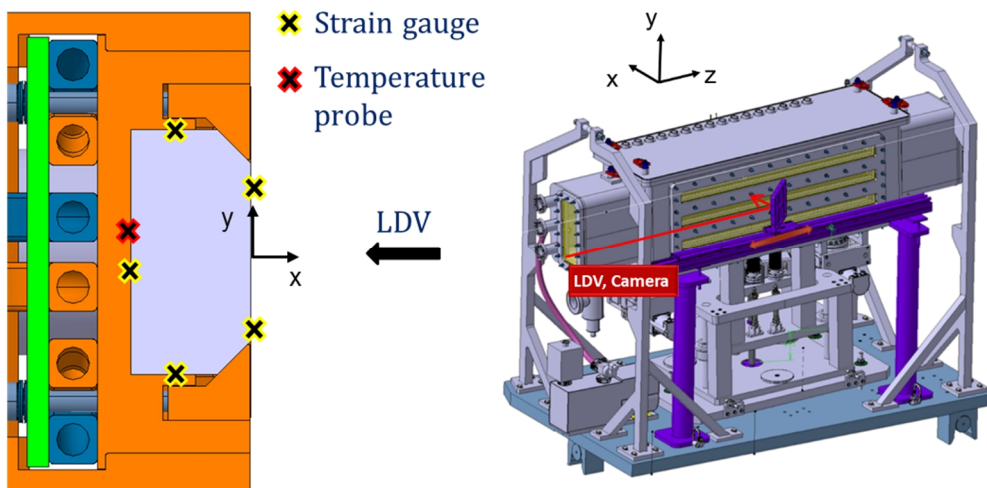


Figure 92. Left: HL-LHC jaw section, strain gauge and temperature probe configuration. Right: movable mirror for laser-Doppler vibrometer and HD camera acquisition.

*Temperature probes.* In total, 42 temperature probes measured online the temperature evolution on the absorber blocks (Figure 92, Figure 93), to evaluate the

thermal response of the system as a function of the different thermal resistances, as well as to define the minimum time interval for adequate cooling between two subsequent high-intensity shots.



Figure 93. Strain gauges and temperature probes on CFC (left) and CuCD (right) jaws.

*Optical microphones.* In collaboration with Graz University of Music and Performing Arts<sup>28</sup> (KUG) and XARION Laser Acoustics<sup>29</sup>, two optical microphones were also installed in proximity of the test bench. The goal was to validate the radiation hardness of the microphone and correlate the beam impact with the acoustic response of the target, in view of possible future installation of the microphones in the LHC as a diagnostic system in case of accidental beam impacts.

*Water pressure sensors.* The two HL-LHC jaw cooling circuits were filled with water and connected to an expansion reservoir; sensors were used to measure the pressure burst in the coolant (Figure 94).

*Optical fibres.* Optical fibres were adopted to measure the deformations of the Glidcop housing (Figure 94). Because of the relatively low acquisition rate of this system, the fibres were not used to benchmark the strain gauge acquisition of the shockwave propagation, but slower phenomena such as flexural vibrations, as well as to detect possible plastic strain of the jaw. Out-of-axis plastic deformations of the jaw would increase the flatness error of the active jaw surface, which has a maximum acceptable value of 100  $\mu\text{m}$  [4].

<sup>28</sup> <https://www.kug.ac.at/kunstuniversitaet-graz.html/>

<sup>29</sup> <http://xarion.com/>

*Ultrasound probes.* On brittle materials, the beam impact could provoke internal cracking and delamination that, online, are not visible with optical systems such as the video cameras. Special probes were installed on the most loaded absorber block of each jaw, with the purpose of detecting such phenomena. The working principle is based on the ultrasonic wave propagation and reflection against free surfaces: the system generates a planar stress wave, propagating through the whole material and reflects back to the probe, which registers the frequency and amplitude of the signal. If a fracture surface is created due to the beam impact, the wave will reflect earlier to the probe and its frequency will be higher.



Figure 94. Left: water reservoir connections for the two HL-LHC jaws. Right: optical fibres on the CuCD jaw.

*High-definition and high-speed cameras.* A HD camera was adopted to verify, after each impact, the integrity of the jaw. It made use of the LDV movable mirror (see Figure 92), to allow a full scan over the jaw length. In case of very high intensity impacts, the CuCD jaw was expected to experience local melting with fracture induced in the surroundings by the propagating stress wave, in particular after reflection with the free surface. The debris produced by spallation were visualized with a high-speed camera, with a maximum sampling frequency of 20 kHz, for a future comparison with SPH simulations (see section 4.5).

*Laser-Doppler vibrometer.* As successfully tested in HRMT-14, the particle horizontal velocity on the free surface of the absorber was measured with an LDV, with a maximum amplitude of 24 m/s.

### 6.2.3 Beam parameters

Several tests at medium and high intensity were performed to evaluate the response of the three jaws. The jaws were impacted by beam pulses at increasing stored energy for a total of 150 impacts. A summary of the test conditions is given in Table 21. The integral number of impacting bunches was about 8500, while the total proton budget was  $1 \times 10^{15}$ .

Table 21: HRMT-23 parameters.  $\eta_x$  is the horizontal distance between the impact point and the free surface of the jaw absorber,  $N_p$  is the total number of thermal pulses,  $E_{tot}$  is the maximum energy stored in a proton pulse.

<b>HRMT-23 summary</b>	
$E_k$ (GeV)	440
$\Delta t$ (ns)	25
$t_{d,max}$ ( $\mu$ s)	7.2
$n_{b,max}$	$1.3 \times 10^{11}$
$n_{tot}$	$1.3 \times 10^{11} \div 3.8 \times 10^{13}$
$E_{tot}$ (MJ)	2.7
$\sigma_x, \sigma_y$ (mm)	0.35 $\div$ 1
$\eta_x$ (mm)	0.18 $\div$ 5
$N_p$	150

All the 150 thermal pulses are of relevant scientific interest in the scope of this work, as they fall within the quasi-instantaneous heating scenario. On the other hand, in terms of validation of materials for use in HL-LHC collimators, it was important to reproduce the accidental design cases discussed in section 5.2, and notably:

- A. *CuCD jaw*: the material is proposed for tertiary collimators and it should sustain the impact of 1 bunch at 7 TeV provoked by an asynchronous beam dump, for a total stored energy of 260 kJ.
- B. *MoGr and CFC jaws*: to be installed (or already installed, in the case of CFC) in primary and secondary collimators, the failure scenario is the beam injection error, consisting in an impact of 288 bunches at 450 GeV

on the absorber. Each HL-LHC bunch has a population of  $2.3 \times 10^{11}$  protons, for a total intensity of the pulse of  $6.6 \times 10^{13}$  protons and a stored energy of 4.6 MJ.

However, in HRMT-23 the beam momentum was different from both *case A* and *case B*, as the facility adopts a 440 GeV beam. In order to qualify the materials for use in the HL-LHC jaws, the objective was thus to reproduce with the HiRadMat beam the same energy and energy density of HL-LHC. This was easily achievable for *case A*, as the energy involved is much smaller than the maximum available in HiRadMat, see Table 21. On the other hand, *case B* is, in terms of energy, above the possibilities of any existing proton testing facility. To reproduce this scenario at least in terms of energy density deposited on the jaw, it was decided to squeeze the HiRadMat beam, reducing its transverse dimension. In Figure 95 it is possible to notice how the energy peak obtained on MoGr in the HL-LHC beam injection error, where the beam sigma is 0.61 mm, can be met by reducing the beam sigma to 0.35 mm and using the top HiRadMat intensity instead.

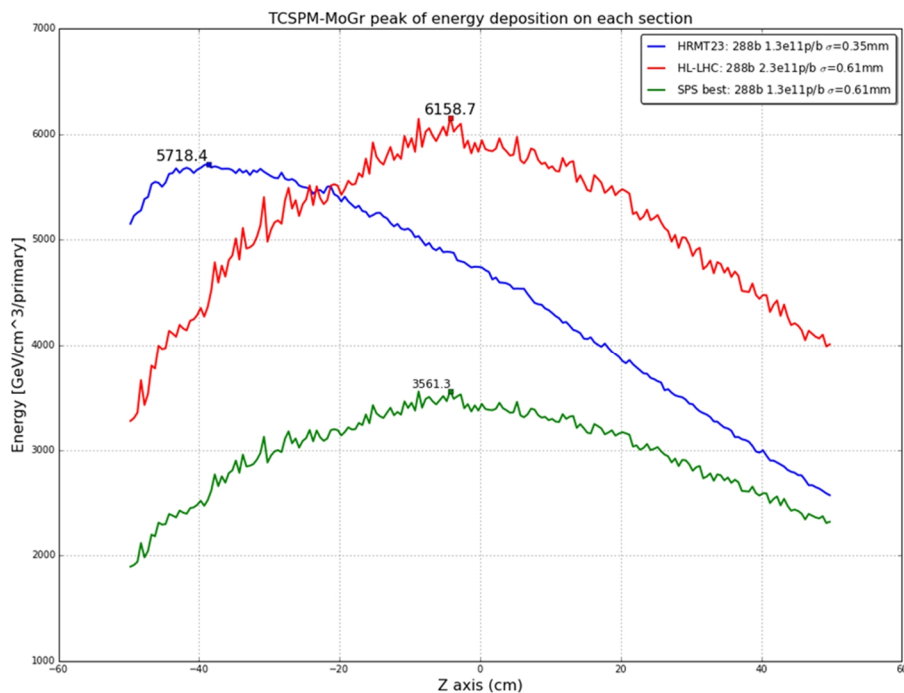


Figure 95. Comparison of peak energy depositions on MoGr for HL-LHC and HiRadMat beams. Fluka analysis courtesy of E. Skordis.

## 6.3 HRMT-23 experimental results

We examine in this section the main results observed offline on the HRMT-23 jaws, at the end of the experiment and after the tank opening, occurred in November 2016. The results in real time acquired with the active instrumentation system will be analyzed for selected case studies, and compared with numerical simulations, in Chapter 7.

### 6.3.1 CFC jaw

The CFC jaw installed in HRMT-23 features a design identical to the configuration currently adopted in the LHC, and it represents the former baseline for secondary collimators. The main differences with respect to the new HL-LHC jaw, described in section 5.2, are: lower flexural stiffness, worse thermal contact between the components (as the clamping force was provided by springs instead of screws), monolithic absorber in CFC, tapering in Glidcop Al-15 instead of MoGr. In particular, concerning the tapering, the requirement is to adopt a material with adequate electrical conductivity, for the transmission of the electro-magnetic signal of the hosted BPM. MoGr's electrical conductivity is high enough to qualify its use for the tapering; this is the solution proposed for HL-LHC collimators, as MoGr is more resistant to beam impacts compared to Glidcop, for the considerations made in section 5.2. This was confirmed during HRMT-23 by the failure due to melting and spallation of the Glidcop tapering (Figure 96).

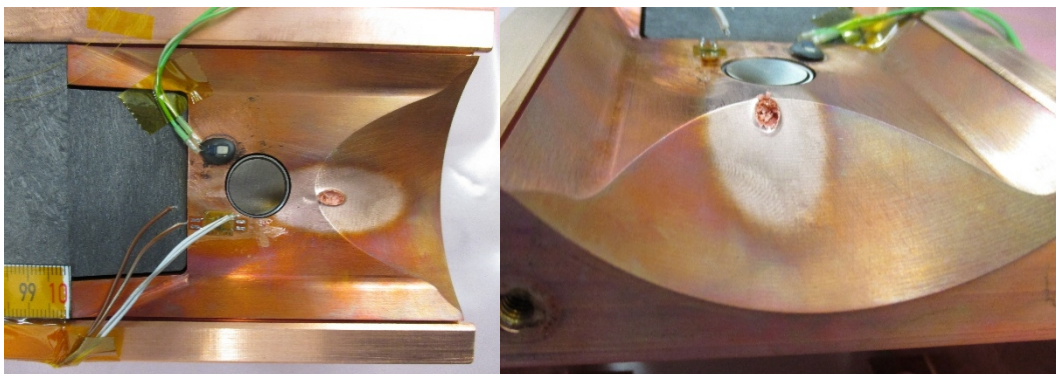


Figure 96. Views of the damage on the downstream Glidcop tapering of the CFC jaw. The high temperatures generated by the impact are also highlighted by the oxidation of the Glidcop surface and of the BPM button.

As anticipated, the jaws were submitted to increasing intensity shots, to evaluate the threshold of damage of the adopted materials. Inspections with the high-definition camera performed during the tests did not put in evidence visible

damage on the jaw for intensities lower than 144 bunches. The CFC jaw was submitted to 13 impacts at the intensity of 144 or 288 bunches, with two different beam sigmas, 0.35 and 0.61 mm. The other main parameter changing during the 13 high-intensity pulses was the distance between the impact point and the free surface  $\eta_x$ , also known as *impact depth*. Small impact depths are typically more severe for the absorber, as the compressive wave induced by the thermal energy deposition immediately turns into a tensile wave, potentially provoking spallation on the free surface. Higher impact depths are less severe for the absorber, as the distance from the free surface is higher and the tensile wave eventually produced after reflection has smaller amplitude, because of the decay related to the cylindrical problem. However, a higher  $\eta_x$  is potentially harmful for the elements surrounding the jaw, such as the cooling pipes and the tapering. The tapering surface is, in fact, offset from the absorber free surface by 8 mm (negative  $x$  in Figure 92). The characteristics of the 13 high-intensity pulses on CFC are reported in Table 22.

Table 22: HRMT-23, high-intensity impacts on the CFC jaw.  $N_b$  is the number of bunches,  $n_{tot}$  the pulse intensity,  $E_{tot}$  the stored beam energy,  $t_d$  the pulse length,  $\eta_x$  and  $\eta_y$  are the horizontal and vertical beam impact coordinate with respect to the origin of the coordinate system defined in Figure 92.

<b>Impact identifier</b>	$N_b$	$n_{tot}$	$E_{tot}$ (MJ)	$t_d$ ( $\mu$ s)	$\sigma$ (mm)	$\eta_x$ (mm)	$\eta_y$ (mm)
#1	144	$1.48 \times 10^{13}$	1.04	3.80	0.35	-1.75	+5.00
#2	144	$1.49 \times 10^{13}$	1.05	3.80	0.35	-1.05	+5.00
#3	144	$1.49 \times 10^{13}$	1.05	3.80	0.35	-0.18	+5.00
#4	144	$1.86 \times 10^{13}$	1.31	3.80	0.35	-1.75	+2.50
#5	144	$1.88 \times 10^{13}$	1.32	3.80	0.35	-1.05	+2.50
#6	144	$1.84 \times 10^{13}$	1.30	3.80	0.35	-0.18	+2.50
#7	288	$3.66 \times 10^{13}$	2.58	7.85	0.61	-3.05	-5.00
#8	288	$3.78 \times 10^{13}$	2.66	7.85	0.61	-1.83	-5.00
#9	288	$3.73 \times 10^{13}$	2.63	7.85	0.61	-0.30	-5.00
#10	288	$3.69 \times 10^{13}$	2.60	7.85	0.35	-1.75	-2.50
#11	288	$3.77 \times 10^{13}$	2.65	7.85	0.35	-1.05	-2.50
#12	288	$3.69 \times 10^{13}$	2.60	7.85	0.35	-0.18	-2.50
#13	288	$3.79 \times 10^{13}$	2.67	7.85	0.35	-5.00	-2.50

As we will see in Chapter 7, the failure of the tapering was provoked by *impact #13*, which is the farthest from the free surface of the jaw (and closer to the BPM button).

Concerning the absorber, no major fracture is highlighted on the free surface. The only traces of the beam impacts are two very light parallel scratches, at the vertical positions  $\eta_y = -2.5 \text{ mm}$  and  $\eta_y = +2.5 \text{ mm}$  (Figure 97). It is not easy at this stage to define whether this is a surface damage, or simply the local detachment of the graphite powders present on the surface after the machining of the component. However, it is clear that, even in the case of a surface damage, the functional behaviour of the component in operation would still be guaranteed, as the jaw inside the collimator tank could be shifted vertically by  $\pm 10 \text{ mm}$ , exposing a fresh surface to the beam passage. This confirms that the CFC jaw is overall robust to particle beam impacts equivalent, in terms of energy density, to the HL-LHC design accidental scenarios.

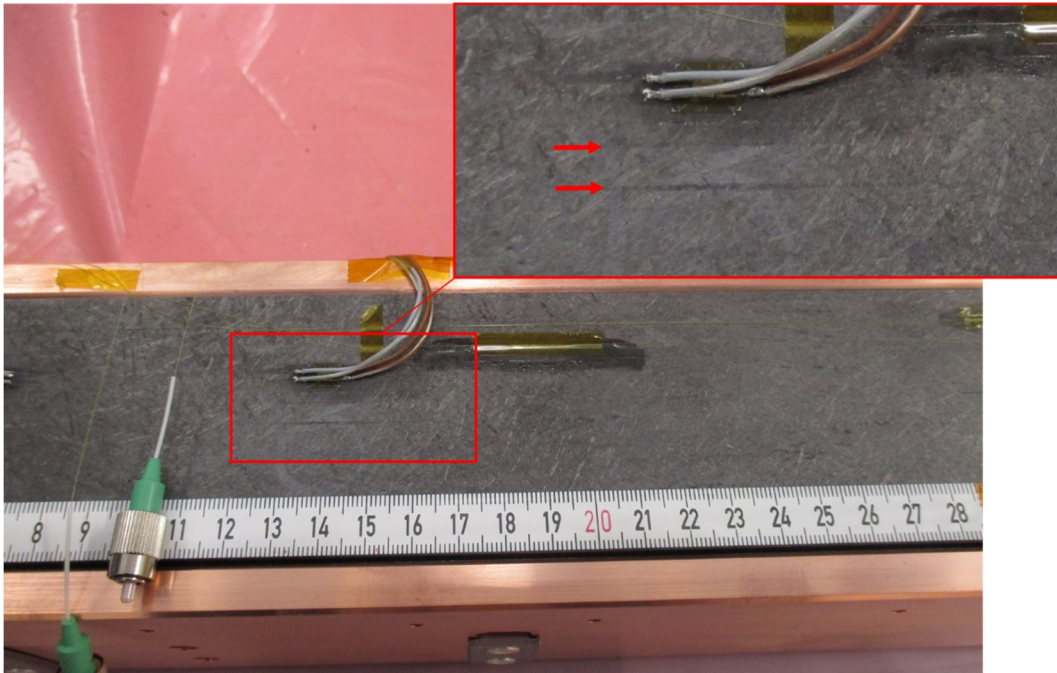


Figure 97. View of a section (between 80 and 280 mm along  $z$ ) of the CFC jaw after extraction from the tank. Top right: zoom of the two scratches at  $\eta_y = -2.5 \text{ mm}$  and  $\eta_y = +2.5 \text{ mm}$ .

At the current stage, the visual inspection performed after dismounting did not put in evidence further damage to other components of the jaw. Future

non-destructive and destructive observations will be done to better evaluate the state of elements such as housing, cooling pipes and stiffener.

### 6.3.2 MoGr jaw

The MoGr jaw was built according to the HL-LHC configuration presented in section 5.1. In this case, on top of the absorber, also the tapering is made of MoGr. MoGr, because of its low density, is proposed to replace CFC in primary and secondary collimators. The design scenarios for the two materials are therefore the same. The jaw was tested at increasing intensities, with a number of high-intensity impacts (144 bunches or more) comparable to that of CFC (Table 23).

Table 23: HRMT-23, high-intensity impacts on the MoGr jaw.

<b>Impact identifier</b>	$N_b$	$n_{tot}$	$E_{tot}$ (MJ)	$t_d$ ( $\mu$ s)	$\sigma$ (mm)	$\eta_x$ (mm)	$\eta_y$ (mm)
#14	144	$1.45 \times 10^{13}$	1.02	3.80	0.61	-3.05	-2.50
#15	144	$1.48 \times 10^{13}$	1.04	3.80	0.61	-1.83	-2.50
#16	144	$1.44 \times 10^{13}$	1.01	3.80	0.61	-0.30	-2.50
#17	144	$1.87 \times 10^{13}$	1.32	3.80	0.61	-3.05	-5.00
#18	144	$1.79 \times 10^{13}$	1.26	3.80	0.61	-1.83	-5.00
#19	144	$1.80 \times 10^{13}$	1.27	3.80	0.61	-0.30	-5.00
#20	216	$2.76 \times 10^{13}$	1.94	5.825	0.61	-3.05	-3.75
#21	216	$2.82 \times 10^{13}$	1.99	5.825	0.61	-1.83	-3.75
#22	216	$2.78 \times 10^{13}$	1.96	5.825	0.61	-0.30	-6.50
#23	288	$3.80 \times 10^{13}$	2.68	7.85	0.61	-3.05	-2.50
#24	288	$3.67 \times 10^{13}$	2.59	7.85	0.61	-1.83	-2.50
#25	288	$3.78 \times 10^{13}$	2.66	7.2	0.61	-0.30	-2.50
#26	288	$3.76 \times 10^{13}$	2.65	7.2	0.35	1.75	0
#27	288	$3.79 \times 10^{13}$	2.67	7.2	0.35	1.05	0
#28	288	$3.70 \times 10^{13}$	2.61	7.2	0.35	0.18	0

Compared to the Glidcop tapering adopted in the CFC jaw, the MoGr tapering is undamaged, as shown in Figure 98.

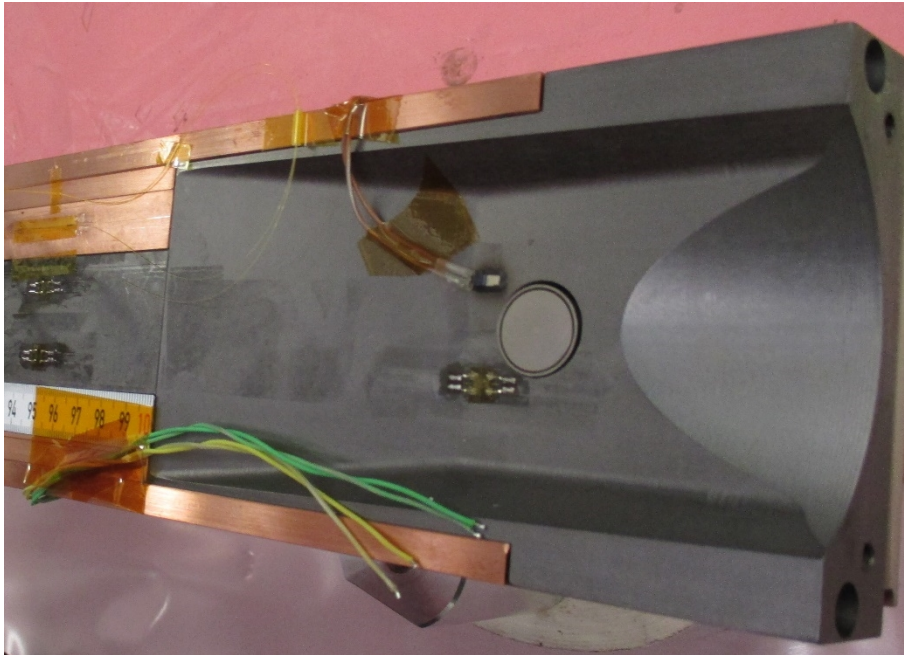


Figure 98. View of the downstream MoGr tapering. No sign of damage to the component or to the BPM is evident.

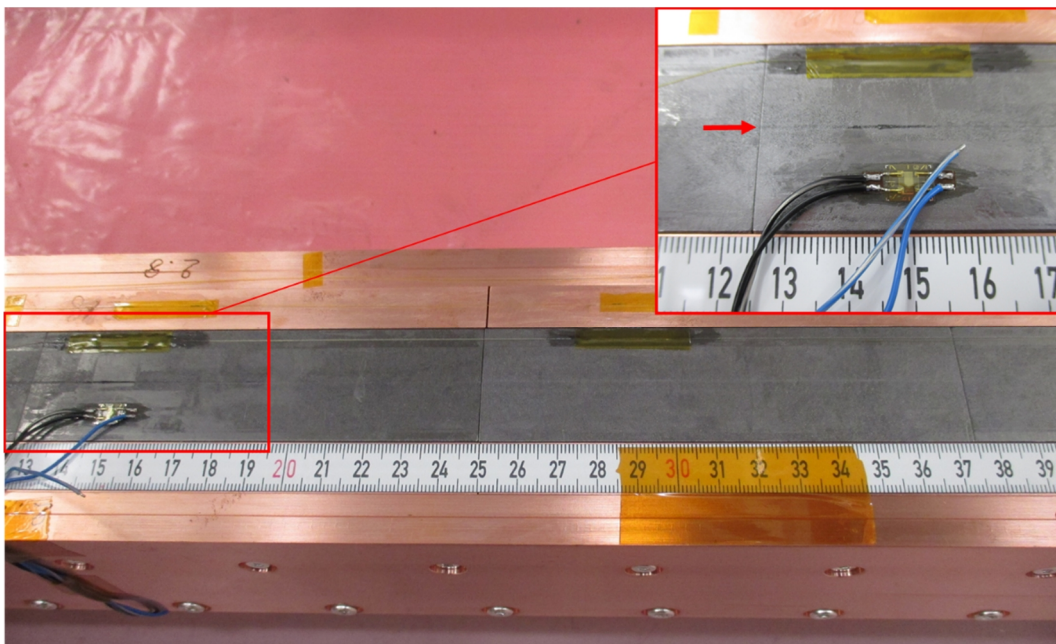


Figure 99. View of a section (between 130 and 390 mm along  $z$ ) of the MoGr jaw after extraction from the tank. Top right: zoom of the scratch at  $\eta_y = 0$ .

Similarly to the case of CFC, the MoGr jaw presents a scratch, shown in Figure 99, at the  $y$  coordinate correspondent to the impact with the minimum  $\eta_x$  (*impact #28*) which is, in this case,  $\eta_y = 0$ . This is coherent with the consideration

made earlier in this chapter, according to which the most severe impact scenarios for carbon-based absorbers are those closer to the free surface, as the stress wave generated by the thermal pulse is immediately reflected into a rarefaction wave, with possible local spallation. Farther from the free surface, the amplitude of the wave quickly decreases because of the cylindrical decay and internal friction, such that the amplitude of the tensile wave, once it originates at the surface, is much less intense.

Also in this case, no sign of damage to the components surrounding the absorber were highlighted during the post-mortem visual inspections.

### **6.3.3 CuCD jaw**

High energy densities on CuCD are reached with less intense proton pulses than CFC and MoGr, because of the higher mass density of the material. For this reason, CuCD is proposed for use in HL-LHC tertiary collimators, replacing the tungsten heavy alloy currently adopted. In this case, the reference design accidental scenario is the asynchronous beam dump, involving the direct impact on the material of 1 bunch at 7 TeV, with a stored energy of 230 kJ. As it can be seen in Table 24, this is equivalent in terms of stored energy to an impact of 24 bunches at 440 GeV in the HiRadMat facility. The jaw was tested also under impacts with intensity higher than 24 bunches, to evaluate the fracture mechanisms of the component.

The CuCD jaw was built according to the HL-LHC configuration. The taperings were therefore in MoGr, and, as in the case of the MoGr jaw, also here the component did not show any damage after the end of the experiment (Figure 100).

Table 24: HRMT-23, medium and high intensity impacts on the CuCD jaw.

<b>Impact identifier</b>	$N_b$	$n_{tot}$	$E_{tot}$ (MJ)	$t_d$ ( $\mu$ s)	$\sigma$ (mm)	$\eta_x$ (mm)	$\eta_y$ (mm)
#29	6	$7.47 \times 10^{12}$	0.05	0.25	0.61	-3.05	0
#30	12	$1.51 \times 10^{12}$	0.11	0.80	0.61	-3.05	0
#31	18	$2.56 \times 10^{12}$	0.18	1.35	0.61	-3.05	0
#32	24	$3.13 \times 10^{12}$	0.22	1.90	0.61	-3.05	0
#33	24	$2.95 \times 10^{12}$	0.21	0.575	0.35	-0.18	+5.00
#34	24	$2.86 \times 10^{12}$	0.20	0.575	0.35	-0.70	+2.50
#35	24	$2.88 \times 10^{12}$	0.20	0.575	0.35	-1.75	0
#36	48	$6.06 \times 10^{12}$	0.43	1.925	0.35	-0.18	-5.00
#37	24	$2.93 \times 10^{12}$	0.21	0.575	0.61	-0.18	+3.75
#38	36	$4.56 \times 10^{12}$	0.32	0.875	0.61	-0.18	+1.25
#39	48	$6.07 \times 10^{12}$	0.43	1.175	0.61	-0.18	+3.75
#40	60	$7.58 \times 10^{12}$	0.53	1.475	0.61	-0.18	+1.25
#41	60	$7.42 \times 10^{12}$	0.52	1.475	0.61	-0.18	+3.75
#42	72	$8.82 \times 10^{12}$	0.62	1.775	0.61	-0.18	+1.25
#43	72	$8.65 \times 10^{12}$	0.61	1.775	0.61	-0.61	+1.25
#44	72	$8.89 \times 10^{12}$	0.63	1.775	0.61	-1.22	0
#45	72	$8.71 \times 10^{12}$	0.61	1.775	0.61	-3.05	-1.25
#46	144	$1.73 \times 10^{13}$	1.22	3.575	0.61	-3.05	-1.25



Figure 100. View of the downstream MoGr tapering of the CuCD jaw. No sign of damage to the component or to the BPM is evidenced.

Due to the structure of the raw CuCD composite, which contains diamonds with a maximum size of 100  $\mu\text{m}$ , the surface flatness is above the value of 40  $\mu\text{m}$  specified for a correct beam cleaning function. A pure copper cladding, with thickness up to 100  $\mu\text{m}$ , is therefore applied to the flat surfaces during the production, to achieve the desired mechanical tolerance. Evidently copper, possessing a density of 8.9  $\text{g}/\text{cm}^3$  compared with the density of the bulk material of 5.4  $\text{g}/\text{cm}^3$ , has a higher stopping power, and relevant energy densities are reached in the cladded area during the beam impact. The pulses close to the free surface of the absorber, such as *impact #33* and *impacts #36-42*, were in the case of the CuCD jaw even more critical than what experienced on CFC and MoGr. In fact, on top of potential fracture of the Cu cladding and of the CuCD composite induced by the rarefaction wave, phenomena of delamination at the cladding/substrate interface could take place. Moreover, the high energy absorption on the copper cladding can lead, at high number of impacting bunches, to local melting of the cladding. This was expected, as it will be seen in Chapter 7, for impacts with at least 36 bunches. The spallation phenomenon of the absorber cladding was acquired with the high-speed camera and is shown in Figure 101.

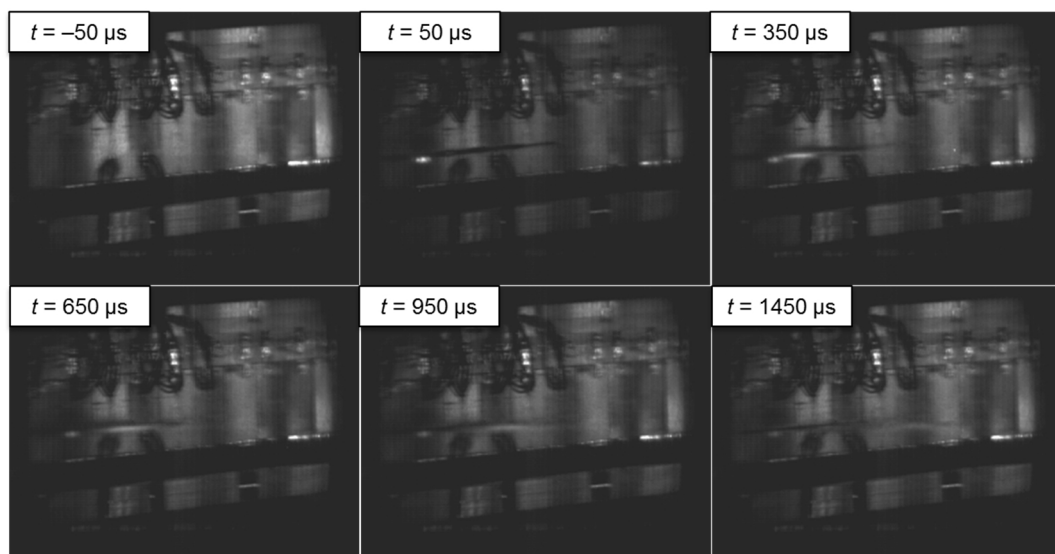


Figure 101. Micro-jetting and micro-spallation of the CuCD jaw under the *impact #39* (48 bunches impacting at a distance of 0.18 mm from the free surface).

In the case of CuCD, damage of the free surface was observed with the high-speed and HD cameras starting from *impact #33* which is equivalent in terms of energy to the asynchronous beam dump design scenario. The damage, compared to what observable on CFC and MoGr, is now more evident, with the removal of

the copper cladding and exposure of the CuCD composite bulk. Post-mortem observations of the jaw highlighted the effects of the impacts at each vertical pulsed position (Figure 102, Figure 103 and Figure 104).

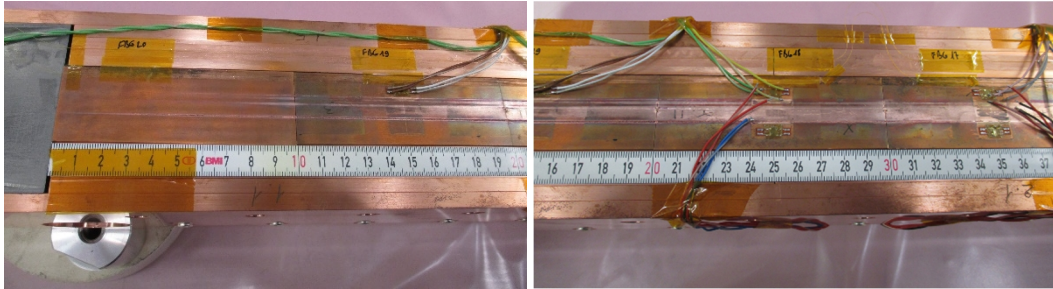


Figure 102. View of the first 37 cm of the CuCD jaw. Note the longitudinal grooves produced by the impacts at medium and high intensity.

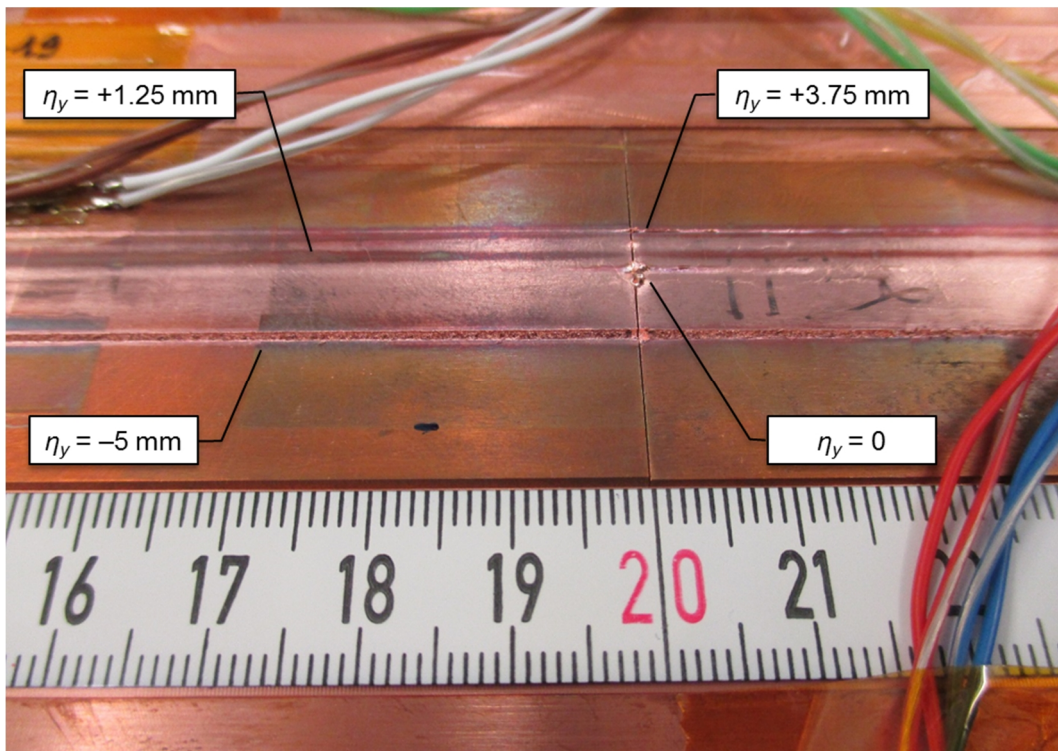


Figure 103. Detailed view of the effect of impacts on the CuCD jaw at different vertical positions.

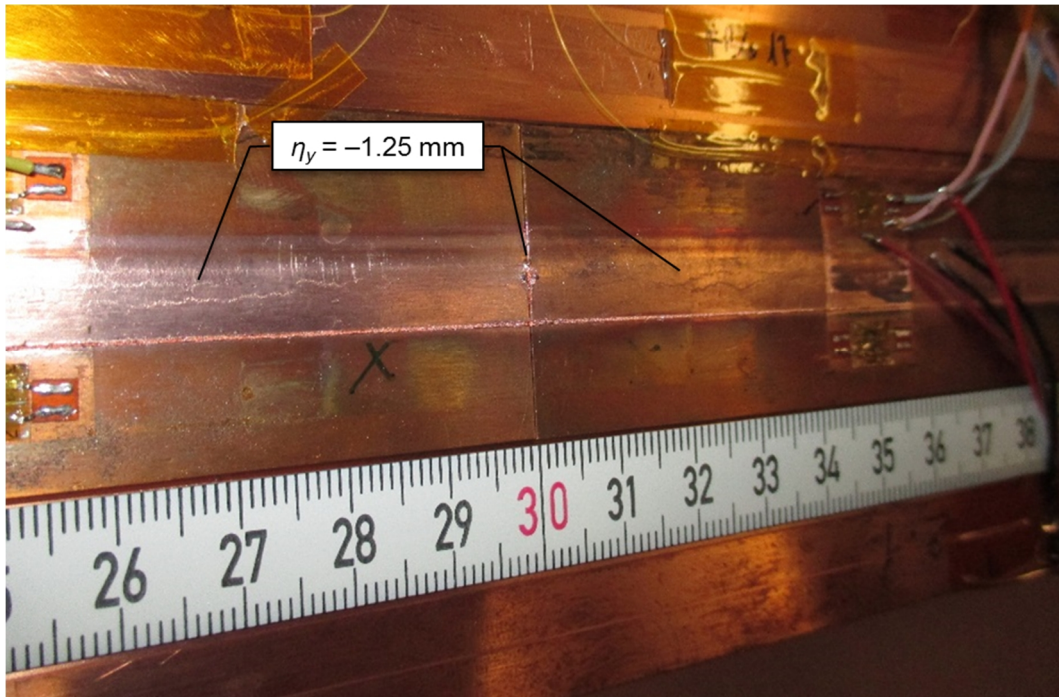


Figure 104. *Impacts #45 and #46*. Note the cracks generated on the free surface of the jaw and the damage at the block/block contact.

As seen in Figure 102, Figure 103 and Figure 104, impacts equivalent to the asynchronous beam dump case produced, for the lowest- $\eta_x$  cases (*impact #33 and #37*), a 40 cm long and 1 mm wide groove, exposing the CuCD bulk composite. The functionality of the collimator, even though the damage is more relevant than what observed on the CFC and MoGr absorbers, can still be recovered in operation by means of the 5<sup>th</sup> axis, which allows a vertical displacement of the jaw of  $\pm 10$  mm, in order to expose an intact absorber surface to the particle beam.

It is interesting to note the different failure mechanisms observed with the test, on top of the surface fracture or melting induced by low- $\eta_x$  impacts, which was discussed earlier. For higher  $\eta_x$  pulses, in fact, at high intensity the material internally melts, while the external wall is still solid and contains the expansion of the core. Therefore, the solid surface experiences a relevant plastic deformation, and cracks locally appear, as highlighted by the case of *impact #46* (Figure 104). This mechanism is similar to the one that was numerically and experimentally described in section 4.3.1, and shown in particular in Figure 58. More details on the failure mechanisms and comparison with the numerical prediction will be given in the next chapter.

## 6.4 Glossary

Symbols are listed in chronological order with respect to their appearance in the text.

Symbol	Definition	SI unit
$E_k$	Kinetic energy	J
$N_b$	Number of bunches	–
$n_b$	Number of particles per bunch	–
$n_{tot}$	Number of particles per pulse	–
$E_{tot}$	Beam stored energy	J
$\Delta t$	Bunch spacing	s
$t_d$	Thermal pulse length	s
$\sigma_x$	Variance of the Gaussian distribution along the x coordinate	m
$\sigma_y$	Variance of the Gaussian distribution along the y coordinate	m
$\eta_x$	Horizontal impact coordinate	m
$\eta_y$	Vertical impact coordinate	m
$N_p$	Total number of impacts	–

## References

- [1] I. Efthymiopoulos *et al.* (2011). HiRadMat: a New Irradiation Facility for Material Testing at CERN. *Proc. IPAC'11*, San Sebastián, Spain.
- [2] F. Carra *et al.* (2014). Mechanical engineering and design of novel collimators for HL-LHC. *Proc. IPAC'14*, Dresden, Germany.

- [3] A. Bertarelli *et al.* (2013). An experiment to test advanced materials impacted by intense proton pulses at CERN HiRadMat facility. *Nuclear Instruments and Methods in Physics Research B*, Vol. 308, pp. 88–99.
- [4] R. Assmann *et al.* (2002). Requirements for the LHC Collimation System. Proc. EPAC 2002, Paris, France.

## Chapter 7

# Numerical analyses of novel materials under quasi-instantaneous heat deposition

As seen in the previous chapter, the three jaws installed in HiRadMat and tested under proton beam impact in the frame of the HRMT-23 experiment functionally survived the accidental design scenarios of HL-LHC collimators. The local damage to the absorber free surface in the most intense impact cases could be recovered in operation by vertically translating the jaw, so to expose an intact surface to the beam halo. In terms of classification of the dynamic phenomena produced during the test and discussed in chapter 2, it will be shown that the regime attained was that of elastic and plastic waves, while for the generation of cylindrical shock waves much higher energies are required, as explained in section 4.3.2.

Besides experimentally verifying the survival of the jaws under the HL-LHC design case impacts, the experiment had the goal of benchmarking the numerical models of the jaw materials, built on the basis of the measurements reported in Chapter 5, comparing the simulated results with the experimental data acquisition. As seen in Chapter 5, the absorber materials are advanced composites, in some cases created and developed at CERN in collaboration with international partners. For this reason, the literature is still scarce, and the available data allows building only linear equations of state and strength models independent of temperature and strain rate. The precision of the models built is expected to decrease at increasing energies involved in the impact, where strong nonlinearities, as well as changes of phase, take place. For the numerical benchmarking, one case study per material was identified. In terms of bunch intensity, the cases analysed correspond to the design accidental scenarios of HL-LHC collimator materials reported in section 5.2. The thermal energies involved are thus high, which allowed generating a dynamic phenomenon with sufficient signal-to-noise ratio produced in the measurement stations, keeping in mind that the amplitude of the cylindrical waves decays with

the increase of the radial propagation. The three case studies which will be presented in this chapter are:

- CuCD: *impact #32*
- MoGr: *impact #26*
- CFC: *impact #7*

Given the simplicity of the models adopted and the absence of changes of phase to the absorber in the scenarios studied thermomechanically, the numerical analyses were performed with the implicit solver of ANSYS Workbench, similarly to the study shown in section 4.2. Thermal transient simulations were run first, based on the energy deposition calculated with FLUKA for each impact case. Structural simulations then import the temperature field at each sub-step to evaluate in time the dynamic mechanical response of the component.

Thermal analyses based on FLUKA energy deposition maps represent thus the first stage of the simulation, but they are also important to evaluate the material state at the end of the impact. Indeed, as said the strength models of CFC, MoGr and CuCD are, at the current state, not refined enough to allow accurate thermomechanical simulations at high temperature and high strain rate; on the other hand, purely thermal analyses can be reliably performed to predict the change of phase of the low-melting materials, such as copper (used for the cladding of the CuCD jaw), Glidcop or CuCD<sup>30</sup>. The temperature field, in fact, can be calculated out of the power density map either numerically or analytically, with Eq. (1.16), when the heat capacity is known. Assuming the density as constant up to the melting point, the only unknown variable of CuCD is the specific heat capacity, which for copper is available in literature even above the melting point [1]. For alloys and composites, the specific heat depends mostly on the mass density of the constituents, and its calculation via rule of mixture is typically very accurate [2]. In the case of Glidcop, which is 99.7% made of copper as explained in section 4.4, it is reasonable to assume a specific heat identical to copper. For CuCD, the specific heat adopted in thermal analyses reaching the melting point is identical to the measurement up to 600 °C shown in Figure 81, while it is calculated with the rule of mixture above that temperature, also taking into account the material porosity.

---

<sup>30</sup> The temperature and pressure involved in HRMT-23, on the other hand, were not high enough to provoke a change of phase in CFC and MoGr.

Figure 105 summarizes the specific heat of low melting jaw materials up to 1500 °C.

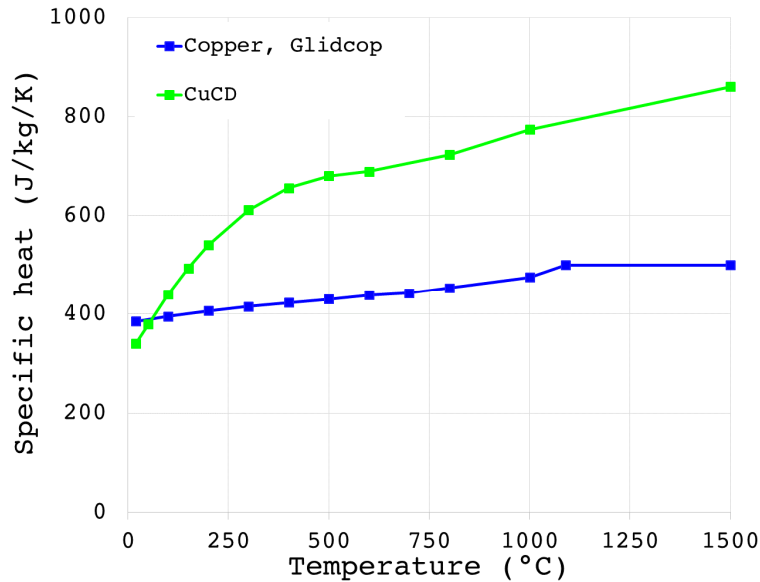


Figure 105. Specific heat of copper, Glidcop and CuCD as a function of temperature. The specific heat of CuCD is calculated by rule of mixture above 600 °C, with the diamond properties with temperature referenced in [3].

Thermal analyses were therefore performed, in addition to those related to the three case studies, to evaluate the behaviour of the tapering under high intensity shots since, as explained in Chapter 6 and shown in Figure 96, the Glidcop tapering of the CFC jaw experienced local melting. This was expected to happen only for *impact #13*, which had the highest impact depth  $\eta_x$  (5 mm). Indeed, as highlighted in Figure 106, at lower depths the temperature distribution changes significantly, and the peak temperature on the tapering decreases by almost one half.

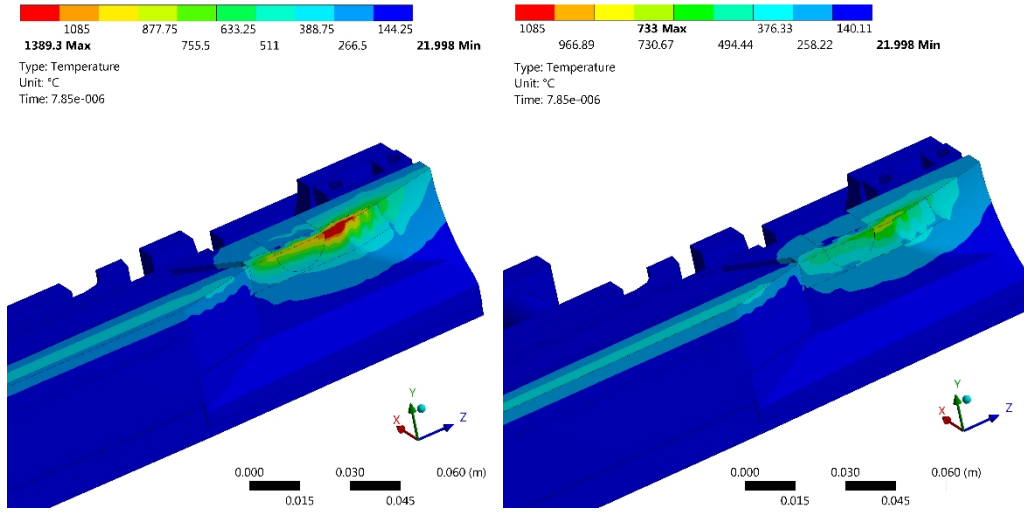


Figure 106. Temperature on the downstream tapering of the CFC jaw after impact #13 (left) and impact #7 (right). Areas in red are above the melting point of Glidcop. The model is symmetric on the section plane parallel to  $XZ$ . The main difference between the two cases is the  $\eta_x$  parameter, equal to 3.05 mm in impact #7, and to 5 mm in impact #13.

In this chapter, a summary of the numerical models adopted for the jaw materials will be given, and the numerical results for the three identified case studies will be presented. Attention will be mostly given to the dynamic stress waves acquired, as the thermal diffusion phenomenon, although monitored during the test and simulated, is mostly relevant to slow-transient problems and not of particular interest in the scope of this thesis.

## 7.1 Numerical models

Since the case studies do not involve changes of phase of the absorbers, the equation of state adopted for the three jaw materials has the linear form:

$$p(\rho, E) = K \left( \frac{\rho}{\rho_0} - 1 \right) + \gamma_0 E ; \gamma_0 = \frac{\alpha K}{\rho_0 c_v} \quad (3.8)$$

The properties needed for the construction of the EOS are derived from the characterization reported in section 5.4.

In terms of constitutive laws, two types of models were built based on the expected mechanical behaviour seen in 5.4: purely elastic and, for CuCD, which presents an inelastic behaviour due to plasticity of the copper matrix, an additional elastoplastic model.

### 7.1.1 Linear elasticity

Under this hypothesis, the material presents a constitutive law based on the Duhamel-Neumann equations, which in an isotropic homogeneous continuum have the form (1.8),(1.9). In general, the relation between stress and strain depends on the stiffness and compliance matrixes, which are built on the base of the elastic constants measured for the three jaw materials with the method reported in section 5.4.2. The elastic constants are summarized in Table 25.

Table 25: Summary of the elastic constants for the three jaw materials. The reference system is always as per Figure 75.

Property	Direction	CFC	MoGr	CuCD
Young's modulus (GPa)	$x$	2.8	4.7	160.0
	$y$	57.5	76.7	160.0
	$z$	93.0	76.7	160.0
Shear's modulus (GPa)	$xy$	3.5	3.8	75
	$yz$	10.6	33.0	75
	$zx$	6.5	3.8	75
Poisson's ratio (-)	$xy$	0.11	0.10	0.07
	$yz$	0.10	0.16	0.07
	$zx$	0.10	0.10	0.07

### 7.1.2 Elastoplasticity

While a purely elastic model, disregarding dissipation related to internal friction, is suitable to materials such as CFC and MoGr, which have an orthotropic or transversely isotropic behaviour similar to laminar carbon composites widely adopted in the industry, the inelasticity shown by CuCD even under quasi-static testing cannot be neglected. The inelasticity is clearly visible in Figure 85, and is likely related to plasticity in the copper matrix. For CuCD, a second model is also proposed, based on strain-rate-independent plasticity.

However, the stress in a 4-point bending test, such as that performed at the CERN Mechanical Laboratory, is typically calculated according to International Standards [4]:

$$\sigma_f = \frac{3Fd_1}{bh^2} \quad (7.1)$$

where  $\sigma_f$  is the bending stress,  $F$  is the force applied,  $d_1$  the distance between the inner loading roller and the outer support,  $b$  the width of the tested sample and  $h$  its thickness. This relation is valid for linear elastic materials. In the case of plasticity, the stress distribution is no more linear along the specimen section (Figure 107). A correction is thus needed.

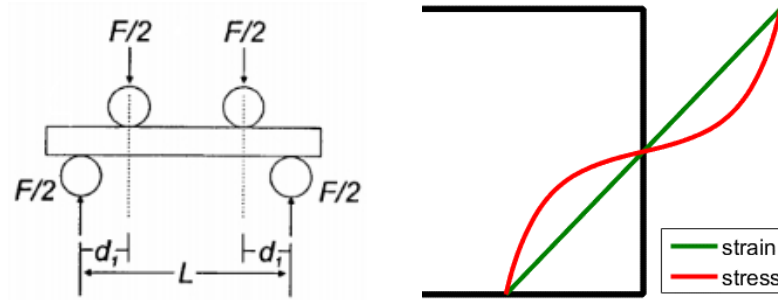


Figure 107. Schematic of the 4-point bending test (left) and axial strain and stress distribution through the thickness of the sample (right).

During the test, the applied force  $F$  (Figure 107, left) and the axial strain  $\varepsilon_{max}^{tot}$  at the bottom centre of the sample are recorded. From  $F$  and distance  $d_1$  follows directly the maximum moment  $M = (Fd_1) / 2$ , which is constant in the section between the points of load application. For isotropic beams under uniform moment, the curvature is constant along its length and the central plane of the beam retains its original length – the so-called neutral axis. The axial strain at the neutral axis must therefore be zero, while for small curvatures it is linearly distributed through the thickness (Figure 107, right). This purely geometric statement upholds independent from the material behaviour. The strain distribution in the sample is thus known, since its maximum value  $\varepsilon_{max}^{tot}$  at the bottom of the specimen is measured. However, as a result of the (a priori unknown) nonlinear elasto-plastic stress-strain relation, there must be a non-linear stress distribution through the thickness (Figure 107, right). The integration of the stress distribution must yield the (known) moment  $M$  according to:

$$M = b \int_{-h/2}^{h/2} \sigma_z(x) x dx \quad (7.2)$$

$x$  being the vertical coordinate,  $h$  the sample height and  $b$  its width. In terms of total strain the equation reads:

$$M(\varepsilon_{max}^{tot}) = 2b \int_0^{h/2} \sigma_z \left( \frac{2x}{h} \varepsilon_{max}^{tot} \right) x dx \quad (7.3)$$

Here,  $\sigma_z \left( \frac{2x}{h} \varepsilon_{max}^{tot} \right)$  denotes the stress-strain curve which, if the constitutive model can be reproduced by a power law, can be numerically derived from (2.14), given the measured curve  $M(\varepsilon_{max}^{tot})$  for a range of  $\varepsilon_{max}^{tot}$ . Note that due to the nonlinear distribution of stress, the above  $\sigma_z \left( \frac{2x}{h} \varepsilon_{max}^{tot} \right)$  is, in general, not equal to the flexural strength calculated with Eq. (7.1), which can also be expressed as:

$$\sigma_f(\varepsilon_{max}^{tot}) = \frac{M(\varepsilon_{max}^{tot}) h}{I_x} \frac{1}{2} \quad (7.4)$$

where  $I_x$  is the flexural moment of inertia. The measured  $M(\varepsilon_{max}^{tot})$  curve of a bending specimen of CuCD is shown in Figure 108, left. The resulting flexural strength  $\sigma_f(\varepsilon_{max}^{tot})$ , the hardening curve  $\sigma_z(\varepsilon_{max}^{tot}) \equiv \sigma_{eq}(\varepsilon_{eq}^{tot})$  and the corresponding stress  $\sigma_{eq}(\varepsilon_{eq}^{pl})$  as a function of the accumulated plastic strain, are shown in Figure 108, right. The latter curve forms the basis of the multilinear hardening input into ANSYS.

The assumption of linear strain sometimes is, in some cases, not accurate, especially at high curvatures caused by the presence of internal hinges. However, the method adopted is valid whenever the strain field on the specimen is known, and verifications in this sense may be done in the future with techniques such as *Digital Image Correlation* (DIC).

As a result of the ductility of the copper matrix, CuCD shows a considerable amount of plastic hardening. However, its behaviour is assumed to be identical in tension and compression, which may be valid only in a limited range of strain. At large compressive strains the diamond particles may come into contact, while under large tensile strains the adhesion between matrix and particles may be lost.

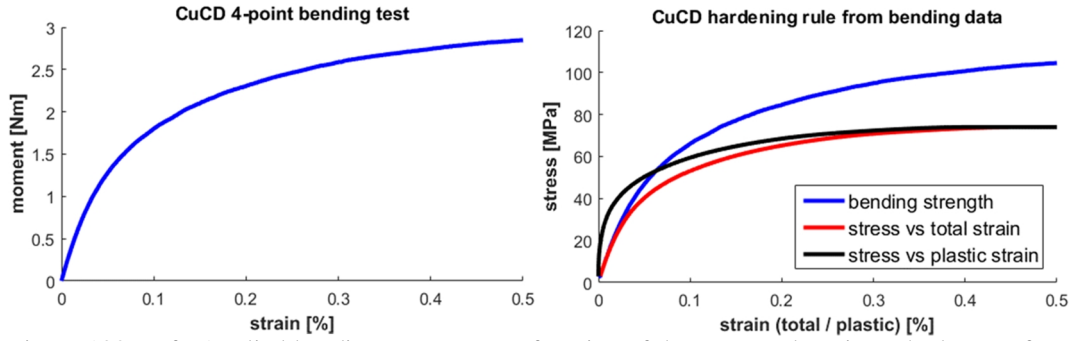


Figure 108. Left: Applied bending moment as a function of the measured strain at the bottom face of the sample. Right: flexural strength  $\sigma_f(\varepsilon_{max}^{tot})$  (blue), the hardening curve  $\sigma_{eq}(\varepsilon_{eq}^{tot})$  (red) and  $\sigma_{eq}(\varepsilon_{eq}^{pl})$  (black) for the CuCD bending test.

## 7.2 Numerical results

This section reports the results of the numerical calculations performed on each of the three cases studies identified (*impacts* #32, #26 and #7), and the comparison with the experimental measurements performed during HRMT-23. The experimental data are extracted from the strain gauge measurements, with the configuration recalled in Figure 109.

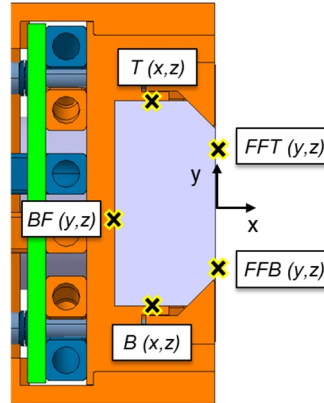


Figure 109. Strain gauge positioning and nomenclature, with the acquired strain direction in each point under parenthesis.  $T$  is the top face,  $B$  the bottom face,  $BF$  the back face,  $FFT$  and  $FFB$  the front face top and bottom gauges.

### 7.2.1 CuCD

The case study for the CuCD jaw is *impact* #32 (Table 26). As explained in Chapter 6, this specific impact is relevant to the design of new collimators, as it corresponds to the design accidental scenario equivalent to the HL-LHC asynchronous beam dump. The thermal energy distribution over the jaw length is

reported in Figure 110. As a reminder, the CuCD absorber is made of 10 blocks, 100 mm long each, for a total length of 1 m. As shown in Figure 110, the peak energy is attained on block 3, while the total energy over the  $xy$  section is maximum at block 4.

Table 26: Characteristics of the case study for CuCD.

Impact identifier	$N_b$	$n_{tot}$	$E_{tot}$ (MJ)	$t_d$ ( $\mu$ s)	$\sigma$ (mm)	$\eta_x$ (mm)	$\eta_y$ (mm)
#32	24	$3.13 \times 10^{12}$	0.22	1.90	0.61	-3.05	0

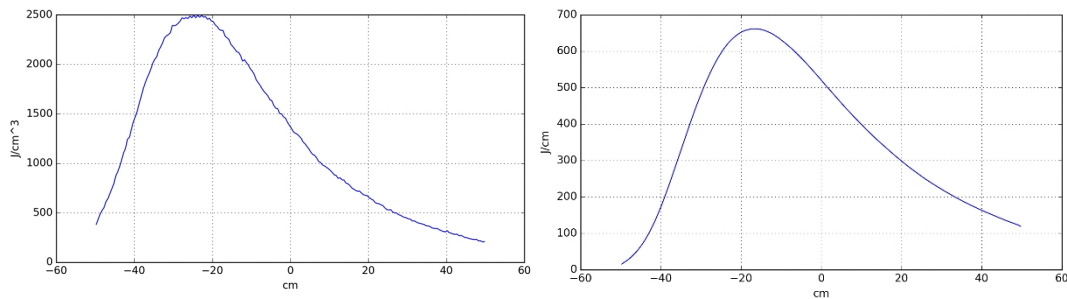


Figure 110. Left: energy peak on the CuCD absorber over the  $z$  coordinate for impact #32. Right: total energy per longitudinal section. FLUKA maps are courtesy of E. Skordis.

The thermal energy deposited on the CuCD jaw during the impact is significant, but the maximum temperature induced on the components is still below the melting point (Figure 111). The use of a linear EOS is thus justified.

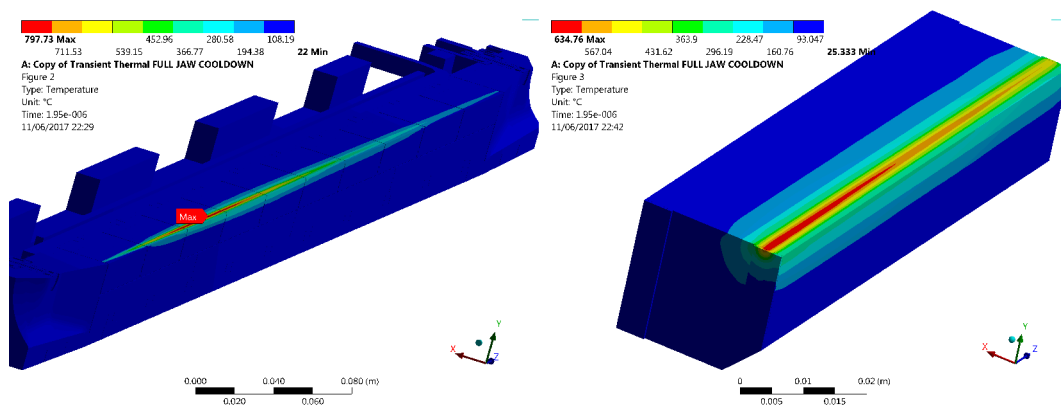


Figure 111. Left: temperature distribution after *impact* #32 on the CuCD jaw. The peak is found on the 3<sup>rd</sup> CuCD block. The model presents a symmetry along the section plane parallel to  $XZ$ . Right: temperature distribution on the 5<sup>th</sup> CuCD block ( $z = 400 \div 500$  mm).

The structural analysis performed with ANSYS Workbench imports the temperature field at every time step. Several structural models were prepared at increasing complexity, starting with the simulation of a single-block, with adequate boundary conditions to correctly reproduce the wave transmission and reflection at the interface with the other blocks and jaw components (Figure 112, left). The single-block model represents the most efficient solution allowing for a high spatial and temporal resolution of the dynamic behaviour within reasonable computational time. In terms of boundary conditions imposed when modelling a single-block of the absorber, it is necessary to calculate the shock impedance of the block and the surrounding elements, since this is the key parameter in the determination of the wave behaviour at the interfaces, as discussed in section 4.4.

$$Z_{CuCD} = \rho_{CuCD} c_{CuCD} = 5250 \frac{kg}{m^3} \cdot 5550 \frac{m}{s} = 29.1 MPa \frac{s}{m} \quad (7.5)$$

$$Z_{Gl} = \rho_{Gl} c_{Gl} = 8900 \frac{kg}{m^3} \cdot 4740 \frac{m}{s} = 42.2 MPa \frac{s}{m}$$

where  $Z$  is the shock impedance,  $\rho$  the density and  $c$  the speed of sound; the subscripts  $CuCD$  and  $Gl$  are referred to Copper-Diamond and Glidcop respectively. The amplitude of the reflected and transmitted waves at the CuCD/Glidcop interface, with respect to the incident compressive wave propagating from the Copper-Diamond block, can be calculated with Eq. (4.27):

$$\frac{\sigma_T}{\sigma_I} = \frac{2Z_{Gl}}{Z_{Gl} + Z_{CuCD}} = 1.18 \quad (7.6)$$

$$\frac{\sigma_R}{\sigma_I} = \frac{Z_{Gl} - Z_{CuCD}}{Z_{Gl} + Z_{CuCD}} = 0.18$$

On the other hand, at the longitudinal interfaces between each CuCD block and the precedent and subsequent ones,  $\sigma_T/\sigma_I = 1$  and  $\sigma_R/\sigma_I = 0$ . The boundaries imposed at the interface between the CuCD block and the Glidcop housing, as well as the longitudinal interfaces between subsequent blocks, simulated the transmission and reflection of the waves based on the impedance results above.

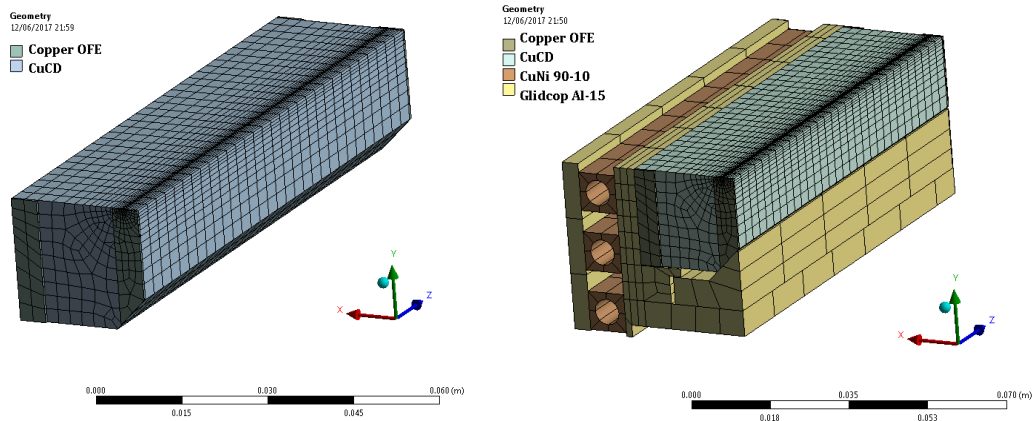


Figure 112. Left: single CuCD block FE model. Right: model of a jaw section around a single-block. The models are symmetric along a plane parallel to XZ.

The single-block model can be extended to include a section of the collimator, as well as the clamps with the corresponding pre-tension, the housing and cooling pipes (Figure 112, right). This model realistically replicates the frictional contact conditions between the block and the back wall as well as the clamping force.

Further complexity can be added by including the adjacent absorber blocks and the surrounding clamps, housing and cooling pipes (Figure 113, left). Axial waves originating near the studied block will continue to propagate to the adjacent absorber blocks during the first moments after impact. In order to more precisely capture the axial dynamic behaviour, as well as the flexural motion, a model of the whole jaw is required (Figure 113, right). However, due to the high number of elements required to simulate the full jaw ( $\sim 150\,000$ , with 3 000 time steps in order to reproduce the first 300  $\mu\text{s}$  of the dynamic phenomenon), the computational time is significant ( $\sim 50$  h).

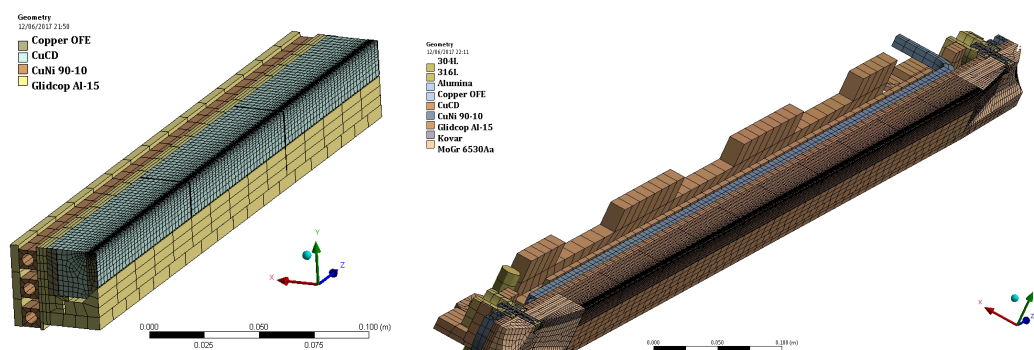


Figure 113. Left: FE model of three adjacent CuCD absorber blocks including the clamps, housing and cooling pipes. Right: FE mesh of a full collimator jaw. The models are symmetric along a plane parallel to XZ.

The initial simulations, performed on the single-block model, were intended to understand the influence of the mechanical model adopted for CuCD. First, only block 5 was simulated for a duration 300  $\mu\text{s}$  with a time step of 0.1  $\mu\text{s}$ . The two models derived for CuCD, purely elastic and elasto-plastic, described in sections 7.1.1 and 7.1.2, were compared with the experimental measurements performed with strain gauges (Figure 109). The back face strain gauge was typically adopted as a reference for the benchmarking, as its signal was neater than the others, due to the favourable geometrical position with respect to the beam impact point.

As evident in Figure 114, which shows the transverse strain  $\varepsilon_y$  on the back face of the block, large differences occur in the material response between elastic and plastic properties. Clearly the stresses of the initial impact exceed the yield value, and plasticity of the copper matrix takes place, with energy dissipation. The strain amplitudes of the elastic simulation (*cyan*) vastly overestimate the measured values (*black*), whereas the elastoplastic model (*blue*) better approximates the correct strain amplitudes in the immediate aftermath of the impact. Note that the first  $\sim 20\mu\text{s}$  of the measurement data are affected by the electromagnetic disturbances inflicted on the electronics by the passing proton beam, and the first stress wave reaching the back face strain gauge is hidden by this disturbance. The experimental signal is recovered afterwards, and the second wave reflection is evident.

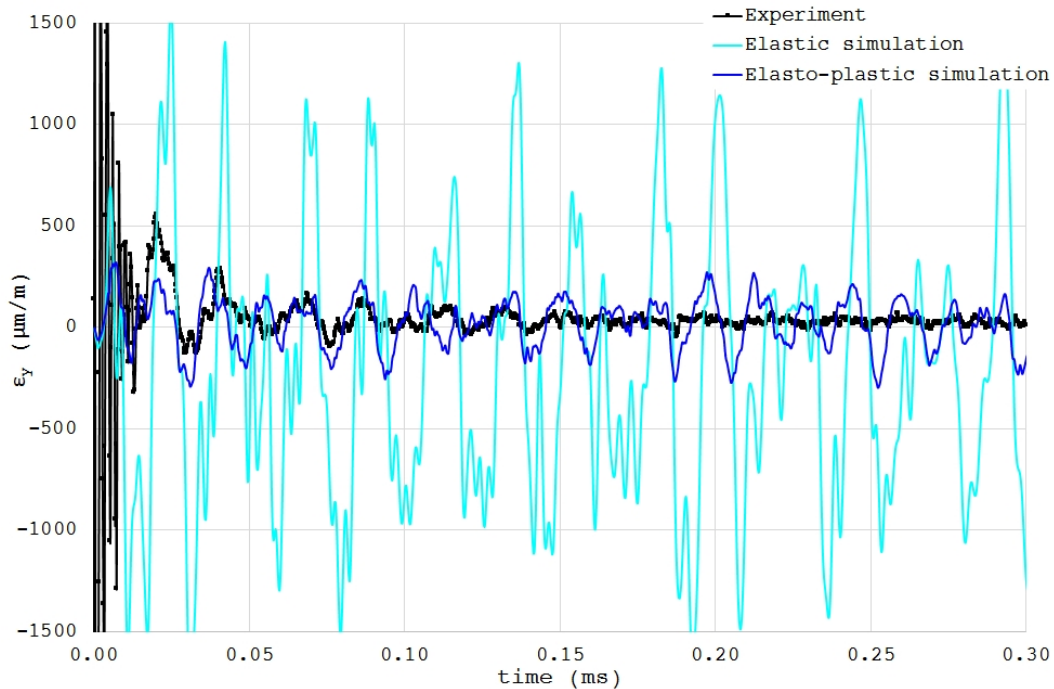


Figure 114. *Impact #32*, CuCD: transverse strain on the back face of block 5, single-block model. Comparison between experimental data, elastic model and elasto-plastic model.

The experimentally measured strain signal quickly subsides after a few oscillations in just  $\sim 0.15$  ms, and disappears in the background noise of the strain probes. In the numerical elastoplastic model, plastic deformation is induced at the impact location, but subsequently the stress waves decay in amplitude below the elastic limit and no more energy dissipation is induced, except for a tiny numerical damping factor introduced by default in the FE software to stabilize the transient solution. As a result, the stress waves within the block continue to reflect elastically at the boundaries and continue to oscillate indefinitely.

The first strain oscillations of experiment and simulation agree quite well, as shown by the Fourier transforms in Figure 115, with two large peaks at 45.8 kHz and 64.1 kHz in the experimental data, and 45.0 kHz and 62.5 kHz in the elastoplastic simulation. As the level of measured and simulated wave amplitude is mostly in the elastic domain, this is a good indication of a material well characterized in its elastic constants.

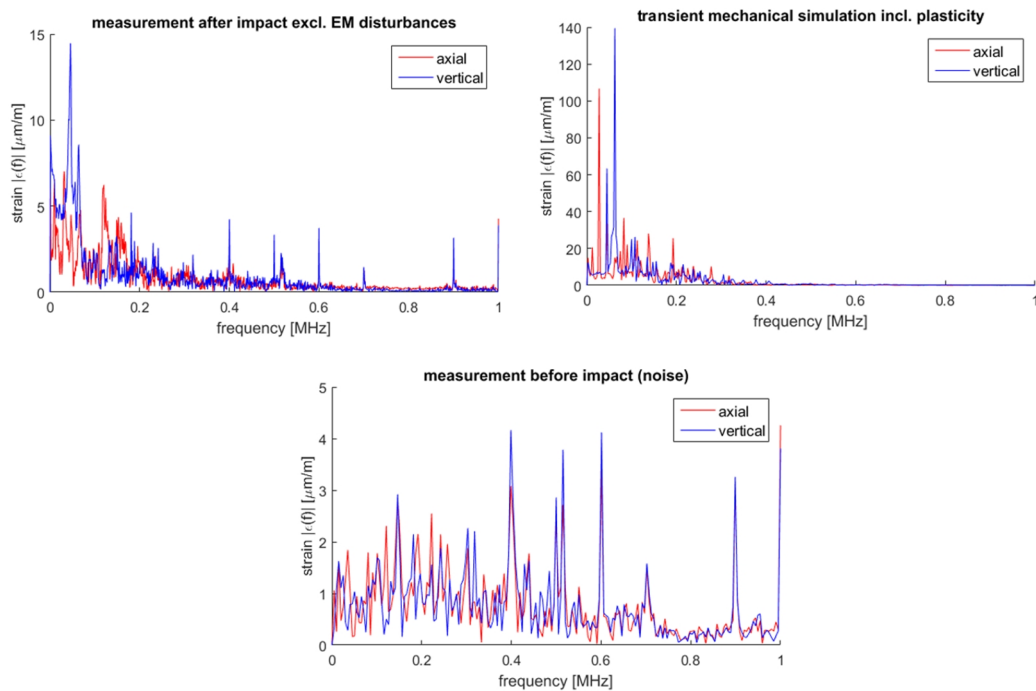


Figure 115. *Impact #32* on CuCD, Fourier transform of measurement and simulation (top left and right). Note that much of the high-frequency content in the measurement signal is attributable to the intrinsic noise of the probes (bottom).

The model was then extended to include three blocks and parts of the casing (Figure 113, left), or the whole jaw (Figure 113, right). The appropriate clamping force was applied and frictional contacts among the clamped bodies of the jaw were introduced. The increase in model complexity does not yield significant differences compared with the single-block model of block 5. It is interesting to note that the introduction of frictional contacts hardly contributes to the decline in strain amplitude over time, see Figure 116. The dissipative effect of contact friction is therefore too small to justify the rapid decay in the experimentally measured strain. This is particularly evident in Figure 117, which shows that the frictional model of blocks 4 to 6 yields only a very small reduction in amplitude compared to a frictionless and non-dissipative model.

Figure 116. *Impact #32*, CuCD, transverse strain on the back face of block 5: comparison between different FE models.

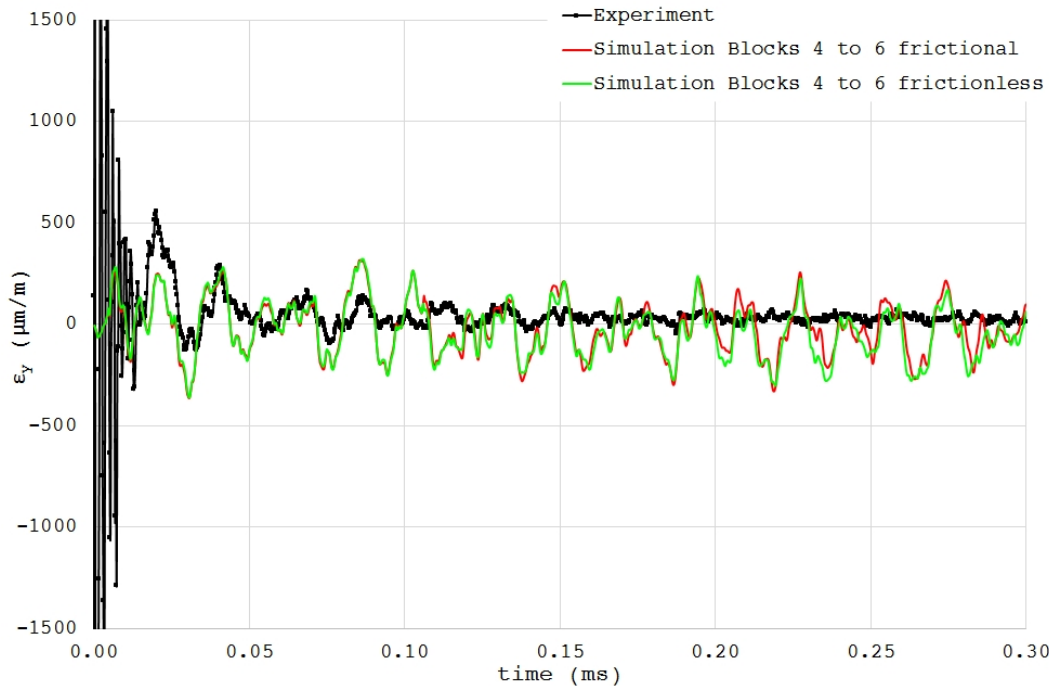


Figure 117. *Impact #32*, CuCD, transverse strain on the back face of block 5: three-block model with varying coefficient of friction (frictional:  $c_f = 0.3$ ; frictionless:  $c_f = 0$ ).

From the macroscopic point of view, the measured amplitude decay, not observed numerically, can be related to dissipation in the material. Authors like Kolsky [5] use the term *internal friction* to indicate the entirety of the dissipative phenomena in a material. As discussed in section 3.2, material dissipation is typically modelled through strain-rate-independent plasticity as well as viscoplastic models. However, in the CuCD case, the amplitude decay takes place at strains down to  $10^{-5}$  m/m, until the signal is in the range of the background noise. To the author's opinion, this indicates a contribution of viscoelasticity to the signal damping.

Another possible explanation for the quick amplitude decay might be found in the inhomogeneous mesoscale structure of CuCD which, as described in section 5.3.3, consists of 66%<sub>vol</sub> diamond particles between 40 and 200  $\mu\text{m}$  in size embedded in a copper matrix (Figure 80). Stress waves propagating from one medium to the other will be split into reflected and transmitted portions according to the shock impedance of the two media. The impedance of diamond is, due to its very high speed of sound, almost two times larger than the value for copper. In the case of an elastic wave in uniaxial stress conditions (Table 2), in fact:

$$Z_D = \rho_D c_D = 3530 \frac{kg}{m^3} \cdot 17500 \frac{m}{s} = 61.8 MPa \frac{s}{m} \quad (7.7)$$

$$Z_{Cu} = \rho_{Cu} c_{Cu} = 8900 \frac{kg}{m^3} \cdot 3800 \frac{m}{s} = 33.8 MPa \frac{s}{m}$$

where the subscripts *D* and *Cu* are used for diamond and copper respectively. The amplitude of transmitted and reflected waves at the copper/diamond interface can therefore be calculated as:

$$\frac{\sigma_T}{\sigma_I} = \frac{2Z_2}{Z_1 + Z_2} = \begin{cases} 1.29 & \text{for Cu} \rightarrow \text{D} \\ 0.71 & \text{for D} \rightarrow \text{Cu} \end{cases} \quad (7.8)$$

$$\frac{\sigma_R}{\sigma_I} = \frac{Z_2 - Z_1}{Z_1 + Z_2} = \begin{cases} 0.29 & \text{for Cu} \rightarrow \text{D} \\ -0.29 & \text{for D} \rightarrow \text{Cu} \end{cases}$$

for incident waves passing from copper to diamond (denoted by Cu→D) and from diamond to copper (D→Cu). At the transition from diamond to copper, for example, the reflected and transmitted waves will have inverse signs. The equations above presume that the wavelength of the stress wave is small compared to the size of the inhomogeneity. If the wavelength is much larger than a diamond particle, then the particle will do not see a discernible propagation of a stress wave on its length scale. On the macroscopic scale, any reflection caused by the transition of the wave from the matrix into the particle will almost immediately be cancelled by the following reflection occurring when the wave propagates forth to the matrix, as seen in the second equation of the system (7.8).

The effect of the particle impedance mismatch was examined through a dedicated 2D simulation in which an infinitely long bar was submitted to a sine excitation at one side, and the transverse propagation of the wave through the rod thickness was monitored. The response of homogeneous CuCD modelled with a purely elastic and a viscoelastic approach was compared to a mesoscale model of CuCD, where irregular diamond polygons were generated within a copper matrix (Figure 118). The analysis was aimed at qualitatively evaluating the wave dispersion at the diamond/copper interface, and for computational time purposes the total volume of diamond was 30% of the total volume, with about 2 mm – wide diamond particles. The strength model adopted to simulate viscoelasticity is identical to that described in section 3.2.1. The decay constant  $\beta$ , in the absence of

literature data in this sense, was assumed based on measurements done on porous materials [6], and is adopted to provide a qualitative-only expression of the viscoelastic damping, compared to the dispersion observable with a mesoscale model. Data of the three models are reported in Table 27.

Table 27: CuCD homogeneous and inhomogeneous model parameters.

	Homogeneous Elastic	Homogeneous Viscoelastic	Inhomogeneous Mesoscale	
$E$ (GPa)	160	160	Cu	130
			D	1200
$\nu$	0.07	0.07	Cu	0.3
			D	0.2
$\rho$ (kg/m <sup>3</sup> )	5250	5250	Cu	8900
			D	3530
$\beta$ (ms <sup>-1</sup> )	–	200		–

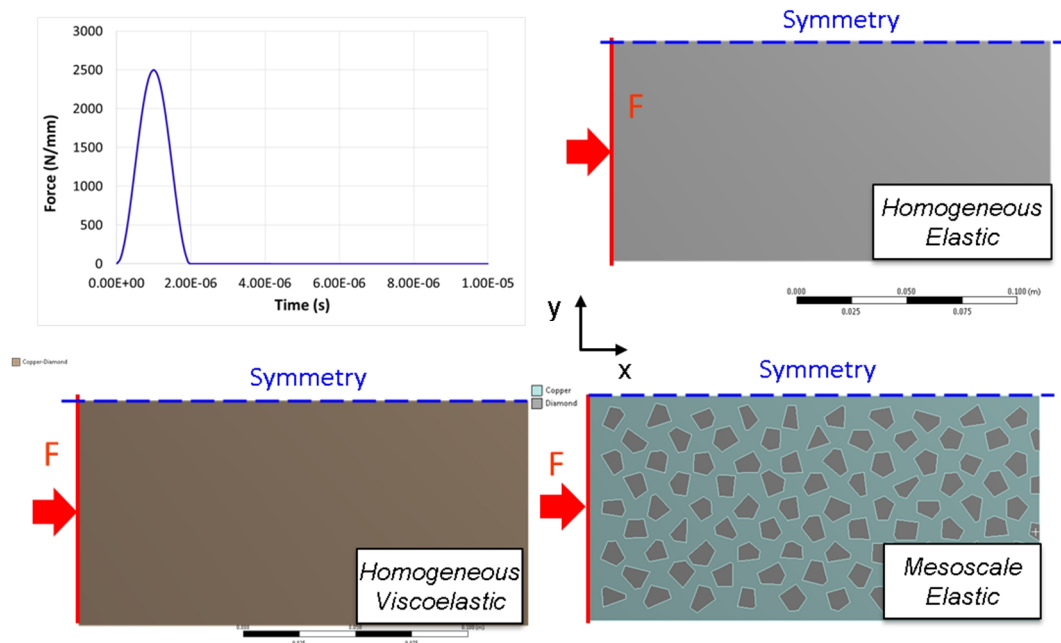


Figure 118. Homogeneous elastic (top right), homogeneous viscoelastic (bottom left) and mesoscale elastic (bottom right) models of a CuCD rod impacted at the left side with the sine excitation with half-period 2  $\mu$ s shown on the top left. The 2D model assumes plain strain conditions.

The response of the material, in the three different scenarios, to a sine excitation  $2 \mu\text{s}$  long is shown in Figure 119. It is possible to observe that a slight decay in amplitude is present also in the homogeneous elastic model, and is related to dispersive phenomena similar to those described in section 4.2.1. The homogeneous viscoelastic analysis, on the other hand, shows an amplitude decay due to the combination of dispersion and dissipation imposed by the time-dependent model. Finally, in the case of a mesoscale model with diamond particles distributed in a copper matrix, a strong dispersion is observed in the signal, due to the continuous wave reflection at the particle/matrix interfaces. As mentioned, the entity of the dispersion is related to the wave length, which corresponds to the pulse length multiplied by the speed of sound of the material. In the case just analyzed, for a time pulse of  $2 \mu\text{s}$ , the wavelength is in the order of  $7 \text{ mm}$ . The analysis was repeated with a load applied five times slower, for a total pulse duration of  $10 \mu\text{s}$  (Figure 120).

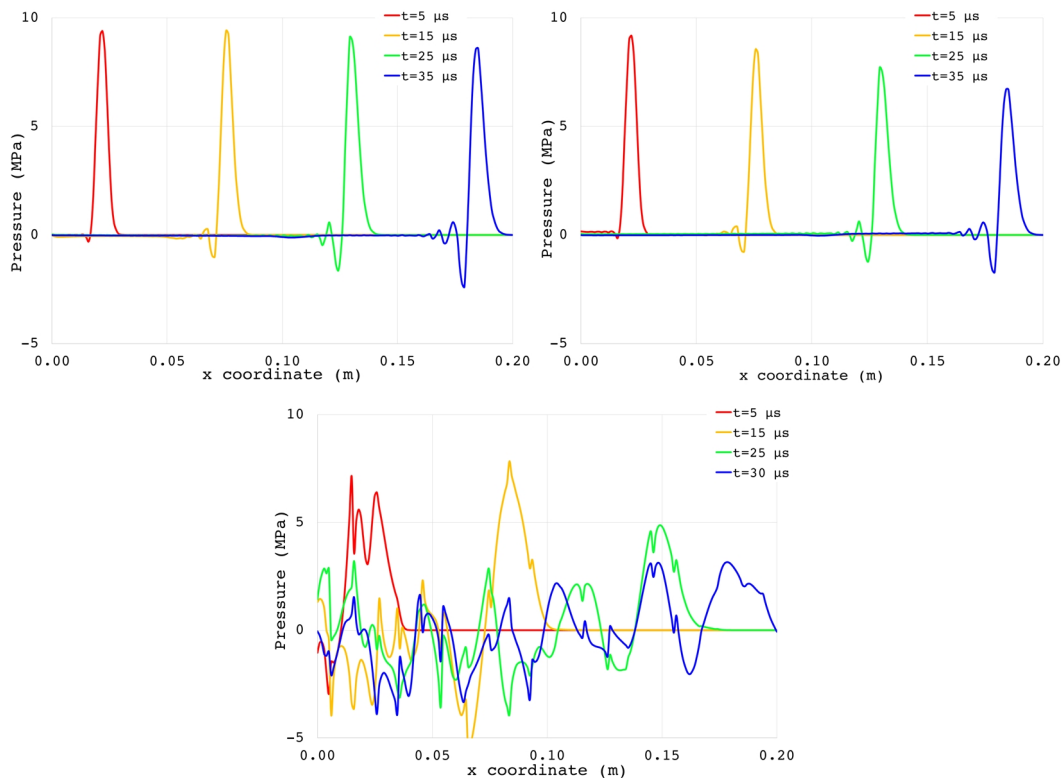


Figure 119. Pressure wave along the bar transverse coordinate in the three different models, as a response to the sine excitation with half-period  $2 \mu\text{s}$  shown in Figure 118: homogenous elastic (top left), homogeneous viscoelastic (top right) and inhomogeneous mesoscale elastic (bottom).

As expected, in the case of a five time longer wavelength, the dispersive effects are less relevant in all models. Qualitatively, the mesoscale model now approaches in terms of decay the viscoelastic simulation.

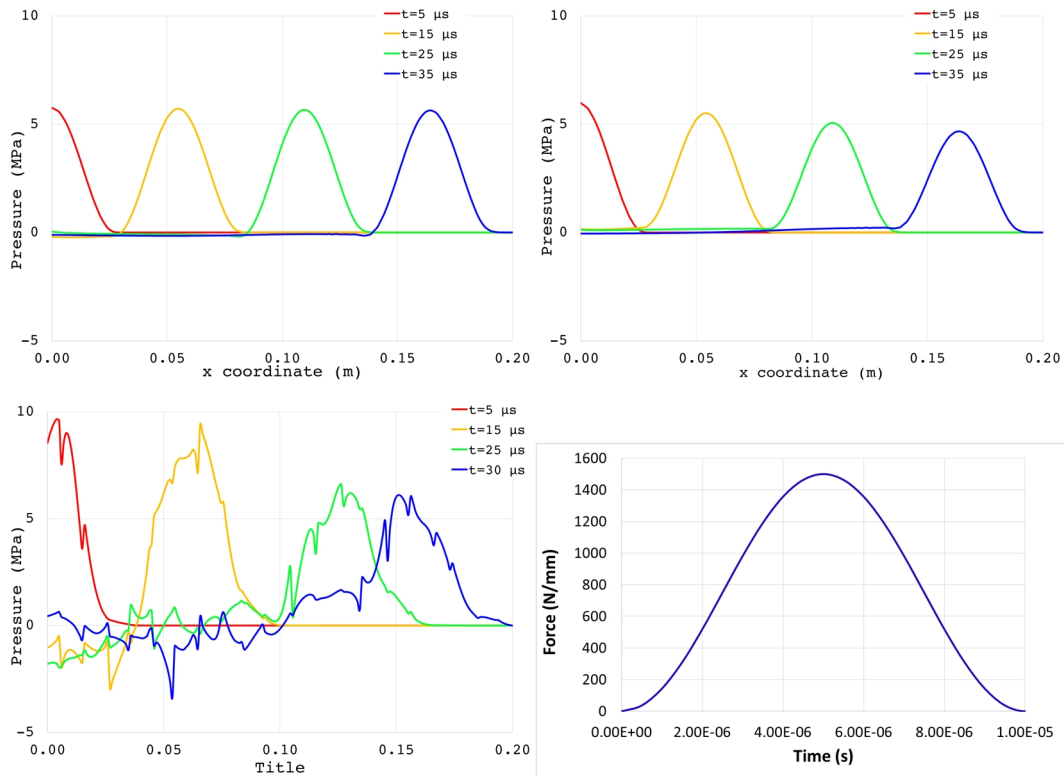


Figure 120. Pressure wave along the bar transverse coordinate in the three different models, as a response to the sine excitation with half-period 10 μs (bottom right): homogenous elastic (top left), homogeneous viscoelastic (top right) and inhomogeneous mesoscale elastic (bottom).

Coming back to the case of CuCD embedded in the HRMT-23 jaw, it is evident that the observed signal damping might be related to a similar mechanism of wave dispersion at the particle/matrix interface only in case of wavelengths close to the diameter of the diamond particles, which is comprised between 40 and 200 μm for the grade adopted, with an average value of 100 μm. As seen in the Fourier transforms in Figure 114, the dominating frequencies detected by the strain gauges on the back face correspond to wavelengths in the range of dozens of millimeters. However, this is a result of the modal response of the block as a whole, which amplifies wavelengths that match the dimensions of the block. Indeed, the frequency spectrum of the initial stress wave must be independent of the block geometry when it is first emerges around the impact location. Instead, it depends mainly on the beam parameters, for example the bunch, batch and pulse lengths. By the time the stress wave reaches the back face, it has already traversed a myriad of

diamond particles and was reflected at various boundaries. Furthermore, the acquisition rate and finite size of the strain probes limit the measurement of high frequency, small wavelength signals. At high frequencies, dynamic effects caused by the probe itself may also play a significant role.

The blue curve in Figure 121 qualitatively shows the thermal strain caused by the pulse structure. During the *impact #32* the beam was not only made of bunches, with a structure similar to what depicted in Figure 39, but a further separation into packets of six bunches each, called *batches*, was imposed by machine constraints. Each batch was separated by the precedent and following one by a time spacing equal to 225 ns, as depicted in Figure 121. The red curve represents the resulting strain amplitude in the frequency domain. Of course, most of the amplitude content is concentrated in the low frequency range. The first minimum at about 450 kHz corresponds to  $1/t_d$ , where  $t_d$  is the overall duration of the pulse. Because there are four separate batches, however, the frequency range around  $1/(4t_d)$  or 1.8MHz is not completely negligible. This frequency corresponds to below 2 mm wavelength, and is still one order of magnitude larger than the diamond particles.

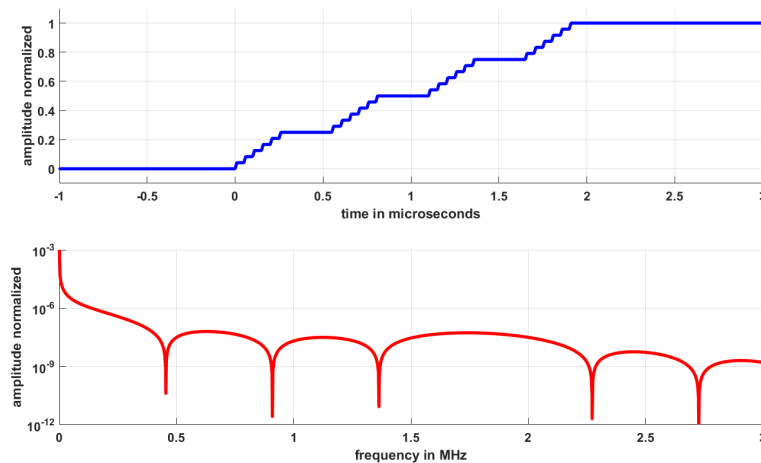


Figure 121. Qualitative temperature evolution for the beam parameters of the analysed CuCD *impact #32*: 4 batches of 6 bunches each, with 50 ns bunch length and 225 ns spacing between batches (top). The largest amplitudes are below 450 kHz but there is some notable frequency content up to about 2MHz (bottom).

As a conclusion of the analysis, the dynamic response of the CuCD jaw tested during HRMT-23 can be quite well replicated numerically, except for the observed decay in the amplitude of the stress wave during time. The phenomenon can be related to a combination of viscoelastic and viscoplastic behaviour of the

constituting porous composite material. This could be confirmed by future dynamic tests aimed at deriving the constitutive laws controlling the strain-rate-dependent response. Additionally, an inhomogeneous mesoscale model, imitating the random distribution of diamond particles inside the copper matrix of the material, was built. This model can reproduce the wave dispersion at the interface between the material constituents; however, it is computationally demanding, and should be adopted only when strictly necessary, *i.e.* when the expected wavelengths are very short and in the order of the diamond size. Moreover, a mesoscale model introduces further complexities related to the modelling of the copper/diamond interface, which should be carefully characterized in terms of adherence, assumed to be ideal in the scope of this work.

### 7.2.2 MoGr

For MoGr, the case study analysed is *impact #26* (Table 28). The impact represents, in terms of energy density deposition on the material, the design accidental case for HL-LHC secondary collimators. The thermal energy distribution over the jaw length is reported in Figure 122. The MoGr absorber is made of eight blocks, 125 mm long each, for a total length of 1 m. As shown in Figure 122, left, the peak energy is attained on block 2, while the total energy over the  $xy$  section is maximum at block 8.

Table 28: Characteristics of the case study for MoGr.

Impact identifier	$N_b$	$n_{tot}$	$E_{tot}$ (MJ)	$t_d$ ( $\mu$ s)	$\sigma$ (mm)	$\eta_x$ (mm)	$\eta_y$ (mm)
#26	288	$3.76 \times 10^{13}$	2.65	7.2	0.35	1.75	0

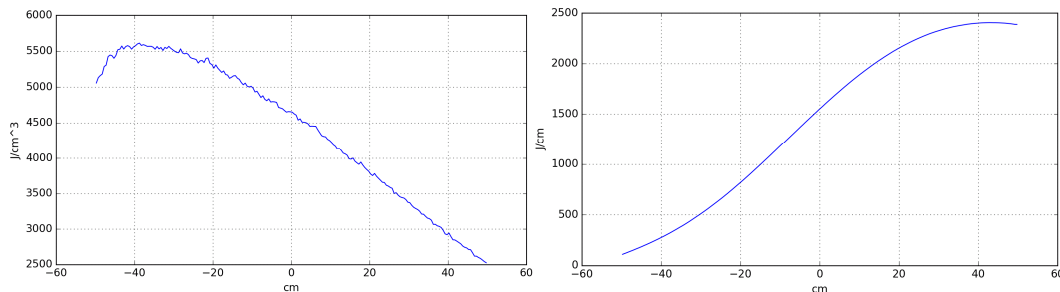


Figure 122. Left: energy peak on the MoGr absorber over the  $z$  coordinate for *impact #26*. Right: total energy per longitudinal section. FLUKA maps are courtesy of E. Skordis.

The thermal energy deposited on the MoGr jaw during the impact leads to a temperature which is lower than the melting point of the different components (Figure 123), again justifying the use of a linear EOS.

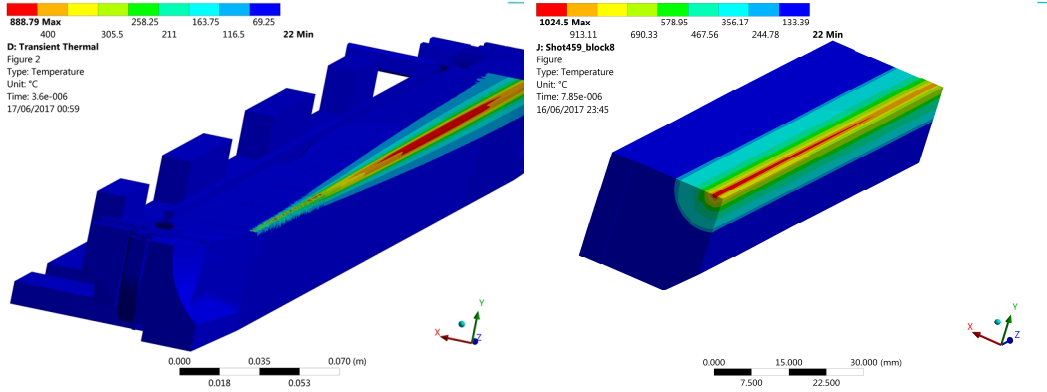


Figure 123. Left: temperature distribution after *impact #26* on the MoGr jaw. The peak is found on the 2<sup>nd</sup> MoGr block. The model presents a symmetry along the section plane parallel to *XZ*. Right: temperature distribution on the 8<sup>th</sup> MoGr block ( $z = 875 \div 1000$  mm), which is loaded with the highest total energy (Figure 122, right).

Also in this case, a single-block model was prepared for the mechanical analysis; the modelled block is the last one (block 8), as it is the most loaded one in terms of total thermal energy (Figure 122, right). Again, the shock impedance of the block must be calculated and compared to that of the Glidcop housing, to define the adequate boundary conditions. MoGr has an orthotropic structure, and the speed of sound changes along the direction of propagation. The MoGr/Glidcop interface is parallel to the *YZ* plane (Figure 123) and the shock impedance must be assessed considering the direction of wave propagation *x*. With reference to Table 18 and Eq. (7.9), the results are:

$$Z_{MG} = \rho_{MG} c_{x,MG} = 2500 \frac{kg}{m^3} \cdot 1680 \frac{m}{s} = 4.2 MPa \frac{s}{m} \quad (7.9)$$

$$Z_{Gl} = 42.2 MPa \frac{s}{m}$$

The amplitude of the reflected and transmitted waves at the MoGr/Glidcop interface, with respect to the incident compressive wave propagating from the Molybdenum-Graphite block, can be calculated with Eq. (4.27):

$$\frac{\sigma_T}{\sigma_I} = \frac{2Z_{Gl}}{Z_{Gl} + Z_{MG}} = 1.82$$

$$\frac{\sigma_R}{\sigma_I} = \frac{Z_{Gl} - Z_{MG}}{Z_{Gl} + Z_{MG}} = 0.82$$
(7.10)

The situation is therefore quite close to an infinitely rigid contact, due to the high impedance mismatch between the two materials. Again, at the longitudinal interfaces between each CuCD block and the precedent and subsequent,  $\sigma_T/\sigma_I = 1$  and  $\sigma_R/\sigma_I = 0$ . Based on the results shown for CuCD in section 7.2.1, where the single-block model provided results very close to the model of the full jaw, the former only was investigated and shown in this paragraph. The finite element model is thus analogous to Figure 112, left, with the only difference in the material adopted (MoGr instead of CuCD, without any copper cladding).

In terms of experimental measurements, the signal considered is the one acquired with the strain gauge at the bottom face of the block with reference to Figure 109 (B). In fact, *impact #26* is one of the last at high intensity, and several other strain gauges at the time of the pulse were no more active, as they had been damaged by previous shots.

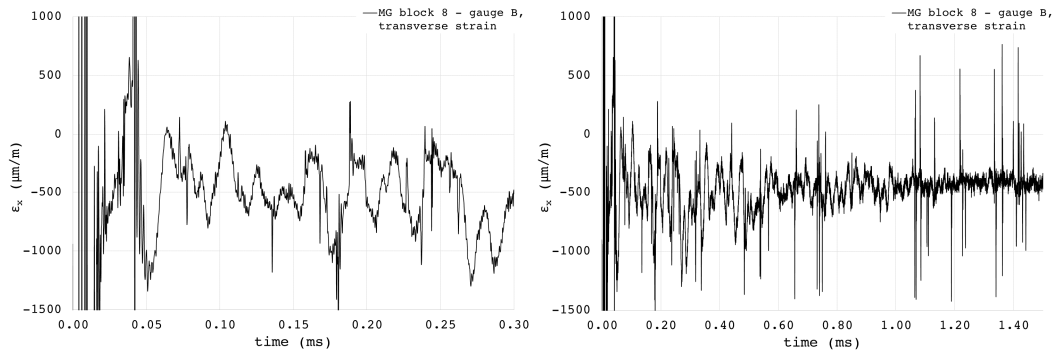


Figure 124. *Impact #26*, MoGr: transverse strain on the bottom face of block 8. Time history of 300  $\mu$ s (left) and 1.5 ms (right).

The experimental signal is shown in Figure 124. Note again the electromagnetic disturbance occurring in the first 20  $\mu$ s after the beam impact. Some spike is also observable all along the signal, most probably due to the strong radiation dose to which the strain gauge was exposed during the testing campaign. It is interesting to consider that the amplitude decay is much less relevant than in the case of CuCD, and the signal enters in the noise amplitude range only after 1 ms, as visible in Figure 124, right. We remember that, in the case of CuCD, the signal/noise ratio

was approaching 1 already after 100  $\mu\text{s}$ , indicating a much more significant relaxation. This is possibly due to the higher compaction of MoGr with respect to CuCD. The porosity of MoGr is estimated in less than 1% [7] while in the case of CuCD it is typically about 7% [2], and in CFC it can reach 25%.

The numerical simulation was performed adopting the linear elastic model described in section 7.1. A time of 175  $\mu\text{s}$  with time steps of 0.1  $\mu\text{s}$  was simulated, with the single block 8 modelled with 45 000 hexahedral elements. The comparison between experimental and numerical results is shown in Figure 125.

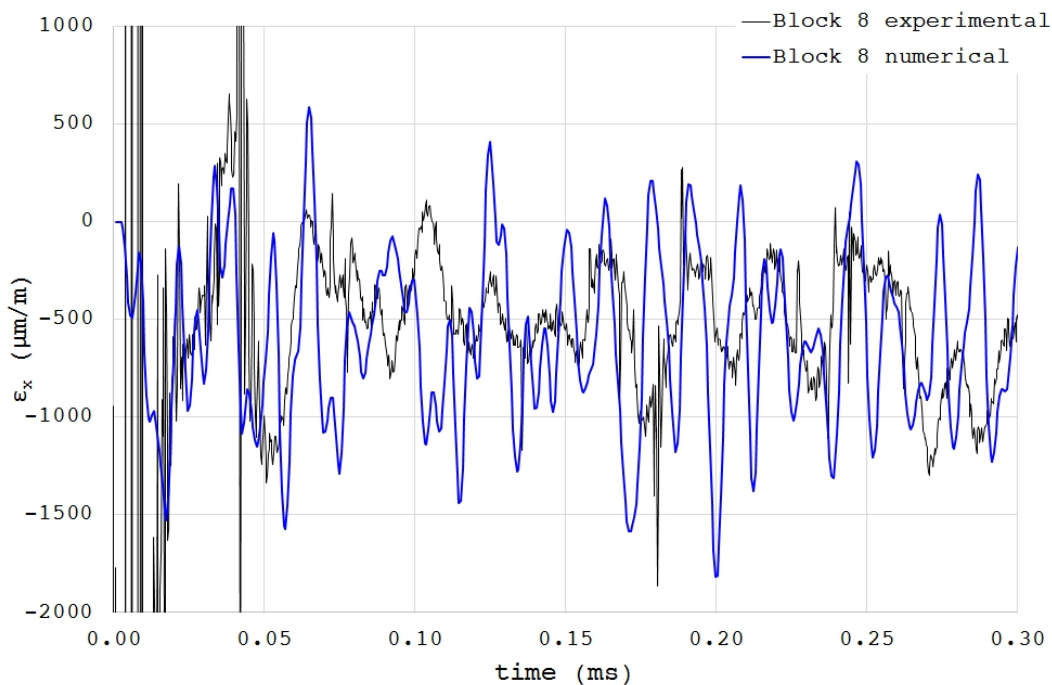


Figure 125. *Impact #26*, MoGr: transverse strain on the bottom face of block 8. Comparison between experimental and numerical results.

As seen in Figure 125, in terms of amplitudes the numerical and experimental results are quite similar, with the linear elastic model which, as expected, slightly overestimates the transverse strain in the control point. Some inelasticity, although much less relevant than in the case of CuCD, is characteristic of the material, as shown in Figure 86, right. Moreover, the porosity of MoGr likely yields to the time-dependent response seen in Figure 124. The construction of a viscoelastic model through dedicated static and dynamic tests, similar to the one built for isostatic graphite and shown in Figure 33 [6], is expected to improve the accuracy of the numerical results.

On the other hand, the main inaccuracy of the numerical model in the strain estimation is related to the characteristic frequencies of the signal. The numerical signal seems, in fact, to include higher frequency content than the experimental data. This is confirmed by an FFT performed on the data and shown in Figure 126.

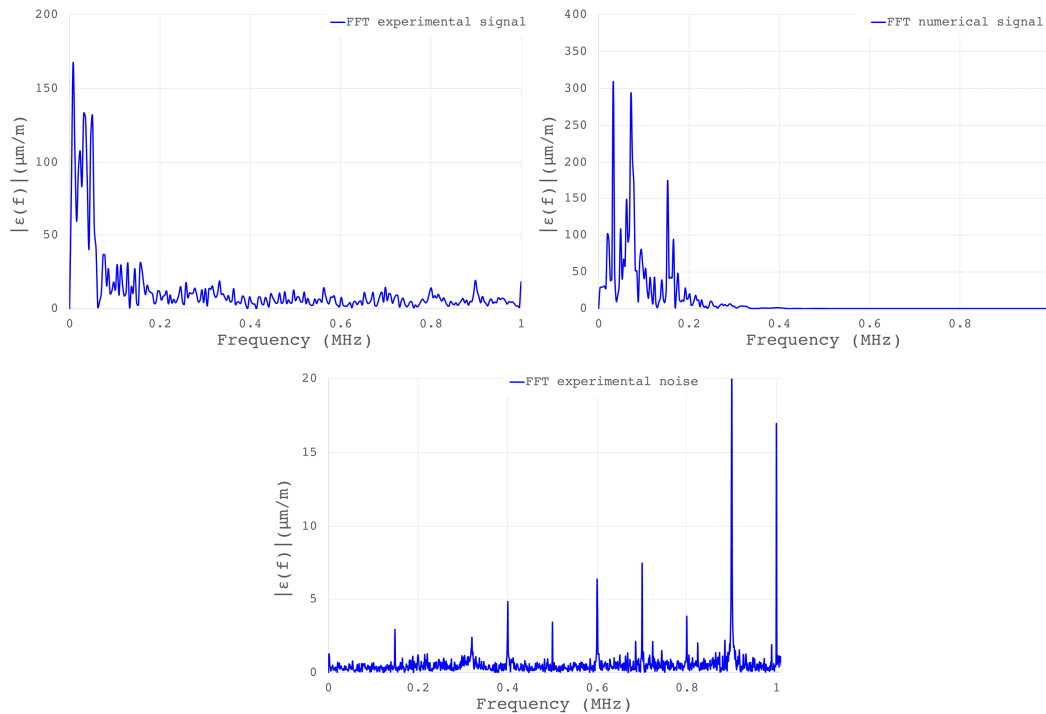


Figure 126. *Impact #26* on MoGr: Fourier transform of measurement and simulation (top left and right). An FFT of the acquired signal before the impact, indicative of the noise, is also shown (bottom).

With respect to the similar exercise done for CuCD, in this case the contribution of noise to the experimental signal is lower, and no frequency peaks related to noise are highlighted in Figure 126, top left. As confirmed by Figure 126, bottom, the intensity of the frequencies associated with noise are indeed almost negligible with respect to those associated with the dynamic wave propagation. Comparing experimental and numerical frequency peaks, the differences already observed in the time domain are confirmed. Peaks at 8 – 23 – 31 – 50 kHz are clearly identified in the experimental signal; peaks close to these can be found also in the numerical response (7 – 19 – 32 – 49 kHz). However, in the FFT of the numerical data, higher frequency content, at 150 kHz and 166 kHz, appears, contrarily to the experimental measure. This could be related to material damping at higher frequencies.

Concluding on the analyses done on the MoGr jaw, the numerical response quite well matches in terms of strain amplitude the experimental acquisition;

however, higher numerical frequencies, most likely associated with the intrinsic material damping, are not observed in the measurement. It is interesting to note that the wave decay occurs, in the case of MoGr with respect to CuCD, at a time one order of magnitude higher. This means that, if the damping is simulated through a viscoelastic model, for the condition of full relaxation (*i.e.* when the wave amplitude is in the range of the background signal) it is possible to evaluate the characteristic decay constants:

$$e^{-\beta_{CuCD}t_{CuCD}} = e^{-\beta_{MG}t_{MG}} \Rightarrow \beta_{MG} = \frac{\beta_{CuCD}t_{CuCD}}{t_{MG}} \sim 0.1\beta_{CuCD} \quad (7.11)$$

where  $\beta_{MG}$  and  $\beta_{CuCD}$  are the decay constants of Molybdenum-Graphite and Copper-Diamond to be used in a viscoelastic model similar to that described in Eqs. (3.33),(3.39), and  $t_{MG}$  and  $t_{CuCD}$  are the full relaxation times, highlighted in Figure 114 and Figure 124, right.

The lower damping observed in MoGr is believed to be correlated with the higher compaction rate, which is above 99% in contrast with the 93% typically achieved on CuCD. The numerical results observed are overall quite satisfying, considering that a simple linear elastic model was adopted to reproduce the MoGr response under proton beam impact; future developments shall include the derivation of inelastic models for the material, time and strain dependent.

### 7.2.3 CFC

In the case of CFC, the shot studied is *impact #7* (Table 29). This scenario was chosen as a reference as it represents the beam injection error case for LHC secondary collimators, and involves a high thermal energy deposition on the jaw, so to generate the highest intensity signal on the strain gauge measuring points. Unfortunately, in spite of this precaution, due to the low density of CFC the energy absorption of the material under beam impact is still very low, and the entity of the stress waves propagating from the impact point can hardly be distinguished from the background noise, as it will be further detailed. The thermal energy distribution over the jaw length is reported in Figure 127. The CFC absorber is made of one monolithic bar, 1 m long. As shown in Figure 127, left, the peak energy is attained on at the middle of the jaw, while the total energy over the *xy* section is maximum at 90 cm from the beginning of the absorber.

Table 29: Characteristics of the case study for CFC.

Impact identifier	$N_b$	$n_{tot}$	$E_{tot}$ (MJ)	$t_d$ ( $\mu$ s)	$\sigma$ (mm)	$\eta_x$ (mm)	$\eta_y$ (mm)
#7	288	$3.66 \times 10^{13}$	2.58	7.85	0.61	-3.05	-5.00

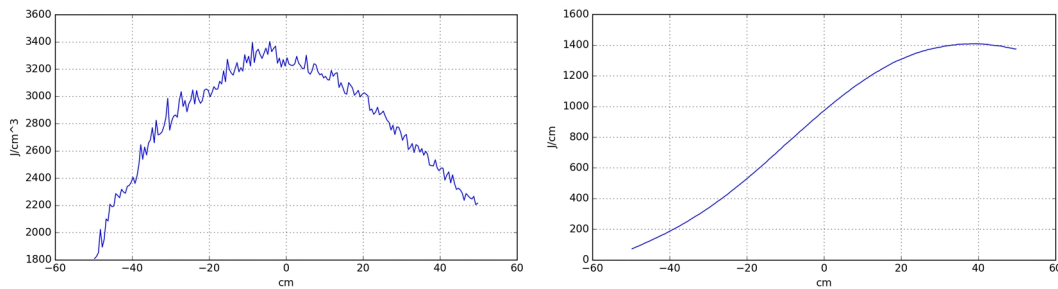


Figure 127. Left: energy peak on the CFC absorber over the  $z$  coordinate for *impact #7*. Right: total energy per longitudinal section. FLUKA maps are courtesy of E. Skordis.

The model adopted for the analysis is not symmetric along the  $XZ$  plane, as the impact presents a 5 mm offset in the  $y$  direction (see Table 29). A full model was therefore conceived, and the temperature distribution on the absorber after the impact is shown in Figure 128.

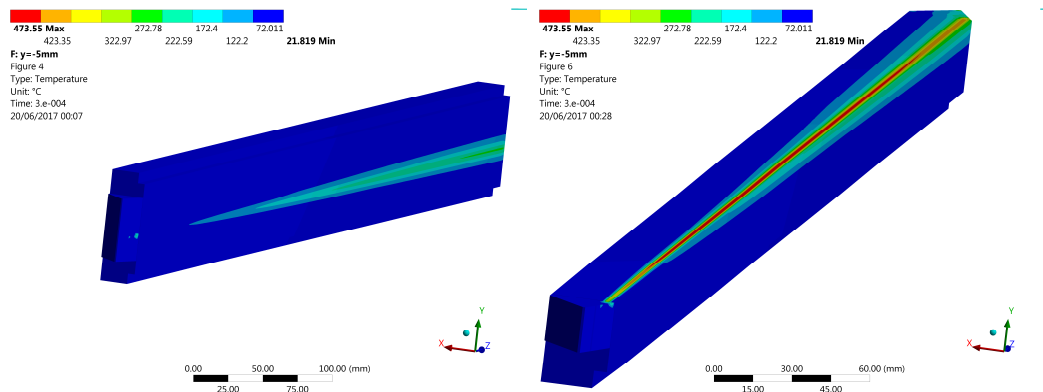


Figure 128. Left: temperature distribution after impact #7 on the CFC absorber. Right: section view of the absorber along a plane parallel to  $XZ$ , vertically offset by  $-5$  mm, showing the maximum temperature achieved.

The 3D model entails the full CFC absorber; again, looking at the results of the CuCD calculation, the surrounding elements (clamps, housing) were not included in the model. The numerical simulation was performed adopting the linear elastic model described in section 7.1. A time of  $300 \mu$ s with time steps of  $0.1 \mu$ s was simulated, with the jaw modelled with 254 000 hexahedral elements. In terms of

shock impedance of the CFC with respect to the Glidcop components, the values are:

$$Z_{CFC} = \rho_{CFC} c_{x,CFC} = 1890 \frac{kg}{m^3} \cdot 1220 \frac{m}{s} = 2.3 MPa \frac{s}{m} \quad (7.12)$$

$$Z_{Gl} = 42.2 MPa \frac{s}{m}$$

The amplitude of the incident, reflected and transmitted waves at the CFC/Glidcop interface, is equal to:

$$\frac{\sigma_T}{\sigma_I} = \frac{2Z_{Gl}}{Z_{Gl} + Z_{CFC}} = 1.90 \quad (7.13)$$

$$\frac{\sigma_R}{\sigma_I} = \frac{Z_{Gl} - Z_{CFC}}{Z_{Gl} + Z_{CFC}} = 0.90$$

The adequate boundary is even closer to an infinitely rigid contact than in the case of MoGr.

As anticipated, the amount of energy absorbed by the CFC jaw, even in a case of high intensity entailing impact of 288 bunches, was not high enough to induce a relevant thermo-structural response of the component, and the acquired signal is in the noise range, with a strain amplitude lower than 100  $\mu\text{m}/\text{m}$  (Figure 129). On top of low thermal energy absorption, this is due to the specific heat of CFC, which is higher than in the case of CuCD and MoGr (Figure 81, right). The induced temperature on the jaw in the examined scenario is therefore less than one half of the level reached on CuCD and MoGr (Figure 111, Figure 123 and Figure 128).

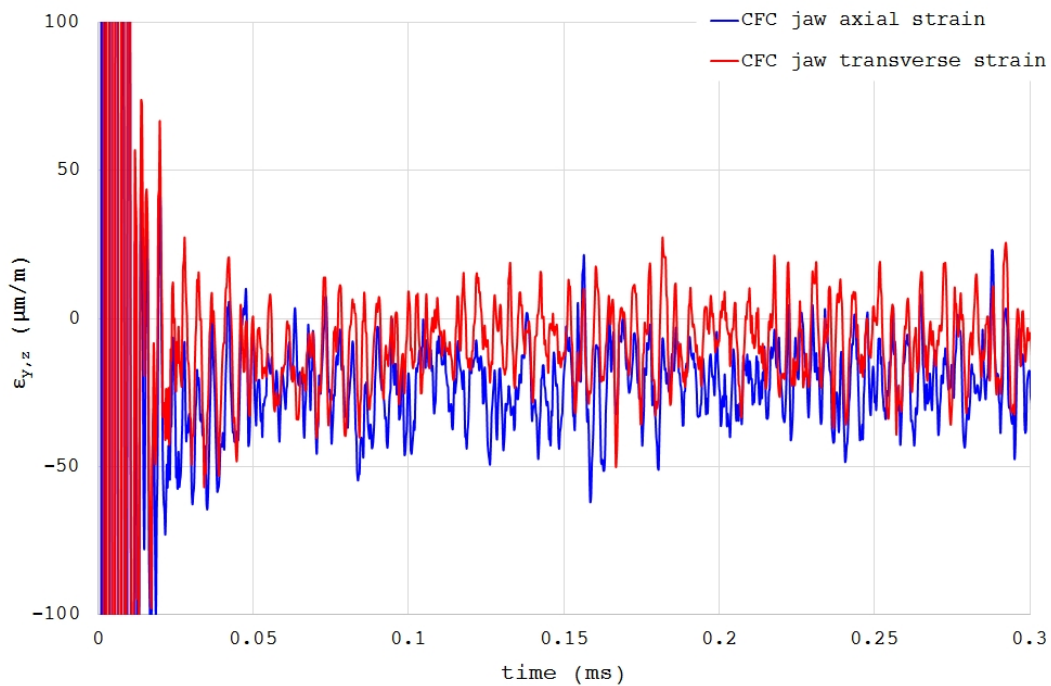


Figure 129. *Impact #7*, CFC: experimental transverse and axial strain on the back face of the jaw, at a longitudinal coordinate  $z = 780$  mm.

The low amplitude of the strains achieved during *impact #7* is also confirmed by the numerical analysis run with a perfectly elastic model. Numerically calculated strains, shown in Figure 133, have an average amplitude of about  $100 \mu\text{m}/\text{m}$ . As observed in the case impacts for CuCD and MoGr, perfectly elastic models naturally overestimate the simulated strain; moreover, the material damping, which is expected to be significant for MoGr, as it is by far the most porous analysed material (25%, compared with CuCD 7% and CFC less than 1%). It is therefore not surprising that the strain gauges, at the end of the electromagnetic perturbation duration, lasting  $20 \mu\text{s}$ , do not distinguish the physical signal from the background noise.

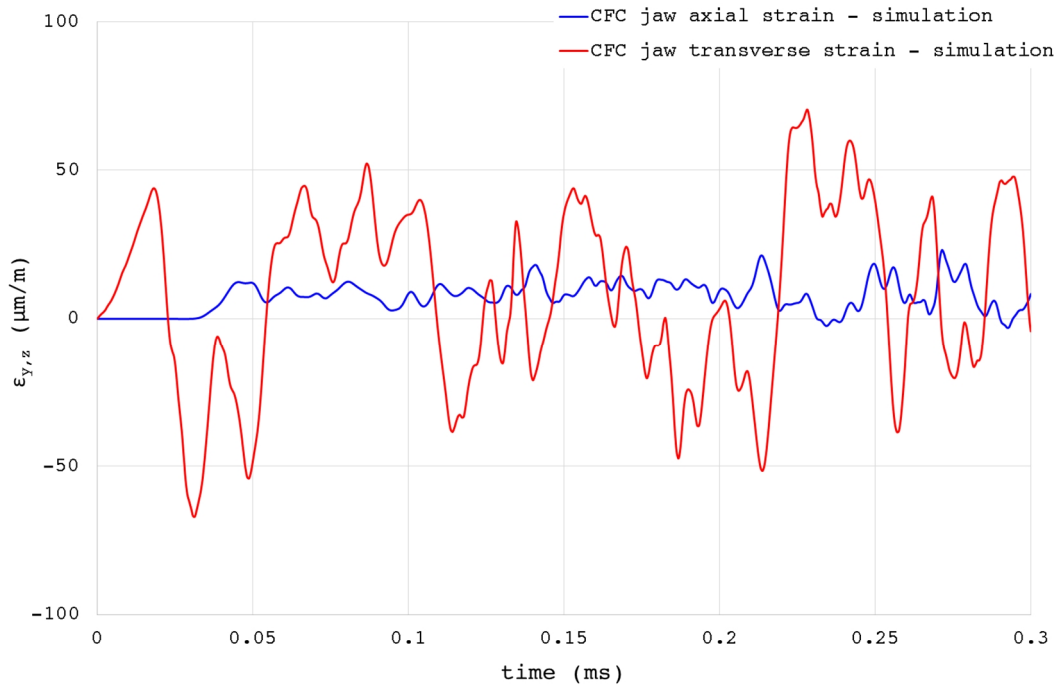


Figure 130. *Impact #7*, CFC: numerical transverse and axial strain on the back face of the jaw, at a longitudinal coordinate  $z = 780$  mm.

In spite of the limitations in the signal acquisition for the case of CFC, it is interesting to examine more in detail the results of the numerical simulation, as an impact on the monolithic jaw block falls within the scenario described in section 4.2.1. The jaw size, in fact, is  $1000 \times 80 \times 25$  mm<sup>3</sup> and the component can be approximated to a 1D body. In Figure 130, differently from what observed in section 4.2.1, the amplitude of the transverse strain, associated with the wave propagating radially to the back surface from the impact point, is higher than the amplitude of the longitudinal strain induced by the two rarefaction waves propagating from the free ends. As the ratio of length over height/thickness is comparable to the graphite rod analysed in section 4.2.1, the difference is likely explained by the anisotropy of CFC. In particular,  $E_x$  is only 2.8 GPa, while  $E_y$  and  $E_z$  are 57.5 and 93 GPa respectively. The wave propagating along  $x$  produces therefore a higher deformation due to the lower stiffness of the material in that direction. The triaxiality of the problem, in spite of the rod-like geometry, is therefore not negligible but, on the contrary, is very significant.

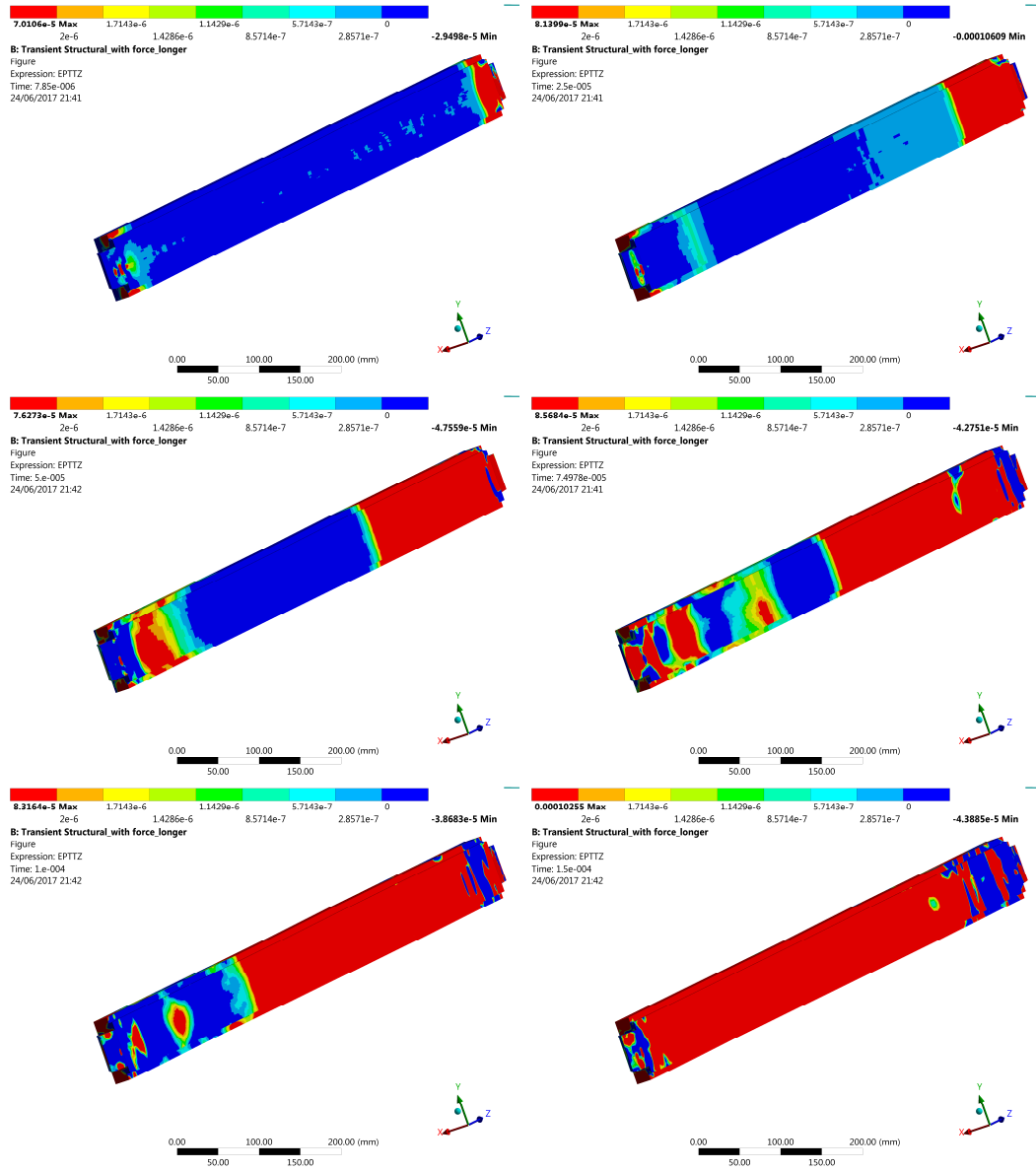


Figure 131. *Impact #7, CFC*: images of the total axial strain at different time instants: 7.85  $\mu$ s (top left), 25  $\mu$ s (top right), 50  $\mu$ s (center left), 75  $\mu$ s (center right), 100  $\mu$ s (bottom left) and 150  $\mu$ s (bottom right).

The origination and propagation of the two rarefaction waves on the CFC jaw is shown in Figure 131. Note that, as observed in the study presented in section 4.2.1, the amplitude of the stress wave propagating from the downstream end is significantly higher than in the other one, coming from the upstream end. This is related to the unbalanced thermal energy deposition along the  $z$  coordinate (Figure 127, right).

The velocity of the axial shock waves on the CFC jaw can be calculated with the second equation of system (2.12):

$$c_z = \sqrt{\frac{E_z}{\rho}} = \sqrt{\frac{93 \times 10^9}{1890}} = 7014 \text{ m/s} \quad (7.14)$$

This can be confirmed by looking at the time at which the rarefaction wave originated at the downstream free end reaches the control point placed at  $z = 780$  mm. The distance of this point from the downstream end is 220 mm, and the time of the wave passage is:

$$t_{z,780} = \frac{0.22 \text{ m}}{7014 \text{ m/s}} = 31.3 \mu\text{s} \quad (7.15)$$

which is confirmed examining the blue curve in Figure 130.

As a conclusion on the study of the CFC jaw response, the material presents low density and thermal energy absorption, such that the acquired strains are in the order of magnitude of the background noise. The behaviour of the jaw was then assessed only by numerical means, profiting of the considerations on rod elements impacted by particle beams, given in section 4.2.1. The jaw response shows similarities with the aforementioned graphite rod element, with two rarefaction waves propagating from the free ends, and the cylindrical compressive wave propagating radially towards the CFC lateral surfaces. Differently from the case of the graphite rod, here the transverse strains are relevant, and actually of amplitude higher than the axial strains. This is due to the anisotropy of the material, which is significantly more compliant in the  $x$  direction with respect to the two directions of the planes along which the carbon fibres are dispersed. From the robustness point of view, the low dynamic strains induced by the impact are a positive outcome of the test, as the material proved to be almost insensitive event to the highest intensity impacts; this, however, also means that an in-depth experimental/numerical benchmarking of the phenomena taking place after proton impact must involve an optimized design of the CFC target during future HiRadMat tests. This will be the core of the *Multimat* experiment [8], scheduled in HiRadMat in late 2017. More on the experiment will be mentioned in the final chapter of this thesis.

### 7.3 Glossary

Symbols are listed in chronological order with respect to their appearance in the text.

<b>Symbol</b>	<b>Definition</b>	<b>SI unit</b>
$\eta_x$	Horizontal impact coordinate	m
$p$	Pressure	Pa
$\rho$	Density	kg·m <sup>-3</sup>
$K$	Bulk modulus	Pa
$E$	Energy density	J·m <sup>-3</sup>
$\gamma_0$	Grüneisen parameter	–
$\alpha$	Thermal expansion coefficient	K <sup>-1</sup>
$\rho_0$	Initial density	kg·m <sup>-3</sup>
$c_v$	Specific heat capacity at constant volume	J·kg <sup>-1</sup> ·K <sup>-1</sup>
$\sigma_f$	Bending stress	Pa
$F$	Force	N
$d_1$	Distance between the inner loading roller and the outer support	m
$b$	Width of the flexural specimen	m
$h$	Thickness of the flexural specimen	m
$M$	Bending moment	N·m
$\varepsilon_{max}^{tot}$	Maximum total axial strain	–
$\sigma_z$	Axial stress	Pa
$I_x$	Moment of inertia around the $x$ axis	m <sup>4</sup>
$\sigma_{eq}$	Equivalent stress	Pa

---

$\varepsilon_{eq}^{tot}$	Total equivalent strain	–
$\varepsilon_{eq}^{pl}$	Equivalent plastic strain	–
$N_b$	Number of bunches	–
$n_b$	Number of particles per bunch	–
$n_{tot}$	Number of particles per pulse	–
$E_{tot}$	Beam stored energy	J
$\Delta t$	Bunch spacing	s
$\sigma$	Variance of the Gaussian distribution	m
$\eta_y$	Vertical impact coordinate	m
$Z$	Shock impedance	Pa·s·m <sup>-1</sup>
$c$	Speed of sound	m·s <sup>-1</sup>
$\sigma_T$	Stress amplitude of the transmitted wave	Pa
$\sigma_I$	Stress amplitude of the incident wave	Pa
$\sigma_R$	Stress amplitude of the reflected wave	Pa
$c_f$	Friction coefficient	–
$E$	Young's modulus	Pa
$\nu$	Poisson's ratio	–
$\beta$	Amplitude decay constant	s <sup>-1</sup>
$t_d$	Duration of the thermal pulse	s
$E_x$	Young's modulus along the $x$ direction	Pa
$E_y$	Young's modulus along the $y$ direction	Pa
$E_z$	Young's modulus along the $z$ direction	Pa

---

$c_z$                                       Speed of sound in the  $z$  direction                                       $\text{m}\cdot\text{s}^{-1}$

## References

- [1] V. Y. Chekhovskoi, V. D. Tarasov and Yu. V. Gusev (2000). Calorific properties of liquid copper. *High Temperature*, Vol. 38, No. 3, pp. 394–399.
- [2] N. Mariani (2014). Development of Novel, Advanced Molybdenum-based Composites for High Energy Physics Applications, CERN-THESIS-2014-363.
- [3] A. C. Victor (1962). Heat capacity of diamond at high temperatures. *The Journal of Chemical Physics*, Vol. 36, pp. 1903–1910.
- [4] ASTM C1161-02c (2002). Standard Test Method for Flexural Strength of Advanced Ceramics at Ambient Temperature. *American Society for Testing and Materials International*.
- [5] H. Kolsky (1963). Stress waves in solids. Dover Publications, ISBN 0486610985.
- [6] L. Peroni, M. Scapin, F. Carra and N. Mariani (2013). Investigation of dynamic fracture behavior of graphite. In B. Basu, *Damage assessment of structures X*, Trans Tech Publications Inc, pp. 103-110. ISBN 978-303785796-0.
- [7] J. Guardia, A. Bertarelli, F. Carra, N. Mariani and S. Bizzaro (2017). Development and properties of high thermal conductivity molybdenum-carbide-graphite composites. *Submitted to Carbon*.
- [8] F. Carra *et al.* (2017). The “Multimat” experiment at CERN HiRadMat facility: advanced testing of novel materials and instrumentation for HL-LHC collimators. *Proc. IPAC’17*, Copenhagen, Denmark.

# Chapter 8

## Conclusions

In the present work, the mechanisms correlated with a quasi-instantaneous temperature change on the matter were explored. The understanding of the phenomenon allows designing engineering materials and components with an optimal behaviour when, due to the short time scales involved with the heating or cooling processes, the body expansion or contraction are initially prevented by its mass inertia. In this case, the dynamic response of the component is excited and stress waves originate and propagate inside the material, with potential consequences on its structural resistance. From the practical point of view, it is much easier to rapidly inject energy into a system than removing it; additionally, the consequences of a high and rapid temperature increase on a component are more serious than the opposite case of fast cooldown, as they entail a decrease of the material strength and potentially transition to the liquid, gas and plasma phases. For this reason, the focus of this PhD thesis is on quasi-instantaneous heating processes, in particular those induced by means of particle beam impacts, which entail high energy and energy densities on the impacted material. Similar rapid thermal loads on materials can be achieved also with lasers and electrical pulses. However, laser beams store low energies, and the most extreme phenomena (spallation, micro-spallation, as well as gas and plasma generation) are achieved only on a small surface spot of the material. On the other hand, electrical pulses are typically slower and the temperatures, pressure and velocities which can be reached on the material are lower. The study of the behaviour of components impacted by hadron or lepton beams is of paramount importance in the design of particle accelerators.

After an overview of the relations analytically describing the three main domains of thermal phenomena in terms of heating rate (quasi-static, slow-transient and quasi-instantaneous), experimental examples, occurred mostly in particle accelerators, were given on the fastest heating scenario. The dynamic response of materials to quasi-instantaneous heating was then evaluated as a function of the stress waves originated. At low thermal energies, stress waves remain below the yield stress of the material, in the elastic regime, and the dynamic problem, in

simple geometries, can often be solved analytically. When the amplitude of the wave surpasses the yield stress of the material, plasticity takes place and the signal is dispersed into an elastic wave travelling at the speed of sound, and plastic waves with different amplitudes propagating at lower velocity, equivalent to the slope of the  $\sigma - \varepsilon$  curve for each specific amplitude. The evolution of the flow stress above yielding depends on strain, strain rate and temperature. The dynamic response in this regime can thus be solved analytically only in simple cases, for example under the hypothesis of bilinear or power hardening, independent of strain rate and temperature. Finally, the shock regime can be attained only at critical levels of energy and pressure induced by the fast heating. In this scenario, an elastic precursor is followed by plastic waves at subsonic speed; when the shock condition is reached, supersonic waves originate behind the elasto-plastic train, compacting the wave front and generating a sharp discontinuity in temperature, pressure and density. An analysis was performed to demonstrate that the critical shock condition, when the load is thermally driven, can be reached only at temperatures above the melting point (and in some case above vaporization) of the material. The shock regime, involving strong material nonlinearities and discontinuity of the main functions, requires the adoption of finite element codes for the study of the thermomechanical problem. The hydrostatic response of shocked materials depends on the equation of state, while the deviatoric contribution to the stress tensor is controlled by the strength model. Failure models govern fracture mechanisms given by void coalescence, spallation and micro-spallation. Examples of the main categories of EOS, strength and failure models, were given. A new method to explore unusual regions of the EOS, based on intense isochoric heating driven by particle beams, was presented and detailed.

In the second part of the thesis, the phenomena induced by a quasi-instantaneous heating, due to particle beam impact on the matter, were explored in detail. At the impacted volume, changes of phase in the material structure may take place, especially at high thermal energies. From the impact point, compressive cylindrical elastic, elastoplastic and, in some extreme case, shock waves develop and propagate, radially and axially, through the structure, potentially leading to a failure of the structure. The most common failure scenario involves a reflection of the wave at the interface with a material with lower shock impedance, including the case of free surface. The reflected wave turns into a tensile wave, generating a fracture by spallation of the surface when the spall strength of the material is overcome. When the impact is close to a free surface, the material may be in the liquid state and the tensile wave induces, in this case, a pulverization of

the surface into tiny droplets, ejected towards the surrounding. The phenomenon is called micro-spallation. In the intermediate scenario, when the molten material is contained within a still-solid envelope, the pressure of the expanding liquid can either generate plasticity into the solid, or even provoke its failure, with an ejection of combined liquid and solid particles from the body. The axial oscillation of impacted bodies, on the other hand, is more relevant in the case of slender rods, where the radial inertia effects are negligible. Two rarefaction waves propagate from the free surfaces and superpose to a statically compressed material state, with an amplitude which, for a constant thermal energy, inversely increases with the decrease of the rod section. In the case of an impact offset with respect to the neutral axis, flexural waves of more significant amplitude and period are originated on the rod. To explore the mechanisms of each phenomenon, numerical studies by means of implicit (ANSYS) and explicit (Autodyn) finite element codes were presented and combined, when available, with analytical methods and experimental tests performed in particle accelerator facilities. An important result of this study is the numerical confirmation that, due to the intrinsic nature of cylindrical waves, the shock condition can rarely be reached in existing particle beam testing facilities, and only for heavy, high-energy absorbing materials. However, the shock regime can be more commonly experienced in high energy accelerators, such as the HL-LHC and the FCC, and should be considered in the design of components interacting with the particle beam.

In the final part of the thesis, the studies performed were applied to the design and engineering of HL-LHC accelerator components known as collimators. These components, closely interacting with the beam particles, are potentially submitted to accidental impacts, whose consequences on the collimator and on the overall machine must be minimized. With this goal, new composites were developed in recent years to replace the currently adopted carbon-fibre-reinforced carbon (CFC), combining the good thermal and electrical properties of metals with the high thermal stability of carbon allotropes such as graphite and diamond. The most promising ones are Copper-Diamond (CuCD) and Molybdenum-Graphite (MoGr); these materials were fully characterized in order to derive EOS and constitutive models necessary for the study of their response under intense isochoric heating. The measurements, performed at the CERN mechanical laboratory and at Politecnico di Torino, were often combined with finite element analyses to extend the thermal and mechanical results to anisotropic materials, complex specimen shapes and different loading conditions from what foreseen by the international Standards. As the materials are still in an R&D phase, at this stage only preliminary

measurements have been performed, and the models rely on linear EOS, as well as on elastic or elastoplastic strain-rate-independent strength and failure models. Nevertheless, the models were believed to produce reliable results when adopted in numerical codes in the study of the accidental scenarios of HL-LHC collimators, due to the limited amplitude of the stress waves expected in these cases. To prove this, and to experimentally verify the collimator resistance under the direct impact of proton beams involving energy densities typical of the HL-LHC design scenarios, a test was devised and performed in 2015 at the CERN HiRadMat facility. Three jaws, in CFC, MoGr and CuCD, were extensively instrumented, and submitted to proton impacts at increasing intensities. The three materials well sustained the accidental design scenarios of HL-LHC, without experiencing a functional failure. From the machine operational point of view, the test also highlighted the importance of adopting MoGr tapered extremities instead of Glidcop Al-15 ones, as the latter failed under high intensity impacts. The acquired data were compared with the results of the finite element analyses, to verify the precision of the models adopted.

The dynamic response of the CuCD jaw tested during HRMT-23 could be quite well replicated numerically, except for the observed decay in the amplitude of the stress wave during time. The phenomenon can be related to a combination of viscoelastic and viscoplastic behaviour of the constituting porous composite material. This could be confirmed by future dynamic tests aimed at deriving the constitutive laws controlling the strain rate dependent response. Additionally, an inhomogeneous mesoscale model, imitating the random distribution of diamond particles inside the copper matrix of the material, was built. This model can reproduce the wave dispersion at the interface between the material constituents; however, it is computationally demanding, and should be adopted only when strictly necessary, i.e. when the expected wavelengths are very short and in the order of the diamond size. Moreover, a mesoscale model introduces further complexities related to the modelling of the copper/diamond interface, which should be carefully characterized in terms of adherence, assumed to be ideal in the scope of this work.

Concerning the MoGr jaw, the numerical response quite well matched in terms of strain amplitude the experimental acquisition; however, higher numerical frequencies, most likely associated with the intrinsic material damping, were not observed in the measurement. An important result is the wave decay occurring, in the case of MoGr with respect to CuCD, at a time one order of magnitude higher. The lower damping observed in MoGr is believed to be correlated with the higher

compaction rate, which is above 99% in contrast with the 93% typically achieved on CuCD.

Finally, in the case of CFC, the material presents low density and thermal energy absorption, such that the acquired strains are in the order of magnitude of the background noise. The behaviour of the jaw was then assessed only by numerical means, profiting of the considerations on rod elements impacted by particle beams, given in section 4.2.1. The jaw response shows similarities with the aforementioned graphite rod element, with two rarefaction waves propagating from the free ends, and the cylindrical compressive wave propagating radially towards the CFC lateral surfaces. Differently from the case of the graphite rod, here the transverse strains are relevant, and actually of amplitude higher than the axial strains. This is due to the anisotropy of the material, which is significantly more compliant in the  $x$  direction with respect to the two directions of the planes along which the carbon fibres are dispersed.

The numerical techniques adopted in this PhD work are mastered and proved to be very precise in case of material models well defined at the expected conditions of temperature, pressure and density, as demonstrated by several observations at the CERN HiRadMat facility, both during HRMT-14 and, partially, HRMT-23. Future developments of this work necessarily involve a continuation of in-depth studies of the novel materials, starting with the full exploitation of the HRMT-23 experimental results. Recently, the test bench has been opened and, at the time of writing, the jaws are being disassembled, to prepare the single material blocks for non-destructive and destructive analyses (Figure 132 and Figure 133). These include the following measurements:

- Thermophysical properties
- Dimensional control of the blocks, to evaluate the extent of permanent deformation (if any)
- Non-destructive tests (x-rays, ultra-sounds, *etc.*) for potential inner fracture
- Profilometry of the surface scratch on the active face
- Micro-hardness
- Optical and SEM microscopy
- Destructive tests for the analyses of possible internal delamination and other fracture mechanisms

- Evaluation of the behaviour of the surrounding structure, such as cooling pipes, clamps, housing, BPM

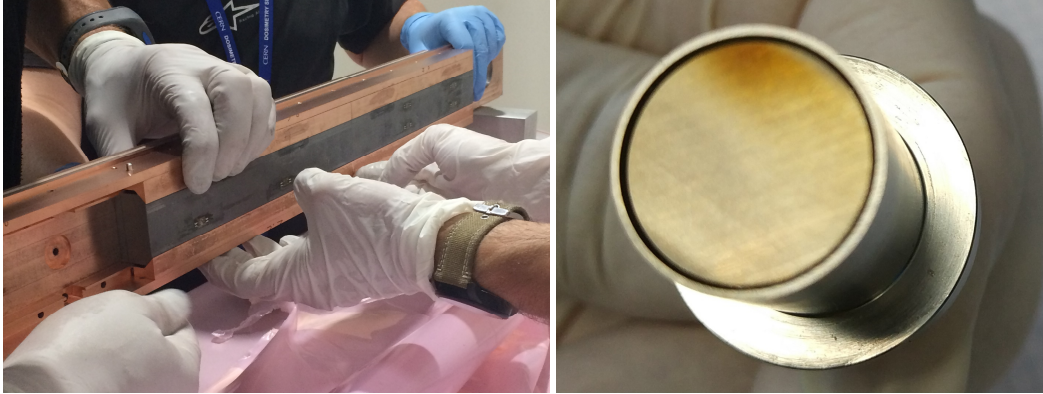


Figure 132. HRMT-23 post-mortem: dismounting of the MoGr jaw (left) and of the oxidized BPM button of the CFC downstream tapering (right).

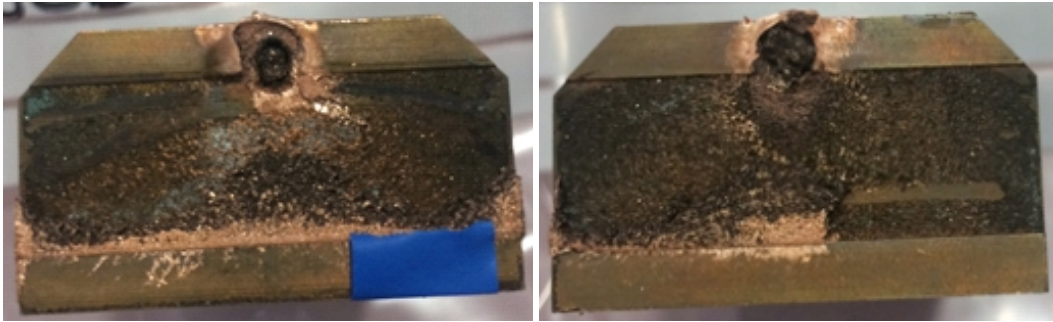


Figure 133. HRMT-23 post-mortem: CuCD block 4, upstream (left) and downstream (right).

In general, even with simple material models, the comparison between experimental and numerical results is satisfying however, further model improvements are planned in the near future to address some limitations which appeared during the analyses. These also require further in-depth experimental characterization. In the case of CuCD, for example, the elastoplastic model should be extended to the case of strain rate and temperature dependent flow stress. Moreover, the experimental damping observed at low stress amplitude must be addressed including a viscoelastic component in the model. Concerning MoGr, the material inelasticity has to be taken into account; for this scope, a test with the split-Hopkinson pressure bar at Politecnico di Torino is already planned, and the specimens for the characterization are under preparation (Figure 134).



Figure 134. M6 specimens in MoGr for experimental characterization with the split-Hopkinson pressure bar.

In the case of CFC, the main limitation of the HRMT-23 setup was the low signal-to-noise ratio achieved even at the maximum intensities available in HiRadMat, which impeded a reliable benchmarking with the numerical simulations performed. This was an intrinsic restriction of the material itself, which has a very low energy absorption under beam impact, and of the test bench, whose main goal was to validate full-scale collimator jaws for HL-LHC. To address such limitations, a new experiment called *Multimat* [1] is planned in HiRadMat in late 2017. The test will characterize materials using simple rod-like shapes, similar to the geometry of the problem studied in section 4.2.1. The simplicity of the geometry will allow disentangling the different contributions to the overall dynamic response, and the small section of the targets will increase the beam-induced axial stress waves. Several strain gauges will be mounted at different longitudinal positions, to assess the dissipative behaviour of the material. For the lightest materials, the amplitude of the signal may still be too small compared to the background noise; in this case, the flexural oscillation of the component will be activated by off-centred impacts. As seen in section 4.2.2, flexural stresses are of higher amplitude and lower frequency, and will be easy detected by the instrumentation system.

The Multimat test bench (Figure 135) will allow testing up to 15 materials and new electronic devices; it features a leak-tight aluminium container hosting 16 target stations<sup>31</sup>, each 1 m long and supported on a rotatable sample holder, separated by protective metal sheets. The target stations will be extensively instrumented, with strain gauges, pressure sensors and thermal probes, as well as

---

<sup>31</sup> One target line will remain free, to be used as a parking position.

remote instrumentation such as rad-hard camera and LDV placed in a shielded bunker.

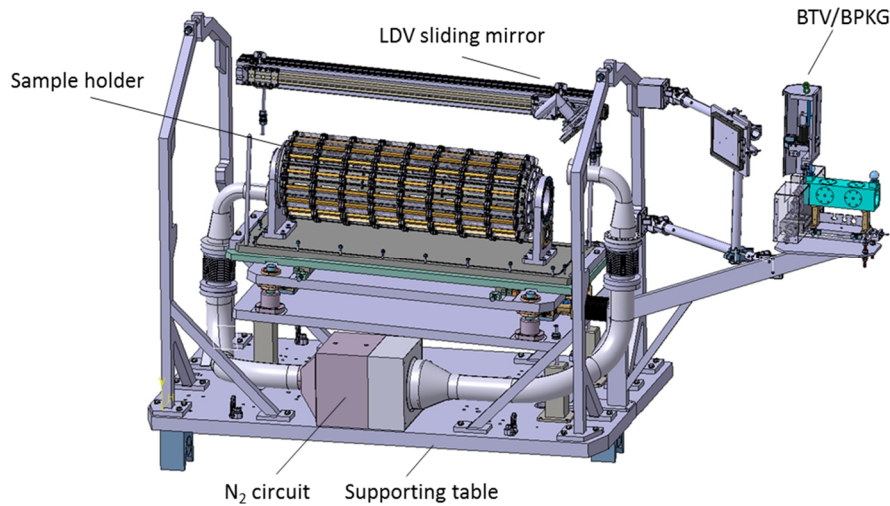


Figure 135. Inner view of the Multimatt test bench. The aluminum tank is hidden in this view. The beam comes from the right.

An actuation system will guarantee the rotation of the sample holder and the vertical/horizontal adjustment of the specimen position in the plane perpendicular to the beam line. Stepper motors and leadscrews will be used for the horizontal and vertical movement of the whole tank. The rotation of the sample holder ( $\pm 180^\circ$ ) will be assured by a Geneva mechanism, consisting of a stainless steel driven wheel and a brass cam. Extensive calculations were performed to optimize the geometry and verify the stresses and accelerations on the elements in operation. Moreover, due to the criticality of the mechanism, a mock-up was built and tested, to verify the precision and repeatability of the system after a high number of cycles (Figure 136). The sample holder is an aluminium rotatable barrel, with 16 positions for material samples and instrumentation, featuring elliptical holes for the passage of the instrumentation wires.

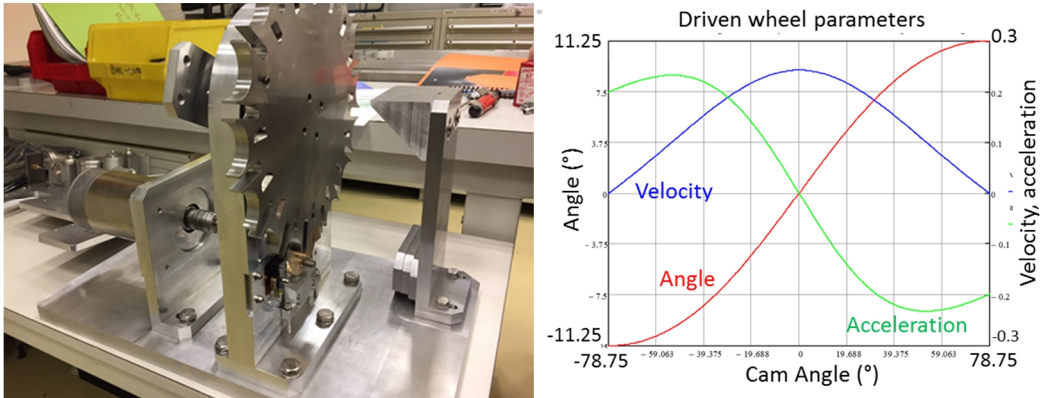


Figure 136. Left: mock-up of the Geneva mechanism. Right: driven wheel parameters as function of the cam angle.

The supporting system hosts targets of variable length, for a total of 1 m per line, and a section with typical dimension comprised between 8 and 12 mm. Supports are adjustable by means of pins, to match the required specific length for each material (Figure 137, left). The targets will include CFC, CuCD and MoGr, as well as other materials of use for beam intercepting devices, like graphite, SiC and heavy alloys, and novel materials considered for future accelerators such as carbon foams (Figure 137, right). The specimens will be positioned on graphitic elastic supports at the two extremities, with a contact pressure granted by springs. A spacer is adopted to change the spring pre-compression adapting the specimen to the desired size. Graphite was chosen because of the transparency to the beam, for its shock damping properties [2] and low shock impedance.

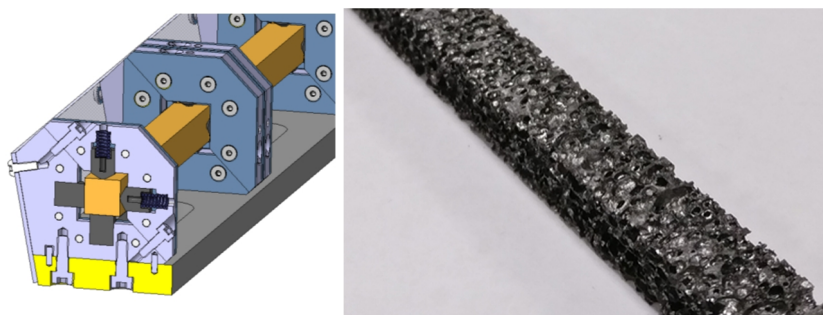


Figure 137. Left: specimen supporting system. Right: carbon foam rod.

As a final word, the author believes that the core of this work goes beyond the goals related to the design of components interacting with particle beams and lasers. The methods presented can be adopted whenever a material is submitted to a fast heating, and the novel metal-carbon and ceramic-carbon composites developed for

use in HL-LHC collimators present properties that are appealing for several high-end industrial applications. Examples include thermal management for electronics, turbines for energy production, high-temperature aerospace components, advanced braking systems in automotive, and, more in general, every application where shock-resistant and heat-diffusive materials are required.

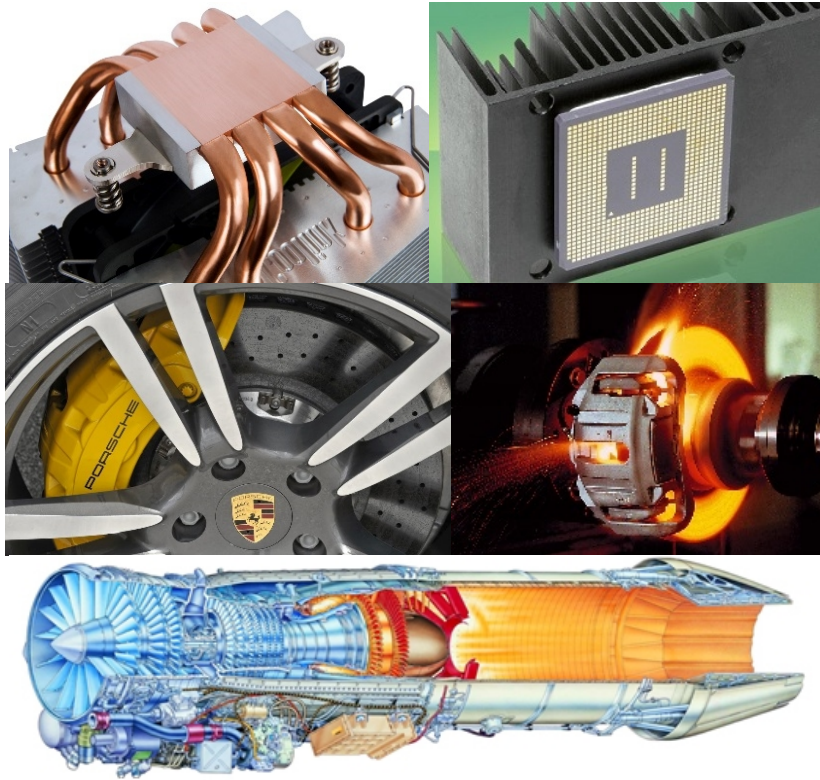


Figure 138. Examples of potential industrial applications for the novel metal-carbon and ceramic-carbon composites under development for particle accelerators, studied in this PhD thesis.

## References

- [1] F. Carra *et al.* (2017). The “Multimat” experiment at CERN HiRadMat facility: advanced testing of novel materials and instrumentation for HL-LHC collimators. *Proc. IPAC’17*, Copenhagen, Denmark.
- [2] L. Peroni, M. Scapin, F. Carra and N. Mariani (2013). Investigation of dynamic fracture behavior of graphite. In B. Basu, *Damage assessment of structures X*, Trans Tech Publications Inc, pp. 103-110. ISBN 978-303785796-0.